Test Beam Measurements for the Upgrade of the CMS Pixel Detector and Measurement of the Top Quark Mass from Differential Cross Sections

Dissertation
zur Erlangung des Doktorgrades

im Fachbereich Physik
der Fakultät für Mathematik, Informatik und Naturwissenschaften
der Universität Hamburg

vorgelegt von Simon Spannagel
Hamburg, 2015

Gutachter der Dissertation:	Prof. Dr. Erika Garutti	Universität Hamburg
	Prof. Dr. Joachim Mnich	DESY/Universität Hamburg
	Prof. Dr. Martin Pohl	Université de Genève
Gutachter der Disputation:	Dr. María Aldaya Martín	DESY
	Prof. Dr. Elisabetta Gallo	DESY/Universität Hamburg
	Prof. Dr. Erika Garutti	Universität Hamburg
	Prof. Dr. Jan Louis	Universität Hamburg
	Prof. Dr. Joachim Mnich	DESY/Universität Hamburg
Datum der Disputation:		22. April 2016

Some results presented in this thesis have been shown previously in the following publications:

[166] H. Jansen et al., "Performance of the EUDET-type beam telescopes", (2016). Submitted to *Eur. Phys. J. Tech. Instrum.* arXiv:1603.09669.

[185] S. Spannagel, "Status of the CMS Phase I Pixel Detector Upgrade", *Nucl. Instr. Meth. Phys. A* (2016) doi:10.1016/j.nima.2016.03.028, arXiv:1511.06084.

[156] S. Spannagel, B. Meier, and H. Perrey, "The pxarCore Library - Technical Documentation, Reference Manual, and Sample Applications", Technical Report CMS-NOTE-2016-001, CERN, Geneva, Oct, 2015.

[184] S. Spannagel, "Test beam campaigns for the CMS Phase I Upgrade pixel readout chip", *J. Instrum.* **9** (2014), no. 12, C12001, doi:10.1088/1748-0221/9/12/C12001, arXiv:1410.1399.

Abstract

In this dissertation, two different topics are addressed which are vital for the realization of modern high-energy physics experiments: detector development and data analysis. The first part focuses on the development and characterization of silicon pixel detectors. To account for the expected increase in luminosity of the Large Hadron Collider, the pixel detector of the Compact Muon Solenoid (CMS) experiment will be replaced by an upgraded detector with new front-end electronics. Comprehensive test beam studies are presented which have been conducted to verify the design and to quantify the performance of the new front-end in terms of tracking efficiency and spatial resolution. The tracking efficiency has been determined to be $99.7\,^{+0.3}_{-0.5}\,\%$, while the spatial resolution has been measured to be $(4.80 \pm 0.29)\,\mu\text{m}$ and $(7.99 \pm 0.23)\,\mu\text{m}$ along the $100\,\mu\text{m}$ and $150\,\mu\text{m}$ pixel pitch, respectively. Furthermore, a new cluster interpolation method is proposed which utilizes the third central moment of the cluster charge distribution and achieves improvements of the position resolution of up to $40\,\%$ over the conventional center of gravity algorithm. In the second part of the thesis, an alternative measurement of the top quark mass is presented. The mass is measured from the normalized differential production cross sections of dileptonic top quark pair events with an additional jet. The measurement is performed on data recorded by the CMS experiment at $\sqrt{s} = 8\,\text{TeV}$, corresponding to an integrated luminosity of $19.7\,\text{fb}^{-1}$. Using theoretical predictions at next-to-leading order in perturbative QCD, the top quark pole mass is measured to be $m_\text{t}^\text{pole} = 168.2\,^{+4.7}_{-2.1}\,\text{GeV}$ with a precision of about $2.0\,\%$. The measurement is in agreement with other measurements of the top quark pole mass within the assigned uncertainties.

Zusammenfassung

In der vorliegenden Dissertation werden zwei verschiedene Themenbereiche behandelt, die für die Durchführung eines modernen Hochenergie-Teilchenphysik-Experiments unabdingbar sind: Detektorentwicklung sowie Datenanalyse. Der erste Teil der Arbeit befasst sich mit der Entwicklung und Charakterisierung von Silizium-Pixeldetektoren. Der Pixeldetektor des Compact Muon Solenoid (CMS) Experiments wird durch einen neuen Detektor mit verbesserter Ausleseelektronik ersetzt, um dem zu erwartenden Anstieg der Luminosität des Large Hadron Colliders Rechnung zu tragen. Um die Funktionalität der neuen Ausleseelektronik zu überprüfen und deren Leistungsfähigkeit in Bezug auf Tracking-Effizienz und Ortsauflösung zu quantifizieren, wurden im Rahmen dieser Arbeit umfangreiche Messungen mit Teststrahlen geladener Teilchen durchgeführt. Die gemessene Tracking-Effizienz beträgt $99.7\,^{+0.3}_{-0.5}\,\%$. Zudem konnte eine Ortsauflösung von $(4.80 \pm 0.29)\,\mu\text{m}$ bzw. $(7.99 \pm 0.23)\,\mu\text{m}$ entlang der $100\,\mu\text{m}$ bzw. $150\,\mu\text{m}$ Pixelabmessung erreicht werden. Des Weiteren wird ein neuer Algorithmus zur Korrektur der interpolierten Position des Teilchendurchgangs vorgeschlagen, der das dritte zentrale Moment der Ladungsverteilung im Pixelcluster verwendet und Verbesserungen der Ortsauflösung von bis zu 40 % im Vergleich zum konventionellen Center-of-Gravity-Algorithmus erreicht. Im zweiten Teil der Arbeit wird eine alternative Messmethode für die Masse des Top-Quarks vorgestellt. Die Masse wird aus dem normierten differenziellen Wirkungsquerschnitt von Ereignissen mit Top-Quark-Paaren und einem zusätzlichem Jet bestimmt. Die Messung verwendet Daten des CMS-Experiments, die bei einer Kollisionsenergie von 8 TeV aufgenommen wurden und einer integrierten Luminosität von $19.7\,\text{fb}^{-1}$ entsprechen. Berechnungen mit NLO-Präzision in störungstheoretischer QCD erlauben die Bestimmung der Pol-Masse des Top-Quarks. Die gemessene Masse beträgt $m_\text{t}^\text{pole} = 168.2\,^{+4.7}_{-2.1}\,\text{GeV}$ mit einer Präzision von ca. 2.0 % und stimmt innerhalb der Unsicherheiten mit anderen Messungen überein.

Contents

List of Figures

List of Tables

Introduction

Already in the thirteenth century, ideas were developed on how science could potentially evolve in the future. The idea of the Arbor Scientiæ [1], or *tree of science*, forecasted a branching into different disciplines — a prediction which eventually became true after the last great polymaths of the renaissance. Instead of covering many different subjects, experts deepened the understanding of their specific fields to a level, where no single person could internalize all knowledge available. Over the centuries, these branches have undergone further ramification, and modern science comprises millions of leaves of different disciplines. However, in today's diverse scientific landscape this foliage has become so dense, that non of these subjects can be treated independently of the others and their differentiation becomes more and more difficult.

High-energy particle physics is no exception to this. The main goal of high-energy physics is the understanding of fundamental processes in nature, and its primary tool to explore the microcosm of the elementary constituents of matter are particle collisions. Elementary or composite particles are accelerated and brought to collision in order to produce new and unknown constituents, or to quantify known processes or parameters of a theory. The underlying theoretical framework for modern high-energy particle physics is the so-called standard model (SM), which represents the current state of knowledge and summarizes all known particles and interactions. Since its first formulation in 1961 [2] it has been constantly refined throughout the latter half of the 20th century, and by now provides high-precision predictions for many phenomena measured in nature.

The first particle accelerators have been built in the early 1930s [3–5], and since then the collision energy has constantly been increased in order to probe new regimes and to challenge the predictions provided by the SM. With the requirement for higher collision energies, both the particle accelerators and the detectors have grown larger and larger over the past decades, and now constitute the largest and most complex machines ever built. Designing and conducting such an experiment requires detailed understanding of all physics and technology involved — from the working principles of the basic detector building blocks, to data acquisition, particle identification and reconstruction, and finally to the measurements of the physics processes under investigation. This global and interdisciplinary endeavor would not be possible without the expert knowledge from many different fields of science such as cryogenics, solid state physics, material science, microelectronics, or high performance computing.

The currently largest particle accelerator is the Large Hadron Collider (LHC), located at CERN near Geneva, Switzerland, which accelerates hadrons along its 27 km ring and brings them to

collision at a center-of-mass energy of $\sqrt{s} = 13\,\text{TeV}$[1]. One of the experiments recording these collisions is the Compact Muon Solenoid (CMS) experiment, a 14 000 t general purpose particle detector with a length and diameter of about 22 m and 15 m, respectively. It is one of the two experiments to discover the Higgs boson [6, 7], paving the path for the 2013 Nobel Prize in physics [8]. However, many questions are still waiting to be answered and both the LHC accelerator and the experiments are undergoing constant changes and improvements in order to push the boundaries of human knowledge.

The work presented in this thesis provides an insight into the diversity of problems to be solved in order to successfully conduct a high-energy physics experiment, and is thus devoted to two different parts. After a general introduction to the field of particle physics in Chapter 1 and to the CMS experiment in Chapter 2, Part I describes the endeavor of designing, constructing, and commissioning a new pixel detector for CMS. Part II presents a measurement of the top quark mass from data recorded by the CMS experiment at $\sqrt{s} = 8\,\text{TeV}$.

The CMS Pixel Detector is a hybrid silicon pixel tracking detector and constitutes the innermost component of the CMS experiment. It provides spatial information about the path of charged particles with high resolution, and hence is a crucial part of the experiment for the reconstruction of particle trajectories and for the identification of secondary decay vertices. The current CMS Pixel Detector has been designed for an instantaneous luminosity of $\mathcal{L} = 1 \times 10^{34}\,\text{cm}^{-2}\text{s}^{-1}$ and performs well under these operation conditions. However, the luminosity provided by the LHC will exceed the design value by a factor of two or more within the next years, and the present pixel detector would be subject to severe inefficiencies arising from dead time and limited buffering capabilities of the front-end electronics. Thus, the CMS Collaboration has decided to replace the pixel detector with a new device, which represents an advancement of the current design including a new readout chip (ROC). The new detector is currently being built by a collaboration of many institutes, and the replacement of the present detector is foreseen for the year-end technical stop of the LHC in 2016/17. The new front-end electronics also require a new data acquisition (DAQ) framework for laboratory tests and operation of prototypes, which has been implemented as part of this thesis and is in use by the entire CMS Pixel Collaboration for the quality control and calibration of detector modules.

In this thesis, test beam measurements for the characterization and design verification of the new ROC are presented. Test beams are beams of ionizing radiation which allow to assess the characteristics of particle detectors, and provide the opportunity to operate the devices in conditions close to the final deployment situation in the experiment, i.e., with external trigger signals and in synchronization with other detectors. The measurements have been performed at the DESY test beam facility using a reference detector for tracking which allows to predict the particle impact position in the so-called device under test with micrometer resolution. Precision measurements of the spatial resolution and tracking efficiency of the new ROC are presented and compared to detailed simulations of the charge deposition and collection in the silicon sensor material. Furthermore, the charge distribution among the different pixels of a cluster is studied in detail and a new method for the determination of the track impact position based on the third central moment of the charge distribution is proposed.

The first part is structured as follows. An introduction to semiconductor tracking detectors is given in Chapter 3, followed by a description of the Phase I pixel detector for the CMS experiment in Chapter 4. Chapters 5 and 6 provide information about the simulation of CMS Pixel Detector modules using the PIXELAV software and about the pxarCore DAQ framework, respectively. Chapter 7 describes the DESY test beam facility as well as the experimental setup

[1] Natural units are used throughout this thesis, with $c = \hbar = 1$. Consequently, energy, mass, and momentum are given in units of electron Volts (eV). Electric charge is expressed in units of the elementary charge e.

for the test beam qualification of the ROC. The analysis strategy and results of the test beam measurements are discussed in Chapter 8. Finally, Chapter 9 presents a new algorithm for the improvement of the spatial resolution of pixel detectors using the charge distribution within clusters.

The second topic of this thesis studies the heaviest known particle of the SM, namely the top quark. It has only been discovered in 1995 at the Tevatron accelerator [9, 10], and to this day only the Tevatron and the LHC have reached the collision energy necessary to produce top quarks. At a collision energy of $\sqrt{s} = 8\,\text{TeV}$ the inclusive cross section for the production of top quark pairs ($\text{t}\bar{\text{t}}$) is about $\sigma = 245\,\text{pb}$, and therefore about five million $\text{t}\bar{\text{t}}$ events have been produced at the LHC in the $19.7\,\text{fb}^{-1}$ of data recorded in 2012. Owing to its high mass, the top quark has large implications for various parameters of the SM and allows detailed tests of quantum chromodynamics (QCD). The top quark does not form bound hadron states but predominantly decays directly to a bottom quark and a W boson, and thus allows to study the properties of a bare quark. Moreover, top quarks play an important role in searches for possible physics beyond the SM.

The top quark mass is usually either measured directly by reconstructing the event topology from its decay products and inferring the mass from this kinematic reconstruction, or via the mass dependency of the inclusive $\text{t}\bar{\text{t}}$ production cross section. The currently most precise combination of direct measurements performed by the CMS collaboration yields a mass of $m_\text{t} = 172.44 \pm 0.13\,(\text{stat}) \pm 0.41\,(\text{syst})\,\text{GeV}$ [11] with a relative uncertainty below 0.3 %. However, the kinematic approach does not allow for the determination of a theoretically well-defined Lagrangian parameter in terms of perturbative QCD which can be related to the top quark mass. On the other hand, measurements from the cross section do not provide the same experimental precision but allow for the measurement of a well-defined mass parameter.

In this thesis, an alternative measurement is presented, which determines the top quark mass from differential cross sections using a global χ^2 template fit method. The differential cross section is determined from dileptonic $\text{t}\bar{\text{t}}$ events, where both W bosons decay into lepton-antineutrino pairs, and which contain additional jet activity ($\text{t}\bar{\text{t}}$+jet). The observable ρ_S is proposed in [12] and is defined as the inverse of the invariant mass of the $\text{t}\bar{\text{t}}$+jet system. The mass is determined by comparing the differential cross section as a function of ρ_S to theoretical predictions with different top quark mass hypotheses. The measurement is performed both at the level of reconstructed particles from the detector response, and after correction for detector acceptance, resolution, and efficiency. This allows to compare the sensitivity and the influence of different sources of systematic uncertainty on the methods. The theoretically well-defined pole mass of the top quark is measured using calculations of the $\text{t}\bar{\text{t}}$+jet matrix element at next-to-leading order (NLO) precision [13] with subsequent parton showering.

The second part of the thesis is organized as follows. After a brief introduction of physics with top quarks in Chapter 10, the simulation of collision events with the Monte Carlo (MC) method is presented in Chapter 11. The analysis strategy and event selection is described in Chapter 12, and the sources of systematic uncertainty relevant for the measurement presented are discussed in Chapter 13. The global χ^2 template fit method and the measurement of the top quark mass from the normalized ρ_S event distributions are presented in Chapter 14. Chapter 15 describes the unfolding of the distributions to generator level, the measurement of the normalized differential $\text{t}\bar{\text{t}}$+jet cross section, and the determination of the top quark mass and top quark pole mass from different theoretical predictions.

Finally, the findings of both parts of the thesis are summarized and a brief outlook on possible improvements of the analyses and additional measurements is given in the Summary and Prospects chapter.

1. Particle Physics at Hadron Colliders

This chapter introduces the relevant theoretical background required for particle physics at hadron colliders. Section 1.1 presents the standard model of particle physics, a theoretical model on which the current understanding of high-energy physics is based. The SM attempts to explain matter and interactions based on elementary particles and serves as foundation and reference for new measurements.

The initial state of the scattering experiments conducted at hadron colliders is particularly complicated and necessitates phenomenological models in order to understand the effects influencing the measurement. The relevant hadron for this thesis is the proton and important concepts for proton-proton collisions are introduced in Section 1.2.

The measurement of the particles emerging from the collision requires modern particle detectors implementing the most advanced technologies available. Section 1.3 gives an overview of the main detector types used to detect particles and to quantify their properties such as energy or momentum. More detailed descriptions of specific detector types follow throughout the thesis when relevant.

Finally, Section 1.4 introduces the Monte Carlo method which is the basis for almost any simulation in particle physics and which facilitates the comparison of statistically-driven theory predictions with the detector responses recorded in collisions.

1.1 The Standard Model of Particle Physics

The standard model (SM) of particle physics summarizes the present understanding of matter and the observed interactions between fundamental particles. Developed mainly in the second half of the 20th century, it has shown to be capable of predicting experimental measurements with an unprecedented precision. Following its historic precursors it attempts to describe nature by the notion of elementary particles.

In the SM, these fundamental particles are divided into two categories. Matter is composed of fermions, while the interactions between them are based on the exchange of the force mediating bosons. Electromagnetism, the weak force, and the strong force are the three interactions described by the SM. These interactions lead to a transfer of energy and momentum as well as the alteration of quantum numbers of the participating particles. The strength of the force

is determined by the coupling constant and defines the probability of the fermion to emit or absorb a mediating boson.

Over the last couple of decades, the SM has been remarkably successful in predicting and explaining various effects. By now, it is experimentally verified to an extremely high precision on the per-mille level, and covers a wide range of energies from a few eV to the TeV scale. With the recent discovery of the Higgs boson by the ATLAS [6] and the CMS [7] experiments, yet another piece of the puzzle has been found and the SM has again demonstrated its ability to describe many fundamental concepts of nature at the energy scales accessible by modern particle physics.

Nevertheless, the SM has some shortcomings and fails to explain experimental observations such as gravity, non-zero neutrino masses or the existence of dark matter. An overview of these phenomena as well as theoretical considerations concerning physics beyond the SM are summarized in Section 1.1.4.

Mathematically, the SM is described by relativistic quantum field theories (QFTs), and its equations of motion are derived from the Lagrangian density $\mathcal{L}$ by assuming a stationary action with $\delta S = 0$. In this picture, fermions are represented by spinor fields, and gauge bosons by vector fields. Interactions between the different fermions are introduced by demanding local gauge invariance of the fermion spinors. This means that the action S as the time integral of the Lagrangian remains unchanged under local gauge transformation, viz.

$$S = \int \mathcal{L}\left(U(x)\Psi\right) dt \stackrel{!}{=} \int \mathcal{L}\left(\Psi\right) dt, \tag{1.1}$$

where Ψ is the fermion spinor function, and $U(x)$ the gauge transformation applied. Additional terms in the Lagrangian resulting from this requirement can be identified as the interaction terms of the forces.

An extensive description of the mathematical concepts of QFT and the SM can be found e.g. in [14], while the currently known elementary particles, their properties and interactions are reviewed in detail in [15]. This chapter focuses on the most important aspects of the SM relevant for this work.

1.1.1 Particles and Interactions

In the SM, matter consists of particles referred to as *fermions*, which can be grouped according to the forces they experience as illustrated in Table 1.1. Quarks experience all three forces, while leptons cannot participate in the strong interaction. According to the sign of their electric charge, quarks are classified as *up*-type for positively charged and *down*-type for negatively charged quarks. Charged leptons interact via the electromagnetic and weak force, while neutrinos are liable to the weak force only. Within these groups, fermions are arranged in three generations. The respective particles share most of their properties, but their mass increases from generation to generation. The heaviest particle known is the top quark, which plays a special role in modern particle physics and will be described in more detail in Chapter 10.

In addition to the twelve fermionic particles, also their antiparticles exist which exhibit identical properties as their partners but feature opposite charge. The concept of antiparticles has first been proposed by P. Dirac [16] in 1928 in order to allow positive or negative energy as solutions of the Dirac equation. Experimentally, the antielectron or positron was found in cloud chamber experiments shortly after by C. Anderson [17]. In the following, the phrase *particle* implicitly includes the respective antiparticle as they behave the same.

Table 1.1: The SM fermions and bosons. Braces indicate which fermions take part in the interaction, indices L, R denote the chirality of the fermions. The $W^{\pm}$ bosons only couple to left-handed fermion and right-handed antifermion states.

	Fermions			Gauge Bosons	
	1st Generation	2nd Generation	3rd Generation	Electroweak	Strong
Quarks	$\begin{pmatrix} u_L \\ d_L \end{pmatrix}, u_R, d_R$	$\begin{pmatrix} s_L \\ c_L \end{pmatrix}, s_R, c_R$	$\begin{pmatrix} t_L \\ b_L \end{pmatrix}, t_R, b_R$	$W^{\pm}$, Z, γ	g
Leptons	$\begin{pmatrix} e_L \\ \nu_{e,L} \end{pmatrix}, e_R$	$\begin{pmatrix} \mu_L \\ \nu_{\mu,L} \end{pmatrix}, \mu_R$	$\begin{pmatrix} \tau_L \\ \nu_{\tau,L} \end{pmatrix}, \tau_R$		
Higgs	H				

The forces of the SM are mediated by gauge bosons. The interactions between fermions are described as the exchange of bosonic particles. Since the interactions are derived from local gauge invariances, each gauge boson holds one or more conserved physical quantities which can be identified as the quanta of the respective force.

The conserved quantity of the electromagnetic force is the electric charge, the quantum of the associated field is the photon (γ). The interaction is described by quantum electrodynamics (QED) which is based on the symmetry group $U(1)_{em}$ and introduces the coupling constant of the interaction $\alpha = e^2/4\pi$. Since α is small ($\alpha \ll 1$) it can be used as expansion parameter in perturbation theory as described in Section 1.1.2. Due to the massless and electrically neutral force carrier, the range of the electromagnetic force is unlimited.

Strong interactions are described by quantum chromodynamics (QCD), inheriting the symmetry group $SU(3)_C$. The corresponding charge is named *color* and has the three eigenstates red, green, and blue. The mediating gauge bosons of the strong interaction are the massless *gluons*. Because of the structure of the symmetry group, gluons form an octet and carry both color and anticolor which allows for self-interaction. The strength of the interaction is quantified by the strong coupling constant α_s which depends on the momentum transfer Q^2 of the interaction regarded. As a result of the gluon self-interaction, the coupling becomes large for small values of Q^2 leading to a phenomenon called *confinement* which restricts the range of the interaction. At certain distances between the participating quarks, the creation of a new quark-antiquark pair is energetically favorable over further increase of the potential energy. This sequential pair production is called hadronization. Consequently, bare quarks and gluons cannot be observed. At small distances, or high Q^2, α_s becomes small, an effect called *asymptotic freedom*. The characteristic scale of asymptotic freedom is $\Lambda_{\mathrm{QCD}} \approx \mathcal{O}(100\,\mathrm{MeV})$, where the coupling constant reaches the order of unity. In this regime, processes can be calculated using perturbative QCD (cf. Section 1.1.2).

Due to the confinement, bound quark states have to be color singlets, either mesons consisting of a quark-antiquark pair, or baryons with three quarks or antiquarks. Other combinations such as pentaquarks are theoretically possible combinations, and strong indications towards their existence have been found recently [18]. The constituents of stable matter, proton and neutron, are baryons with three valence quarks, *up-up-down* and *up-down-down*, respectively. A more detailed picture of the proton structure is given in Section 1.2.

The weak interaction has historically been introduced by E. Fermi to describe the β-decay [19]. Two different types of weak interactions have been observed, electrically charged current reactions

exchanging $W^{\pm}$ bosons, and neutral current reactions mediated by neutral Z^0 particles. These gauge bosons have large masses ($m_W = 80.4\,\text{GeV}$, $m_Z = 91.2\,\text{GeV}$ [15]) which significantly restrict the interaction range. Weak and electromagnetic interaction can be described as different low-energy manifestations of the unified electroweak theory following the Glashow-Salam-Weinberg (GSW) model [2, 20]. As a consequence, the strength of the two interactions becomes comparable at energies of a few 100 GeV, which has been verified experimentally [21, 22].

The weak interaction has a few peculiarities, namely CP violation and flavor mixing. Since the weak interaction only couples to left-handed fermions and right-handed antifermions, the parity P [23] and charge conjugation C symmetries are violated. The observed P violation can be described by introducing *chirality* states for fermions, denoted as left-handed and right-handed. The chirality of massless particles corresponds to their helicity, while this is not necessarily the case for massive particles where the helicity depends on the reference system. $W^{\pm}$ bosons only couple to left-handed fermions and right-handed antifermions and hence violate parity. The combined CP symmetry is almost conserved, however small violations can be measured [24] and only CPT including time inversion T is fully conserved.

The weak eigenstates of quarks are not identical to their mass eigenstates. Hence, the quark flavors can be transformed in weak interactions, and even the quark generation can be changed based on the coupling to the $W^{\pm}$ bosons. Flavor-changing neutral current reactions involving Z^0 bosons are not observed. The mixing between weak and mass eigenstates is described by the unitary Cabibbo-Kobayashi-Maskawa (CKM) matrix [25, 26]

$$\begin{pmatrix} d' \\ s' \\ b' \end{pmatrix} = \begin{pmatrix} V_{ud} & V_{us} & V_{ub} \\ V_{cd} & V_{cs} & V_{cb} \\ V_{td} & V_{ts} & V_{tb} \end{pmatrix} \times \begin{pmatrix} d \\ s \\ b \end{pmatrix}, \tag{1.2}$$

where d, s, b denote the mass eigenstates while d', s', b' are the weak eigenstates. The terms V_{ij} represent the mixing amplitudes of the quark flavors i and j. Transitions within the same generation are favored, leading to large diagonal elements of the CKM matrix. Especially the mixing amplitude of the top and bottom quarks are close to unity $|V_{tb}| \approx 1$, which has consequences on the top quark decay as discussed in Chapter 10. Neutrinos exhibit similar mixings [27, 28], and the observation has recently been awarded with the Nobel Prize [29]. These neutrino flavor oscillations are described by the Pontecorvo–Maki–Nakagawa–Sakata (PMNS) matrix [30] and indicate non-zero masses for the particles.

Unlike the previously described bosons, the recently discovered Higgs boson [6, 7] is a scalar spin 0 particle. The Higgs mechanism yielding the masses of the gauge bosons and fermions is introduced in Section 1.1.3.

1.1.2 Perturbation Theory and Renormalization

The equations of motion derived from the Lagrangian of the SM can in general not be solved analytically, but it is possible to expand the solution as power series in orders of the coupling constant. The state $|\Psi\rangle$ of system $|\Psi_i\rangle$ after the hard scattering process S can then be written as

$$|\Psi\rangle = S\,|\Psi_i\rangle = \left(\sum_{n=0}^{\infty} g^n C_n\right)|\Psi_i\rangle\,, \tag{1.3}$$

where g denotes the charge of the interaction, the coupling constant is $\alpha \propto g^2$. Each of the coefficients C_n in the perturbation series can be associated with a specific physical process and contributes to the total interaction. The first term of the series containing C_0 corresponds to no interaction between the particles, while C_1 has to be zero due to energy and momentum

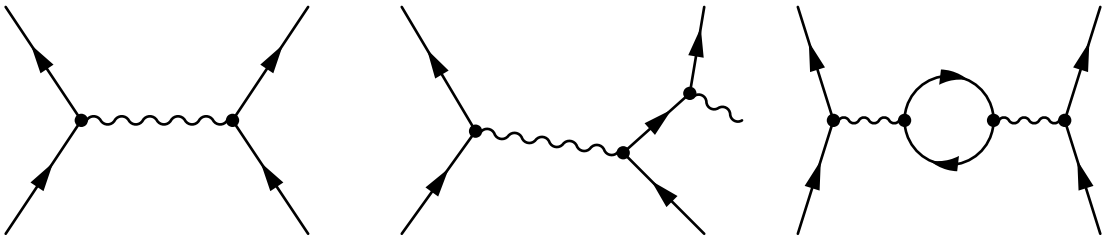

(a) Leading order process **(b)** Final state radiation **(c)** Virtual loop

Figure 1.1: Examples for higher-order contributions to $2 \to 2$ scattering processes. While (a) and (b) have finite integrals, the virtual loop shown in (c) requires renormalization of the perturbative series.

conservation. The first non-trivial coefficient C_2 is called leading order (LO) of the interaction and can be related to $2 \to 2$ processes such as the example shown in Figure 1.1a. This process only contains two vertices with the coupling $\sqrt{\alpha}$ each. C_3 represents the *next-to-leading order (NLO)* with three vertices, an example of an NLO process is shown as Feynman diagram in Figure 1.1b.

The coefficients C_n can in principle be deducted following the *Feynman rules*, but owing to the complexity of the calculations and the increasing number of possible diagrams per additional order of α only the first few orders are known in practice. This is, however, often sufficient when comparing the contribution of additional orders to the precision expected from the experimental measurement.

Problems in this perturbative expansion arise from diagrams containing virtual loops as shown in Figure 1.1c. The momenta of the virtual fermions in the loop are not constrained and the associated integrals are thus divergent. In principle, these divergences would cancel with opposite contributions when calculating all orders of the perturbation series. But since this is not possible, the finite order perturbation series contains divergent integrals.

In order to be able to obtain physical observables from perturbative expansions, the theory has to be *renormalized* [31]. The renormalization theorem states that the re-parametrization of the theory in terms of a physical quantity is enough to turn the perturbation expansion into a well-defined expansion with finite contributions from every order. The arising divergences are temporarily regularized by introducing an arbitrary cut-off μ_R to the loop momenta, often called the renormalization scale. The free parameters of the Lagrangian are then redefined such that the divergences are absorbed in the coupling constant $\alpha \to \alpha\left(\mu_r^2\right)$. The reference value $\alpha\left(\mu^2\right)$ has to be determined experimentally since the coupling strength is a free parameter of the Lagrangian and cannot be predicted by the SM.

Using the renormalization technique, physical observables such as cross sections remain finite to any order of perturbation theory and are calculated from the matrix element of the interaction

$$\sigma \propto \left|\mathcal{M}_{fi}\right|^2 \quad \text{with } \mathcal{M}_{fi} = \langle \Psi_f \,|\, S \,|\, \Psi_i \rangle \,. \tag{1.4}$$

The divergences are absorbed into unphysical (non-observable) Lagrangian parameters. It is worthwhile pointing out that only local gauge-invariant theories are renormalizable.

1.1.3 Electroweak Symmetry Breaking

The GSW model requires all gauge bosons to be massless in order to conserve gauge symmetry, explicit mass terms in the Lagrangian are incompatible with gauge invariance. Fermion masses are possible within the theory as long as the masses in the multiplets formed by the symmetry group are the same, and the interaction conserves chirality. Both does not comply with data since the fermion masses differ across the groups, and the masses of the gauge bosons Z^0 and $\mathrm{W}^\pm$ are measured to be large.

A solution to the problem is the *Higgs mechanism* [32–34] which requires the Lagrangian to be invariant under transformations, but not the vacuum state, a concept referred to as electroweak symmetry breaking (EWSB). Introducing the Higgs field as $\mathrm{SU}(2)$ doublet with charged and neutral scalar components and requiring the invariance of the Lagrangian yields the Higgs potential

$$V(\Phi) = \mu^2 \Phi^\dagger \Phi + \lambda \left(\Phi^\dagger \Phi\right)^2, \tag{1.5}$$

with its parameters λ defined as real and positive, and $\mu^2 < 0$. The potential exhibits minima at $\Phi_0^\dagger \Phi_0 = -\mu^2/2\lambda$ which lead to a non-vanishing vacuum expectation value

$$\langle 0 \,|\, \Phi \,|\, 0 \rangle = v = \sqrt{\frac{-\mu^2}{2\lambda}}. \tag{1.6}$$

In order to allow the photon to be massless, the vacuum state is chosen to be electrically neutral which yields one massive and three massless bosons, the latter being *Goldstone bosons* [35]. By exploiting the freedom of gauge invariance, the three Goldstone bosons can be eliminated resulting in the Higgs field

$$\Phi = \frac{1}{\sqrt{2}} \begin{pmatrix} 0 \\ v + H \end{pmatrix}, \tag{1.7}$$

where H represents the massive Higgs boson. Introducing this field into the Lagrangian yields additional terms describing the interaction between the massive H and the $\mathrm{W}^\pm$ and Z bosons as well as the self-coupling of the Higgs boson. The coupling strength is proportional to the vector boson masses. By substituting Equation 1.7 in the Lagrangian, some relations between the masses can be obtained, namely

$$\begin{aligned} m_\mathrm{H} &= \sqrt{2}\mu \\ m_\mathrm{W} &= \frac{1}{2} g v \\ m_\mathrm{Z} &= \frac{m_\mathrm{W}}{\cos\theta_W}, \end{aligned} \tag{1.8}$$

where θ_W is the Weinberg angle and m_H the mass of the Higgs boson. Owing to the experimentally measured mass of the W boson, the vacuum expectation value can be obtained as $v = 246\,\mathrm{GeV}$. The value for the parameter μ and thus for the Higgs boson mass is not predicted by the SM and can only be derived from measurements, which have recently been conducted at the Large Hadron Collider. The newly discovered boson complies with the characteristics expected from a SM Higgs boson, and its mass has been measured to be $125.09 \pm 0.21\,(\mathrm{stat}) \pm 0.11\,(\mathrm{syst})\,\mathrm{GeV}$ [36].

1.1.4 Beyond the Standard Model

Despite its success, the SM is incomplete as it does not address all problems posed by nature. Many open questions are still waiting to be answered, arising from both experimental observations and theoretical considerations.

First of all the SM does not provide a coherent description of gravitation. Its influence can be neglected at the energies probed in high-energy particle physics since it is weaker than the other forces by many orders of magnitude, but it becomes relevant at energies around the Planck scale $\Lambda_P \approx 10^{19}\,\mathrm{GeV}$. To this day, no formulation of a renormalizable theory of gravitation is available.

Observations of spiral galaxies, the mass distribution in galaxy clusters, and gravitational lensing [37, 38] as well as anisotropies in the cosmic microwave background (CMB) [39, 40] imply the existence of a new type of matter (*dark matter*) with properties incompatible with the SM. Furthermore, detailed studies of the CMB as well as distant type Ia supernovae [41, 42] indicate that the universe is expanding at an accelerated pace, an observation awarded with the Nobel Prize in 2011 [43] and commonly attributed to an unknown form of energy (*dark energy*). Together, dark energy and dark matter constitute about 96 % of the mass of the universe, with only the remainder being described by the SM. These remaining four percent pose yet another puzzle caused by the excess of matter over antimatter in the universe. The observed CP violation arising from the imaginary components of the CKM matrix is not large enough, and a stronger violation would be required in order to explain the excess of matter in current models of the baryogenesis.

More conceptual shortcomings of the SM are the total number of free parameters, the arbitrariness of the particle content as well as of the number of fermion generations. The hierarchy problem between the electroweak unification scale and grand unification scale, uniting strong and electroweak forces, requires extreme fine-tuning of the Higgs mass with respect to radiative corrections. This is of course not impossible but considered an undesired feature in a fundamental theory.

Many theories have been developed in order to solve these enigmas, such as supersymmetry [44], a complex of theories based on a symmetry between fermions and bosons; Extra dimension [15]; Little or Composite Higgs models [45] or string theory, which replaces particles with one-dimensional string objects. A brief summary of prevailing theories is given for example in [46].

With the LHC pushing the energy frontier further, new energy scales can be explored both by direct searches for signatures of a specific theory and by more model-independent searches for the unexpected.

1.2 Proton-Proton Collisions

At hadron colliders, beams of hadrons such as protons or atomic nuclei are accelerated, circulated, and collided. Choosing these composite and complex objects allows to significantly increase the energy regime accessible to the accelerator compared to the acceleration of elementary particles such as electrons or positrons. Charged particles circulating in a storage ring lose energy by means of synchrotron radiation which has to be compensated after every turn of the beam. Relativistic particles which are accelerated along the collider ring undergo synchrotron radiation at a rate proportional to [15]

$$P \propto \frac{E^4}{\left(mc^2\right)^4 R^2}, \tag{1.9}$$

where E is the energy and m the rest mass of the particle. The parameter R denotes the radius of the acceleration path, i.e., the radius of the bending magnets. Owing to the fourth power, the mass of the particle to be accelerated plays a predominant role, and the total beam energy can be significantly increased by colliding heavier particles.

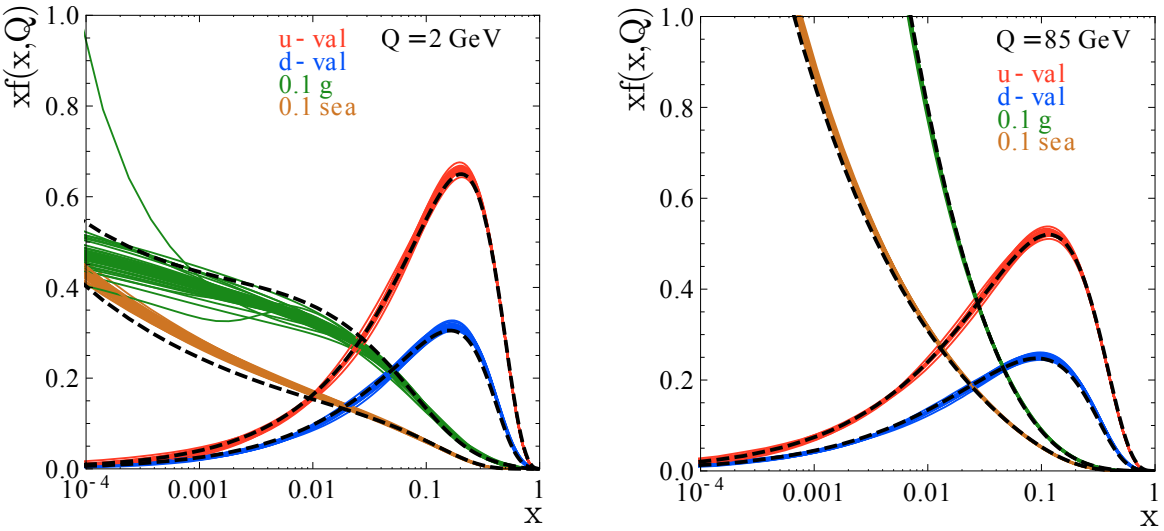

Figure 1.2: next-to-next-to-leading order (NNLO) PDFs from the CT10 Collaboration for $Q^2 = 2\,\text{GeV}$ and 85 GeV. At high values of x the valence quarks (u, d) dominate, while at low x gluons and sea quarks (g, *sea*, scaled by a factor 10) represent the major contribution. From [47].

This section describes the proton as the initial state of the scattering experiment to be investigated and introduces some concepts used in the theoretical description of the scattering processes. The proton is a hadron consisting of three valence quarks which determine its quantum numbers and dominate its behavior at low energies. At higher energies, additional virtual quark-antiquark pairs (*sea quarks*) come into play, which stem from gluon splitting. A constant flux of gluons and sea quarks, balanced by the continuous annihilation of sea quark pairs and radiation of gluons, defines the structure of the proton probed at high energies. The behavior of these so-called *partons* is characterized by the parton distribution functions (PDFs) described in the following section.

Because of this phenomenological description of the quark content, it is necessary to disentangle different energy regimes via the factorization theorem as described in Section 1.2.2. Remnants of the hard collision form the underlying event described in Section 1.2.3.

1.2.1 Parton Distribution Functions

Owing to the complex structure of the proton, the initial state of the hard scattering process of partons is not well-defined and has to be described using phenomenological models. The distribution of partons inside the proton is described by PDFs of the form $f_{i|\text{p}}\,(x, \text{Q}^2)$. The PDF provides the probability density of finding a parton i carrying a certain momentum fraction x at the momentum scale Q^2 in the proton p.

Due to the non-perturbative information included, PDFs cannot be derived directly from perturbative QCD calculations but need to be extracted from data. Usually, this is performed by global fits combining the results from several experiments including deep inelastic scattering, fixed target experiments as well as data from collider experiments. With a given parametrization of the starting distribution obtained from data, the Q^2 scale dependence (or factorization scale, see section below) can be treated using the Dokshitzer-Gribov-Lipatov-Altarelli-Parisi (DGLAP) evolution equations [48–50]. The results are combined to PDF sets such as MSTW [51], HERAPDF [52], or CTEQ [47, 53, 54] as shown in Figure 1.2, and can be used in simulations to obtain distributions of the initial collision state. PDFs are assumed to provide a universal

description of the parton content of the respective hadron and to be independent of the scattering process regarded. At collision energies provided by modern hadron colliders such as the LHC, the PDFs are dominated by gluon contributions as can be seen from Figure 1.2, and most processes are gluon induced.

1.2.2 The Factorization Theorem

The factorization theorem [55] allows to isolate phases of the collision process which are governed by different dynamics and can thus be treated separately using the appropriate techniques. The description of the high-energy scattering process in perturbative QCD can be decoupled from phases described by phenomenological models such as the complex initial state characterized by the PDF, and from the final formation of hadrons.

The cross section of a given process $\sigma_{\mathrm{pp}\to\mathrm{X}}$ can be reformulated using the factorization theorem as a convolution of the partonic cross section $\hat{\sigma}_{ij\to\mathrm{X}}$ calculated in perturbative QCD and the measured PDFs of the proton $f_{\mathrm{p}|j}\left(\mu_F, x\right)$, where μ_F denotes the factorization scale separating the two energy regimes. The partonic cross section $\hat{\sigma}$ for a given process can be calculated perturbatively by integrating the squared matrix elements of the interaction over the available phase space as described in Section 1.1.2. The long-distance effects are obtained from the PDF set, where additional initial state radiation is included in the proton structure description up to μ_F. The total inclusive cross section of the process is obtained by integrating over all momentum fractions x_i and x_j of the two partons, and summing over all possible initial state partons i, j as

$$\sigma\left(\mathrm{pp}\to\mathrm{X}\right) = \sum_{i,j} \int_{x_i} \int_{x_j} f_{\mathrm{p}|i}\left(x_i, Q\right) f_{\mathrm{p}|j}\left(x_j, Q\right) \hat{\sigma}_{ij\to\mathrm{X}} dx_i dx_j. \tag{1.10}$$

1.2.3 Underlying Event and Pile-Up

Contributions to the overall collision event which are not attributed to the hard scattering process of interest are usually referred to as *underlying event (UE)*. This activity originates from multiple partonic interactions [56] where further partons of the colliding protons undergo interaction, as well as from the proton remnants which are not in a color singlet state. The amount of UE activity to be expected increases with both the center-of-mass energy $\sqrt{s}$ of the colliding beams and the momentum transfer Q of the primary hard interaction.

Additional activity can arise from the interaction of multiple protons in the colliding bunches, the so-called *pile-up*. Especially at high instantaneous luminosities (cf. Section 2.1.1) this can lead to a significant contamination of the event and complicate the particle reconstruction and separation from the primary interaction.

1.3 Basic Detector Concepts

Particles emerging from the collision have to be detected and their properties such as energy, momentum, and direction have to be measured in order to allow their identification and reconstruction. Only with fully reconstructed particle information, the global event description of the scattering process can be obtained and conclusions about the underlying physics can be drawn. Particle detectors are complex instruments usually optimized to measure one or a few of the above particle properties with high precision. Modern particle physics experiments thus combine several of these highly optimized detectors in order to gather the most precise event information available. In general, these detectors can be attributed to two types, tracking detectors measuring the particle path, and calorimeters measuring the energy.

1.3.1 Tracking Detectors

The main purpose of tracking detectors is the reconstruction of trajectory and momentum of charged particles emerging from the collision. This requires good spatial resolution as well as a low material budget in order to minimize effects from multiple scattering which deteriorate the measurement precision. Material budget is a term used to describe the amount of material present in the detector and is often expressed in fractions of the radiation length X_0. Two main classes of tracking detectors can be distinguished, both relying on collecting ionization charge on segmented readout electrodes.

Gaseous detectors consist of a gas-filled chamber and segmented electrodes such as thin wires which provide the spatial resolution. Gas molecules are ionized by traversing charged particles, and the resulting free charge carriers are collected at the electrodes via an electric field. The gas mixture of ionization gas and quench gas as well as the bias voltage are usually adjusted such that the drifting charge is amplified proportionally to the drift length. The main advantage of this technology is the very low material budget introduced by the gas, and the comparatively low cost.

However, the ionization energy for gases is of the order of 30 eV which limits the number of produced charge carriers per deposited energy. The required ionization energy in the solid state material of **semiconductor detectors** only requires a few eV and thus produces a larger signal at the cost of more bulk material to be traversed by the particle. The basic working principles of semiconductor trackers are detailed in Chapter 3.

Tracking detectors are typically placed in a magnetic field in order to bend the particle trajectories through the Lorentz force. This allows the simultaneous measurement of trajectory and momentum via the curvature of the path. The radius of the curvature r and the momentum perpendicular to the field direction p_T are related by [15]

$$p_T = 0.3 q B r, \tag{1.11}$$

where B denotes the magnetic field density in units of T, and q the charge of the particle under investigation. The curvature $\kappa = 1/r$ follows a normal distribution, and its uncertainty can be estimated by [15]

$$(\delta\kappa)^2 = (\delta\kappa_{\text{res}})^2 + (\delta\kappa_{\text{ms}})^2, \tag{1.12}$$

where $\delta\kappa_{\text{res}}$ is the contribution arising from the finite intrinsic measurement resolution, and $\delta\kappa_{\text{ms}}$ denotes the curvature uncertainty caused by multiple Coulomb scattering in the detector material.

1.3.2 Calorimeters

Calorimeter detectors have the task to determine the particle energy, which requires both the energy measurement and the spatial separation of different particles. The latter is a task becoming more and more important at hadron colliders with large instantaneous luminosities. Calorimeters consist of dense matter in which the incident primary particle induces a cascade of secondary particles with successively less energy. Finally, low-energy photons are created in a scintillator material proportional to the energy deposited by the primary particle, and photo detectors sample the signal.

The cascade development is referred to as *particle shower* and exhibits a significantly different behavior, depending on whether the shower is initialized by hadrons, or by electrons and photons. An overview of calorimetry is given for example in [57] while this section will only briefly discuss the main characteristics and differences between electromagnetic and hadronic showers.

At energies higher than approximately 1 GeV, electrons and photons initiate **electromagnetic showers**. Electrons lose their energy predominantly by means of bremsstrahlung, which produces high energetic photons. These photons, just as primary photons, undergo pair conversion and create electron-positron pairs which in turn produce more bremsstrahlung photons. The longitudinal extend of such a shower is described by the radiation length X_0, the lateral development is quantified by the Molière radius. The shower maximum with the most particles present is reached at a depth usually around a few X_0, afterwards the shower intensity gradually decreases. Owing to the multiplication process, the material required to contain the full electromagnetic shower is small compared to the requirement for hadronic calorimeters.

The strong force dominates the behavior of **hadronic showers** initiated by hadrons. The description of hadronic showers is inordinately more difficult due to a number of effects. About 90 % of the produced particles are pions, with the neutral π^0 decaying into 2γ and initiating additional electromagnetic showers. These electromagnetic contribution to the shower is very energy dependent which renders the calorimeter response to hadrons non-linear and yields large variations in the shower profiles stemming from high-energetic π^0. Furthermore, the signal is distorted by nuclear reactions. In order to liberate a proton or neutron from the atomic nucleus, the binding energy has to be overcome. This *invisible energy* does not show up in the sampled calorimeter signal and makes up more than 30 % of the total energy. The longitudinal extend of hadronic showers is governed by the *nuclear interaction length* λ_{int} which denotes the average travel distance for hadrons before inducing a nuclear interaction.

1.4 Simulations using the Monte Carlo Method

Many problems in modern particle physics require the solution of equations or the calculation of integrals which are too complex to be solved analytically. Some of these problems arise directly from the statistical nature of quantum mechanics, others have their origin in systems with many coupled degrees of freedom.

A widely used technique is the statistical solution of these problems by means of the so-called Monte Carlo (MC) method [58]. The MC method essentially uses pseudo-random numbers to represent the statistical components of processes, and to sample the integrand of high-dimensional functions. In this repeated random sampling, numbers are drawn from the fundamental distributions, i.e., either the process or the integrand function, and the calculations are performed at this exact point. By repeating this process, the final distribution can be reconstructed without actually solving the underlying equation. This allows to model stochastic processes or compute complex integrals exploiting the power of modern computers, and since many problems can be split into statistically independent components the computation can be parallelized on computing grid infrastructure.

MC simulation has proven to be an invaluable tool at almost all stages of a particle physics experiment. Simulations help designing the experiment and optimizing the sensitivity to the processes under investigation, and later on assist in interpreting the response of the detectors to physical processes. Basically all detector calibrations at least partly rely on simulated responses using MC tools. And last but not least, MC simulation allows to mimic the processes of the SM and helps to understand the theoretical implications. With simulation describing the data recorded by the experiments, precise predictions about future measurements can be made.

In this thesis, MC methods are employed for the simulation of semiconductor tracking detectors in Chapter 5 as well as for the description and simulation of particle collisions in Chapter 11.

2. The CMS Experiment at the LHC

Since the very first measurements with α particles performed by H. Geiger, E. Marsden and E. Rutherford [59], scattering experiments have become one of the most important tools in experimental particle physics. Increasing collision energies allow to resolve smaller and smaller structures, and to probe the fundamental constituents of matter and their interactions.

Modern particle accelerators provide the possibility to produce collisions in a controlled and well-understood environment. Beams of electrons, protons or nuclei are accelerated to high energies and brought to collision by intersecting them at one or several interaction points. Large and complex particle detector systems are built around these interaction points in order to measure the properties of the emerging collision products.

The LHC marks a milestone in the development of particle accelerators. It provides particle collisions at unprecedented energies and with a twenty-fold increase in instantaneous luminosity compared to its predecessor Tevatron. This chapter briefly describes both the LHC accelerator and the CMS experiment. Section 2.1 covers some basic aspects of the LHC and introduces the concept of luminosity, while Section 2.2 provides an overview of the CMS experiment and its subdetector systems. Finally, Section 2.3 gives a brief outlook on forthcoming upgrades of the CMS experiment.

2.1 The Large Hadron Collider

The Large Hadron Collider (LHC) is currently the largest particle accelerator world wide with a circumference of 27 km and a design center-of-mass energy of 14 TeV. It is located at the European Organization for Nuclear Research (CERN) in Geneva and resides 100 m below ground in the tunnel originally excavated for the Large Electron-Positron Collider (LEP) [60]. The LHC operates in either proton-proton, proton-nuclei or nuclei-nuclei collision mode, of which only the proton mode is discussed here.

The protons are generated by ionizing ultrapure hydrogen. Before being injected into the LHC, the protons are accelerated to the injection energy of 450 GeV by a series of pre-accelerators, namely a linear accelerator, the Proton Synchrotron (PS), and the Super Proton Synchrotron (SPS). This pre-accelerator complex is also used for other experiments such as NA62 at the SPS [61], irradiation of detector samples and material at the PS, or test beams at the SPS-fed Experimental Hall North beamlines.

In the LHC the two counter-rotating proton beams circulate in two evacuated beam pipes. The beams are kept on orbit and in focus by the magnetic field of superconducting dipole and quadrupole magnets, and are accelerated by radio frequency cavities. All magnets and cavities are cooled down to 1.9 K by liquid helium to maintain the superconducting regime. Additional magnets are used for focusing of the beams at the interaction point (IP) of the respective experiment.

At nominal beam configuration, the LHC contains 2808 bunches with a bunch spacing of 25 ns. After initial problems with the quench protection of the dipole magnets, the LHC operated at $\sqrt{s} = 7\,\text{TeV}$ from 2010 to 2011, and at 8 TeV in 2012. The center-of-mass energy of $\sqrt{s} = 13\,\text{TeV}$ has only been reached after the Long Shutdown 1 (LS1) conducted from 2013 to 2015. First papers using data recorded at $\sqrt{s} = 13\,\text{TeV}$ have already been published [62].

More detailed information on the LHC machine can be found elsewhere [63, 64].

2.1.1 Luminosity and Event Rate

The rate dN/dt of events of a given process depends on the cross section σ of the process under investigation and on the instantaneous luminosity $\mathcal{L}$, viz.

$$\frac{dN}{dt} = \sigma \cdot \mathcal{L}. \tag{2.1}$$

The instantaneous luminosity $\mathcal{L}$ is a function of beam parameters and defined as

$$\mathcal{L} = \frac{N_b N_p^2 f}{A}, \tag{2.2}$$

where N_b denotes the number of bunches in the ring, N_p the number of protons per bunch, and $f \approx 11\,\text{kHz}$ is the revolution frequency around the ring. Parameter A is the effective cross section of the beam and depends on the beam focus as well as the beam crossing angle and the size of the bunches.

The LHC has been designed to deliver an instantaneous luminosity of $\mathcal{L} = 1 \times 10^{34}\,\text{cm}^{-2}\text{s}^{-1}$ with a nominal filling of $N_p = 1.15 \times 10^{11}$ protons per bunch. In order to limit beam-beam interactions, the LHC has been operating with a bunch spacing of 50 ns and thus a reduced number of 1374 bunches in the ring until summer 2015. The proton intensity per bunch had been increased [65] to reach the intended instantaneous luminosity. However, this leads to a higher pile-up (cf. Section 1.2.3) and is a challenge for the experiments due to higher occupancy of the detectors.

To obtain the total number of events recorded for a given process, Equation 2.1 has to be integrated over time. The integrated luminosity $\int \mathcal{L} dt$ is usually given in units of inverse femto barn fb^{-1}, where $1\,\text{b} = 1 \times 10^{-24}\,\text{cm}^2$.

In 2012, a maximum instantaneous luminosity of $7.7 \times 10^{33}\,\text{cm}^{-2}\text{s}^{-1}$ was reached and a total integrated luminosity of $\int \mathcal{L} dt = 21.8\,\text{fb}^{-1}$ has been recorded by the CMS experiment [66] as depicted in Figure 2.1. Data corresponding to an integrated luminosity of $19.7\,\text{fb}^{-1}$ have been validated and released for physics analysis as shown in Figure 2.1b.

The instantaneous luminosity can be obtained from the inverse of Equation 2.1. By measuring the event rate of a process with precisely known cross section, the luminosity can be calculated. In the CMS experiment the current method for online luminosity measurement is the so-called *zero-counting* method using information from the hadronic calorimeter [68]. For offline luminosity

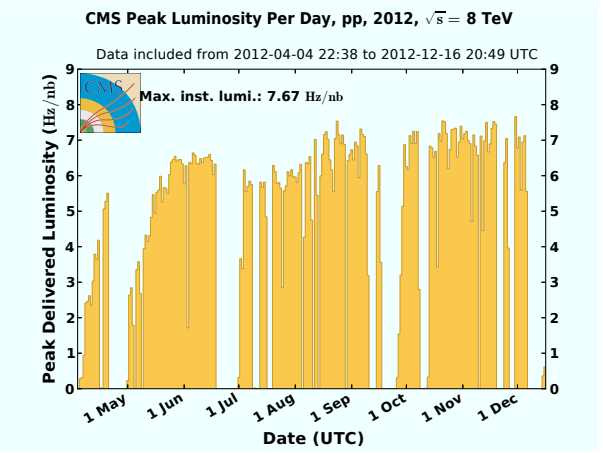

(a) Instantaneous luminosity for the 2012 LHC running period. From [66].

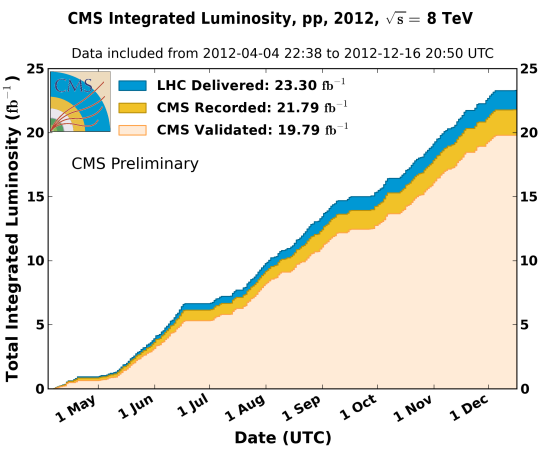

(b) Integrated luminosity delivered, recorded, and validated (beige). From [67].

Figure 2.1: Evolution of the instantaneous (a) and integrated (b) luminosity. Blue denotes the luminosity delivered by the LHC while orange marks the luminosity recorded by the CMS experiment.

determination in recorded data, several different methods are available [69]. The luminosity presented in Figure 2.1 is obtained using the *pixel-cluster-counting* method which counts the number of clusters in the pixel system per bunch crossing [70].

The absolute luminosity calibration is performed with Van-der-Meer separation scans [71] in which the event rates of the online luminosity method is measured as a function of transverse beam separation. This allows to determine the effective beam profile and to calculate the absolute luminosity according to Equation 2.2.

2.1.2 Experiments

The LHC ring supplies four main experiments as well as a set of smaller detectors with particle collisions.

The experiments A Toroidal LHC ApparatuS (ATLAS) [72] and Compact Muon Solenoid (CMS) [73] are the two large general purpose detectors at the LHC. The detectors are not tailored to one specific measurement, but are designed to be able to cover a broad range of physics. Their main objectives are precision measurements of the SM, discovery and exploration of the mechanism of EWSB, and to shed light on physics beyond the SM and possible explanatory theories as discussed in Section 1.1.4.

The A Large Ion Collider Experiment [74] is dedicated to heavy ion physics with the principal goal being the investigation of quark-gluon plasma. The Large Hadron Collider beauty (LHCb) [75] experiment is specialized in physics involving hadrons with b-quark content.

The two smaller experiments LHCf [76] and TOTEM [77] measure the total inelastic cross section of proton-proton collisions. Both are so-called *forward experiments* and are located in vicinity to the ATLAS and CMS experiments, respectively. The Monopole and Exotics Detector At the LHC (MoEDAL) [78] has been installed in the vicinity of the LHCb IP during the LS1 and will commence its search for magnetic monopoles and other exotica soon.

2.2 The Compact Muon Solenoid

The Compact Muon Solenoid (CMS) experiment [73, 79] is one of the two general purpose detectors at the LHC and located at the interaction point 5 near the french village Cessy. With a length of 21.6 m, a diameter of 14.6 m and a gross weight of 14 000 t it is one of the largest and most complex particle detectors built to date.

Its design is driven by the challenges of high energy physics at hadron colliders. Many interesting physics channels exhibit only a small cross section, while QCD jet production dominates the background contributions. Especially the precise reconstruction of lepton signatures is vital for the detection of many rare processes, and an optimal efficiency at high rejection power of background events is required. The CMS detector is designed following the concept of excellent muon and electron identification and momentum resolution. This is rendered possible by the high granularity of the electromagnetic calorimeter and the extensive muon tracking systems described in Sections 2.2.2 and 2.2.4, respectively.

For an efficient identification of heavy flavor quarks and τ lepton decays the precise measurement of secondary vertices and impact parameters is essential. The 3.8 T superconducting solenoid described in Section 2.2.3 provides the bending power for a good p_T discrimination of traversing particles by the all-silicon pixel and strip tracking detectors. These inner tracking detectors are introduced in Section 2.2.1 and allow for the precise determination of particle trajectories and vertices.

CMS employs a right-handed coordinate system to describe positions in the experiment [79]. The z-axis is defined along the LHC proton beam, while the x-axis points towards the center of the LHC ring. The equivalent polar coordinates are defined as follows. The radial distance from the beam pipe is denoted as r, the polar angle θ is measured with respect to the z-axis, and the azimuthal angle ϕ is measured against the x-axis. Usually the pseudorapidity η is favored over the polar angle and is defined as

$$\eta = -\ln \tan \theta/2. \tag{2.3}$$

Momentum and energy transverse to the beam are denominated as p_T and E_T, respectively. Missing energy in the transverse x-y-plane is denoted as E_T^{miss}.

2.2.1 Tracking Detectors

CMS features an all-silicon tracking system with a total active area of about 200 m^2 covering the solid angle up to pseudorapidities of $|\eta| < 2.5$. It consists of a high-granularity pixel detector close to the interaction region and a silicon strip tracker which covers radii from 0.2 m to 1.2 m as depicted in Figure 2.2.

The demands on the tracking system are high: At LHC design luminosity more than 1000 charged particles emerge from the interaction region every bunch crossing, passing through the tracking detectors and leaving hit information. This information needs to be buffered until the event has been validated by a trigger signal and the full event information is retrieved from all detectors (cf. Section 2.2.5). At the same time the overall material budget has to be minimized in order not to deteriorate both the momentum measurements via multiple Coulomb scattering and the calorimetric energy measurement by early energy loss. Moreover, the large flux of ionizing particles near the interaction point requires radiation hard tracking detectors and front-end electronics, especially since these detectors are operated for almost a decade without the possibility of maintenance or repair.

Since LS1 the tracking detectors are operated at temperatures below $-15\,^{\circ}\text{C}$ to mitigate effects from radiation damage and reduce the leakage current through the sensor (cf. Section 3.1).

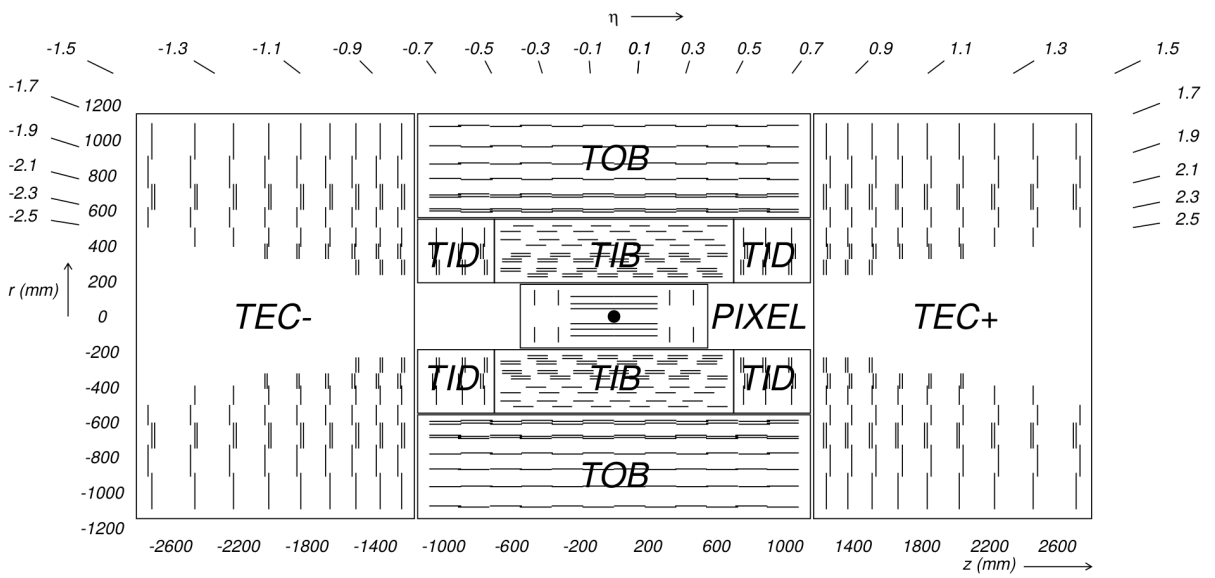

Figure 2.2: Geometry of the CMS inner tracking system. Shown is the rz view of the detector with the positions of the subdetectors and their modules. Double lines indicate back-to-back mounted modules for stereo angle interpolation, the nominal IP is marked with a black dot. From [73].

The Silicon Pixel Detector

The CMS Pixel Detector consists of three concentric barrel layers at radii of 4.4 , 7.3 , and 10.2 cm as well as two endcap discs on each side at distances of $z = \pm 34.5$ cm and ± 46.5 cm from the nominal interaction point. The pixel detector covers a pseudorapidity range up to $|\eta| \leq 2.2$ with three hits, and $2.2 < |\eta| < 2.5$ with two hits per trajectory with single hit detection efficiencies above 99 % [80].

The detector consists of 1440 modules comprising the segmented silicon sensor with a pixel pitch of 100 µm × 150 µm as well as the front-end electronics. In total, the detector has about 66 million readout channels which are operated in zero-suppression mode. Only pixels with a charge above an individually configurable threshold contribute to the event data. The pulse height information of every pixel hit as well as the pixel address are transmitted as analog signal and sampled by analog-digital converters (ADCs) in the front end drivers (FEDs) of the CMS data acquisition (DAQ) system.

The geometry of the pixel detector and the pixel sensor cells has been carefully chosen to yield optimal spatial resolution. While the barrel modules are mounted with the sensor surface parallel to the magnetic field of the solenoid, the forward detector modules in the endcaps are tilted by 20°. By this, the charge carriers produced by a charged particle traversing the detector are distributed over several pixels, either by the Lorentz drift or by the geometrical arrangement. This permits interpolation of the charges to calculate a more precise track impact point (cf. Section 3.3). The intrinsic spatial resolution of the detector has been determined to be 10 µm in the $r\phi$ direction, and $20 - 45$ µm along the z axis, depending on the incidence angle of the particle track [80].

The pixel detector will be replaced by a new detector in the extended year-end technical stop of the LHC 2016/2017. This so-called Phase I Pixel Detector is described in detail in Chapter 4.

The Silicon Strip Tracker

Around the pixel detector, the silicon strip tracker of CMS is located. Instead of segmenting the silicon sensor in two dimensions, the strip sensors feature implants which are divided into long strips. This allows to reduce both the very high manufacturing cost of a pixel detector caused by the complicated front-end electronics and bump bonding process, and the granularity of the detector while covering large areas.

The layout of the CMS tracker can be inferred from Figure 2.2. The Tracker inner barrel (TIB) and Tracker inner disks (TIDs) are located around the pixel detector in the center, while the Tracker outer barrel (TOB) and Tracker endcaps (TECs) form the outermost part of the tracker. Additional thermal shielding and air-tight sealing shields the tracker volume from the surrounding detector and allows flushing with dry air. This is of importance since the tracker is operated at temperatures of around $-15\,^{\circ}\mathrm{C}$ and the humidity has to be controlled in order to avoid condensation.

In order to provide a measurement for the second local coordinate, some of the detector modules consist of two strip sensors which are mounted back-to-back and rotated by a small stereo angle with respect to each other. Correlating the responses of the two sensors in the offline analysis allows to reconstruct the missing coordinate. However, this concept only performs well at low occupancy since the signal will otherwise be dominated by matching ambiguities.

Tracking

CMS employs a combinatorial Kalman filter (CKF) for tracking [81, 82]. The CKF is a recursive procedure which estimates the track parameters starting from an initial trajectory and updates the estimators with every successive hit added to the trajectory. Several methods are being used within CMS with the *inside-out* approach being the most prevalent one [83].

The track fitting is performed in three consecutive stages. Initial trajectory candidates, so-called *seeds*, are constructed from pixel detector information including constraints on the position of the beam spot and on a minimal transverse momentum p_T. This approach makes use of the high precision measurement of the pixel detector with its fine granularity and the very clean, low-noise signal.

The trajectories built from the initial seeds are then propagated from layer to layer to the outside, always accounting for multiple scattering and energy loss. The track parameters and uncertainties are updated on every layer, and new trajectories are created for every compatible hit. The total number of track candidates is limited by a maximum global χ^2 requirement of the track fit and by the number of missing hits for the complete trajectory. Ambiguities are solved by selecting the best trajectories based on the overall track fit quality and the number of shared hits.

After all information has been added to the track candidates, the final track fit is performed. The track resolution already reaches an asymptotic value after the first five hits have been added to the candidate. This enables the high level trigger (HLT) (cf. Section 2.2.5) to use tracking information, and allows to interrupt the tracking procedure as soon as enough information is acquired. These tracks are used for online vertex reconstruction and b-tagging [81].

Precise and stable tracking is especially important for the particle flow (PF) algorithm described in Section 12.2, which relies on tracking every single charged particle and assigning it to a calorimeter cluster.

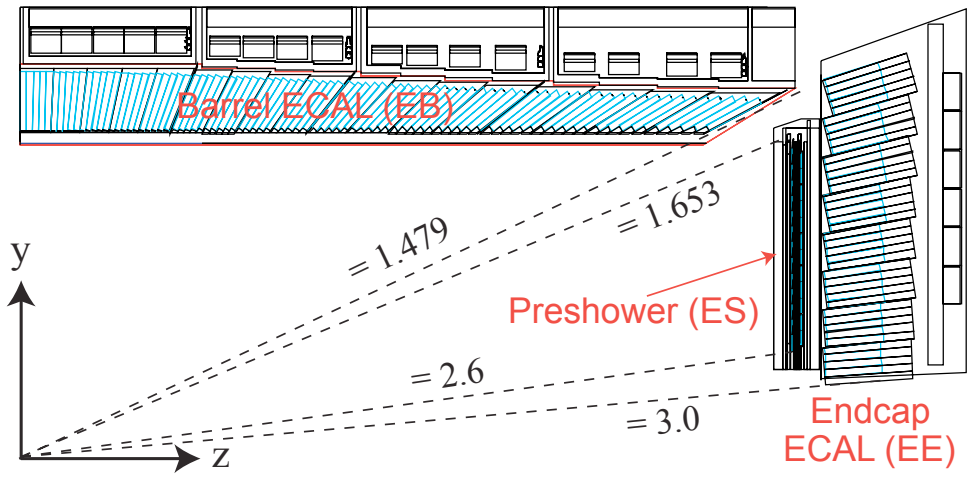

Figure 2.3: Geometry of the CMS Electromagnetic Calorimeter. Shown is one transverse section through the ECAL indicating the positions of the EB, the EE and the ES detectors. From [79].

2.2.2 Calorimeters

The task of measuring the particle energy is accomplished by the calorimeter detectors. Calorimeters are usually made of high-density materials in which the particles initialize showers as described in Section 1.3.2. In order to gain information about both the energy and the direction of the particles, calorimeter detectors are segmented. This allows to distinguish multiple particles or jets and enables matching with the tracks recorded by the tracker system (cf. Section 12.2).

Electromagnetic Calorimeter

The CMS Electromagnetic Calorimeter (ECAL) measures the energy of particles which primarily interact via the electromagnetic force. It is a hermetic detector covering the solid angle up to pseudorapidities of $|\eta| < 3$. The ECAL is divided into the barrel calorimeter (EB), the endcap calorimeter (EE), and is completed by the additional preshower calorimeter (ES) as shown in Figure 2.3.

The detector consists of scintillator crystals made of lead tungstate ($PbWO_4$). These crystals provide both a very fast response time [84] and a high radiation tolerance, both being crucial parameters for the ECAL. The high density of $8.3\,\mathrm{g/cm^3}$ allows for the construction of a relatively compact calorimeter while still containing most of the showers. With a crystal length of 23 cm in the barrel region, and 22 cm in the endcaps, the ECAL provides $25.8\,X_0$ ($22\,X_0$) of showering material in the barrel (endcap) detector. The ES preshower adds additional $3\,X_0$ of lead absorbers with silicon strip sensors in the pseudorapidity range $1.65 < |\eta| < 2.6$, before the EE detector. The light output of the scintillator crystals varies strongly with temperature and makes temperature stabilization of the ECAL detector a necessity.

The fine granularity of the detector using crystal faces with a size of $22 \times 22\,\mathrm{mm^2}$ in the barrel detector and $28.6 \times 28.6\,\mathrm{mm^2}$ in the endcaps provides good angular resolution and allows for precise matching with the tracking information using the PF algorithm (cf. Section 12.2).

The scintillation light from every crystal is detected by avalanche photo diodes and vacuum phototriodes in the EB and the EE detectors, respectively. Both devices have been extensively characterized in magnetic fields and under heavy irradiation to ensure stable operation for more than ten years.

Hadronic Calorimeter

The energy of hadrons is measured by the CMS Hadron Calorimeter (HCAL), a sampling calorimeter composed of alternating layers of massive absorbing brass plates and plastic scintillator tiles. Just like the other subdetector systems, it is divided into a barrel part comprising the barrel (HB) and tail-catching outer calorimeter (HO) up to $|\eta| < 1.3$, and endcap detectors. The endcaps include the endcap calorimeter (HE) for the pseudorapidity range $1.3 < |\eta| < 3$ and the additional forward calorimeter (HF) extending the HCAL acceptance up to $|\eta| < 5.2$ for hermetic coverage of the solid angle.

The barrel detector separation into HB and HO arises from the limited space available to the barrel detector. The HB detector is located inside the coil of the superconducting magnet, and is supplemented by the HO located outside the solenoid coil, right before the muon chambers. The HO thus works as tail-catcher to improve the energy measurement of jets and E_T^{miss} [85, 86]. It uses the solenoid itself as absorber material. Combining HB and HO, the barrel HCAL provides material to contain showers up to 11.8 interaction lengths λ_{int}.

The scintillation light collected from the scintillator tiles is converted using wavelength shifting fibers, and measured by hybrid photodetectors (HPDs) [87] which will eventually be replaced by silicon photomultipliers (SiPMs) as detailed in Section 2.3. During the LS1, the HO detector has already been completely equipped with SiPMs [88]. To improve the detection of early showers developing in the material between ECAL and HCAL, the first layer of scintillating tiles are placed before the first absorber plate. The last layer of scintillator tiles is located behind the last absorber layer in order to detect late showers which are leaking out of the detector.

The HF is exposed to a high level of radiation despite its remote location at $z = \pm 11.2\,\text{m}$ away from the nominal interaction point and thus uses a different detection technology. Energies of around 760 GeV at center-of-mass collision energies of 14 TeV are deposited in the HF, compared to an average of 100 GeV in the rest of the HCAL, and require the use of steel absorbers with embedded quartz fibers. These fibers detect the Cherenkov light produced by charged particles in the developing showers and are thus mainly sensitive to the electromagnetic fraction of the hadronic shower (cf. Section 1.3.2).

For jets with an energy of 50 GeV the relative energy resolution of the combined ECAL and HCAL detector systems is about 15% as obtained from test beam data. This can be greatly reduced by applying the PF algorithm described in Section 12.2. A detailed introduction to hadron calorimeters as well as a comparison of the hadron calorimeter performance of the ATLAS and CMS experiments can be found in [89].

2.2.3 The Solenoid

The design of the CMS experiment is centered around its strong superconducting solenoid magnet, which provides a 3.8 T magnetic field. This allows for a precise measurement of the particle momenta owing to the large bending power. The 13 m long coil has an inner diameter of 6 m which allows to house the tracking detectors and to also comprise the calorimetric systems. This improves the energy resolution significantly since the particles do not lose energy by crossing the magnet coil prior to being measured.

The stored energy at full magnetic field is about 2.6 GJ, with the magnetic flux returned through an iron return yoke. The return yoke also hosts the muon systems, and the 2 T magnetic return field allows for precise muon momentum determination.

2.2.4 Muon Systems

Muons at moderate energies can be considered minimum ionizing particles (MIPs) and traverse both the tracker and the calorimeters with minimal energy loss. They can thus be efficiently identified by a dedicated muon detector system outside the calorimeters which provides additional information for tracking. Due to the unique characteristics, the muon signal often has a superior signal-to-noise ratio and is heavily used in both trigger and physics analyses.

The muon systems form the outermost part of the CMS detector and are integrated into the magnet return yoke surrounding the solenoid. Gaseous detector chambers have been chosen as the technology for the muon system, providing cost efficient coverage of almost the full solid angle.

Three different types of detectors are employed, depending on their mounting position in the experiment. So-called drift tubes (DTs) are used in the barrel region of the detector, where the magnetic field is homogeneous and both the muon rate and the neutron induced backgrounds are comparatively low. The four layers of DT modules cover a pseudorapidity range up to $|\eta| < 1.2$. Each DT station hosts 12 individual, gas-filled tubes with a diameter of 4 cm and a center electrode. Most of the tubes run along the z axis providing measurements in $r\phi$, whereas the first three layers also feature tubes for z measurement.

The endcap regions covering $0.9 < |\eta| < 2.4$ are subject to a much higher muon flux while the magnetic field is stronger and less homogeneous. Therefore, cathode strip chambers (CSCs) are deployed which feature a faster response time, higher granularity, and better radiation hardness. The CSCs are trapezoidal multi-wire proportional chambers which provide 2D position measurements with the cathode strips running radially from the beampipe.

Resistive plate chambers (RPCs) in both the barrel and the endcap regions provide precise timing information of the order of 1 ns at the cost of a coarser position resolution and are mainly used for bunch crossing assignment and in the trigger system. They consist of two high-resistivity plastic plates with readout strips, separated by a gas-filled volume. The RPCs are operated in avalanche mode.

During LS1, a fourth endcap muon station has been installed, and the readout electronics of the CSCs and DTs have been improved.

2.2.5 The Trigger and Data Acquisition System

With the LHC delivering proton-proton collisions at a rate of 40 MHz, the data produced by the CMS experiment are orders of magnitudes too large to be stored. The typical size of one event recorded by the CMS detector is about 1 MB, and it would be technically impossible to stream about $40\,\mathrm{TB\,s^{-1}}$ to disk. However, even if possible, the added scientific value would be questionable since most of the events only contain low-energy glancing collisions rather than inelastic hard scattering processes.

The required reduction of the event rate is achieved by the so-called trigger system. The task of the trigger is the selection of potentially interesting events and the reduction of the rate to a manageable value of a few hundred Hz.

While most high energy physics experiments use three trigger levels, the CMS trigger system implements a two-stage rate reduction which provides additional flexibility. The first stage is the Level 1 Trigger (L1) [90] which is fully implemented in hardware using Field Programmable Gate Arrays (FPGAs) and Application Specific Integrated Circuits (ASICs). It reduces the initial rate to around 100 kHz with a maximum latency of 3.4 µs, limited by the tracker system readout.

During this latency all data are buffered in pipelines in the detector front-end electronics. Because of this time constraint, only data from the calorimeters and the muon systems are processed and contribute to the trigger decision. First, simplified local reconstruction algorithms are executed in the subdetector systems, and trigger primitives are generated and subsequently merged into the L1 global trigger decision. Only after a L1 acceptance signal has been issued, all subdetector systems send their buffered data to the DAQ system.

The data are then collected and synchronized by the event builder and sent to the next stage of the triggering system, the high level trigger (HLT) [91]. The HLT is software based and consists of several thousand CPUs running analysis algorithms for a full reconstruction of all events in search of interesting signatures. Time-consuming algorithms, such as tracking using the full silicon tracker information, are only applied to regions of interest since the latency of the HLT is limited to 50 ms. Events are finally stored for offline analysis if the requirements of at least one of the trigger paths are met. These trigger paths are configurable and are described in the trigger menus [92].

In case of very high rates, single trigger paths can also be prescaled to only store a fraction of the triggered events to disk. In addition, CMS also records so-called minimum bias data which are subject to only very few constraints. These data are for instance used to model the underlying event.

The final event rate which is transmitted to the CERN Tier-0 computing center and stored on tape is about 100–300 Hz.

2.3 Upgrades to the CMS Experiment

The CMS detector will undergo several major upgrades during the next decades of its operation owing to the challenges arising from higher luminosities, the performance degradation induced by damage from ionizing radiation, and to the availability of new technologies. These upgrades aim at sustaining and improving the overall performance under the increasingly demanding conditions imposed by the LHC operation. Furthermore, the maintainability of the experiment over this long period of operation has to be ensured.

The LHC schedule and the experiment upgrade plans are divided into two parts. During the Phase I until 2023 the LHC will operate at an energy of $\sqrt{s} = 13\,\text{TeV}$, and the instantaneous luminosity will be increased up to $\mathcal{L} = 2 \times 10^{34}\,\text{cm}^{-2}\text{s}^{-1}$. For this period, two long shutdowns are planned of which the first (LS1) has just been successfully completed, and improvements to the subdetector systems of CMS have been installed which allow to fully exploit the luminosity delivered by the LHC.

After 2023 a major machine upgrade will be carried out in the extended long shutdown LS3 to achieve higher instantaneous luminosities. This marks the start of the Phase II and the operation of the High-Luminosity LHC (HL-LHC). Also the CMS experiment will undergo major transformations in order to handle the higher luminosities, such as the replacement of the full inner tracking system.

2.3.1 The Phase I Upgrades

The challenges addressed by the Phase I upgrades concern both the instantaneous and the integrated luminosity experienced by the CMS experiment. With the high instantaneous luminosity delivered by the LHC, the experiment has to deal with an in-time pile-up of 60 and more, creating numerous problems for subdetectors and the L1 trigger.

Since the trigger performance would decrease at high pile-up, some parts of the trigger system such as the regional calorimeter trigger will be rebuilt using new technologies available [93]. This allows to use the full detector granularity including the additional CSC stations added during LS1 and will enable the trigger to cope with higher occupancies and more complex events. Furthermore, a new timing and trigger control system based on modern telecommunication technology will be implemented for improved performance.

Towards the end of Phase I, CMS will have collected a total integrated luminosity of about $300\,\mathrm{fb}^{-1}$. The absorbed ionizing radiation damages the detector material and some subsystems will be subject to severe efficiency loss. Especially the pixel detector system and the HF absorb high doses.

The pixel detector will be completely replaced with a new detector featuring four barrel layers and three disks at each end. High bandwidth readout electronics will improve the efficiency at high occupancies, while relocated service electronics and a lightweight support structure will reduce the material budget in the tracking volume. A CO_2-based two-phase cooling allows for a lower operational temperature. The new pixel detector and its components are described elaborately in Chapter 4.

The HCAL upgrade plans [94] comprise new QIE10/QIE11 ADC chips as well as new control electronics to reduce single event upsets (SEUs). All HPDs in the HE and HB detector systems will be replaced with SiPMs. The HPDs faced several problems with electrical discharges, gain drifts, and increased noise levels, while the proposed SiPMs have a better quantum efficiency, higher gain, and better immunity to magnetic fields. Due to the small size of the SiPMs, the replacement also facilitates an additional depth segmentation of the detector which improves tracking of the shower development. In the HF detector, the existing photomultiplier tubes (PMTs) will be replaced with multi-anode tubes.

A more detailed description of all improvements planned and implemented for the CMS Phase I upgrades can be found in the technical proposal [95].

2.3.2 The Phase II Upgrades

The main goal of the HL-LHC operation is a recorded integrated luminosity of $3000\,\mathrm{fb}^{-1}$ by 2035. The conditions foreseen are an average pile-up of about 140 and a leveled instantaneous luminosity of $\mathcal{L} = 5 \times 10^{34}\,\mathrm{cm}^{-2}\mathrm{s}^{-1}$. The main challenges for the CMS experiment are similar to those of Phase I but more severe. The detectors will experience significant radiation damage which leads to a progressive degradation of the overall detector performance. As comparison, the annual dose expected to be delivered to the detector per year at the HL-LHC is similar to the total dose received in all operations from the start of the LHC up to LS3.

The dose as well as the effect of the radiation damage vary strongly from subdetector to subdetector. The two detectors affected most are the silicon tracker and the forward calorimeters. In silicon, ionizing and non-ionizing radiation induce surface and bulk damage, leading to an increased leakage current through the sensor, trapping of charge carriers on their drift to the readout electrodes, and defects in the front-end electronics. In order to fully deplete the sensor material, the bias voltage has to be increased until it reaches an unsustainable level, while operating partial depleted sensors leads to a degradation of the signal. In the calorimeters the main problem has been identified as the transport of the scintillation light from the point of the particle interaction to the readout electronics. Especially the $PbWO_4$ crystals lose their translucence leading to a reduced signal.

The second main challenge concerns pile-up. At the nominal luminosity of the HL-LHC the pile-up is expected to be around 140 on average, but further increase of the luminosity results

in higher pile-up. This causes a higher occupancy in the tracking system and will eventually lead to an increased rate of misidentified tracks. Also the identification of isolated leptons will become more challenging with more soft interactions accompanying the hard scattering process.

In order to deal with these demands and to maintain an adequate track reconstruction performance, the granularity of both the strip tracker and the pixel detector will be increased by a factor of 4. Special double-sensor modules in the strip tracker will be capable of providing p_T-discriminated track information to the L1 trigger at 40 MHz and thus reducing the data by a factor of 20. This permits powerful background rejection already at the earliest stage of event selection.

The calorimeters will be replaced by a high-granularity calorimeter with an electromagnetic and a hadronic section. The electromagnetic part uses silicon sensors as active material and provides around $25\,X_0$ but only about $1\,\lambda_{\text{int}}$ hadronic interaction lengths. The hadronic part comprises a front section also featuring silicon sensors and provides a depth of $3.5\,\lambda_{\text{int}}$. It is followed by the backing hadron calorimeter with a design similar to the current HE calorimeter (cf. Section 2.2.2), providing an additional depth of approximately $10\,\lambda_{\text{int}}$.

The muon systems will be enhanced in the region $1.4 < |\eta| < 2.4$ with additional chambers in order to maintain a good L1 muon trigger acceptance. In some regions with high magnetic fields, gas electron multiplier chambers will be used.

The L1 trigger latency will be increased to 12.5 µs which is sufficient for hardware track reconstruction using new technologies such as associative memory. This implies upgrades to many of the existing readout electronics of subdetector systems. The L1 accept rate will be increased to 500 kHz at a pile-up of 140, and to 750 kHz at pile-up 200. The HLT is expected to have an output rate of up to 10 kHz.

Extensive design studies have been carried out, and detector prototypes are in production, but many projects are still in their R&D phase and changes to these proposals are to be expected. A more elaborate description of the proposed design and infrastructure for Phase II operation of the CMS experiment can be found in the technical proposal [96].

Part I

Test Beam Measurements and Data Acquisition for the Phase I Upgrade of the CMS Pixel Detector

3. Basic Concepts of Semiconductor Tracking Detectors

Tracking detectors are a crucial component of any modern particle physics experiment, especially in the high-occupancy regimes at hadron colliders. They provide measurements for the determination of particle trajectories, from which their basic properties such as momentum and charge as well as origin and direction can be deducted. In particle detectors at hadron colliders additional challenges have to be addressed by the tracking detectors, such as pile-up mitigation and tracking of single particles within dense jet structures to enable advanced reconstruction techniques such as the CMS particle flow (cf. Section 12.2).

The performance of the tracking detectors is vital for all physics analyses, but especially heavy flavor physics such as top quark measurements rely on a superior resolution of secondary decay vertices for b quark tagging. The material, design, and front-end electronics have to be carefully chosen in order to optimize the detector performance for high tracking efficiency and good spatial resolution.

The technology favored by most of the current high energy particle physics experiments is silicon semiconductor detectors due to a number of advantages over alternative detector concepts. Silicon sensors are solid-state ionization chambers in which incident charged particles create electron-hole pairs. These charge carriers drift to the electrodes under the influence of an electric field. The induced current at the electrodes is then amplified, shaped, and read out by the front-end electronics.

The mean ionization energy of silicon is much lower compared to gaseous tracking detectors. This results, together with the high material density, in a large number of charge carriers produced. On average about 73 electron-hole pairs are created by an incident MIP per µm of silicon [15]. This induces a sufficiently large signal of about 22 ke in a typical sensor with a thickness of 300 µm. The high charge carrier mobility leads to a comparatively short collection time and a fast readout of $\mathcal{O}(10\,\text{ns})$. This is of special interest at accelerators like the LHC where the time between collisions is as low as $\delta t = 25\,\text{ns}$.

Furthermore, silicon is a widely used material, and the design and manufacturing of silicon tracking detectors profits from the established fabrication processes available in industry.

The position sensitivity of silicon sensors is achieved by segmenting the implants and electrodes. The design of these segmentations can be either strip-like effectively providing a one-dimensional

position measurement, or pixel-like providing two coordinates for the point of incidence. With modern devices, spatial resolutions of 10 µm or lower can be reached. In order to reconstruct the full trajectory of the passing particle, the measurements from multiple layers of the detector are combined.

This chapter aims at giving only a brief overview of silicon detector technology and pattern recognition algorithms since both topics are exhaustively discussed in standard literature. Reviews of silicon detectors and an overview of different sensor types and technologies can be found for example in [97–100]. A detailed review of pattern recognition in particle physics is given in [101].

An essential topic for long-term operation of silicon detectors at hadron colliders is resilience against radiation induced damage. This is, however, not within the scope of this thesis. Extensive information on the effects of radiation damage on both silicon sensors and the readout electronics can be found elsewhere [102–104].

3.1 Semiconductor Sensors and Signal Formation

Semiconductors are a class of solid materials classified by their electrical properties. Owing to the density of energy levels in the lattice structure of a crystalline material, some simplifications to the description can be made. When forming the lattice structure, the atomic orbitals of the constituents start overlapping and the energy state density increases because of shifts caused by the interaction. Eventually, a continuous band structure forms, which can be used to describe the electrical properties of the material. This energy band model allows to divide matter into the three categories — conductor, insulator, and semiconductor, — depending on their band configurations.

With the electrons following the Pauli principle, the occupancy of energy states can be expressed using the Fermi-Dirac distribution. It yields the probability density of encountering an electron with a given energy and is defined as

$$f(E) = \frac{1}{e^{(E-E_F)/k_B T} + 1}, \tag{3.1}$$

with k_B being the Boltzmann constant and T the temperature. The term E_F denotes the Fermi energy at which the occupancy probability is

$$f(E = E_F) = \frac{1}{2}.$$

At $T = 0\,\mathrm{K}$ all energy states up to E_F are filled, at higher temperatures some electrons will occupy excited states above the Fermi energy. In the energy band model, the valence band represents the highest band completely filled with electrons at $T = 0\,\mathrm{K}$. The next higher energy band is the conduction band which is only partially filled with electrons. Due to the free available energy states within the band, electrons can move freely within the crystal lattice and thus contribute to the conductivity of the material.

Figure 3.1 shows the different configurations of the two bands for conductors, semiconductors and insulators. If the Fermi energy E_F lies within the conduction band or the valence and conduction bands overlap, the material contains free charge carriers and is considered a conductor. For insulators the opposite case applies. The Fermi energy lies above the valence band, and the energy gap between the two bands is too large for electrons to be excited into the conduction band even at high temperatures. At a temperature of $T = 0\,\mathrm{K}$ semiconductor materials behave

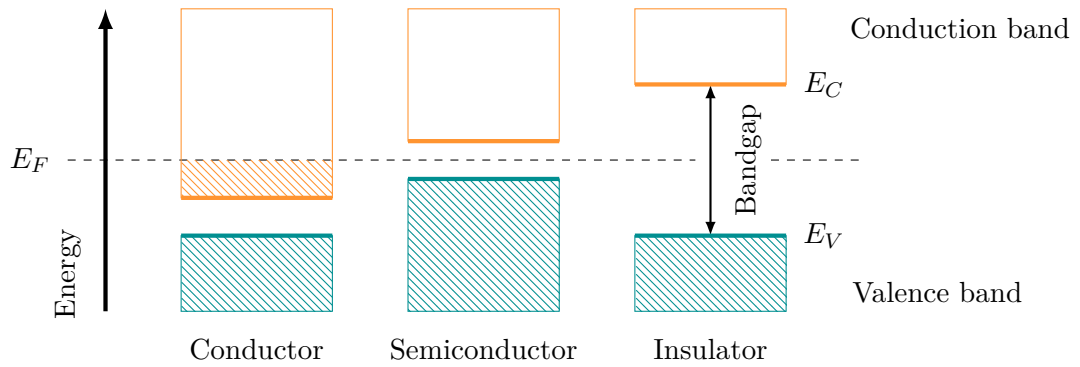

Figure 3.1: Fermi energy and band configuration of conductors, semiconductors, and insulating materials in the energy band model. While conductors contain free charge carriers even at $T = 0\,\mathrm{K}$, semiconductors and insulators have Fermi energies below the conduction band. The difference between the latter is the size of the band gap $E_G = E_C - E_V$.

just as insulators with the Fermi level being above the valence energy E_V. However, the band gap E_G is much smaller which allows thermally excited electrons to reach the conduction band. These electrons are so-called intrinsic charge carriers, and the pure matter is referred to as intrinsic semiconductor accordingly.

The size of the band gap depends on the material and strongly influences its characteristics. Germanium has a relatively small band gap of about $E_G = 0.74\,\mathrm{eV}$ which results in a very low mean ionization energy. Thus, germanium is mostly used in spectrometers where a superb energy resolution is a key feature. Since the small band gap also leads to a high number of free charge carriers at room temperature, the detector has to be cooled e.g., by liquid nitrogen to reduce thermal noise. This is not feasible for tracking detectors and thus usually silicon is chosen as semiconductor material. With the larger band gap of $1.12\,\mathrm{eV}$ at $T = 300\,\mathrm{K}$ the number of thermal excitations into the conduction band and therefore the noise is much lower.

3.1.1 Extrinsic Semiconductors

The properties of intrinsic semiconductors can be modified by introducing artificial impurities into the lattice. This process of replacing silicon atoms with impurity elements is usually referred to as doping. The impurity materials create additional energy levels within the band gap which alter the electrical conductivity.

Doping silicon with a group-V element, such as phosphorus, adds an additional valence electron which is only loosely bound. The additional energy band is called a shallow donor and is located close to the conduction band as shown in Figure 3.2 (center). Thus the quasi-free electron can easily be excited, and the remaining phosphorus atom becomes a positive ion (hole). This material is referred to as n-type silicon, with the majority charge carrier being electrons.

Shallow acceptor states close to the valence band as shown in Figure 3.2 (left) can be created by introducing a group-III element such as boron into the silicon crystal. With one valence electron fewer than the surrounding silicon atoms this effectively introduces a hole which can be occupied by valence band electrons. The majority charge carriers in this material are holes and the material is denominated as p-type silicon.

If the majority of charge carriers stem from the dopant materials, the semiconductor is referred to as being extrinsic. Beside doping bulk silicon material it is also possible to produce precisely

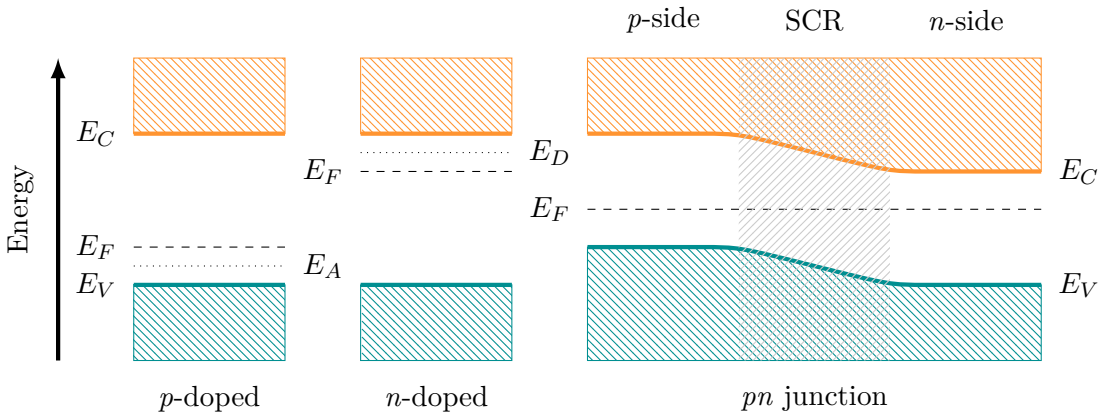

Figure 3.2: Band structure and energy levels of n-doped and p-doped silicon. The acceptor (E_A, left) and donor (E_D, center) energy levels introduced by the dopant alter the Fermi energy E_F of the material. When joining them (right) a common Fermi level develops and a space-charge region (SCR) forms.

differentiated implantations of one or the other type. This allows to introduce segmentations into the silicon sensor material as described in Section 3.1.4. A variety of doping technologies is available, and different doping profiles and concentrations can be produced.

Hereafter, implant dopings are denoted as n^+ and p^+, emphasizing the higher dopant concentration, while bulk doping is labeled as n and p, respectively.

3.1.2 The *pn*-Junction

In 300 µm intrinsic silicon the number of free charge carriers is $\mathcal{O}(10^9)$ while the signal expected from incident particles is only about $\mathcal{O}(10^4)$ as described in Section 3.1.5. In order to separate the signal from this noise contribution, the amount of free charge carriers has to be reduced.

This can be achieved by combining p- and n-type silicon in a so-called pn-junction and by operating the junction in reverse bias mode. Figure 3.2 shows both the separated p- and n-type silicon materials with their Fermi energies altered by the dopant levels E_A, E_D and the joined pn-junction. By joining the materials, a gradient of charge carrier concentration between the differently doped regions forms. Free charge carriers drift through the material via diffusion in order to level out the different Fermi energies. Since the donor and acceptor ions are immobile, an electric field builds up as the charge carriers diffuse, counteracting the diffusion process until an equilibrium is reached.

The charge carriers near the junction recombine with dopant impurities of the other type forming a space-charge region (SCR) depleted of free charge carriers as shown in Figure 3.2 (right). This depleted region as a whole is charge neutral but consists of a negatively charged area at the p-doped side and a positively charged on the n-doped side of the junction. Depending on the relative doping concentration, one or the other might be significantly thicker. The electrostatic potential within the pn-junction is called the built-in voltage U_{bi} and can be calculated by a twofold integration of the Poisson's equation given by

$$\frac{d^2\Phi(x)}{dx^2} = -\frac{\rho(x)}{\epsilon_r \epsilon_0}, \tag{3.2}$$

where $\rho(x)$ denotes the charge density and $\epsilon_0\epsilon_r$ the permittivities of vacuum and silicon. The

integration yields the electrostatic potential

$$\Phi(x) = \begin{cases} -\frac{N_A}{2\epsilon_r\epsilon_0}(x+d_p)^2 & \text{for } -d_p < x < 0 \quad \text{(p-doped region)} \\ \frac{N_D}{2\epsilon_r\epsilon_0}(x-d_n)^2 & \text{for } 0 < x < d_n \quad \text{(n-doped region),} \end{cases} \tag{3.3}$$

where d_n and d_p are the thickness of the SCR in the n-doped and p-doped material, respectively. N_A and N_D denote the individual doping concentrations, while the effective doping concentration is given by $N_{\text{eff}} = N_D - N_A$. The built-in voltage between the boundaries of the SCR can be calculated from Equation 3.3 as

$$U_{\text{bi}} = \frac{1}{2\epsilon_r\epsilon_0} \cdot |N_{\text{eff}}| \cdot d^2, \tag{3.4}$$

where d is the total thickness of the depleted SCR. The extend of the SCR changes with the additionally applied external voltages U_{bias} and can be calculated by inverting Equation 3.4. The thickness d is then given by

$$d(U_{\text{bias}}) = \sqrt{\frac{2\epsilon_r\epsilon_0}{|N_{\text{eff}}|} \cdot (U_{\text{bias}} + U_{\text{bi}})}. \tag{3.5}$$

The built-in voltage is usually of the order of millivolts creating a SCR of only a few microns. However, with the external voltage applied, the thickness of the depleted region can be increased or decreased, depending on the polarity. A voltage reducing the SCR is called a forward bias, while the polarity increasing the thickness is denoted as reverse bias and is the normal operation mode for semiconductor sensors.

3.1.3 Depletion Voltage, Capacitance, and Leakage Current

The voltage at which the SCR spans the entire sensor volume and the whole device is depleted of free charge carriers is called the depletion voltage U_{dep}. Neglecting the comparatively small built-in voltage, U_{dep} follows directly from Equation 3.5 as

$$U_{\text{dep}} = \frac{|N_{\text{eff}}| \cdot D^2}{2\epsilon_0\epsilon_r}, \tag{3.6}$$

where D is the total sensor thickness. Since the SCR acts as plate capacitor, the capacitance of the device can be calculated from the thickness of the depleted region

$$C \propto \frac{\epsilon_r\epsilon_0}{d(U_{\text{bias}})} \propto \begin{cases} \sqrt{\frac{\epsilon_r\epsilon_0 |N_{\text{eff}}|}{2 \cdot U_{\text{bias}}}} & \text{for } U_{\text{bias}} \leq U_{\text{dep}} \\ \frac{\epsilon_0\epsilon_r}{D} & \text{for } U_{\text{bias}} > U_{\text{dep}}, \end{cases} \tag{3.7}$$

where the proportionality constant is the surface area of the pn-junction regarded. At full depletion the bulk capacitance C is directly related to the thickness of the sensor. This means that the capacitance can be used as a measure for the depletion of the sensor. As soon as the full depletion is reached, the capacitance does not further increase with higher bias voltage, and the full depletion voltage U_{dep} can be read from the kink of the curve $1/C^2$ versus U_{bias}.

If the bias voltage is increased to values above U_{dep}, an additional electric field inside the silicon sensor builds up. Thermally excited electrons in the conduction band are attracted by the electrodes and are removed from the sensor volume. This charge drift through the sensor is the

so called leakage current or reverse current. It is an important parameter for silicon sensors since it strongly affects noise and power consumption of the detector. In an ideal *pn*-junction the leakage current is completely determined by the diffusion of thermal charge carriers. In real devices, however, impurities introduced during processing or radiation induced defects add additional energy levels near the middle of the band gap which increase the leakage current considerably.

Owing to the temperature dependence of the density of free charge carriers in the conduction band, also the leakage current scales with temperature. With the leakage current measured at temperature T_1, the current at any other temperature T_2 can be calculated using

$$I\left(T_2\right) = I\left(T_1\right) \cdot \left(\frac{T_2}{T_1}\right)^2 e^{-\frac{E_{\text{eff}}}{2k_B}\left(\frac{1}{T_2}-\frac{1}{T_1}\right)}, \tag{3.8}$$

where $E_{\text{eff}} = 1.21\,\text{eV}$ is an effective band gap energy [105]. Operating the sensor at lower temperature thus leads to a reduced leakage current.

3.1.4 Implant Segmentation

The *pn*-junctions used in the design of silicon sensors are usually asymmetric. While the bulk material has a typical thickness of 50 µm to 500 µm to allow for sufficient charge carrier generation, the implant is usually only a few microns thick.

In order to achieve a position measurement, the implants on the top side are segmented into sections either in one direction for strip sensors, or two-dimensional for pixel sensors. Each of these implants creates a separate *pn*-junction with the backside of the sensor bulk. The distance between the pixel or strip implant centers is usually referred to as their pitch.

When using n^+-doped silicon as implant material, an electron accumulation layer forms at the insulating silicon dioxide layer around the implants. Since this would short the individual implants, an isolation preventing the electron accumulation is necessary. This is usually realized either via the *p*-spray technique, where a thin layer of *p*-dopant is deposited on the entire implant side of the silicon wafer, except for the n^+-implant regions. Alternatively, one or several confined implants of p^+-dopant are placed between the n^+ implants. This is known as *p*-stop isolation.

Additional guard ring implants have the task to shape the electric field inside the sensitive area and to prevent breakdowns caused by high electric fields near the cutting edge of the sensor.

In pixel sensors, the individual implants are equipped with a metal pad which is directly connected to the readout electronics. While strip sensor implants can be wire-bonded at the chip edge, the single pixel implants have to be bump-bonded one by one to a readout chip (ROC) which features the same geometry and pixel pitches. This process is usually referred to as flip-chip bonding and the detector is called a hybrid pixel detector.

Another possibility is the combination of both sensor and readout electronics on the same silicon wafer. These so-called monolithic active pixel sensors (MAPS) can therefore be very thin and lightweight, but have other disadvantages such as speed or radiation tolerance which currently make them unsuitable for high energy physics at hadron colliders [106].

Since the charge from every implant has to be read out and amplified separately, the pitch of pixel sensors is mostly driven by space requirements of the readout electronics to accommodate all necessary components (see Section 3.2). However, also other considerations such as the required granularity and aspired position resolution have to be taken into account. Because of the fine segmentation and the accompanying complex front-end electronics, pixel detectors in general have a higher power consumption compared to silicon strip detectors. This necessitates a larger cooling power and consequently a more involved support structure design.

3.1.5 Signal Formation

In order to detect traversing particles, charge carriers have to be produced, collected, and measured. The signal formation in silicon detectors is a process involving several mechanisms which have been carefully studied and quantified. Elaborate reviews can be found for example in [15, 107].

Charge Creation

Charged particles passing through a semiconductor material create electron-hole pairs along their path. The main process mediating the energy loss depends on the energy of the incident particle, and is described by the Bethe formula [15] for particles heavier than the electron rest mass. The formula is usually given as a function of $\beta\gamma$, where β is the particle speed in units of c, and $\gamma = 1/\sqrt{1-\beta^2}$ is the relativistic Lorentz factor of the particle.

This parametrization allows to characterize different regions of the Bethe formula. At low values of $\beta\gamma$, the incident particle is highly ionizing and usually stopped in the material resulting in the pronounced Bragg peak in the energy deposition. The minimum ionization is reached around $\beta\gamma \approx 3$. Particles with these properties such as muons at momenta around 300 MeV are called minimum ionizing particles (MIPs). At large $\beta\gamma$ radiative processes start to dominate the energy loss.

The actual energy loss is subject to large fluctuations. When incident particles experience a head-on collision with an orbital electron of an atom, a large momentum is transferred to the respective electron and it is knocked out of the orbit. These knock-on electrons or delta rays traverse the material creating further electron-hole pairs and thus leading to a large fraction of absorbed energy [107].

The Landau-Vavilov distribution [108, 109] is an approximative distribution describing the energy loss including delta ray effects. It features a Gaussian core with a pronounced tail towards large energies, and the most probable value (MPV) is significantly lower than the mean of the distribution.

Charge Collection

The charge carriers created by the incident particle have to be collected at the sensor implants in order to be detected. An externally applied electric field causes the electrons and holes to drift to the electrodes. In n-bulk sensors with p^+-implants, holes are collected at the implant side while electrons drift to the sensor backplane, in p-bulk with n^+ implants or in n^+-in-n sensors the reverse occurs.

Owing to the Shockley-Ramo theorem [110, 111] a current is induced at the electrodes during the full drift time. The current strongly depends on the actual geometry of the implant segmentation due to varying weighting potentials. The weighting potential for one specific electrode is obtained by setting its potential to 1 V, while requiring the potential of all other electrodes to be zero. In the simplest case of a diode detector without any segmentation, the induced current scales linearly with sensor thickness, the number of charge carriers, and the drift velocities.

The charge carrier drift velocity is a function of the position dependent electric field $E(x)$, leading to different drift velocities of charge carriers depending on their position inside the sensor. Due to different scattering mechanisms depending on the field strength, the dependence on E is non-trivial. In low electric field regions, the drift velocity depends linearly on the field strength and the low-field mobility μ_0, and is given by $v_d(x,t) = \mu_0 E(x)$. In high field regions the drift

velocity saturates at $v_d = v_{\text{sat.}} = \text{const}$. The actual values of v_d are usually parametrized and interpolated between the two regimes [112].

The observable, however, is the total integrated charge Q, induced by the drifting charge carriers. The charge collection efficiency (CCE) is defined as the ratio between total induced charge Q and originally deposited charge $Q_0 = eN_0$, viz.

$$CCE = \frac{Q}{Q_0}, \tag{3.9}$$

and depends on many factors such as the electric field configuration inside the sensor, and the implant geometry and isolation technique of the pixels. The CCE is an important parameter of silicon tracking detectors since it has a direct influence on the hit detection efficiency and position resolution.

An additional drift can be caused by an external magnetic field, which exerts the Lorentz force on the charge carriers. The resulting Lorentz angle θ_L for the charge carrier drift can be expressed as

$$\tan\theta_L = r_{\text{H}}\mu B, \tag{3.10}$$

where $r_{\text{H}} = \mu_{\text{H}}/\mu$ represents the Hall scattering factor relating the Hall mobility μ_{H} and the drift mobility μ without magnetic field. The magnetic field is denoted as B. Different Hall scattering factors apply for electrons and holes ($r_{\text{H}} = 1.15$ and $r_{\text{H}} = 0.7$, respectively [113]), and thus different Lorentz angles are to be expected for the two charge carrier types. The Lorentz drift can be exploited in the design of the sensor in order to optimize the charge sharing between sensor implants.

During the drift to the electrodes, the charge diffuses in the lateral direction. The extend of the charge cloud l_d is given by the Einstein diffusion equation

$$l_d = \sqrt{2Dt}, \qquad \text{with} \quad D = \mu\frac{k_B T}{e}, \tag{3.11}$$

where D is the diffusion constant and t the total drift time. Since the mobility μ cancels with $t \propto 1/\mu$ the diffusion width is the same for electrons and holes.

3.2 Front-End Electronics and Detector Readout

The charge collected at the individual pixel implants is processed by the front-end electronics in order to extract the hit information necessary for particle tracking. In hybrid pixel detectors, the pixel implants are usually DC-coupled to the sensor readout pads. The pixel cells of the front-end electronics are connected to the pads via bump bonds, and are appropriately adapted to the small input capacitances. The large amount of readout channels makes zero suppression a necessity since the readout bandwidth would not suffice to transmit samples for every pixel cell. Thus, the signals received from the sensor are usually discriminated against noise already in the pixel cell electronics.

The typical building blocks of pixel detector front-end electronics are outlined in Figure 3.3. The charge collected in the sensor is first fed to the preamplifier and the shaper circuits. The subsequent comparator discriminates between signal and noise for zero suppression.

Usually, the threshold of the comparator is configurable which allows the adaption to different signal-to-noise scenarios and facilitates the mitigation of aging processes such as radiation damage and reduced CCE in the sensor. Two different thresholds can be defined. The absolute

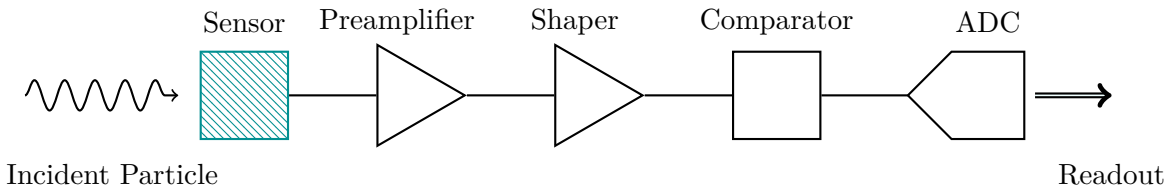

Figure 3.3: Typical building blocks of pixel front-end electronics. The incident particle induces a signal in the sensor, which is processed by the preamplifier and shaper. The comparator discriminates the signal before it is digitized by the ADC and read out. Modified from [98].

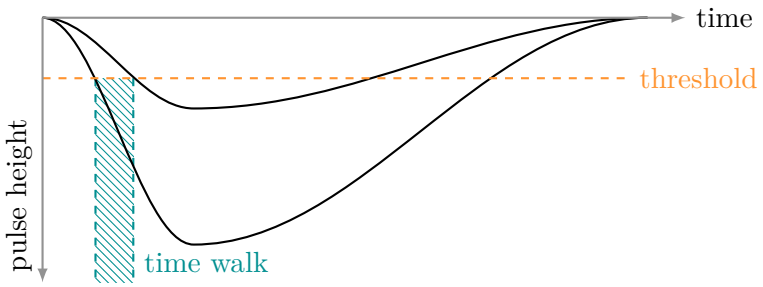

Figure 3.4: Time walk effects in the comparator. Small pulses reach the threshold later than large pulses, the time difference between the sampling is the so-called *time walk* of the comparator.

threshold indicates the charge at which the comparator triggers the readout of the pixel. However, especially small signals are subject to time walk effects, where the triggering time of the comparator at a fixed threshold depends on the absolute pulse height as sketched in Figure 3.4. Whenever the time of arrival is of importance, it has to be guaranteed that the threshold decision is taken within the allotted time frame. The minimal charge resulting in a time walk within the requirement is referred to as the *in-time threshold* and can be significantly different from the absolute threshold, depending on the chip design and time walk behavior.

If the signal has passed the charge threshold, it can be sampled by an ADC in order to quantify the collected charge. The digitized charge information is read out together with the pixel address information. This readout mode is referred to as **charge sensitive** as the full pulse height of the signal is sampled, and the additional information about charge sharing between neighboring pixel cells can be exploited. In some cases, the signal is transmitted to the DAQ system as analog pulse height and sampled only outside the detector.

If a fast timing is of concern, the **binary mode** can be chosen, where only the information about the exceeded threshold is transmitted. This approach is often used in either very fast devices or front-end electronics with very fine pixel pitches which cannot accommodate the additional components necessary for buffering and sampling of the pulse height.

Electronic noise describes random fluctuations in electric signals and is of concern for front-end electronics since it deteriorates the precision of the pulse height sampling, or, if large enough, might even pass the charge threshold and create noise hits. Thus, the noise amplitude can be a limiting factor for the minimum threshold achievable. The main noise sources in front-end electronics are stray capacitances from other electrical components in the vicinity of the analog signal line and electronic noise arising from the amplification process. Therefore, careful routing of supply voltage lines can significantly improve the analog performance of the device.

3.3 Pattern Recognition and Tracking

Pattern recognition in high-energy physics usually refers to the task of reconstructing the trajectory of the original particle from the abstract raw detector data. The first step in this intricate process is the local hit reconstruction. The individual pixel hits are combined to clusters and algorithms try to provide estimates on where exactly the particle traversed the sensor material, e.g., by exploiting charge sharing effects as described above. In a second step, this local information from all detector parts is combined to tracks in order to reconstruct the entire particle trajectory.

The figure of merit for track reconstruction is the spatial resolution of the final trajectory, be it for secondary vertex resolution or extrapolation to other subdetector systems. Unlike hodoscope detectors, pixel and strip trackers can utilize the fact that usually the charge from a particle passage is deposited below more than one implant to improve their intrinsic resolution.

The following sections provide a brief introduction to the field of pattern recognition. Section 3.3.1 addresses the clustering process for local hit reconstruction while Section 3.3.2 introduces the tracking algorithms relevant for this thesis.

3.3.1 Clustering

In most cases, charge is deposited below several adjacent pixel implants and thus shared among their readout cells, either by diffusion, by Lorentz drift, or because the incident particles traverses the sensor at an angle. Clustering describes the procedure of grouping all these pixels above threshold.

From this collection of pixel hits a first estimator on the actual particle impact point can be interpolated. Especially with individual charge information available, weighted position calculations can be performed which improve the spatial resolution of a given detector significantly. Several algorithms serving this purpose are available and summarized in [114]. A few of them will be briefly presented in the following.

The η **algorithm** [115] can be applied if charge is shared predominantly between two pixels. The point of incidence in one dimension is calculated as

$$x_\eta = p \cdot f(\eta) + x_{\text{left}}, \tag{3.12}$$

where p denotes the pixel pitch and x_{left} is the position of the first of the two pixels. $f(\eta)$ is a monotonically growing function with the characteristics $f(0) = 0$ and $f(1) = 1$. The variable η is defined as the ratio between one pixel charge and the sum of both charges:

$$\eta = \frac{Q_{\text{left}}}{Q_{\text{left}} + Q_{\text{right}}}. \tag{3.13}$$

Owing to the diffusion process and the angular dependence of the charge cloud width, the η distribution is not flat, and $f(\eta)$ is given by the integral of the η distribution normalized to the total number of events considered.

The **center of gravity (CoG) algorithm** is probably one of the most commonly used algorithms for clustering. It is based on the first raw moment of the cluster charge distribution, and the cluster center is given by

$$x_{\text{cog}} = \frac{\sum_i Q_i x_i}{\sum_i Q_i}, \tag{3.14}$$

where Q_i denotes the individual charge collected on pixel i and x_i is the pixel coordinate. This algorithm is, in contrast to the η algorithm, not restricted to two pixels and can thus be applied for all track incidence angles.

For very long clusters it can be beneficial to apply the **Head-Tail algorithm** [116] which considers the fact that the energy loss in silicon is roughly proportional to the particle path length. Thus, the central pixels of the cluster do not contribute much information since the track is already defined by the entry and exit points. The cluster position is thus calculated as

$$x_{\mathrm{ht}} = \frac{x_{\mathrm{head}} - x_{\mathrm{tail}}}{2} + \frac{Q_{\mathrm{tail}} - Q_{\mathrm{head}}}{2Q_{\mathrm{avg.}}} p. \tag{3.15}$$

The first term in this equation is the simplest possible approach, neglecting all charge information available and just interpolating the position of the first and last pixel. However, when available, the charge sharing information can be taken into account by weighting the position with the relative charges of the head and tail pixels as shown in the second term of Equation 3.15. Here, $Q_{\mathrm{avg.}}$ is the average pixel charge of the cluster, and p denotes the pitch. The CMS standard interpolation method [117, 118] is derived from the Head-Tail algorithm and uses additional information of the track angle to estimate its impact point.

More advanced algorithms such as the **Template Matching** [81, 119, 120] employed by the CMS experiment involve the detailed simulation of detector responses as a function of the particle incidence angle and other parameters such as radiation damage. In template-based reconstruction algorithms, the full distribution of the observed cluster charge is compared to the expected distributions derived from the device simulation for different hit positions. As the detector ages under radiation damage, the drift and thus the charge collection behavior changes. New template sets accounting for these changes allow to mitigate the effect on the spatial resolution of the detector.

A new algorithm based on the third central moment of the cluster charge distribution is proposed in Chapter 9.

The determined cluster centers have to be transformed from the local on-sensor coordinates to a global frame of reference in order to allow the track reconstruction of the traversing particle. Usually these three-dimensional space points are referred to as hits.

3.3.2 Trajectory Reconstruction

From the hit positions in the global frame of reference, the particle trajectory can be reconstructed. For optimal parametrization, a suitable track model has to be selected. For test beam measurements with a collinear beam and no magnetic field, a simple straight line often suffices. Depending on the beam properties and the experimental setup it might be necessary to consider multiple scattering of the beam particles.

In the final deployment situation in collider experiments a magnetic field is vital for the momentum determination. In the homogeneous magnetic field the particle trajectory can be described as a helix with curvature $\kappa = 1/r$. The radius r is determined by the transverse momentum p_T of the particle and the strength of the magnetic field.

A plethora of different tracking algorithms have been developed over the years, some with special attention to scalability and speed, others with optimal track resolution as a maxim. An overview of several methods is given in [101]. In the following, only the methods relevant to this thesis are briefly discussed.

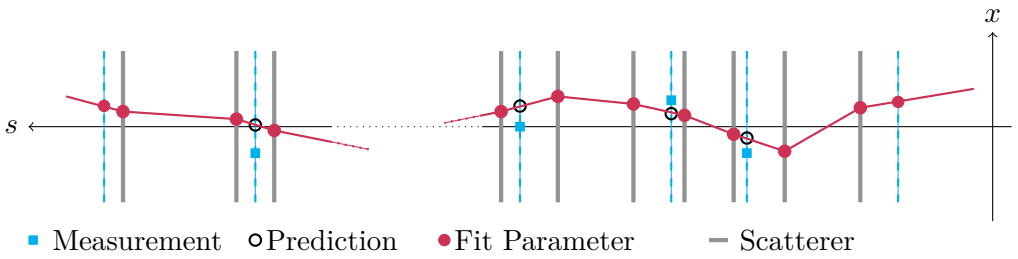

Figure 3.5: Sketch of a GBL track re-fit. The material between the different measurements is represented as thin scatterers. The initial and final measurements are added as fit parameters. The track residuals can be calculated from the distance between the predicted and the measured hit positions.

The **triplet method** is a relatively simple possibility of obtaining track residuals. With three measurements available, either a straight line or another parametrization is fitted to two of the hits. Depending on the number of degrees of freedom, additional constraints such as the curvature might be necessary to allow for fitting. The resulting track is interpolated or extrapolated to the position of the third measurement. The distance between the track extrapolation and the measured hit position is called the **residual** and is given by

$$\Delta x = x_{\text{track}} - x_{\text{meas.}}, \tag{3.16}$$

and can be used as discriminator for track candidates. Tracks with a residual below a threshold $\Delta x < \Delta_{\text{thr.}}$ are accepted as viable track candidates, others are rejected as random hit combination.

A more sophisticated approach to track fitting is provided by the **General Broken Lines (GBL) algorithm** [121, 122]. Since particles experience Coulomb scattering when traversing material, random changes in direction are induced. The mean deflection of this process is zero, the variance depends on the particle momentum as well as on the material involved [15].

The broken lines model allows to include scattering material in the re-fit of an already selected particle track and is able to calculate the full covariance matrix for all track parameters. For this purpose, the scattering material between two measurements is represented as thin scatterers with zero thickness as shown in Figure 3.5. The scatterers between measurement i and $i+1$ should be placed at positions along the arc-length s given by

$$s_{\text{scat}} = s_i + \frac{s_{i+1} - s_i}{\sqrt{12}} \qquad \text{and} \qquad s_{\text{scat}} = s_{i+1} - \frac{s_{i+1} - s_i}{\sqrt{12}}. \tag{3.17}$$

The trajectory is built from an initial seed, the measurements, and the thin scatterers enclosing the measurement. The fit parameters are determined using a χ^2 minimization of these contributions. After the fit has been performed, the track parameter uncertainties at any position along the trajectory can be retrieved from the covariance matrix.

GBL is mathematically equivalent to the reference Kalman filter algorithm [82] which steps through the measurements sequentially by adding scatterer and measurements one-by-one while updating the prediction and fit uncertainties. The advantage of GBL is the global covariance matrix provided for each track, while the Kalman filter only calculates the covariance matrices at single points. This is usually not sufficient for global alignment methods. However, extensions to the Kalman filter algorithm providing this feature exist [123].

3.4 Detector Alignment

Since the position resolution of modern silicon tracking detectors easily outperforms the tolerances and mechanical precision of the detector itself, the data recorded have to be corrected for these misalignments.

As for tracking, a variety of alignment algorithms exist, based on simple track residual minimization, more advanced histogramming techniques, and matrix methods [124]. All these track-based alignment methods have in common that recorded data of the detector under investigation are used, and that the overall deviation of the track fit and the measurements is minimized.

The method used both in the CMS experiment and in the test beam analysis presented in this thesis use the Millepede-II (MP-II) algorithm [124, 125] which implements a global minimization approach. It is capable of fitting $\mathcal{O}(10^6)$ parameters and millions of tracks simultaneously and is thus perfectly suited for complex detectors such as the CMS silicon tracker.

Alignment involves the minimization of the χ^2 equation including all tracks and measurements available for all possible alignment parameters simultaneously, given by

$$\chi^2(\vec{p},\vec{q}) = \sum_{\text{tracks}} \sum_{\text{hits}} \vec{r}_{ij}^{\,T}(\vec{p},\vec{q_j})\, V_{ij}^{-1} \vec{r}_{ij}(\vec{p},\vec{q_j}), \tag{3.18}$$

with the alignment parameters $\vec{p}$ and track parameter $\vec{q}$. The term $\vec{r_{ij}}$ represents the track residual for a given hit i on track j, and V_{ij} is the covariance matrix of each measurement. The required inversion of the matrix V is a very slow and memory-consuming operation. MP-II uses the Minres algorithm [126] which performs an iterative inversion and only requires the non-zero matrix elements as input. This allows to speed up the computation and to decrease the memory required by large factors. MP-II automatically detects data with bordered band matrices as provided by some algorithms such as GBL to further speed up the processing.

So-called weak modes pose a problem for alignment. Weak modes are deviations in the alignment parameters on which the algorithm is not sensitive. An example for weak modes in the very simple geometry of parallel planes of pixel detectors with straight particle tracks would be a constant shift of all planes to one direction. The residual width would not change since the relative alignment of the planes for the data available is unchanged. Additional constraints such as fixing certain parameters or additional data have to be introduced in order to eliminate weak modes.

In the CMS experiment, one of the weak modes for alignment is a twist of the tracker barrel detector, since all tracks produced in particle collisions originate from the interaction point and are insensitive to this deformation [127]. In this case, additional data from cosmic rays can be used to constrain this weak mode because of their different origin and signature. For simpler detectors such as beam telescopes (cf. Section 7.2) it is usually enough to either fix two planes or require the mean shift of all planes to be zero.

3.5 Intrinsic Resolution

The spatial resolution of tracking detectors is one of their main figures of merit. The resolution of a detector is defined as the width of the unbiased residual distribution. A residual is called unbiased if the measurement which shall be compared with the track prediction according to Equation 3.16 does not enter the track fitting procedure and thus does not bias the measurement.

One has to distinguish between the measured resolution read from the obtained residual width, and the intrinsic resolution as the actual detector property. Since the residual width does not

only depend on the intrinsic resolution of the device under test (DUT) but also on the quality of the tracks, the resolution is given by

$$\sigma^2_{\text{meas}} = \sigma^2_{\text{int}} + \sigma^2_{\text{track}}, \tag{3.19}$$

where σ_{meas} is the measured residual width and σ_{int} the intrinsic resolution of the DUT. The term σ_{track} denotes the pointing resolution of the tracks used to calculate the residual distribution. The pointing resolution includes the resolutions of the other measurements used for the track fit as well as additional contributions stemming from multiple Coulomb scattering of the traversing particles. In order to obtain the intrinsic resolution of the DUT, the track resolution has to be known precisely and subtracted quadratically from the measured residual.

In the simplest case of a detector with binary readout and no charge sharing information available, the position resolution is given by the variance of the uniform distribution of hits over a pixel, namely

$$\sigma_{\text{int}} = p/\sqrt{12}, \tag{3.20}$$

where p denotes the pixel pitch. As soon as the charge is shared between two or more pixels, the interpolation algorithms described in Section 3.3.1 allow to improve the achieved position resolution.

Determination of the Distribution Width

Measuring the width of a distribution is a non-trivial task since not every residual follows the shape of a Gaussian distribution. Delta rays (cf. Section 3.1.5) add non-Gaussian tails, and also clustering algorithms can distort the shape of the residual distribution significantly. Because of these non-Gaussian contributions, the root mean square (RMS) of the distribution usually overestimates the actual width. Other approaches provide results which are more stable against large fluctuations. Accordingly, the value of a detector resolution is only meaningful with the extraction method given.

The simplest choice is either quoting the full width at half maximum of a Gaussian fit to the distribution or the RMS of the full distribution. The non-Gaussian tails usually can be suppressed efficiently in the analysis owing to their origin from delta rays and the resulting correlation with large absolute signals. To further reduce the sensitivity on these tails, the quoted RMS can be calculated on, e.g., 96% of the sample, excluding large residual values. This is usually referred to as the Gaussian core of the distribution.

Alternative fit functions might be more suitable for certain applications and provide more flexibility concerning the shape of the distribution. The functions used in the quantification of position resolutions in this thesis are given here. The **generalized error function** is defined as

$$f(x) = a + \frac{b}{\sqrt{8}\sigma}\frac{\beta}{\Gamma(1/\beta)}\exp\left(-\left|\frac{x-\langle x\rangle}{\sqrt{2}\sigma}\right|^{\beta}\right), \tag{3.21}$$

where the background a, area b, width σ, mean $\langle x\rangle$, and β are free parameters of the fit, while $\Gamma(x)$ denotes the gamma function. For a value of $\beta = 2$ the standard Gauss distribution is obtained. The **Student's t function** is given by

$$f(x) = a + \frac{b}{\sigma\sqrt{\pi\nu}}\frac{\Gamma((\nu+1)/2)}{\Gamma(\nu/2)}\exp\left(-\frac{\nu+1}{2}\ln\left(1+\frac{1}{\nu}\left[\frac{x-\langle x\rangle}{\sigma}\right]^2\right)\right), \tag{3.22}$$

with the free fit parameters a, b, $\langle x\rangle$, σ, and ν. The Student's t function interpolates between a Gaussian distribution and a Breit-Wigner curve and thus accounts for non-Gaussian tails.

In both cases the parameter σ describes the width of the function and is taken as the spatial resolution extracted from the respective distributions.

4. The CMS Pixel Detector for Phase I

Over the years of operation, the CMS Pixel Detector has proven to be an indispensable part of the experiment. Essentially all physics analyses rely on its excellent performance [128, 129]. It provides high resolution measurements of the first three space-points for charged particles emerging from the interaction region up to pseudorapidities of $|\eta| < 2.5$ [130]. The single hit efficiency is well above 99 %, and dynamic data losses caused by buffer overflows are below 4 % in the innermost layer of the detector at luminosities of $\mathcal{L} = 1 \times 10^{34}\,\mathrm{cm}^{-2}\mathrm{s}^{-1}$ [131].

However, the LHC schedule is subject to changes, and some of the original LHC design parameters have already been surpassed. Due to its close location to the IP, the pixel detector is one of the components most strongly affected by operational changes. The performance of the present pixel detector would degrade significantly at increased instantaneous luminosities and higher pile-up. With the luminosity growing by a factor of two, the dynamic inefficiency of the ROCs in the innermost detector layer would increase to about 16 % at 25 ns bunch crossing operation [131]. These inefficiencies arise from increased dead time during the double column drain and limitations in the data buffers which cache the pixel hits during the L1 trigger latency. The tracking efficiency would decrease significantly and the mis-identification rate would see a steep rise because of the more difficult pattern recognition.

In order to keep up with the demands imposed by the LHC operation, the CMS Collaboration has refined the detector concept of the pixel tracker. New requirements and constraints have been set up, and major parts of the detector have been revised and redesigned. A completely new detector is presently being built which is designed to withstand even higher particle fluxes, is able to manage events with higher pile-up, and is capable of delivering data at higher L1 trigger rates [132].

The barrel detector will be equipped with four sensor layers and closes the present gap between the pixel and strip trackers. This improves the tracking efficiency both by limiting the extrapolation distance to the first strip tracker measurement and by providing 3-of-4-hits triplets for track seeding instead of relying on three measurements only. The innermost layer is situated closer to the IP yielding an improved secondary vertex resolution and better separation power of vertices for high pile-up events. The four measurements per track concept is extended up to $|\eta| < 2.5$ by the forward pixel detector, which is composed of three disks on each side.

The individual components of the new pixel detector are detailed in the following sections. The design of the active sensor has been retained unchanged from the current detector and is

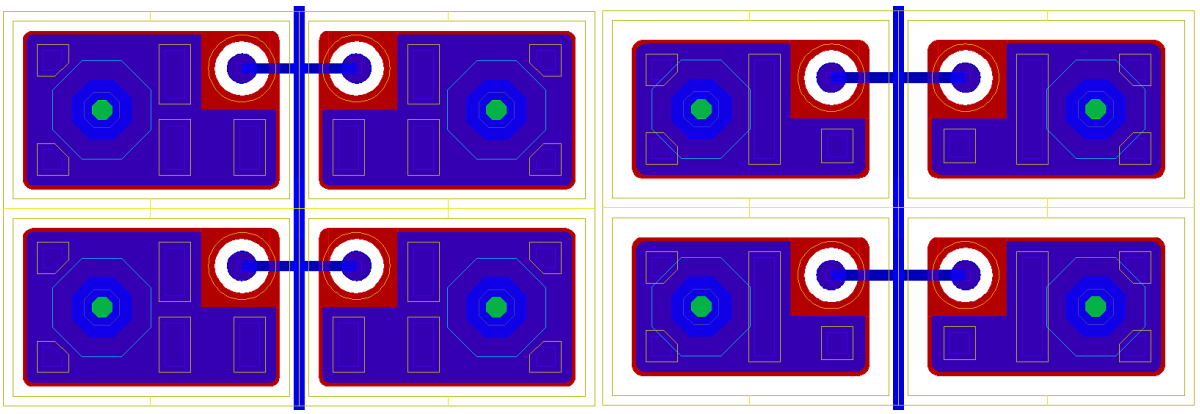

Figure 4.1: Pixel implant layout for CMS barrel pixel sensors. The *dot1* design is used in the module production of the Phase I pixel detector (left), while the alternative *gap30* design has been used in test beam measurements (right). The pixels are separated by *p*-spray isolation with a width of 20 µm and 30 µm, respectively. The punch-through grid runs vertically and connects the bias dots in the pixel cells [133].

presented in Section 4.1. The new front-end chip described in Section 4.2 is an advancement of the existing ROC, which implements many improvements and removes limitations. Section 4.3 introduces the detector module assemblies as well as the Token Bit Manager (TBM) chip, while Section 4.4 details the geometry of the detector. Finally, Section 4.5 provides an overview of additional modifications and improvements in the infrastructure.

4.1 Sensor Design

The silicon sensors of the Phase I pixel detector implement an n^+-in-n design consisting of n-doped silicon substrate with a nominal thickness of 285 µm and highly doped n^+ pixel implants for the electrode segmentation. The backside is uniformly p-doped to form the backplane electrode. The n^+-in-n design allows the collection of electrons. The higher mobility of electrons compared to holes is advantageous since it leads to shorter collection times, and to a larger Lorentz drift and thus better charge sharing as described in Section 3.1.5. After radiation damage, the n-doped bulk material will undergo type inversion [134] and thus the sensor will be depleted from the implants. This guarantees a long lifetime of the detector and facilitates operation even in underdepleted mode. Also here, the high mobility is beneficial since it makes the electrons less susceptible for trapping and thus leads to a higher signal charge.

The isolation of the pixel implants is ensured by additional moderated p-spray or p-stop structures surrounding the pixel cells. Different designs of the isolation structures are available and shown in Figure 4.1, differing in the width of the p-implants. The *gap30* design features a 30 µm wide p-spray isolation, while the *dot1* design used in the actual detector separates the n-implants by 20 µm from each other. The punch-through biasing grid visible in Figure 4.1 allows biasing of the sensor without attached ROC by providing the ground potential, and prevents single pixels from floating to bias potential in case of missing bump bonds.

The pitch of the pixel implants of 100 µm × 150 µm is optimized for spatial resolution in the 3.8 T magnetic field of the CMS solenoid. In $r\phi$-direction of the barrel detector, charge is spread by the Lorentz force exerted on the drifting charge carriers. With a Lorentz angle of about 25° and the nominal sensor thickness, the optimal charge sharing over two pixel cells is achieved with

a pitch of 100 µm [135]. The pitch in the other dimension is mostly stipulated by technological constraints on the size of the pixel cells in the front-end electronics. However, the tilt angle of the forward pixel detector blades is adapted to optimally share charge over two pixels in both dimensions with pitches of 100 µm and 150 µm.

Owing to the structure of the detector modules and the size of the front-end chips, some pixels on the sensor need to be larger in pitch to allow placement of the ROCs without insensitive regions in between. These edge pixels have a pitch of 100 µm × 300 µm, the few pixels located at the corners of a ROC even have a fourfold size of 200 µm × 300 µm compared to a normal pixel implant.

Two different sizes of the sensor are available. For the actual pixel detector only full-size sensors with dimensions of 65 mm × 16 mm are used, which hold 16 ROCs as described in Section 4.3. For qualification measurements, test beams, and irradiation studies, smaller sensors are available with a size of about 8 mm × 8 mm. These sensors and a single ROC are used to build so-called single chip modules (SCMs).

The connection between the sensor and the front-end electronics is established via bump bonds. Throughout the collaboration, different bonding technologies are available and in use. The production line for detector modules and SCMs at DESY employs a single solder ball deposition technique using tin-silver alloy spheres.

4.2 The Readout Chip

The ROC is the front-end electronics of the CMS Pixel Detector. It measures, amplifies, and discriminates the charge collected on every individual sensor implant, stores the information, and eventually transmits it to the TBM.

The ROCs are fabricated in a 250 nm radiation hard CMOS process. Additional measures for radiation hardness such as single event upset (SEU) protected storage cells have been implemented in the chip design [136]. In addition, the performance of each ROC in the experiment will be continuously monitored and the ROCs can be re-programmed in case of an SEU. The radiation tolerance of the chip design has been extensively tested using irradiations at various accelerators [137, 138]. The irradiated samples have been characterized both in lab measurements and comprehensive test beam campaigns at DESY and elsewhere.

A detailed comparison between the PSI46V2 ROC of the present CMS Pixel Detector and the new PSI46digV2.1-r can be found e.g. in [139–141]. This section focuses on the features of the PSI46digV2.1-r version of the chip which is used for the Phase I Pixel Detector.

The chip is supplied with the LHC clock running at 40 MHz, which enables beam-synchronous data acquisition. Two independent power supplies for the analog and digital parts of the circuitry minimize the influence of digital signal processing on the analog performance. A set of digital-to-analog converters (DACs) are used for the configuration of the chip, the communication is implemented as custom-designed 40 MHz Inter-Integrated Circuit (I^2C) interface. The DAC names used hereafter are internal designations and do not necessarily translate to an intelligible description.

The ROC has a total size of 7.9 mm × 10.2 mm and can be divided into three main regions. The active area accommodates 4160 pixels which are organized in 26 double columns (DCols) of 80 × 2 pixels each. Every pixel is represented by one pixel unit cell (PUC) which houses all necessary components for amplification and discrimination of the signals. The pitch of these single PUCs matches the implant pitch on the sensor to facilitate the bump bonding process.

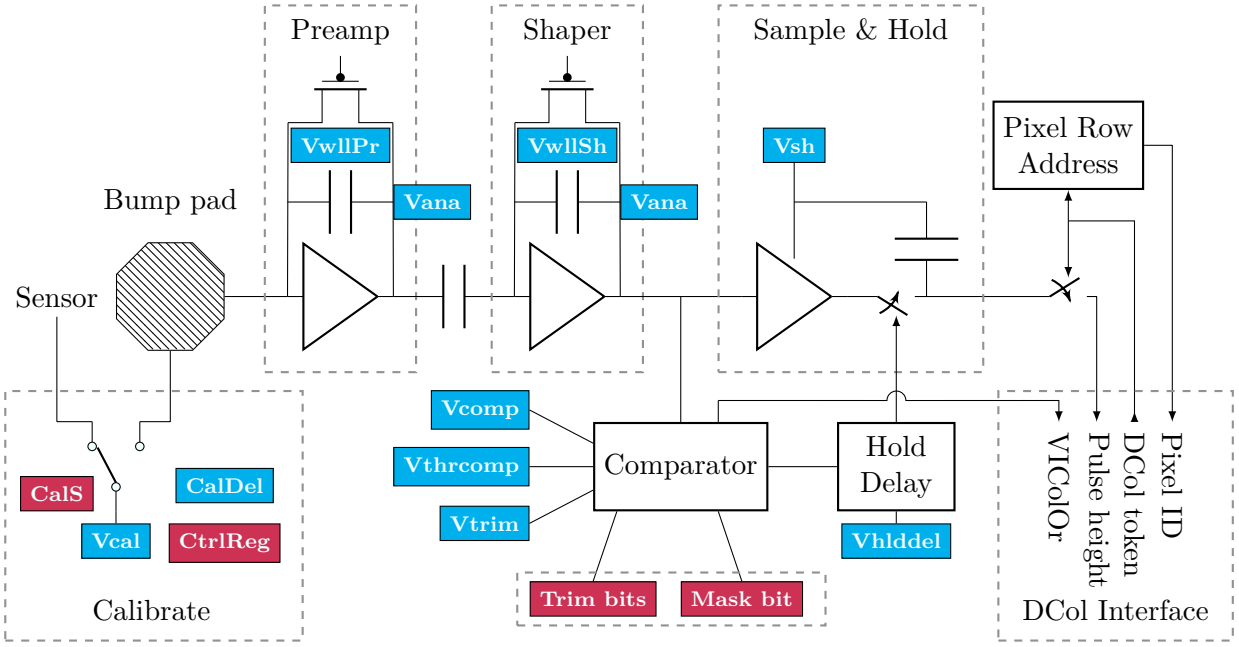

Figure 4.2: Block diagram of the PUC. Shown are the preamplifier and shaper blocks, the comparator, the sample and hold circuit, and the circuit for the injection of internal calibration pulses. The double column interface (DCI) connects the PUC with the DCol periphery. The colored boxes indicate DAC settings (blue) and registers (red) for the respective circuits.

The DCol peripheries house the main memory of the chip. All pixel hit information is temporarily buffered here until a L1 trigger decision has been taken. Finally, the ROC controller and interface (RCI) comprises the ADC, the data transmission logic, and the infrastructure for the chip control. The following sections will describe the ROC components in more detail.

4.2.1 The Pixel Unit Cell

The PUC contains all components for signal reception and processing. This includes a preamplifier and shaper circuit, the charge discriminator (comparator), as well as the sample and hold circuit for buffering of the pulse height after discrimination. Figure 4.2 shows a simplified block diagram featuring the most important components and DACs. All PUCs are connected to the periphery via the double column interface (DCI).

The bump bond pad is located far from the DCI in order to reduce cross-talk from the transmission lines on the analog primary signal as shown in Figure 4.3. The analog and digital supply voltage lines have been carefully routed in order to minimize cross-talk on the analog power line controlled by the VANA DAC. Since VANA serves the sensitive preamplifier and shaper, this allows to effectively reduce the induced noise in the signal.

The key parameter of the PUC is the analog performance, i.e., the lowest achievable charge threshold, the noise, and the time walk behavior. The lower the effective threshold can be configured, the longer is the lifetime of the entire detector. The reason for this is the reduced CCE after irradiation, when charges are trapped, the sensor is operated underdepleted, and not the entire charge can be collected (cf. Section 3.1.5).

The discriminator threshold is configurable on a per-pixel level. The global VTHRCOMP DAC

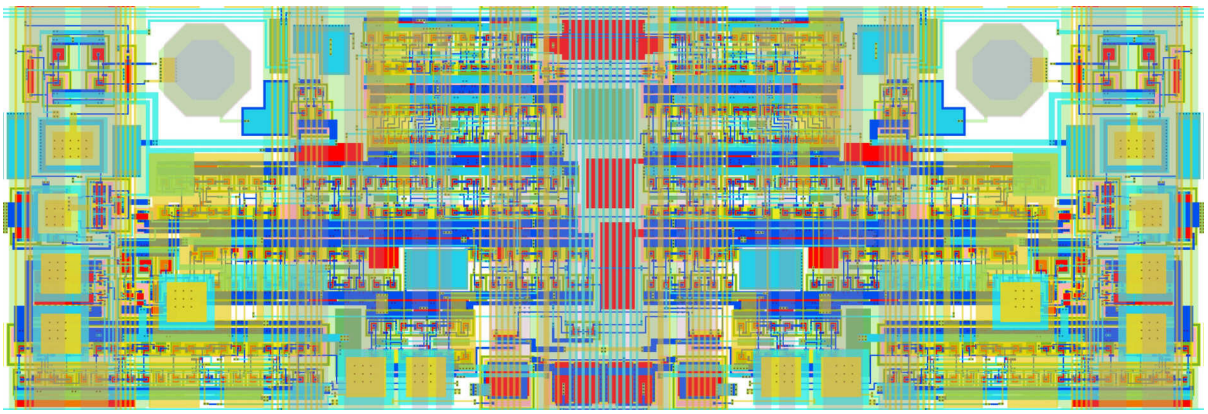

Figure 4.3: Layout of two axially symmetric PSI46digV2.1-r PUCs with the double column interface (DCI) in the center. The bump bond pads are located away from the double column interface (DCI) while maintaining sufficient clearance to the neighboring pads in the next DCol [142].

sets the global baseline for all pixel thresholds, while the threshold of the individual PUCs are then adjusted via the VTrim and trim bit settings which allow to decrease the charge threshold starting from the baseline value. An additional mask bit allows to switch off single PUCs for which no viable threshold can be found. The charge discriminator has been designed with special attention to its time walk behavior to minimize the difference between absolute and (effective) in-time threshold (cf. Section 3.2). With the PSI46digV2.1-r ROC an absolute threshold of less than 1.8 ke can be achieved, while no increase of the in-time threshold due to time walk is observed.

For calibration purposes, an internally generated pulse can be injected into the PUC circuit. The charge of this pulse can be adjusted using the VCal DAC. Alternatively, the calibration pulse can also be induced in the sensor via the air capacitor represented by the gap between the sensor and the dedicated calibration pad in the PUC. This feature is enabled by the Cals register, and can be used to test the bump bond connectivity.

The PUC is self-triggering. As soon as a charge above the configured threshold is registered, the DCol periphery is notified via the VIColOr signal, and the pulse is buffered in the sample and hold circuit until the arrival of a DCol token. The token initializes the transmission of both the pixel address and the pulse height as indicated in Figure 4.2. The transmission of one pixel hit requires two cycles of the 40 MHz clock.

4.2.2 The Double Column Periphery

The DCol periphery houses the lion's share of the buffer cells on the entire ROC. Every pixel hit from all bunch crossings has to be stored for the total period of the L1 trigger latency. Every DCol provides 80 data buffer cells and 32 time stamp buffer cells.

The DCol periphery is responsible for the readout coordination of the PUCs. The so-called column drain is initialized by the VIColOr signal from one or multiple PUCs arriving via the DCI. Upon arrival of the VIColOr signal, a timestamp with the current bunch crossing (BC) is stored in one of the timestamp buffer cells. The DCol periphery issues a token which propagates up in the left pixel column, and returns in the right column. Every PUC with a signal above threshold transfers its data to the DCol buffers, and then retransmits the token to the next PUC in line. The pixel hits are stored in the data buffers, and are assigned to the recorded timestamp.

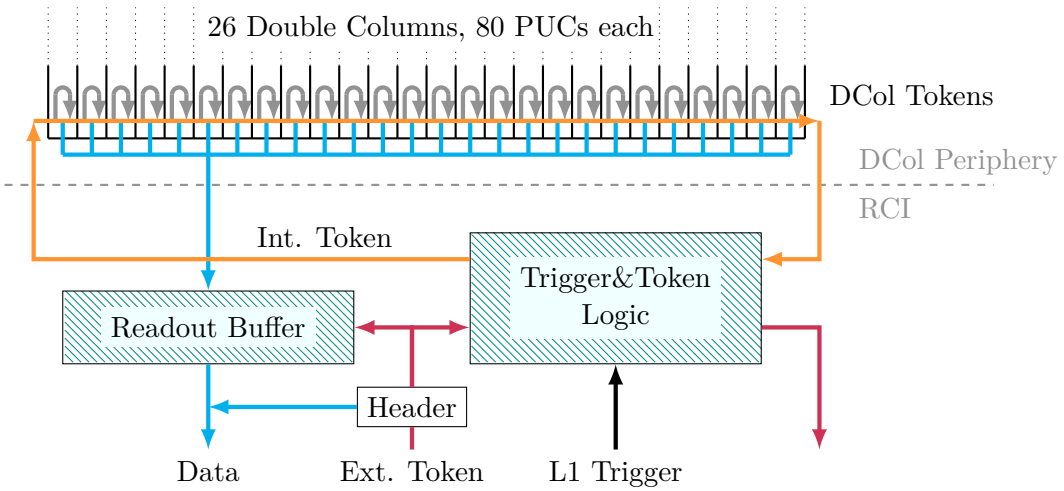

Figure 4.4: Mechanism of the internal and external ROC tokens. Pixels receiving a charge above threshold initiate the DCol readout token to store the pixel hits in the DCol periphery. The arriving L1 trigger releases the internal token which collects the data from the DCol buffers, and transmits them to the global readout buffer. Upon arrival of the external readout token, the ROC header is transmitted, followed by the pixel data.

Once a L1 trigger decision has been taken and distributed to the DCols, the pixel hits linked to the corresponding timestamp are validated. At this point the DCol goes into dead time and does not accept new pixel hits from the PUCs in order not to overwrite or flush the validated pixel hits from the buffers. The DCol readout is initialized by the ROC internal readout token generated by the RCI. All pixel hits with the requested timestamp are then transmitted to the RCI for further processing. After transmitting all validated hits, the DCol is active again and can receive new pixel hits.

Pixel hits that have not been validated within the configured trigger latency are discarded and the buffer cells are cleared. Chip-internally, this buffer latency is configured via the so-called WBC register. A flowchart summarizing the different token mechanisms is given in Figure 4.4.

4.2.3 The ROC Controller and Interface

The RCI is responsible for the coordination of the readout and the data transmission. It contains a global first-in first-out (FIFO) readout buffer, ADCs, the phase-locked loop (PLL), and the data serializer.

When the L1 trigger signal is received by the RCI, both a trigger signal and the internal readout token are issued to the DCols and the pixel hits are subsequently read out and stored in the global FIFO. This procedure allows to greatly reduce the dead time of the detector to below 1% [141] since the DCols are not blocked until the external readout token arrives, but only for the duration of the internal token pass as depicted in Figure 4.4. This is of special importance since the external readout token is passed through several ROCs on a module in series, and is only passed on from one ROC to the next once the data transmission is finished.

The ADC is responsible for the digitization of the pulse heights recorded by the PUCs. It is implemented as 8 bit successive approximation current ADC and is located between the DCol buffers and the global readout FIFO. Incoming pulse heights are sampled when read out from

the DCols with the internal token and stored digitally in the readout FIFO. The sampling range is programmable via the DACs PHScale, PHOffset and VCompADC.

The PLL generates an 80 MHz clock for the ADC and a 160 MHz signal for the data transmission from the 40 MHz input clock. The data transmission of the ROC header and pixel hits from the global FIFO is started as soon as the external readout token reaches the RCI. The digital 160 MHz data link provides enough bandwidth to efficiently read out all pixel hits at the occupancies expected for the LHC Phase I. The format of the transmitted data is detailed in the next section.

The RCI contains a so-called power-up reset circuit which initializes the ROC to a low power state after start-up. This ensures that no high power consumption can be provoked by malfunctioning ROCs in the detector. Furthermore, a readback mechanism allows introspection of chip parameters such as regulated voltages, temperature, or DAC settings. The value to be read can be selected via the Readback register and is transmitted in the D bits of the ROC header over a period of 16 events as described in the subsequent section. Analog values are converted using a second, slow ADC in the RCI periphery.

4.2.4 Header and Pixel Data Format

Data from the ROC are transmitted as 160 MHz digital signals. After receiving the readout token, the ROC first sends its own 12 bit header identifier which consists of the hexadecimal pattern `0x7f8`. The last two header bits contain additional information. The S bit is a start marker for the data transmitted in the D bit. The S bit marks the start of a 16-bit word, which is transmitted bit by bit using the D bit in the following 16 readouts.

One pixel hit consists of 24 bits. The first 6 bits contain the address of the DCol (C), the following 9 bits the pixel id within this DCol (R). The 8-bit pulse height information (P) is separated by an additional `0` bit in the center in order to preclude the emergence of another ROC header identifier:

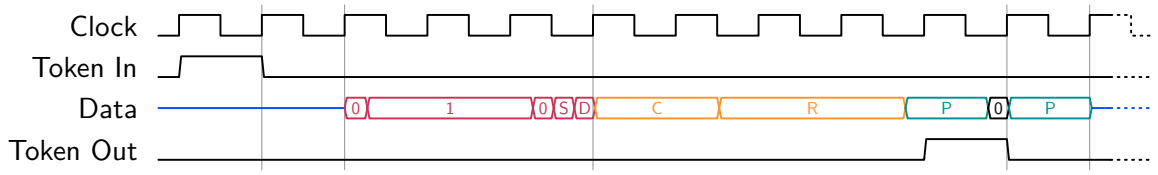

The pixel addresses are encoded using Gray code [143], a binary encoding which enforces single bit flips between two consecutive numbers.

The chip for Layer 1 of the Phase I detector uses a different mechanism for the column drain and only calculates the individual pixel addresses in the ROC periphery. The pixel address is thus simply the linearly encoded column and row number, spaced with fill bits to avoid header patterns:

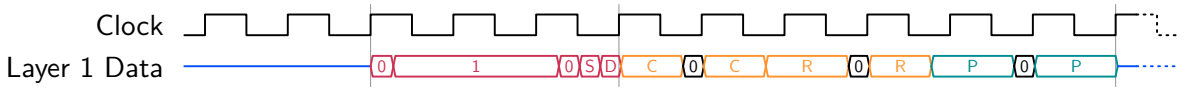

The overall length of one pixel hit as well as the encoding of the ADC response remain the same.

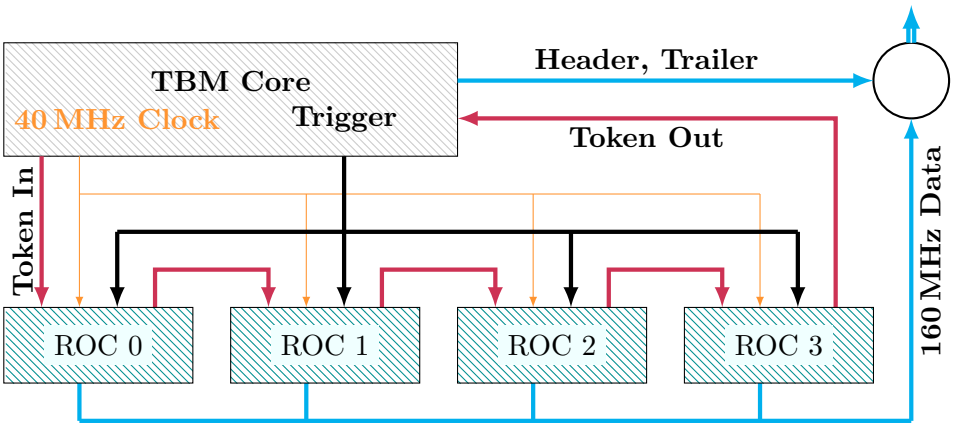

Figure 4.5: Schematic of the TBM readout chain with one TBM core and several ROCs. The clock and L1 trigger signal are distributed synchronously to all ROCs while the readout token is passed from one ROC to the next until it returns to the TBM core. The core adds header information to the data stream, and appends its trailer after receiving the readout token back.

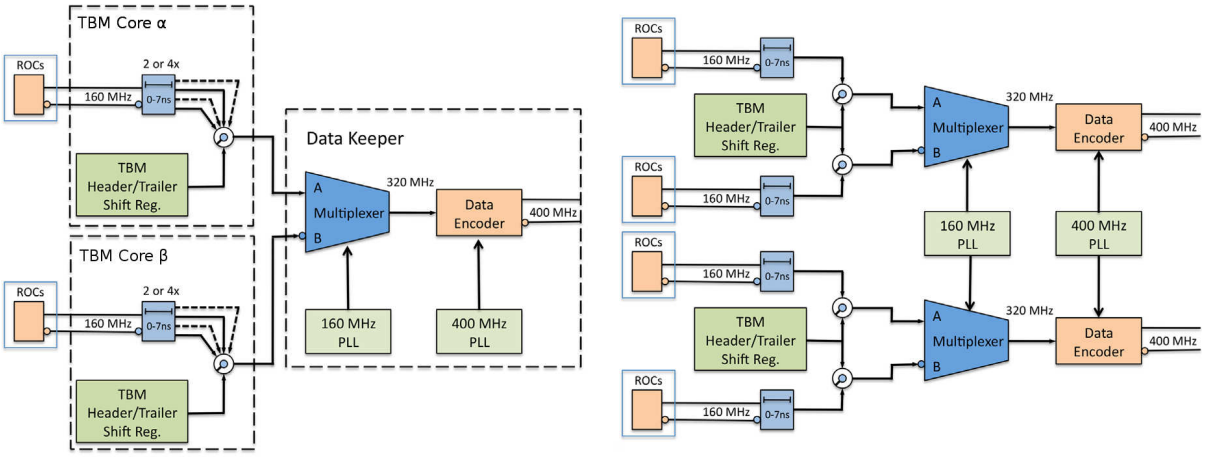

Figure 4.6: Schematics of the TBM08c (left) with two cores and one Data Keeper and 400 MHz data links, and the TBM09c (right) with two Data Keepers and data links. Modified from [141].

4.3 Detector Modules and the Token Bit Manager

The smallest independent unit of the pixel detector is a module. It comprises one sensor, the high density interconnect (HDI), 16 ROCs and one or two TBM chips. The HDI is an ultra-thin flex print containing the signal line routing; power, clock, and trigger distribution to the ROCs; and some additional components such as filtering capacitors. It is glued onto the backplane of the sensor and connects to the ROCs via wire bonds.

The principal task of the TBM is the handling of the trigger and token distribution and the readout coordination. It distributes the clock signal as well as the L1 trigger and controls the ROC readout by generating the readout tokens. A TBM consists of two TBM cores, Data Keepers, as well as the Communication and Control hub which distributes the I^2C commands to the correct ROC.

After receiving a trigger signal, the external readout token is passed to the ROCs and the TBM header and trailer are added to the data stream as sketched in Figure 4.5. If another trigger arrives before the token is received back and the readout has finished, it is placed on an internal stack with 32 slots. Once 16 slots are filled and not cleared, prospective triggers are stored on the stack but no token is sent to the ROCs. In order to keep the DAQ synchronized, the TBM only returns header and trailer, marked with the `NoTokenPass` flag for these triggers.

Additional features can be controlled via a set of register banks. These include various counters, automatic detection and reset in case of high-occupancy beam-gas events, as well as programmable delays for all data streams and signals. The 160 MHz data streams from the ROCs are multiplexed to form one 320 MHz signal. Using the non-return-to-zero invert technique and 4-to-5 bit encoding the signal is converted to 400 MHz before sending it as differential signal to the optical receivers on the supply tube outside the tracking volume [144]. The encoding maps the binary data to the signal by assigning a transition to every `1` bit to be transmitted, and no transition to all `0` bits. This ensures the integrity of data during transmission.

Several versions of the TBM exist, differing in the number of data channels and the number of ROCs read out in parallel. The TBM08c [145] has two token chains of 8 ROCs each which are merged and send on one data stream as shown in Figure 4.6 (left). This TBM is used for the layers 3 and 4 of the pixel detector. The TBM09c [146] shown in Figure 4.6 (right) supports four token chains with up to four ROCs each, read in parallel and merged into two 400 MHz data streams. Modules for layer 2 are equipped with one TBM09c while layer 1 modules with the highest expected pixel occupancy feature two TBM09c chips and thus four data streams in order to provide the required bandwidth.

4.3.1 TBM Header and Trailer

The TBM header and trailer both start with a unique pattern consisting of 9 (10) consecutive `1` bits for the header (trailer). The header contains the 8 bit event counter providing the current trigger number, as well as additional data. The type of data is identified via two *ID* bits followed by 6 bit of content. Since most of the error conditions are only known after the event has been read out from the ROCs, the TBM trailer mostly contains error flags. In addition, the current filling level of the trigger stack is provided:

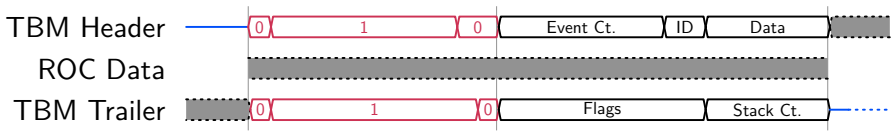

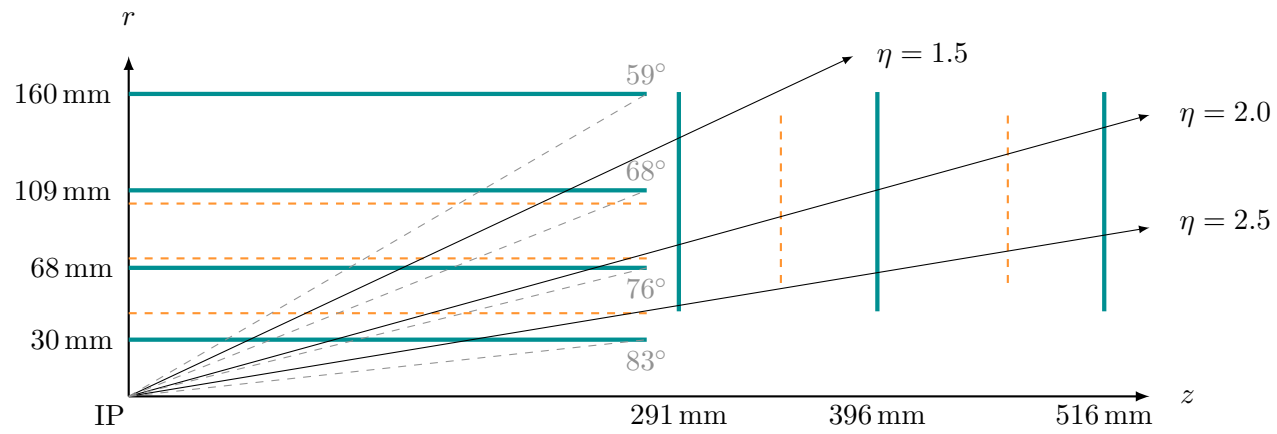

Figure 4.7: Geometry of the Phase I barrel and forward pixel detectors. Shown is one quadrant of the detector, the layer radii and disk positions are given relative to the IP. The orange dashed lines indicate the layer positions of the present pixel detector, the gray dashed lines mark the maximal track dip angle for the four barrel layers.

4.4 Detector Geometry and Material Budget

Close proximity of the first layer to the primary vertex and minimal material of the entire detector are key ingredients for a superior impact parameter resolution. Both parameters will be improved significantly with the new pixel detector. Despite adding additional detection layers and moving the innermost layer closer to the IP, the material budget inside the tracking volume is reduced.

Figure 4.7 presents the geometry of the new pixel detector. The four barrel layers will be mounted at radii of 30 mm, 68 mm, 109 mm, and 160 mm. This is rendered possible by the new beam pipe installed during LS1 with an outer diameter of only 45 mm. The barrel layers are split into two half shells to allow insertion with installed beam pipe. Three disks are placed on each side of the barrel detector at distances of 291 mm, 396 mm, and 516 mm from the IP [131].

In total, the CMS Phase I Pixel Detector comprises around 1200 modules in the barrel detector and around 670 modules in the endcaps. Hence, the total number of readout channels is roughly doubled with respect to the present detector. In order not to increase the material budget by the same factor, several design improvements are implemented. The biggest impact on the material budget arises from the relocation of service electronics and boards further outside on the supply tube of the detector which effectively removes material from the tracking volume.

Also the cooling infrastructure has a large influence on the overall material budget. By using an evaporative two-phase CO_2 cooling, more cooling power can be provided at lower mass of both coolant and piping [147]. Evaporating CO_2 yields a factor 100 higher heat dissipation compared to the currently used one-phase C_6F_{14} liquid cooling [148]. It also allows for lower operating temperatures which is beneficial for both the sensor performance and the detector lifetime.

The support structure of the barrel detector is build from lightweight, 200 µm thick carbon sheets which are glued to the cooling pipes and to the carbon-laminated foam bulk heads on the two ends. The ROCs and TBM chips on the modules are thinned down to further reduce the material budget. The pixel modules have been measured in the DESY test beam to have a radiation length of $0.3\,\%X_0$.

4.5 Power Supply, Readout, and Data Links

The new pixel detector is constrained by the surrounding strip tracker, both in space and in accessibility. This means that the existing patch panels and off-detector services, cooling pipes, cables, and optical fibers have to be reused. Especially the fibers have to suffice to read out almost twice the number of detector channels. Furthermore, the electronics which are mounted on the supply tube are close to the beam line, and have to be SEU safe and radiation hard because of the high dose of ionizing radiation absorbed from glancing collisions. Both constraints impose high requirements on the service electronics.

The change from the 40 MHz analog level encoded signal to the 400 MHz digital readout roughly doubles the bandwidth of each fiber. For the innermost layer of the new detector, several fibers per module have to be used in order to manage the expected data volume. The data collected by the TBMs are transmitted electrically to the pixel optical hybrid (POH) modules on the supply tube which convert and send the signals over the long optical fibers to the front end drivers (FEDs) located outside the experiment.

The same constraints are also present for the existing cables for power supply, which are reused for powering a detector of twice the size. In order to meet this requirement, a higher voltage is supplied on the existing cables, which is stepped down by a custom designed radiation hard DC-DC power converter located directly on the detector supply tube [131, 149]. Both analog and digital supply voltages are generated by the converters and distributed to the pixel modules.

5. Simulation of CMS Pixel Detector Modules

Particle detector simulation is a powerful tool in the process of understanding the detectors, their features, and the underlying processes. Once validated with data, simulations unfold predictive power which can be used to forecast changes in operational parameters of the detector over time, or to improve the performance of algorithms applied to data. The Monte Carlo method described in Section 1.4 is well suited to describe the statistical processes of charge deposition and collection, and is widely used in the simulation of semiconductor detectors [150].

For the work presented in this thesis, the PIXELAV [151, 152] package has been used to simulate the passage of particles through CMS Pixel SCMs. The simulation is later compared to data taken in test beam measurements (cf. Section 8). The software package implements accurate models for charge deposition and transportation, and is capable of simulating charge drift in presence of magnetic fields as well as describing charge trapping induced by radiation damage. The latter is of special importance as it allows to perform studies on the future performance of the CMS Pixel Detector [153].

This chapter gives a brief overview of the concepts used in the simulation which is performed in three consecutive steps. First, the passage of a charged particle through the silicon sensor and the creation of charge carriers is simulated as introduced in Section 5.1. Section 5.2 describes the subsequent transport of the charges towards the readout electrodes by the electric field applied. Finally, the collected charge is passed through a simulation of the front-end electronics and stored for analysis as presented in Section 5.3.

5.1 Charge Deposition

The charge deposition in the sensor is modeled using the elastic pion-electron cross section shown in Figure 5.1a as the PIXELAV package has originally been developed to describe data taken in pion test beams. Due to the very similar ionization of pions and electrons at high energies [107] the description can be used without further modification for data collected at electron beams such as the DESY-II test beam facility (cf. Chapter 7).

In addition to the deposition of charge carriers created by the primary particle, the production of delta electrons is simulated (cf. Section 3.1.5). These scattered electrons produce additional electron-hole pairs and are propagated until they either lost all energy or left the sensor volume.

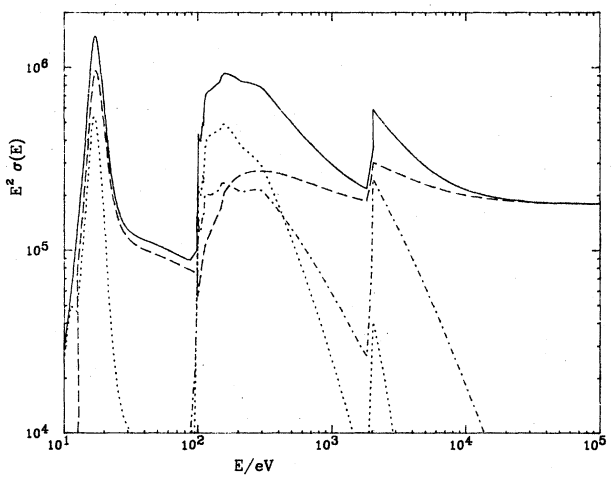

(a) Energy loss spectrum $\sigma(E)$ for 45 GeV pions in silicon [107].

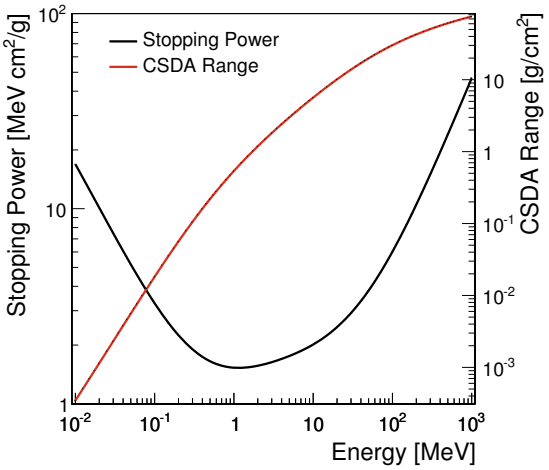

(b) Stopping power and CSDA range of delta electrons in silicon. Data taken from [154].

Figure 5.1: Energy loss spectrum for pions (a). Plotted is $E^2\sigma(E)$ to enhance the visibility of the K, L M shell maxima of silicon. Stopping power and range in the continuous slowing down approximation (CSDA) as function of the initial delta electron energy (b).

The range of the delta rays and the stopping power are taken from the ESTAR database [154] and are shown in Figure 5.1b.

The simulation of these processes yields the charge distribution shown in Figure 5.2. The distribution is well described by the approximative Landau-Vavilov function, convolved with a Gaussian distribution.

5.2 Charge Transport

After all charges have been deposited in the sensor bulk material, the time evolution of the signal propagating through the device is simulated. Since the charge drift is caused by the electric field of the bias voltage applied, an electrostatic simulation using a TCAD tool [155] has been employed to exactly determine the electric field within the single pixel cells. TCAD programs provide algorithms for the simultaneous solution of Poisson's equation (Equation 3.2) and charge carrier continuity equations for both electrons and holes. The charge carrier continuities for electrons and holes are

$$\nabla \vec{J}_n = q \cdot \left(R_{\text{eff}} + \frac{\partial n}{\partial t} \right) \qquad \text{(electrons)} \tag{5.1}$$

$$-\nabla \vec{J}_p = q \cdot \left(R_{\text{eff}} + \frac{\partial p}{\partial t} \right) \qquad \text{(holes)}, \tag{5.2}$$

with the effective recombination rate R_{eff}, the current densities $\vec{J}_n$, $\vec{J}_p$, and the charge carrier densities n, p for electrons and holes, respectively. The equations are solved for each point on a previously generated mesh in the device.

In order to limit the computational effort of the TCAD simulation, the pixel cell was assumed to have a four-fold symmetry, neglecting the bias dot in the original sensor design (cf. Section 4.1).

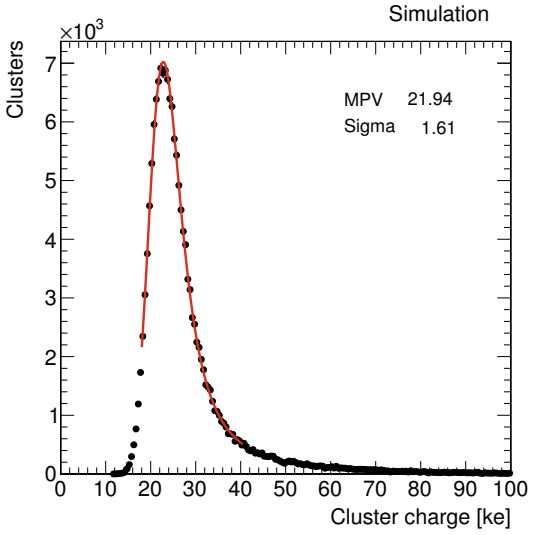

Figure 5.2: Cluster charge distribution obtained from simulation at vertical beam incidence. Shown is the distribution and the fit of a convolved Landau-Gauss function. The fit limits are chosen around the Landau MPV with $18\,\mathrm{ke} < x < 40\,\mathrm{ke}$.

Thus, only one fourth of the pixel cell in the x-y plane has been simulated, and the electric field for the full cell has been calculated by reflecting the simulated section. By this, the mesh size and computing time can be reduced significantly. In order to allow comparison with the simulation, the bias dot regions are removed in the data analysis as will be described in Section 8.4.1.

Using the electric field from the TCAD simulation, the previously deposited charge carriers are transported by numerically integrating their equations of motion [152]. For the simulation of test beam data, no magnetic field needs to be taken into account, and the equations can be simplified to

$$\frac{d\vec{x}}{dt} = \vec{v} \tag{5.3}$$

$$\frac{d\vec{v}}{dt} = \frac{e}{m^*}\left[q\vec{E} - \frac{\vec{v}}{\mu\left(E\right)}\right], \tag{5.4}$$

where m^* denotes the effective mass and $\mu(E)$ the mobility of the charge carrier. The effective masses of electrons and holes in silicon are taken as $0.260\,m_e$ and $0.241\,m_e$, respectively [152].

The equations of motion are simultaneously integrated using a fifth-order Runge-Kutta method, the electric field is updated every 100 steps. In addition, the diffusion process described in Section 3.1.5 is accounted for by adding an offset to each coordinate of the charge carrier. The offsets are randomly drawn from a Gaussian distribution with an RMS of the diffusion length l_D as defined in Equation 3.11. This additional offset is calculated for every drift iteration. Using this technique, every tenth of the originally deposited charge carriers is propagated through the sensor, and the total charge is extrapolated. This maintains most of the information while reducing the computing time significantly.

Pixelav is also capable of simulating trapped charges including charge induction on the implants. With unirradiated sensors and drift times below the actual integration time of the preamplifier circuit in the readout electronics, only charge carriers collected on the implants have to be taken into account for the following signal processing simulation. With trapped charge carriers present,

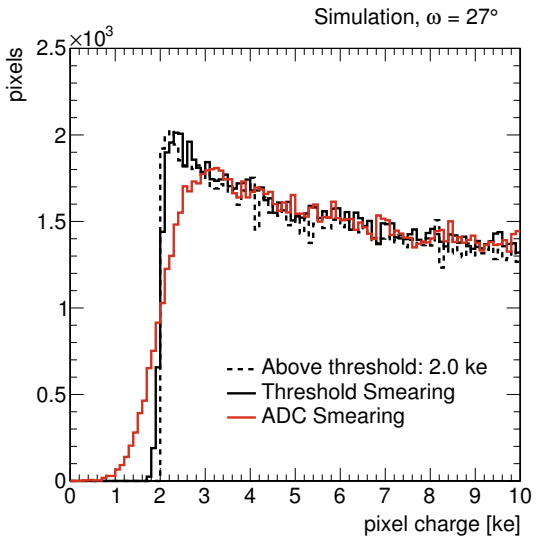

(a) Pixel charge distribution after threshold and ADC response smearing for a track incidence angle of $\omega = 27°$.

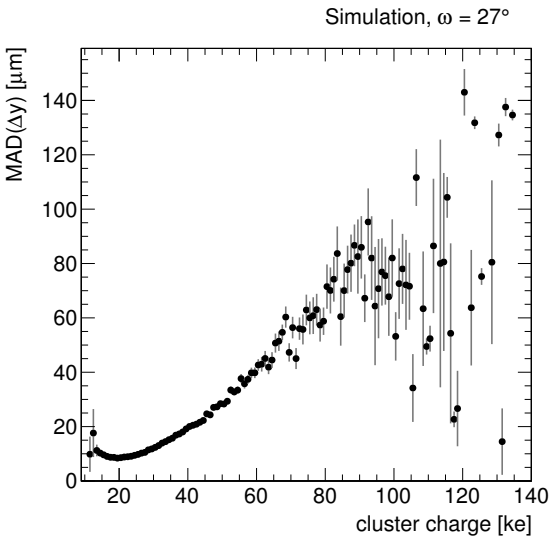

(b) Position resolution (residual MAD) as a function of the cluster charge normalized to vertical track incidence for a pixel pitch of 150 µm.

Figure 5.3: Simulation of the pixel charge distribution smearing and the position resolution as a function of the cluster charge. The resolution is calculated as the mean absolute difference of the residual distribution.

the drift time exceeds the integration time for some of the charge carriers, and only the induced charge from the drift distance covered is measured at the implants.

5.3 Digitization and Reconstruction

The simulation of the readout electronics is performed by an independent analysis processor. This allows to quickly iterate through different readout electronics parameters such as the charge threshold without the need to re-run the time consuming charge transportation simulation. Instead of an involved emulation of the actual front-end electronics, simplified models are used to describe the influence of threshold and electronic noise. The models follow the basic building blocks of the PUC and the ADC described in Section 4.2, and allow to describe the features observed in test beam data reasonably well. All parameters used in the following section are tuned to test beam data.

For every event simulated, Pixelav provides the vector and momentum of the primary particle traversing the sensor, the total number of collected electrons on the implants, and a list of pixels with their individual charges. A thermal noise contribution is added to the collected charge from the sensor, drawn from a Gaussian distribution with an RMS of 180 electrons. Due to the improved routing of supply lines, no cross-talk contribution has to be taken into account for the simulation of PSI46digV2.1-r ROCs.

The configurable signal threshold is smeared by a Gaussian distribution with an RMS of 100 e, and the signal response of the shaper circuit is modeled using the Weibull function which will be discussed in Section 8.2. In order to correctly describe the width of the Landau distribution obtained from test beam data, an additional multiplicative smearing of the preamplifier gain is applied. Pixel charges exceeding the configured threshold are smeared with a Gaussian

distribution with a width of 500 e mimicking the limited precision of the pulse height sampling in the 8 bit on-chip ADC (cf. Section 4.2). Figure 5.3a shows the pixel charge distribution for a track incidence angle of $\omega = 27°$ after passing a simple cut at the threshold value, after threshold smearing, and after the contribution stemming from the ADC sampling.

The position and direction of the primary particle are known as Monte Carlo truth and can be used to reconstruct the original impact point of the particle. To simulate the accuracy of an external tracking telescope (cf. Section 7.2), the truth information is smeared by the predicted telescope track resolution obtained from the GBL calculations presented in Section 7.2.1. The track resolution amounts to about 5 µm, and the smearing is performed using two normally distributed random numbers for the x and y coordinate, respectively. In addition, a flat background is added to the residual distributions in order to match the shapes obtained from test beam measurements.

In the reconstruction process, the methods of the actual test beam data analysis are applied: the pixels are clustered and the cluster center is determined using the CoG algorithm described in Section 3.3.1. The telescope tracks are matched with the reconstructed cluster positions, and the residual is calculated in both sensor coordinates.

The events entering the final residual distributions are selected by imposing requirements on the cluster charge to be within the Landau peak, and thus removing the tail contributions from delta rays which deteriorate the position resolution as shown in Figure 5.3b as the mean absolute difference (MAD) of the residual distribution. The optimal resolution can be achieved around the MPV of the Landau distribution of about 22 ke while large clusters in the Landau tail stem from the delta electrons. A detailed description of the analysis can be found in Chapter 8.

6. The pxar Data Acquisition and Calibration Framework

Building a new detector such as the CMS Phase I Pixel Detector is a major endeavor since the detector components as well as their assembly usually are state-of-the-art technology with no or little expert knowledge and experience available. This situation becomes especially true with a distributed production in many institutions scattered over several continents. Quality control is a key element to the success of the project, and it has to be ensured that functional tests and calibration of the detector modules are performed in a consistent way throughout the collaboration.

Since the front-end electronics of the Phase I pixel detector differ significantly from the present pixel detector both in operational parameters and in the data format returned, new hardware and software are required to test the detector components. The new readout hardware is presented in Section 6.1.

Instead of adapting existing software packages which have evolved over time, from the design to production and operation of the present pixel detector, it has been decided to re-implement all necessary tests and routines from scratch, providing a clean, stable, and maintainable calibration framework for the lifetime of the Phase I detector. It consists of a versatile hardware library described in Section 6.2 which interfaces the readout electronics, and a comprehensive test suite implementing the test procedures and histogramming. Section 6.3 gives a brief overview of the typical module qualification tests applied during production of the Phase I detector.

This chapter does not intend to provide a detailed technical documentation, but rather an overview of the important features and operation modes. The reference manual and examples for applications of the hardware library can be found elsewhere [156].

6.1 The Digital Test Board

The digital test board (DTB) is the readout electronics for laboratory tests during the production of the Phase I pixel detector modules. It has been designed with the flexibility in mind to provide readout electronics for a variety of devices, and thus to allow operation of the present pixel detector modules with analog PSI46V2 ROCs as well as the different flavors of Phase I detector assemblies and possible future derivatives.

It consists of a custom-designed board featuring all necessary components for the detector operation, such as IO modules, trigger capabilities, and a high voltage relay for the bias voltage. The communication is established via USB2.0 and Gigabit Ethernet ports. The core of the device is an Altera FPGA which hosts all required firmware modules and also provides an emulated CPU. A level adapter chip and an ADC allow the reception of 400 MHz low-current differential signals from the TBM and analog level-encoded signals, respectively.

Around 180 DTBs have been produced and distributed among the collaboration institutes. The field of application ranges from wafer probing of the chips after reception from the manufacturer, to testing of the assembly between the different steps of module production, final qualification tests at operational temperature of −20 °C, and to absolute energy calibrations using monochromatic X-rays.

The DTB also implements all features necessary to operate the detectors in test beam environments, such as inputs for triggers and external clock signals.

6.1.1 Deserializers and Data Recording

The incoming data signal has to be treated differently depending on the detector attached. While single ROCs respond with a 160 MHz signal, the full detector modules return a 400 MHz signal from the TBMs. The present pixel detector front-end electronics again return an analog pulse-height encoded signal at a frequency 40 MHz. In order to accommodate this variety of signal, the DTB firmware is fitted with several data receiver modules which sample the incoming data. The appropriate module has to be activated before attempting to record data.

The 160 MHz deserializer module (DESER160) records data streams sent directly by one or more ROCs attached to the DTB. The readout is controlled by the so-called *flying token*. After pixel hits have been validated through the trigger signal, a readout token is sent to the ROCs as described in Section 4.2.3. The DESER160 triggers on the outgoing token signal sent to the detector and starts sampling the incoming data stream after a configurable delay. The signal is recorded until either the token signal is returned by the detector, or a timeout has been reached. In order to correctly sample the data, the phase of the sampling relative to the 160 MHz signal has to be correctly adjusted.

The 400 MHz deserializer module (DESER400) works slightly differently since the TBM sends a recognizable idle pattern if no data are being sent. This allows the DESER400 to lock on the correct signal phase, and no manual phase adjustments are required. Beginning and end of the data transmission can be distinguished from the idle pattern which renders the DESER400 independent from any additional condition such as token signals. The multiplexed data streams from the TBM cores (cf. Section 4.3) are isolated and stored separately, multi-channel TBMs require multiple DESER400 modules to be activated. The firmware block deployed in the DTB is very similar to the one that will be used in the actual pixel detector FEDs outside the CMS experiment.

Data from analog ROCs can be recorded using the internal ADC. Just as for the DESER160, the readout is controlled by the token signal which requires correct delay settings. In addition to the token delays, the sampling point of the ADC has to be adjusted within the 40 MHz clock cycle to avoid a dependence on the pulse height of preceding signals [156].

All data recorders write the sampled data directly into the memory of the DTB. The memory blocks have to be allocated beforehand, and are implemented as ring buffers. Ring buffers feature one read and one write pointer to the allocated memory, and implement a wrap-around at the end of the memory block to enable continuous reading and writing of data. This is useful in scenarios with a constant data flow, e.g., in test beams.

6.1.2 The Nios II CPU

The FPGA design of the DTB includes an emulated *Nios II* CPU [157] which is capable of executing `C` code. Since it only runs at a clock speed of 50 MHz it cannot be used for computing-intense tasks such as decoding of detector data, but it is well suited to provide a convenient interface to control the different firmware blocks of the FPGA. This includes configuration, starting and stopping of the data acquisition, and transmission of I^2C commands to the detector.

Test Loops

In addition to these simple commands, some more complex functionality has been implemented as part of this thesis to allow efficient qualification of modules. Testing a detector module usually involves inspection of every single pixel by sending calibration charges through the analog circuitry and by reading out the pixel hits. Since these test are done pixel-by-pixel, the total number of triggers sent to the module quickly reaches $\mathcal{O}(10^6)$. Beside masking and trimming single pixel cells, also DAC settings are iterated to find suitable operation parameters.

Sending the respective I^2C signals from the PC in between every pixel would create a huge communication overhead via the USB connection. Instead, the so-called *test loops* implement some often-used loops over pixels or DAC settings directly on the Nios II. This greatly reduces the time required to iterate through the different detector conditions and enables triggering at high rates of up to 200 kHz.

The behavior of the test loop functions can be altered by a set of flags, which for example allow to perform cross-talk measurements by activating neighboring pixel cells, or to send the calibration pulse through the sensor pad for bump bond connection tests.

The test loops are self-interrupting. Once the allocated DTB memory is full, the function returns control to the PC which reads all recorded data via the USB interface. After successful transmission of the data, the loop is called again and resumes at the interrupt position. Via this mechanism, large numbers of triggers can be recorded without additional effort for the operator.

6.1.3 Trigger Generation

The DTB provides several methods to generate trigger signals for the attached detector. External triggers are accepted via the LEMO port as TTL signals, internal triggers can be generated as random or cyclic triggers. In addition, the pattern generator can be activated via Nios II calls.

The Pattern Generator

The pattern generator is a firmware module that allows to send configurable patterns of signals which have been programmed ex ante. It consists of a register bank with 256 addresses, each of which can be configured with a signal and a delay. Once activated, the pattern generator iterates through the register bank, sending the signals to the detector. The delay specifies the number of clock cycles to be waited before processing the next register, a delay of zero stops the execution of further register entries.

A typical use case of the pattern generator is the operation of the detector with calibration charges. The trigger validating the calibrated pixel hit has to be transmitted at a fixed time after the calibrate pulse, defined by the configured trigger latency in the detector (cf. Section 4.2.2). The pattern generator then contains the calibration signal and the trigger as well as the delay between the two signals.

The TBM Emulator

When utilizing external triggers, the pattern generator cannot be used and the required functionality such as readout token generation has to be provided by other means. In pixel detector modules, the token generation and trigger stacking is taken care of by the TBM. When operating single ROCs, this functionality is provided by the TBM emulator module which implements the logic of the TBM chip in the DTB firmware.

The TBM emulator also adds header and trailer words to the data of every event which contain the current trigger number as 8 bit value, and the phase of the trigger signal arrival time relative to the 40 MHz clock. All DTB trigger sources can be configured to either send their outputs through the TBM emulator, or to bypass it and send the signals directly to the detector.

6.2 The pxarCore Library

The operation of the DTB requires detailed knowledge of the internal firmware modules and the detector readout mechanism. Thus, it has been decided to write a library which simplifies the usage and communication with the DTB and allows to test, calibrate, and operate PSI46-type devices without extensive additional knowledge of the readout electronics.

The pxarCore library provides this functionality and has been implemented as part of the work described in this thesis. The internal structure and functionality of the DTB is abstracted to allow transparent access of the attached detectors, and to provide users with a set of easy-to-use functions for high-level applications. By now, the pxarCore library is in use by the entire CMS Pixel Upgrade Collaboration, and all modules produced for the Phase I Pixel Detector are tested using the library and one of the user interfaces available. The detailed documentation of the software package is published separately and can be found in [156].

The most commonly used user interface is *Pixel eXpert Analysis & Readout* which implements the full test suite required for module qualification, cold test, and X-ray calibration. Others provide more flexible scripting capabilities using the Python interface provided by the pxarCore library. For test beam operation, the library is fully integrated with the EUDAQ software framework [158] as will be described in Section 7.4.

6.2.1 The Software Architecture

The library consists of two main blocks as depicted in Figure 6.1. The hardware abstraction layer (HAL) represents a transparent layer for the underlying hardware. It is responsible for implementing correct call sequences for the requested operations, and is the only class requiring direct access to the hardware. Only one HAL implementation exists as of now, since currently the DTB is the only available readout electronics for Phase I Pixel Detector modules. However, new hardware support could be added to the library at low effort by providing a HAL class for the respective hardware. The communication between PC and the DTB is implemented as remote procedure call (RPC) protocol, and either USB or Ethernet act as transport layer. Ethernet support is present in the pxarCore library, but the DTB firmware currently lacks the implementation of the interface.

The application programming interface (API) is the library's interface to the applications. Because of the clear separation between the library and the application layer, the function calls provided by the API have been stable since almost the beginning of the development cycle. This allows to implement extensive changes within the library without the need of adapting application code and test suites, and has proven to be an effective concept several times during the development.

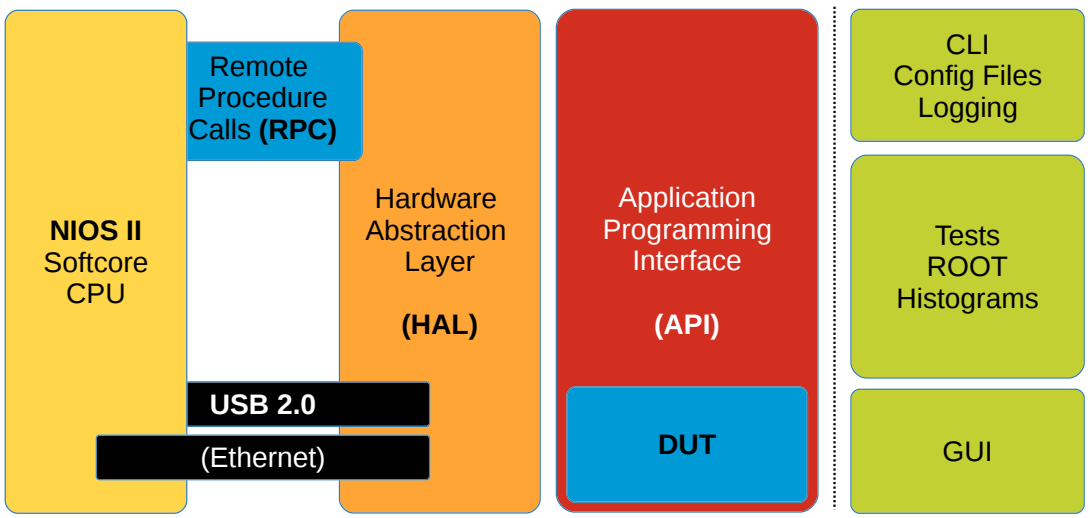

Figure 6.1: Sketch of the software architecture of pxarCore consisting of the HAL and API classes. Applications communicate with the library through the API, the connection to the DTB is established via the RPC interface.

The detector is configured via the DUT object of the API, which allows to keep track of all settings programmed into the device. Calls to test functions are automatically expanded to cover all parts of the detector which have been flagged for testing in the DUT in the most efficient way available, and the data returned via the API are fully decoded and sorted, simplifying the implementation of test algorithms.

Figure 6.2 shows the matrix of available tests in the pxarCore API. The returned data contain either the response efficiency of every pixel for a given number of triggers, the averaged pulse height and variance, or a threshold value for a given DAC parameter.

6.2.2 Event Building and Data Decoding

Owing to the variety of connectable devices, the event building and decoding classes have to be flexible to cope with the corresponding data formats. The different tasks of parsing raw detector data are attributed to separate classes.

The retrieval of raw data from the DTB is accomplished by so-called data sources, where one source is responsible for one DAQ channel, multiple sources have to be set up for TBMs. The data are transferred from the DTB in large blocks to efficiently use the bandwidth available.

The subsequent step in the decoding chain is the splitting of events. The data stream contains special marker bits which are used to identify the beginning and end of the data attributed to one trigger. If only the raw event data have been requested by the application, the decoding chain ends at this point, and the undecoded raw event data are returned.

The central part is the actual decoding of the event content. Detailed statistics are collected during the decoding process to allow investigation of occurring errors in the detector data. At first, a new event is allocated and initialized. If the data have been recorded using a TBM, the header and trailer words are analyzed and stored. Decoder modules for the various types of ROCs then iterate over the remaining data and check every word for the appearance of a ROC header identifier (cf. Section 4.2.4), and otherwise treat the data as pixel hit.

The final event undergoes some validity checks such as the number of ROC headers found. Additional information such as status and error flags in the TBM trailer are taken into account.

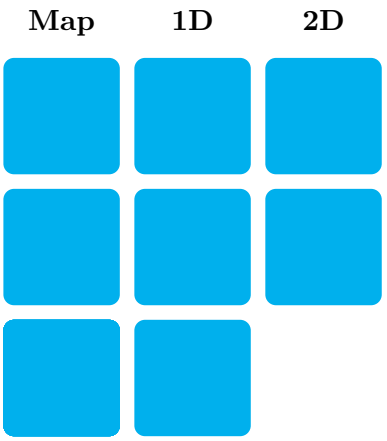

Efficiency (Number of responses)

Pulse Height (Average and variance)

Threshold (Falling/rising edge, configurable level)

Figure 6.2: Test matrix of implemented test functions in the pxarCore library. Rows represent the different data output formats (efficiency, pulse height, or threshold value) while the columns describe the different scopes of the test (covering the device, scan one DAC, scan two DACs).

Also the readback information from the ROC header described in Section 4.2.3 is collected and available for retrieval by the application.

The modules of a decoding chain can be arranged very flexibly, even allowing to change the output format at run time. The event building is done at HAL level, where one event per active DAQ channel is requested from the decoding pipes, and merged into the final detector event. This allows to reliably correlate the different readout channels of a module. If multiple DTBs are operated in parallel, e.g., by EUDAQ as described in Section 7.4.3, the event serial number can be used to correlate the data streams.

6.2.3 Front-End Emulation for System Testing

The DTB emulator class allows detector-independent testing of the pxarCore library and application software. The class emulates the behavior of the DTB at RPC-level responding to the different requests made by the software. Pseudo-data in the original detector raw format are produced and passed through the regular decoding chain until it is returned to the inquiring application. This allows to cover most of the software components and provides a powerful tool to implement unit tests.

Test suites can use the DTB emulator class to validate their algorithms with pseudo-data returned for detector hit maps, DAC scans, and other requests. More involved algorithms such as trimming of a detector device are not expected to converge as no full chip simulation is implemented.

6.3 Phase I Pixel Module Qualification

The module qualification procedure consists of a well-defined set of tests to be carried out at various stages of the module production and integration. Every module assembled at any of the production sites has to pass these tests in order to be accepted for the Phase I Pixel Detector. All individual components are checked for proper functionality upon receiving, and the *IV* curves of the sensors are measured to determine the leakage current (cf. Section 3.1).

The full module qualification is organized in three consecutive steps. The *pretest* checks basic functionality and seeks operational parameters for stable communication of the control and

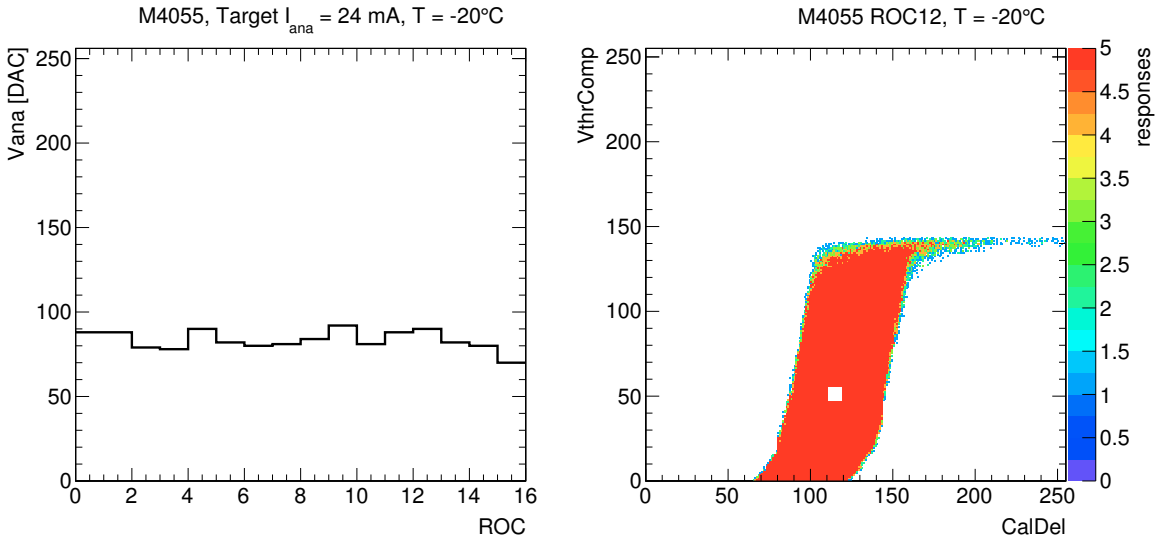

(a) VANA DAC setting per ROC for the target analog current of $I_{\text{ana}} = 24\,\text{mA}$.

(b) Scan of the comparator threshold versus the delay of the calibration signal.

Figure 6.3: Pretest procedures for module qualification. The target analog current per ROC is adjusted by varying the VANA DAC (a). A working point for internal calibration pulses is determined by mapping the number of responses for a pixel in the CALDEL-VTHRCOMP DAC phase space (b). The selected working point is marked by the white square.

readout electronics with the module. The subsequent *fulltest* performs comprehensive checks of the different ROCs and tests the characteristics of every single PUC. Finally, the charge threshold of every module is calibrated using monochromatic X-rays, and additional tests such as high-rate performance with X-rays are conducted. The test procedures are described briefly in the following sections, accompanied by exemplary test results for the detector module identified with the serial number *M4055*.

The same testing procedure also applies to SCM assemblies in the preparation for laboratory tests, irradiation studies, or test beam measurements.

6.3.1 The Module Pretest

The first test to be performed on a module verifies the electrical integrity of the module. The ROCs have to be programmed in order to be functional, since the power-up reset circuit initializes them in a safe state (cf. Section 4.2.3). Thus, establishing communication with the chips in order to program registers is of prime importance. An efficient way to test the communication is scanning through the different settings of the VANA DAC, observing the power consumption of the chips. For each ROC the analog current I_{ana} drawn from the DTB should increase measurably with rising VANA. If all ROCs responded correctly, the VANA settings can be optimized in order to achieve the target analog current of 24 mA per ROC as shown in Figure 6.3a. This analog current is defined by the ROC design specifications, and is limited by the available total current delivered by the DC-DC power converters (cf. Section 4.5).

The subsequent step establishes the reverse communication path for receiving pixel hit data from the module. This requires the TBM to obtain correct phase settings for its internal signal delays which adjust the phase of the TBM header and trailer, the token return signals, and the

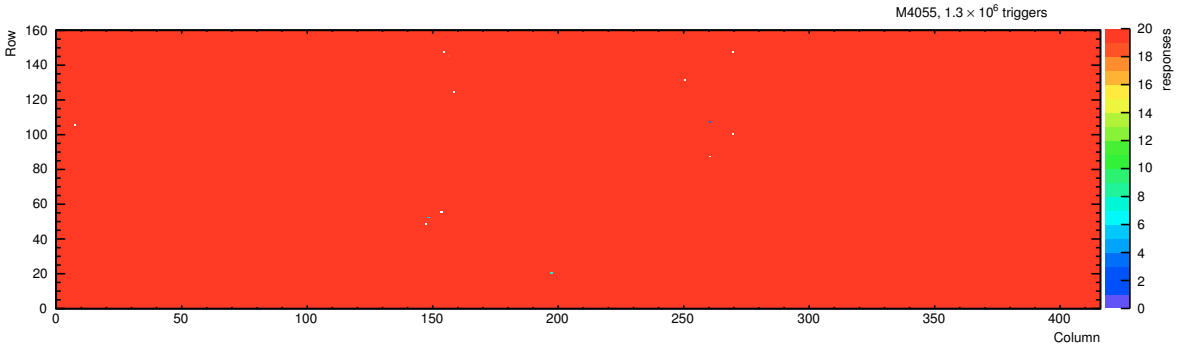

Figure 6.4: Module map of a pixel response efficiency test. Only the few single pixels marked in white and blue are not responding to the calibration charges injected, the dead channels amount to less than 0.02 %.

data signals of each individual ROC [145]. Only if the delays are chosen correctly, the data will be aligned and can be identified by the DESER400. The test is classified as passed, if the TBM header and trailer as well as the headers from all ROCs can be correctly identified in the 400 MHz data stream. Since scanning the full phase space of possible signal combinations is very time consuming, usually a sparse scan is performed starting from a set of default values derived from previous measurements of the TBM chip.

Testing the PUCs requires the calibration signal to arrive with a correct timing to be detected in the triggered bunch crossing. The delay of the signal can be adjusted via the CalDel DAC for each of the ROCs, the optimal value depends on the setting of the charge comparator. The working point is chosen by mapping out the VThrComp versus CalDel phase space and selecting parameters from the center of the so-called *tornado plot* as shown in Figure 6.3b.

With these tests passed and settings applied, the module has demonstrated to be functional and the subsequent *fulltest* procedure is capable of performing comprehensive tests on the PUCs.

6.3.2 The Module Fulltest

The *fulltest* is responsible for testing the detector performance, pixel response, and noise as well as determining optimal operational parameters, and eventually grading the module into the categories *A* (flawless), *B* (with minor issues), and *C* (rejected) [159]. These categories decide whether a module will be integrated into the Phase I Pixel Detector or left as spare. In layer 4 of the new detector, modules with both categories *A* and *B* will be used.

In order to classify the PUCs, a calibration charge is injected in each of the pixels sequentially, and the responses are counted. An example for such a pixel response efficiency map is shown in Figure 6.4, where pixels which are not responding are marked in white and blue, and are considered dead.

For all functional pixel cells, the bump bond connection to the sensor can be inspected by rerouting the calibration signal to the surface pad as described in Section 4.2.1. The charge is induced in the sensor implant via the air capacitance between ROC and sensor, and can subsequently be detected by the pixel. Since this test very much depends on the actual distance between these two components due to the capacitive coupling, several test algorithms have been developed for the different production centers and their individual bump diameters and bonding techniques. Figure 6.5a shows an example for the bump bond test of one ROC on a module using the global threshold value at which the pixels respond as discriminant to distinguish

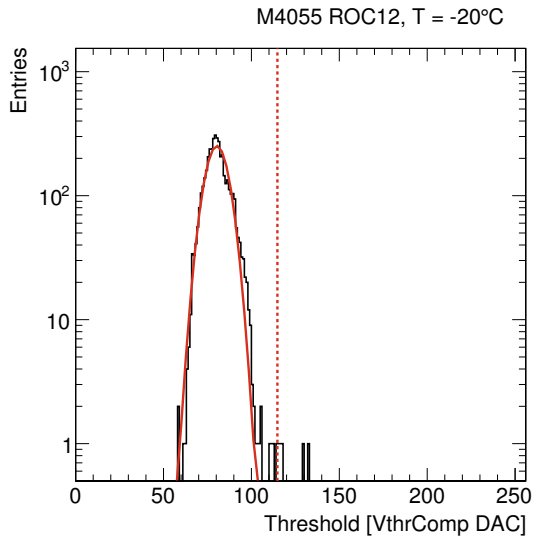

(a) VThrComp threshold distribution for all PUCs. Pixels with a threshold beyond the dashed line are considered disconnected.

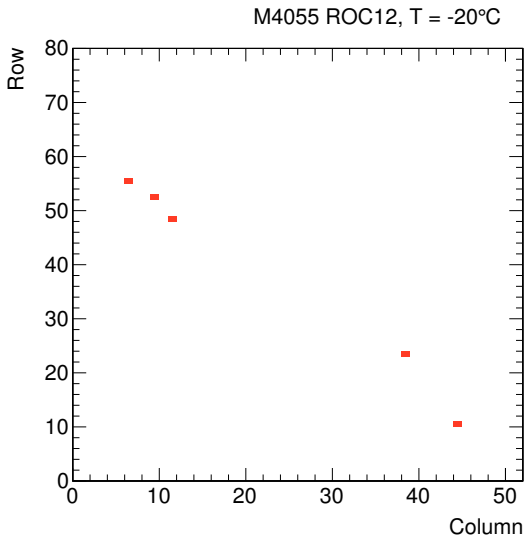

(b) ROC map of missing bump bond connections. The five pixels marked in red have been determined to be disconnected.

Figure 6.5: Bump bonding test using the Cals signal routed to the sensor via the air capacitance. The response threshold is used to distinguish between connected pixels and missing bumps (a). The grading criterion represented by the dashed line is placed 3σ from the mean of the Gaussian fit. The ROC map shows the pixels with missing bumps (b).

between a connected sensor implant and a missing bump bond. Missing bonds are indicated on a chip map as demonstrated in Figure 6.5b.

The noise of the pixels is measured using the so-called *S-curve* technique. Using the calibration signal, the threshold turn-on curve is scanned from 0 % efficiency to 100 % response from the pixel. The resulting s-shaped curve is fitted with an error function, and the width of the error function serves as estimate for the noise in units of VCal DACs under the assumption of a Gaussian noise distribution. The conversion from internal VCal DAC units into electrons will be discussed in Section 6.3.3. Figure 6.6 shows the S-curve width distribution of all PUCs on one ROC, and the mean pixel noise is determined to be around 140 electrons for a fully depleted sensor.

It is of special importance for the modules to have a uniform charge threshold across all pixels in order not to bias cluster center interpolation (cf. Section 3.3.1) and to facilitate the comparison with simulation. The ROCs provide several handles to tune the pixel thresholds. The global baseline for the pixel threshold is set via the VThrComp DAC. However, this does not lead to a uniform threshold because of variations in the silicon processing and the transistors involved. Figure 6.7a shows the threshold map of a ROC with large variations among the individual PUCs.

With the global starting threshold set such that the pixel with the lowest threshold is above the target, the individual pixels thresholds can be tuned using the relation

$$Q_{\mathrm{thr}} = Q_{\mathrm{comp}} - (15 - \mathit{trim\,bits})\, Q_{\mathrm{scale}}, \tag{6.1}$$

where Q_{thr} denotes the absolute charge threshold of the pixel. Q_{comp} and Q_{scale} are the global comparator threshold adjusted via VThrComp and the threshold scale DAC set via VTrim,

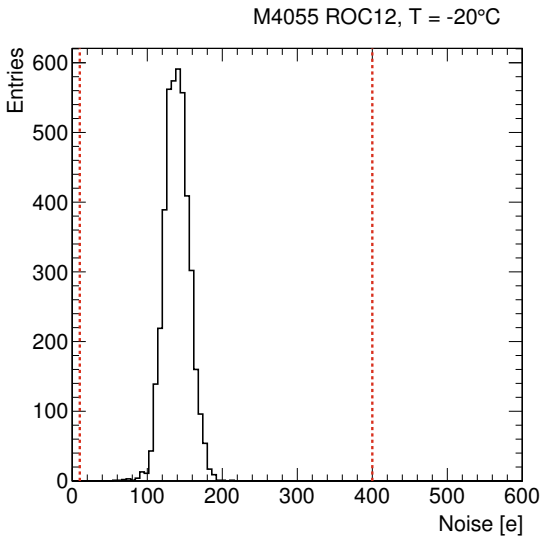

Figure 6.6: Noise distribution of all 4160 pixels on one ROC, the dashed lines mark the acceptance criteria for the fulltest. The mean pixel noise is around 140 electrons with an RMS of 16 electrons. The dashed lines represent the grading criteria for acceptance of the tested module.

respectively. The individual per-pixel threshold is tuned using the four *trim bits* ranging from 0 to 15. Small trim bit values lower the threshold significantly, while larger trim bit configurations only slightly adjust the level. The global impact of the trim bits is controlled by VTrim.

The procedure of finding optimal settings for the two global DACs and the individual pixel trim bits in order to balance threshold differences is called *trimming* and usually performed in several optimization steps. The final result presented in Figure 6.7b shows the threshold distribution of all pixels with correctly configured trim bits, the RMS of the distribution is around 1 VCal DAC unit. Figures 6.7c and 6.7d present the trim bits after the trimming procedure as a map for the ROC and as distribution, respectively.

In order to optimally use the range of the ADC, the pulse heights from the PUCs are scaled using the PHOffset and PHScale DACs. Since the pulse height response from the pixels is not perfectly uniform, a gain calibration is performed for every single pixel. The pulse height of every PUC is recorded for the full range of VCal calibration signals, and the distribution is fitted to obtain an analytical description of the shape. Several fit functions are available and used, the standard implementation in the pXar software uses a hyperbolic tangent to describe the linear rise and saturation at large charges using four parameters:

$$f(x) = p_3 + p_2 \tanh(p_0 x - p_1). \tag{6.2}$$

For the final deployment in the CMS experiment, a linear fit with per-pixel offset and an averaged slope per column is used in order to reduce the database footprint and computational requirements for the reconstruction. This simplification is justified by the mean charge deposited by a MIP (cf. Section 3.1.5), which is within the linear range of the function and not affected by the saturation at large charges.

Finally, additional checks such as the test of the readback function (cf. Section 4.2.3) are performed. The readback is configured via the Readback register to return the unregulated digital voltage $V_{d,\mathrm{unreg}}$ and a scan of the DTB digital supply voltage is performed while retrieving

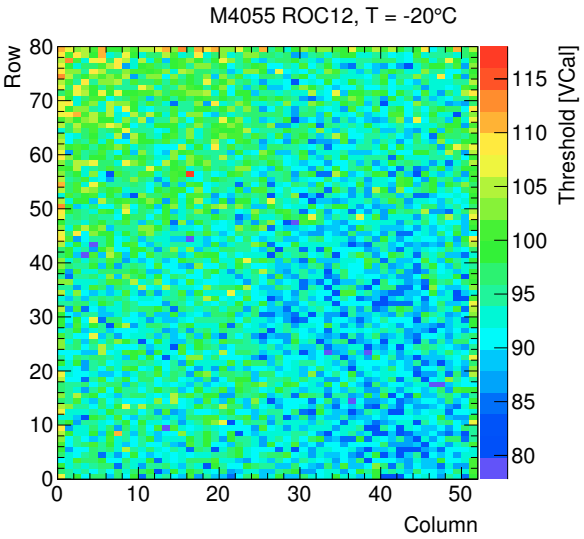

(a) Map of the pixel thresholds without trim bit optimization.

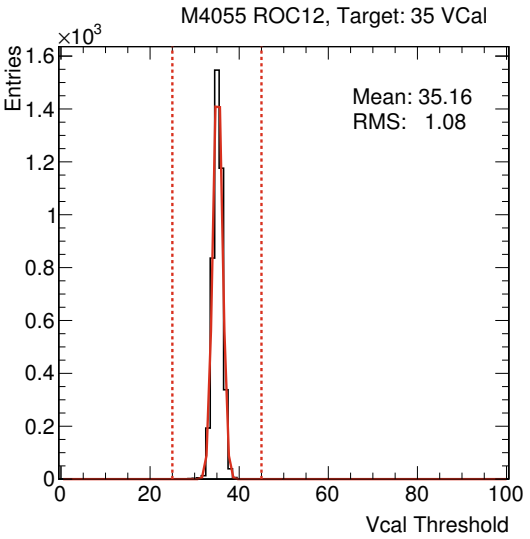

(b) Threshold distribution after trimming with the mean close to the specified target value of 35 VCal DAC.

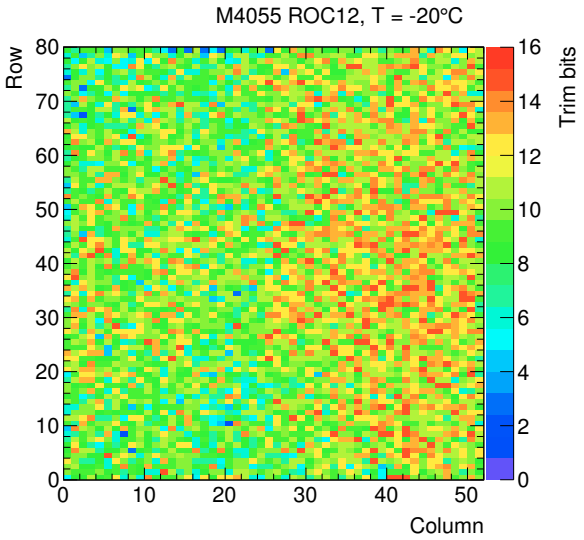

(c) Map of the trim bits set for the individual pixels, the shape from (a) can be recognized.

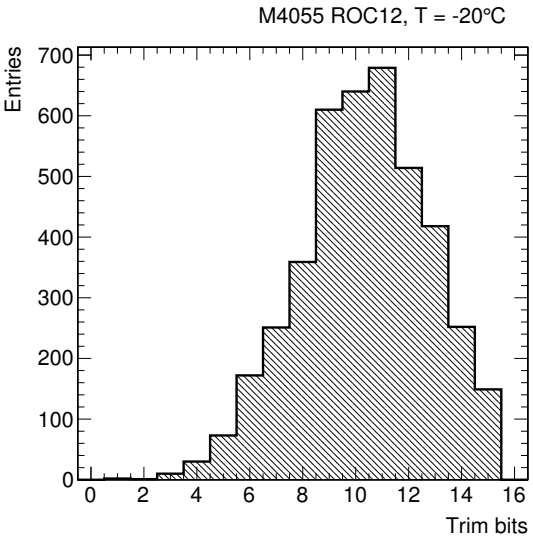

(d) Distribution of the trim bit configuration for all pixels after trimming.

Figure 6.7: Module trimming procedure. The global threshold is set high enough for all pixels to reach the target (a). The VTrim and trim bits are iteratively adjusted until a narrow threshold distribution has been achieved (b). The distribution of trim bit values of the pixels after trimming is shown in (c) and (d).

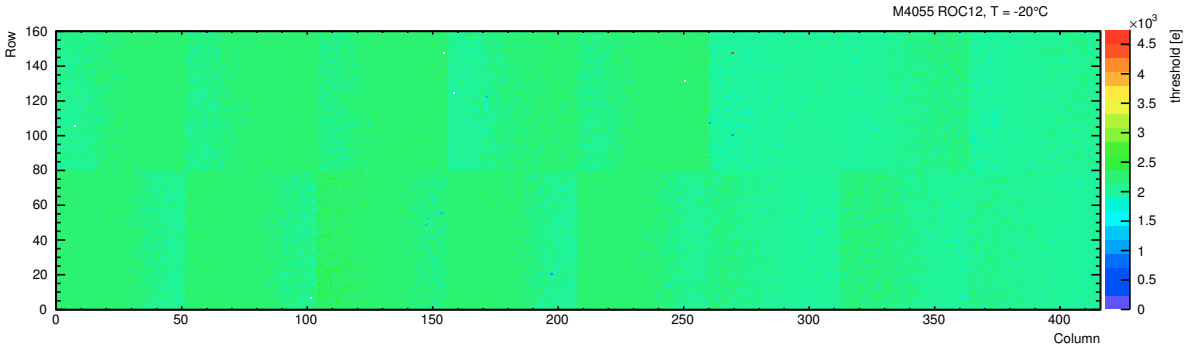

Figure 6.8: Module threshold map after the trimming procedure and the charge calibration. All pixels exhibit a uniform threshold around 2 ke, while only the defect pixels show up with either high or low threshold.

the readback data from the chip. The test verifies the linear dependence of the voltage measurement returned by the ROC on the voltage supplied via the DTB, and allows the calibration of the analog current in the chip.

6.3.3 X-ray Calibration

The relation between VCal DAC units and electrons is determined using the characteristic energy spectrum peaks of monochromatic X-rays. Data are recorded with X-rays from a set of different targets such as Ag, Mo, Zn, and Sn. The resulting spectra are analyzed to obtain a parametrization for the linear relation between DAC units and charge deposited in the sensor. This allows to relate measured pixel charges and thresholds in units of the VCal DACs to actual charges deposited in the sensor, and thus allows to calibrate simulations of the pixel detector accordingly. Figure 6.8 shows the final threshold map in units of electrons per pixel, the few defects seen can be identified with the dead pixels already encountered in Figure 6.4.

7. Test Beams at the DESY-II Synchrotron

Test beams are particle beams which allow to assess the characteristics of particle detectors and thus provide complementary information to simulations and laboratory tests. The application of test beams provides a unique opportunity for detector development since the prototypes are operated in conditions as close as possible to the final deployment situation in the experiment. This includes timing and synchronization with the accelerator as well as processing of externally provided triggers and integration into larger data acquisition systems. Operating the prototype in parallel with other devices and under higher rates than achievable using cosmic rays or radioactive sources is an integral part of the qualification process of new detector developments. New sensor designs can be gauged, and new front-end electronics designs can be tested for resolution, cross-talk, and detection efficiency.

Usually the beam parameters such as particle type, energy, and direction as well as the time structure are well-known properties. Depending on the detector to be characterized and on the scope of the measurement, a test beam with suitable parameters has to be chosen.

7.1 The DESY-II Beamlines

The DESY Test Beam Facility offers medium-rate electron/positron beams of a few GeV and is one of the two main users of the DESY-II synchrotron. With a circumference of around 293 m and a maximum beam energy of about 6.3 GeV, its main purpose is the top-up injection of particles to the PETRA-III synchrotron light source. DESY-II circulates one bunch with a length of approximately 30 ps at a revolution frequency of 1.024 MHz, the length of one acceleration cycle is about 80 ms.

Due to the high number of particles per DESY-II bunch, the test beams are generated from the primary beam via twofold conversion as shown in Figure 7.1. Bremsstrahlung is produced in a carbon fiber moved into the primary DESY-II beam. These photons are subsequently converted to electron/positron pairs in a Cu or Al target. A spectrometer dipole magnet allows for the selection of either electrons or positrons, and enables a momentum discrimination for the final test beams. This reduces the instantaneous rate and allows tracking of single particles in the final, collimated beams delivered to the test beam areas. Three areas are available, each with an independent beam extraction and momentum selection. Further information on the DESY test beam facility and beam generation can be found elsewhere [160].

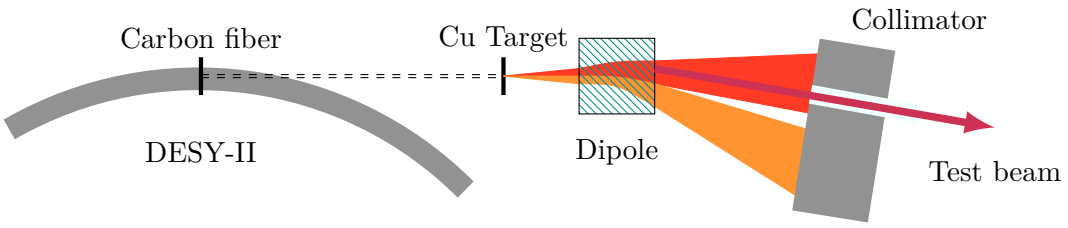

Figure 7.1: Schematic of the test beam generation from the primary DESY-II beam. Bremsstrahlung produced in a carbon fiber is converted into electron/positron pairs in a metal target. The momentum and type of the particles is selected via the dipole magnet and the final beam is collimated before delivery to the test beam areas.

The final beams delivered have a divergence of about 0.5 mrad and an energy spread of approximately 5 % with a minor contamination of low-momentum particles [161, 162]. Depending on beamline and selected beam momentum, rates of a few 10 kHz can be achieved.

7.1.1 Beam Energy Measurement in TB21

The particle momentum in beamline 21 has been measured as a function of the spectrometer magnet current as part of a Summer Student project [163]. The momentum measurement has been performed by deflecting the particle beam in a known magnetic field, and by comparing the measured deflection angles with simulation.

The beam has been deflected after the collimation using a secondary dipole magnet available in the test beam area. Both the primary momenta of the particles selected via the spectrometer magnet, and the magnet currents for the secondary dipole have been varied in order to achieve different deflection angles of the beam. The particle direction after deflection has been measured using the DATURA beam telescope described in Section 7.2.2. A straight track fit including all telescope planes has been performed for the incoming particles, and the angle relative to the normal beam direction has been calculated from the trajectory fits.

Figure 7.2a shows the measured deflection angle of the beam for one beam momentum and different magnetic field strengths of the secondary deflection magnet. As can be seen from the plot, the separation power of the secondary dipole is sufficient to deflect the beam, and the distributions of the deflection angles are clearly separated. This measurement has been repeated for several current settings of the primary spectrometer magnet in order to obtain a relation between the deflection angle and the magnet current.

The particle motion in the field of the second magnet is simulated using the numerical *CYLRAD* method [164] which allows to calculate particle trajectories in arbitrary magnetic fields while conserving their energy. Figure 7.2b shows the simulated deflection angle as a function of the particle momentum. By comparing the measured and simulated deflection angles, the beam momentum can be reconstructed, and a dependency between the spectrometer magnet current and the beam momentum can be calculated. The beam momentum reconstructed with this method agrees well with the calibration provided by the DESY Test Beam Facility as shown in Figure 7.3a, and only small deviations are observed for high spectrometer magnet currents. Es expected, no dependency on the selected deflection angle of the secondary dipole can be observed as demonstrated in Figure 7.3b.

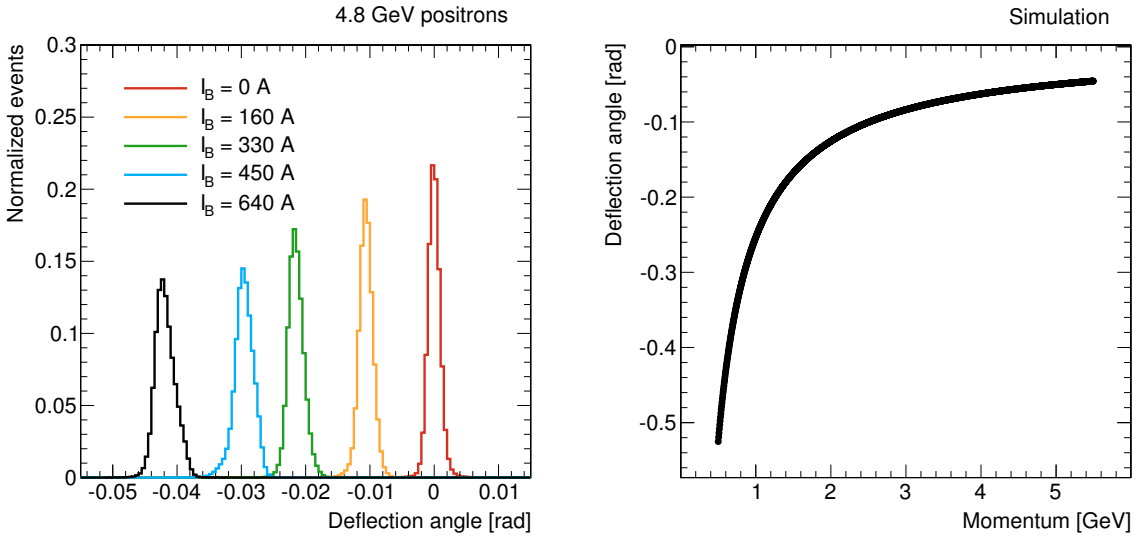

(a) Deflection angle of positrons for different dipole magnet currents. Modified from [163].

(b) Simulation of the deflection angle for different particle momenta. From [163].

Figure 7.2: Deflection angle of fixed-momentum positrons for different dipole magnet currents (a). The number of events is normalized to unity, and presented for different dipole magnet currents. Simulation of the deflection angle as a function of the incident particle momentum in the field of the dipole (b).

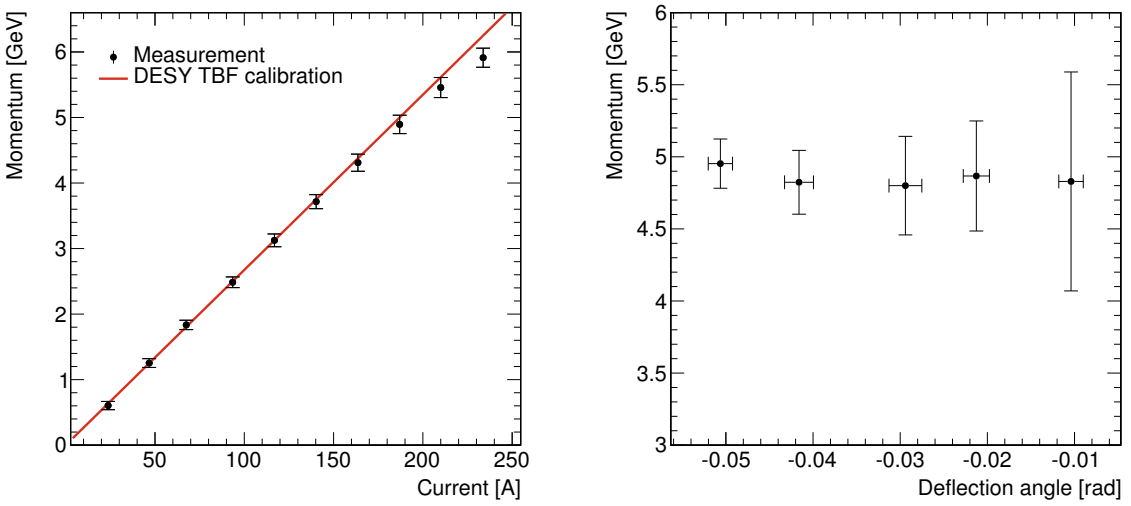

(a) Particle momentum versus spectrometer magnet current. Modified from [163].

(b) Particle momentum as a function of the deflection angle. From [163].

Figure 7.3: Reconstructed particle momentum as a function of the spectrometer magnet current (a), the red line indicates the calibration provided by the DESY Test Beam Facility. Particle momentum as a function of the deflection angle introduced by the secondary dipole (b). As expected, no dependency on the deflection angle can be observed.

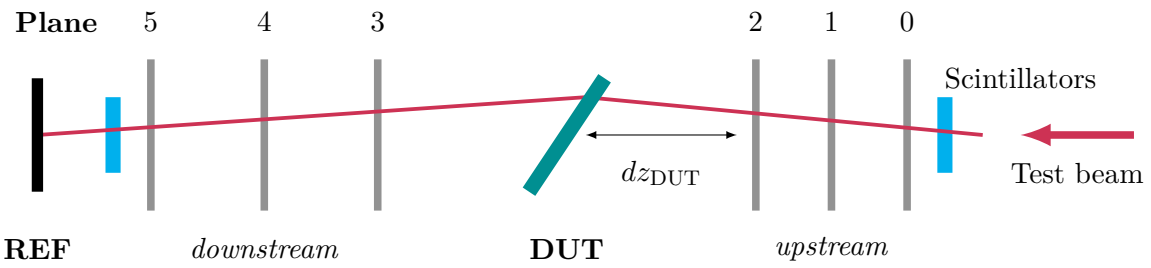

Figure 7.4: Geometry of a typical beam telescope, featuring six tracking planes, scintillators, and the device under test (DUT) between the upstream and downstream arms of the telescope. An additional timing reference detector is placed downstream of the telescope.

7.2 Beam Telescopes

The measurement of capabilities and characteristics of novel detectors such as tracking efficiency or intrinsic resolution requires external and unbiased reference measurements for comparison. These reference tracks can be provided by so-called *beam telescope* detectors mounted around the device under test (DUT). Most telescopes consist of several planes of well-known and characterized silicon pixel or strip detectors with good spatial resolution.

Usually, a telescope is divided into the *upstream arm* referring to the telescope planes mounted before the DUT, and the *downstream arm* which the beam passes only after traversing the DUT. Placing the novel detector as DUT in between the two arms of such a telescope as shown in Figure 7.4 allows to compare its measurements with the particle tracks reconstructed from the telescope data.

Beam telescope installations often comprise a full support system around the telescope itself, consisting of mechanics, beam triggers such as scintillators with PMTs, trigger logic, and the data acquisition system as well as additional hardware for cooling.

In the following, a right-handed Cartesian coordinate system is used to parametrize particle tracks and hit positions in the telescope reference frame. The z-axis is defined along the particle beam, the y-axis points upwards, and the x-axis points outwards from the DESY-II accelerator.

7.2.1 Pointing Resolution

The figure of merit for beam telescopes is the resolution of the reconstructed tracks since the pointing resolution enters the measured DUT residuals as described in Section 3.5. In order to extract the intrinsic resolution σ_{int} of the DUT, the track contribution in Equation 3.19 has to be evaluated.

The intrinsic detector resolution of the telescope sensors and the number of measurement points for the track, i.e., the number of telescope planes, play a predominant role. Due to the extrapolation of the track, also the telescope geometry influences the track resolution. In order to minimize the track extrapolation uncertainty, the DUT should be located as close as possible to the neighboring telescope planes, i.e., minimizing the distance dz_{DUT} indicated in Figure 7.4.

Depending on the beam energy, multiple Coulomb scattering in both the detector material and the surrounding air results in a non-negligible contribution to the overall track resolution and has to be taken into account. The RMS of multiple scattering through small angles is usually described by [15]

$$\theta_{\mathrm{ms}}^{\mathrm{RMS}} = \frac{13.6\,\mathrm{MeV}}{\beta cp} \cdot z\sqrt{\epsilon} \cdot (1 + 0.038 \ln \epsilon)\,, \tag{7.1}$$

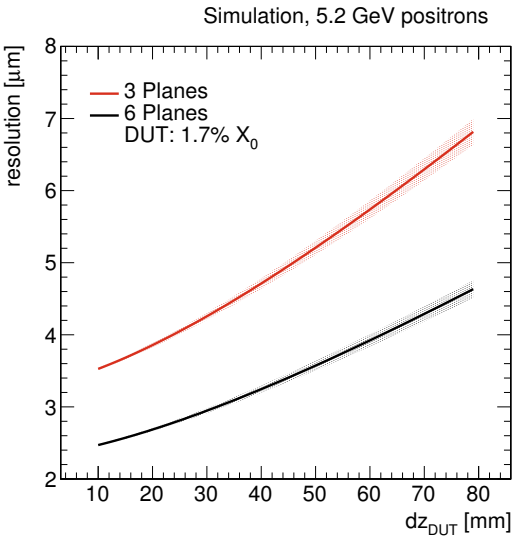

Figure 7.5: GBL pointing resolution of the DATURA telescope with three planes (DUT downstream) and 6 planes (DUT in the center) as a function of the DUT distance dz_{DUT}. The plane distance is $dz = 150\,\mathrm{mm}$. The calculations include scattering in the telescope planes, the DUT, and air. The hatched areas correspond to the resolution uncertainty assuming a beam energy uncertainty of $\pm 5\,\%$.

where p, z and βc are momentum, charge and velocity of the incident particle, and $\epsilon = x/X_0$ denotes the material budget in radiation lengths. The scattering impact of every telescope plane has to be taken into account, at low particle momenta also the air contributes significantly to the overall material budget.

The different contributions to the track resolution can either be estimated individually using geometrical factors for the telescope set-up as applied in [165, 166], or by building GBL trajectories with the measured telescope plane positions, the intrinsic telescope sensor resolution, and the scattering material in between.

The position resolution of the DATURA beam telescope described in the following section is shown in Figure 7.5 as a function of the DUT distance to the nearest telescope planes dz_{DUT} for different configurations. The red curve indicates the track pointing resolution at the DUT when considering the three upstream telescope planes only. This set-up can be beneficial in case of a high material budget present in the DUT installation such as cooling plates or printed circuit boards (PCBs). The black curve represents the track resolution with all six planes contributing to the track, the material budget of the DUT assembly including silicon sensor, front-end electronics and the PCB has been set to $1.7\,\%X_0$ as estimated for the CMS Pixel single chip modules (SCMs). Equation 7.1 has been used to estimate the width of the angular distribution for every scatterer considered.

The hatched areas correspond to the uncertainty of the track resolution at the position of the DUT assuming a spread of the beam energy of $\pm 5\,\%$ from the nominal value [161]. At a beam energy of 5.2 GeV and a distance of $dz_{\mathrm{DUT}} = 40\,\mathrm{mm}$ from the last upstream plane to the DUT, the six-plane telescope measurement yields a pointing resolution of $(3.25 \pm 0.05)\,\mu\mathrm{m}$ at the DUT position, while the extrapolated track of the upstream arm only results in a resolution of $(4.71 \pm 0.07)\,\mu\mathrm{m}$. Additional measurements and simulations of the pointing resolution for EUDET-type beam telescopes such as DATURA can be found in [166].

7.2.2 The DATURA Beam Telescope

The DATURA beam telescope available at Beamline 21 of the DESY Test Beam Facility is one of a few nearly identical telescopes built within the EUDET and AIDA programs [167, 168]. A detailed overview of the detectors, the mechanical setup and infrastructure as well as the measured pointing resolution can be found in [166].

DATURA is a six-planes pixel detector telescope featuring MAPS-type MIMOSA26 (M26) sensors produced in a 350 nm CMOS process with a pixel pitch of 18.4 µm × 18.4 µm. The pixel array comprises 1152 × 576 pixels and covers an active area of 21.1 mm × 10.6 mm [169]. The sensor is thinned down to a thickness of 50 µm to reduce the material budget, the charge carriers are collected from a 20 µm epitaxial layer by diffusion.

The detector is read out at a clock frequency of 80 MHz by a rolling-shutter mechanism, the total integration time amounts to 115.2 µs. The 16 clock cycles required for the readout of one sensor row allow for correlated double sampling (CDS) and zero suppression via the discriminators in the digital chip periphery. The CDS is performed by subtracting samplings of two successive frames in order to remove offsets in the pixel charge. The discriminator thresholds are configurable in four sectors of the sensor independently. Configuration files for all telescope planes with different threshold settings are provided, with the threshold value representing integer multiples of the RMS of the noise for the individual sensors. At a threshold level of 6, i.e., requiring the signal pulse height to be at least six times the noise RMS, the average noise occupancy at room temperature is about 6×10^{-5} per pixel [170]. The intrinsic telescope plane resolution at this threshold setting is about $\sigma_{\text{tel}} = 3.4\,\mu\text{m}$ [166].

The telescope setup is completed by a sturdy mechanical structure. The M26 sensors are mounted in aluminum jigs with a cut-out for the particle beam, and are protected from both sides by a 25 µm thin Kapton foil. A chiller using water as coolant maintains a constant sensor temperature of 18 °C for stable operation of the telescope. The jigs are mounted on rails which enable shifting of the individual telescope planes. Upstream and downstream arms can be moved independently to adapt to different DUT installations in the telescope center. A photograph of the DATURA beam telescope as set up in the DESY-II beamline 21 can be found in the Appendix, Figure A.1.

The total material budget of the telescope amounts to only 300 µm of silicon sensor material, and 300 µm of protective Kapton foil. This minimizes multiple scattering effects and thus makes the telescope optimally suited for measurements at test beam energies of a few GeV.

7.3 The Test Beam Setup

The device setup used in the presented test beam measurements consists of the DATURA beam telescope for reference track measurements, beam triggers, and two CMS pixel SCMs. The DATURA telescope has been described in detail in the previous section.

Four Hamamatsu PMT assemblies with plastic scintillators and light guides are used to generate trigger signals of beam particles traversing the setup. The scintillators are mounted pairwise before the first and after the last telescope plane, respectively. The overlap region of the scintillator pairs is designed such, that an approximately 10 mm × 10 mm large trigger window is formed. This acceptance window maximizes the yield of the CMS pixel DUT which is of similar size. By requiring a fourfold coincidence, the trigger acceptance can be confined to tracks traversing the full telescope.

The following sections detail the individual components of the setup: The DUT and timing reference (REF) detectors are described in Sections 7.3.1 and 7.3.2, respectively, while Section 7.3.3 details the trigger logic used to discriminate the PMT signals.

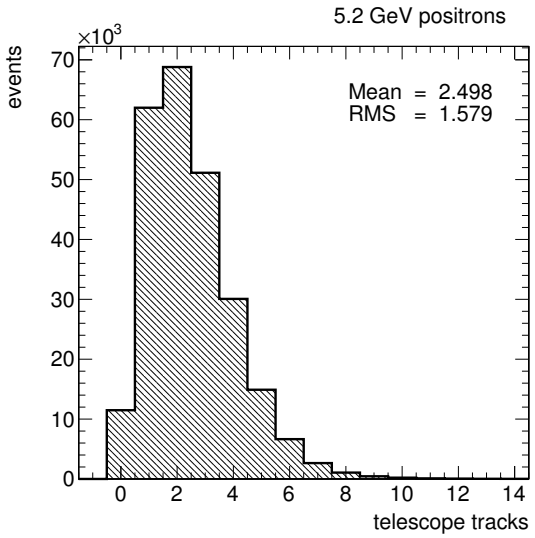

Figure 7.6: Track multiplicity in the DATURA beam telescope within one readout frame of the M26 sensors at a particle energy of 5.2 GeV.

7.3.1 DUT Installation

The DUT detectors are glued to small PCB carrier boards with edge connectors (cf. Appendix Figure A.2) which allow quick exchange of the samples to be measured. The carrier board is attached to the test beam single-readout chip (ROC) adapter shown in Appendix Figure A.3. The adapter card is mounted on a copper cooling block and is connected via a 68 pin ribbon cable to the DTB readout electronics.

The cooling block features a cut-out around the position of the DUT in order to reduce the material budget present in the beam. A cooling loop inside the block allows to circulate coolant from an ethanol-based chiller to stabilize the chip at room temperature or to run at the final detector operation temperature of −20 °C. The whole assembly is surrounded by a polyethylene cover which permits flushing with dry air to avoid condensation. This encasement features two cut-outs at the beam impact point which are covered by thin Kapton foils. For high-resolution measurements of unirradiated SCMs, the DUT is operated without the cover to further reduce the material budget and to facilitate a smaller distance to the upstream telescope plane. In this configuration, the chip is stabilized at a temperature of 17 °C.

The position of the DUT installation within the telescope can be controlled via micrometer precision x-y-stages which allow the correction of misalignments between DUT and telescope, and the optimization of the orientation relative to the beam. The DUT itself is mounted on a hinge and can be rotated by an additional stage which enables tilting of the sensor with respect to the beam axis for angular scans. The full assembly is depicted in Appendix Figures A.5 and A.6.

7.3.2 Timing Reference

The track multiplicity per event in the DATURA telescope is around 2.5 for a beam energy of about 5 GeV as exemplified in Figure 7.6. The actual track multiplicity fluctuates and depends on the beam energy, but also on other operational parameters of the DESY-II synchrotron such as the bunch filling. The high multiplicity is caused by the long integration time of the M26 sensors, which record further particles traversing the telescope after the trigger has been issued.

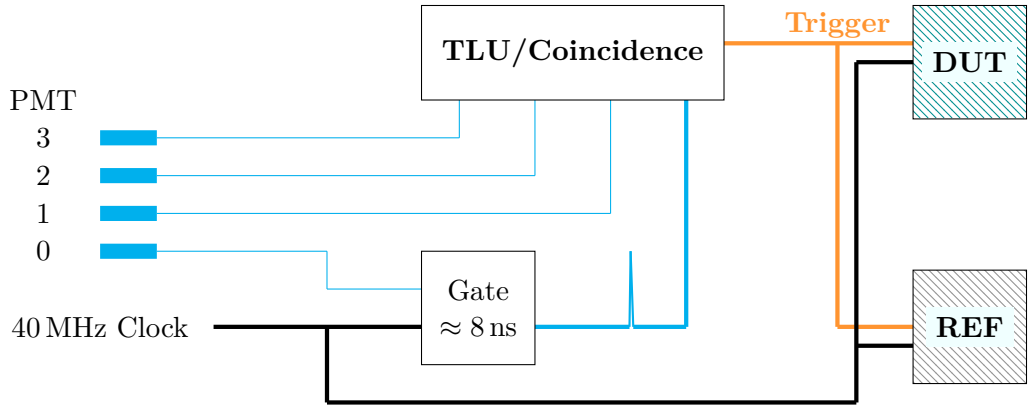

Figure 7.7: Diagram of the test beam trigger logic. One of the PMT signals is gated with the external 40 MHz clock to allow beam-synchronous operation of the detectors. The final trigger decision is based on both the gated and the direct PMT signals via a four-fold coincidence.

The CMS Pixel ROCs have a trigger window of 25 ns prescribed by the LHC clock and thus only record the particle which caused the trigger to be issued. Since the M26 sensors do not provide time-of-arrival information for the individual pixels, an external timing reference is required in order to select the correct track from the telescope to serve as tracking reference.

This tagging is rendered possible by the additional REF detector mounted downstream of the telescope as indicated in Figure 7.4. A second CMS Pixel SCM with the same timing characteristics as the DUT is used, and both are synchronized by operating them on the same externally generated 40 MHz clock.

For efficiency measurements, the telescope tracks are first matched with the REF detectors in order to select the particle within the correct time frame, before the selected tracks are compared to the measurements of the DUT. Since the independent REF measurements only reduce the total number of selected tracks but do not influence the efficiency measurement, no bias is introduced.

7.3.3 Trigger Logic

The trigger logic deployed in the test beams presented is based on the EUDET trigger logic unit (TLU) [171, 172] and additional NIM electronics. The TLU is a programmable trigger logic, based on a commercially available FPGA board and an additional, custom-made coincidence unit with four discriminator boards. It is responsible for generating and distributing the common trigger signal to all connected detectors, and to handle trigger veto conditions such as *busy* signals.

These busy signals can be used by the attached devices to temporarily veto triggers, e.g., during readout. The TLU implements a simple handshake which requires the `busy` to be raised and pulled down again after every trigger broadcasted. The Datura telescope uses the handshake to veto new triggers arriving during the M26 integration time. Fast devices such as the CMS pixel devices can be operated without the `busy` handshake as it can be switched off independently for every trigger output. Trigger and `busy` signals can be either exchanged via standard LEMO connectors with NIM or TTL signals, or as low voltage differential signal signal via the RJ45 connectors provided by the TLU. The latter also allow more sophisticated handshakes with additional information such as the current trigger number being clocked out on additional signal lines.

The TLU connects to a standard PC via the USB interface and enables remote configuration of discriminator inputs, coincidence masks, handshake modes, and the DUT trigger outputs. Furthermore, the triggering can be started and stopped via software which enables automated and synchronized run switch-overs and autonomous data taking, e.g., over night.

In the final deployment situation at the LHC, the CMS Pixel Detector is operated in beam-synchronous mode, running on the 40 MHz accelerator clock. At the DESY Test Beam Facility this is not possible since the 1 MHz clock of the DESY-II accelerator is permanently re-synchronized to the 50 Hz of the power grid before the injection of a new bunch. Generating a stable 40 MHz signal from the accelerator clock has proven to be a challenge due to these phase shifts. Instead another approach has been chosen. To ensure a trigger arrival time within the trigger window of the CMS Pixel ROCs at the beginning of the 25 ns clock cycle, the signal of one PMT is gated with the externally supplied detector clock as shown in Figure 7.7. The width of the gate is configurable and usually set to $6 - 12$ ns. This setup allows to effectively veto all triggers from particles arriving out-of-sync with the CMS detector clock.

7.4 Data Acquisition

The data recorded by the different detectors in the beam have to be collected, consolidated, and stored on disk for offline analysis. This is the task of the data acquisition (DAQ) system which comprises the readout electronics–PC interface for every detector as well as central components for control, storage, and the network interfaces of the different modules.

The Datura DAQ system consists of commercial off-the-shelf components [173] which receive the data frames from the M26 sensors. Data packets which have been marked by a trigger are selected, demultiplexed and the actual readout frames of the detector are built. The CMS pixel SCMs are controlled and read out using the DTB described in Section 6.1. A detailed overview of the integration and the different software components of the CMS Pixel DAQ system is given in Section 7.4.3.

In addition to the detectors, also the TLU provides a data stream containing the timestamps of every trigger issued. The TLU events contain the trigger time in ticks of the TLU-internal clock and the state of the four discriminator inputs, which allows to reconstruct which combination of the attached scintillators caused this particular trigger if no fourfold coincidence is requested.

Since all these devices and their control software run on different nodes in the network, a flexible, distributed DAQ software framework is required to unite the global DAQ control and data streams of all detectors. This framework will be presented in the following sections.

7.4.1 The EUDAQ Data Acquisition Framework

EUDAQ is a modular, cross-platform DAQ framework originally developed for the EUDET telescope project [158] but deployed in many detector R&D activities. The independent framework modules can be executed on different machines, the communication is established over an Ethernet network via TCP/IP connections. Thus, the DAQ network can be flexibly configured which is important for test beams where users and detectors change frequently. A typical EUDAQ network is depicted in Figure 7.8.

In contrast to other solutions existing, EUDAQ has been tailored for test beam measurements and is thus designed to allow easy integration of user DUTs. All important components of a full-featured DAQ system are available, but the inter-process communication library is kept abstract and as simple as possible. The integration of new devices only requires the implementation

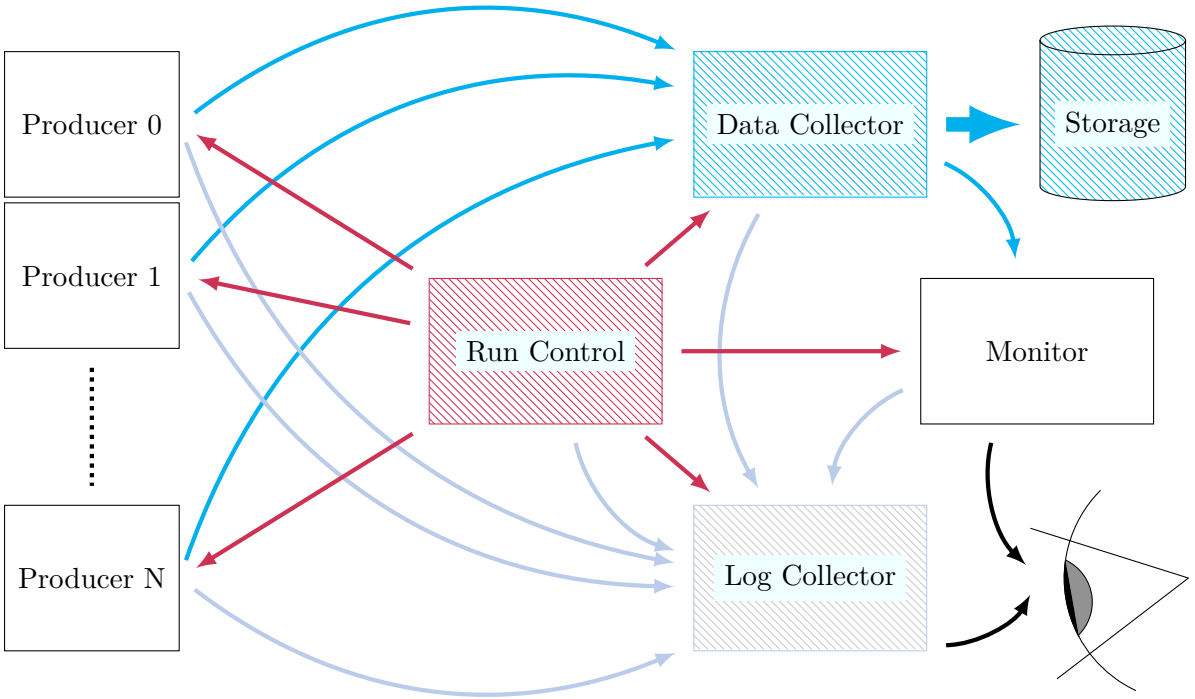

Figure 7.8: Typical components of a EUDAQ network. The Run Control is the central command and control server, the Data Collector builds global events and stores them to disk. The Log Collector handles and displays log messages while the monitor application allows online data quality monitoring.

of a standardized interface between the EUDAQ library and the preexisting control and DAQ software of the detector.

The central component in the DAQ system is the Run Control (RC) which hosts the communication hub and keeps track of all connections to other EUDAQ modules. Every new module in the network registers with the RC, provides its status and receives commands and additional information such as addresses of other relevant modules or configuration parameters. Furthermore, the RC is the central interface to the user. Both graphical user interface and command-line based interfaces are available and provide additional features such as automated run transitions.

The Log Collector gathers and displays all log messages emitted within the EUDAQ network. Several severity levels are available for log messages, the display can be filtered and searched. All log messages broadcasted are collected and stored in a log file.

All detector hardware is controlled and read out by so-called Producers. These user-provided executables assume control over the attached electronics and interface with the EUDAQ library which provides them with the communication infrastructure. In order to be manageable by the RC, producers have to implement a defined set of commands which are invoked, e.g., upon run start or configuration.

Merging event data from several detectors attributed to the same trigger is referred to as *event building*. In EUDAQ the event building process is performed online during data acquisition by one or several Data Collector nodes, the receiving ends of the data streams from all producers. Internal derandomize buffers cache events from every detector until all producers delivered data and the next global event can be built. In addition, basic sanity checks on the event data are preformed such as cross-checks of the event serial number. No data processing or decoding is conducted prior to storage. The raw detector data as delivered by the individual producers are wrapped in a EUDAQ detector event indicating the data type contained, and stored to disk. This preserves as much information as possible and makes the DAQ process and the test beam measurement as a whole less susceptible to potential peculiarities of the software.

EUDAQ is designed as synchronous DAQ system which expects to receive one event per trigger from every detector present in the system. The advantages of such systems are straight-forward event building and online data quality monitoring, but the trigger rate is limited by the slowest device. Future versions of EUDAQ will provide the possibility of recording asynchronous data streams with offline event building.

The configuration parameters for all EUDAQ network components are stored in a central configuration file which is parsed by the RC. The file is subdivided into sections for every module and includes EUDAQ internal parameters such as destination file names for the detector data, but also the detector-specific configurations for every producer. The relevant parameters are distributed over the network to the respective modules and are also stored in the header section of the begin-of-run event (BORE) in the binary data file for later reference.

Stable Software Releases

Due to the wide application of EUDAQ as DAQ system, it is of importance to maintain the software and to provide continuously tested, stable versions. Bug-fixes, improvements and new features have to be carefully reviewed and tested before release in order to avoid delays, data loss or corruption during the precious test beam time.

As part of this thesis, the framework has been ported to the modern version control system *git* and a continuous integration with automated nightly builds has been set up. A stable development

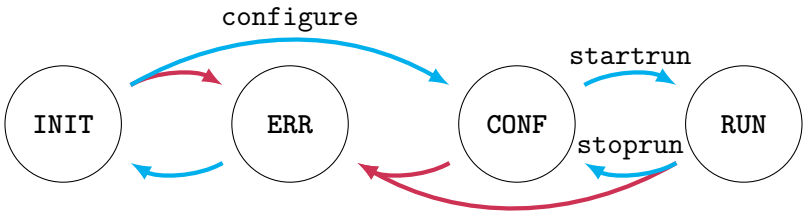

Figure 7.9: States and transitions of the EUDAQ finite-state machine. The `INIT` is the initial state of all modules. The `configure` transition switches to `CONF`, `startrun` and `stoprun` set the system in running mode and back. In case of an error, the FSM transits to the `ERR` state.

branch is now actively maintained, and a continuous release cycle has been introduced with frequent stable point releases containing bug-fixes and corrections.

Code contributions from EUDAQ users are now collected via git and are reviewed before merging them into the main software repository. The changes have been received well and several new producers have already been contributed to the framework, further extending the range of EUDAQ applications.

The EUDAQ Finite State Machine

A finite-state machine (FSM) has been implemented into the EUDAQ RC as part of a Summer Student project [174]. FSMs are abstract machines defined by a finite number of well-defined states. The machine can only occupy one state at a time. Changes from one state to another are called *transitions* and are triggered by external events or conditions. FSMs are widely used in DAQ systems since they allow to control and accurately alter the state of a complex system.

The EUDAQ FSM design shown in Figure 7.9 is rather simple with a limited set of states to maintain the low complexity of DUT integration. The four states are `INIT`, `CONFIGURED`, `RUNNING`, and `ERROR`. All new EUDAQ modules connecting to the RC are in the `INIT` state. The `configure` transition switches the state to `CONFIGURED`, in which all producers have received their configuration parameters and have established communication with their respective hardware components. The `startrun` and `stoprun` transitions set the system into the `RUNNING` mode where data are recorded, and back to the `CONFIGURED` state, respectively. Whenever an error is reported from any EUDAQ module, the FSM transits into the `ERROR` state, which can only be cleared via the `INIT` state and a re-configuration of the modules.

This FSM allows to effectively catch exceptions like additional producers being connected to the RC after the device configuration. Without the FSM it would be possible to start a run without this additional device being properly configured. Since the newly connected device is still in the `INIT` state, the FSM blocks the `startrun` transition for the system until all producers have been configured.

7.4.2 Data Quality Monitoring and Correlations

The possibility of monitoring the data quality during the process of recording is vital to any complex DAQ system which combines independent detectors. This is of course especially true for test beam measurements which usually involve one or more detectors and front-end electronics which are still in their R&D phase.

Within the EUDAQ framework, the Online Monitor tool is available to serve this purpose. It allows to verifying the performance of detectors by providing a set of continuously updated

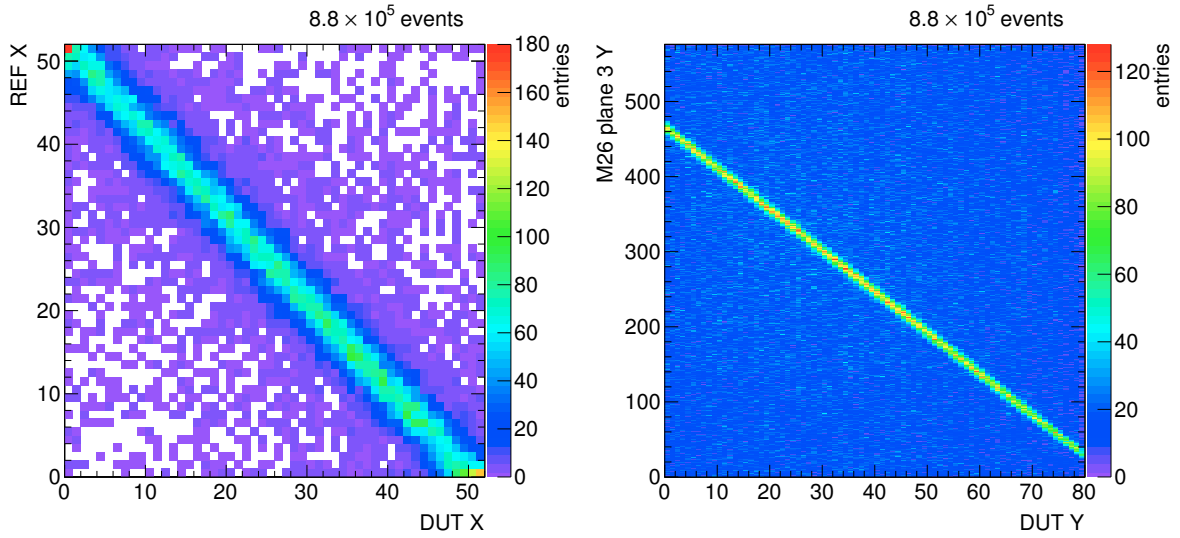

Figure 7.10: Online correlation plots in units of pixels for the DUT with the CMS pixel reference plane (left) and the first downstream M26 plane (right) in x and y, respectively. Both plots show an anti-correlation since the DUT is mounted upside down. Off-diagonal entries originate from random hit combinations.

control distributions. The time synchronization as well as the relative spatial alignment of the different devices can be monitored using correlation histograms.

Correlation histograms are a powerful tool since they contain a vast amount of information despite their simplicity. When plotting the same coordinate of two devices in the setup against each other, the relative alignment of the devices in both time and space can be inferred from the structure in the histograms. A uniform distribution of entries indicates that the correlated devices are running asynchronously, e.g., due to a missed trigger, and the event builder merges non-associative detector events. If the devices are running synchronously, diagonals such as the ones shown in Figure 7.10 indicate the correlation in time, while the features of these diagonals represent the relative spatial orientation of the detectors. Shifts of the diagonal at a constant slope represent a relative shift in the respective coordinate, while different slopes indicate a relative rotation of the two devices. The magnitude of these misalignments can be directly inferred from the correlation histogram if the pixel pitch is known.

The Online Monitor uses the internal converter plugins of the EUDAQ library to decode the raw detector data and thus does not rely on additional integration effort from the user. It connects to the RC process during the data acquisition and requests a fixed fraction of global events from the Data Collector for inspection as indicated in Figure 7.8. Alternatively, it parses EUDAQ data files directly in offline mode and decodes the contained detector data. The ROOT framework [175] is used as underlying plotting framework, and all monitoring plots can be saved to disk as ROOT files.

7.4.3 The CMS Pixel DAQ System

The DAQ system for CMS Pixel SCMs and modules has been fully integrated into the EUDAQ framework using the pxarCore library described in Chapter 6, a first approach to the integration had been implemented as part of a Summer Student project [176]. The EUDAQ module has been merged into the main repository, and CMS Pixel modules and SCMs are available as EUDAQ

DUT since the release of EUDAQ v1.4.5. The integration comprises both the CMSPixelProducer establishing the connection to the DTB, and the appropriate converter plugins to translate the raw detector data.

All functions provided by pxarCore are supported, including the operation of a variety of PSI46 devices such as the production-version PSI46digV2.1-r ROC, analog PSI46V2 ROCs, or custom-built beam telescopes using several PSI46 ROCs as telescope planes. Also beam telescopes with several CMS Pixel modules, featuring 16 ROCs each, have been operated successfully as described in Appendix D.

At configuration stage, the CMSPixelProducer implements many consistency checks for the supplied parameters, including hardware tests such as the presence of clock signals at the DTB. Error messages and exceptions are transmitted to both the RC and the Log Collector which allows to identify an improper detector configuration before attempting to start the actual run. Important parameters for offline interpretation of the data such as type and number of ROCs as well as the TBM type and DAC settings are written into the BORE header.

Log messages inform about the configuration and status of the system. During the runs, the event yield for every detector is calculated as total average and running average of the last one thousand triggers. The event yield is the fraction of events that contain at least one pixel hit over the total number of events, and can be used as immediate feedback on detector parameters such as the trigger window delay relative to the triggered particle. At the end of the run, the total event yield is sent to the Log Collector and thus stored in the log files for later reference.

The converter plugins automatically pick the correct settings for data decoding from the BORE header. When operating full modules with a TBM and multiple ROCs configured, the plugin assembles all ROC data to a module-like pixel plane for both online monitoring and conversion to other formats. The accumulated decoding statistics are printed when the end-of-run event is received.

The documentation of the CMS pixel integration into the EUDAQ framework including all configuration parameters is published separately from this thesis and can be found in [156].

7.5 Offline Track Reconstruction

The particle tracks have to be reconstructed from the raw detector data of the beam telescope in order to be used as reference for DUT studies. In the following, the pattern recognition and reconstruction of the telescope reference tracks is detailed, using the algorithms described in Section 3.3. The analysis of the DUT itself is covered in Chapter 8.

The EUTelescope software [177] is employed to perform most of the reconstruction steps converting the raw data into high-level objects. EUTelescope is a modular software framework based on ILCSoft [178] and using Marlin [179] as event processor. The LCIO data model [180] is used to store the reconstructed objects.

The workflow within the EUTelescope framework is highly modular and customizable with every process being implemented separately. The complete reconstruction chain is compiled by arranging several of these processors and handing over the data collections from one to the other. The chain is configured by providing XML steering files which describe the parameters as well as input and output collections of every processor. Marlin parses these files and hands the data to the processors event by event.

The following sections briefly describe the telescope track reconstruction employed for the DUT analysis presented in this thesis.

7.5.1 Job Submission to Computing Clusters

Varying beam conditions, telescope geometry, and detector setups make changes of the analysis configuration a necessity. To facilitate this task EUTelescope provides a flexible Python job submission tool called `jobsub`. It parses XML steering templates and substitutes placeholder variables with values either read from a central configuration file or from a run database. The run database is a simple comma-separated CSV file which can hold any number of parameters, with their names defined by the header line. The first parameter has to be the run number as it is used to identify the corresponding database entry.

`jobsub` allows to run single jobs and accepts lists or ranges of run numbers to be processed. The final steering files created by `jobsub` contain all parameters necessary for the processors, and the reconstruction is started by executing Marlin with the steering file as parameter.

During this thesis, `jobsub` has been extended to allow direct submission to the computing clusters NAF at DESY and LXPLUS at CERN. This greatly simplifies batch processing of large data sets and enables parallel analysis of many test beam runs within minutes. For both clusters, an additional configuration file has to be provided containing the batch submission parameters for the job to be submitted. Sample configurations have been submitted to the EUTelescope repository.

7.5.2 Clustering and Hot Pixel Suppression

The Datura telescope raw data are decoded and converted to LCIO using the EUDAQ converter plugins. In order to suppress hot pixels of the M26 sensors, the firing frequency of all pixels is calculated from the first few thousand events. Pixels exceeding the frequency threshold of 1 % are marked as hot. Due to the large number of readout channels and the limitation to four configurable threshold regions, typically between 50 and 100 pixels per sensor, i.e., less than 0.2‰, are considered as hot.

The hot pixels are not immediately removed from the data collections but only after clustering. The clusters are formed by a sparse pixel clustering algorithm connecting all adjoining pixel hits. Due to the lack of pulse height information from the binary M26 readout, a simple geometrical interpolation of the cluster center is performed.

Clusters containing a pixel flagged as hot are now removed from the data collection. By removing the full cluster the possibility of introducing a bias on the cluster position and thus on the track resolution is excluded. Only the telescope tracking efficiency is affected, but this is of no concern for a DUT analysis where inferior telescope tracking efficiency would only reduce statistics.

The interpolated cluster positions are translated from the local on-sensor coordinates into the global telescope reference frame using the GEAR geometry description provided in the steering file. These space points are referred to as *hits*.

7.5.3 Telescope Alignment

The relative position of the telescope sensors has to be aligned since the geometry description and mechanical alignment is not sufficient for high resolution tracks. The applied software alignment algorithms are described in Section 3.4. The DUT and REF detectors are excluded from the telescope alignment procedure. For maximum precision a two-step procedure is used.

As first step, a simple pre-alignment based on the residual method is performed. The hits in x and y of all neighboring telescope plane combinations are correlated, and the resulting residual distributions are shifted to minimize the means. This pre-alignment only corrects for shifts

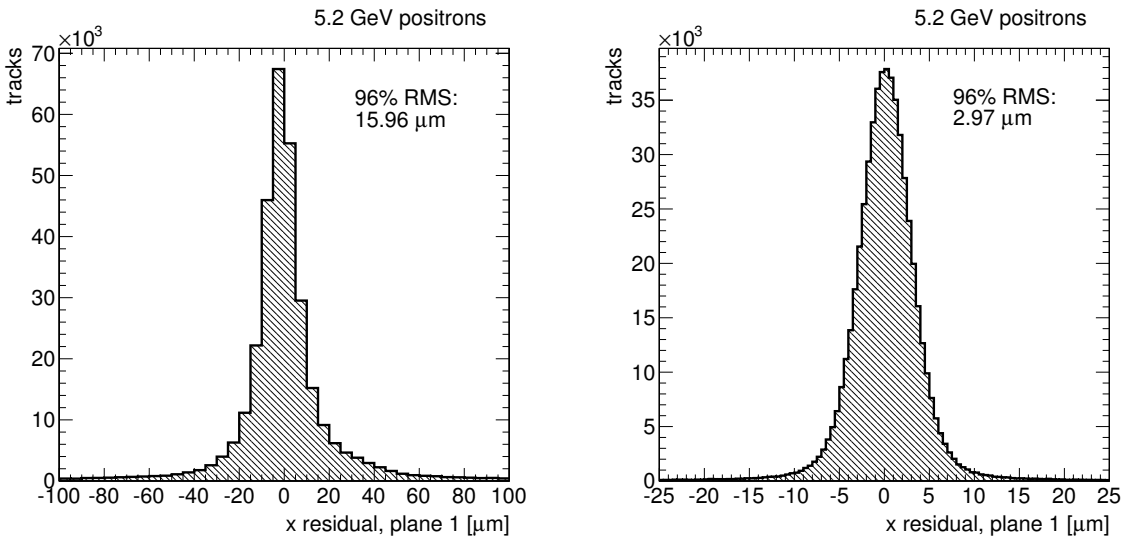

Figure 7.11: Triplet residuals of telescope plane 1 after pre-alignment (left) and alignment (right). Shown are the biased track residuals as obtained from the GBL trajectory fit.

in these two coordinates, and the precision of the algorithm is of the order of a few hundred micro meters. The main effect is the correction of global misalignments like rotations of the full telescope with respect to the beam, but the selection of track candidates and track fitting already benefits from these rough shifts. The residual distribution after prealignment is exemplified for telescope plane 1 in Figure 7.11 (left).

The second iteration requires full telescope tracks to be reconstructed. This procedure is described in the following section since it is the same method as applied for the final track reconstruction after alignment. The selected telescope tracks are collected and delivered to the Millepede-II (MP-II) algorithm which minimizes the global χ^2 and returns the alignment constants for each plane. Only the three parameters x, y, and sensor plane rotation around z are considered in the telescope alignment. The fit of the remaining three parameters is as well possible but unnecessary due to the reduced sensitivity in z for geometric reasons, and the tight constraints imposed by the telescope mechanics.

In order to constrain weak modes, the first and second telescope plane are fixed in their initial positions. The two planes have been selected due to the additional scattering material from the DUT installation present between the two telescope arms. Selecting a downstream plane to be fixed would affect the alignment precision, while a difference in alignment precision between selecting the first and second or the first and third plane cannot be observed.

By applying the MP-II alignment procedure, the width of the track residuals can be greatly reduced, yielding a track pointing resolution of a few micron as shown in Figure 7.11 (right).

7.5.4 Tracking

A track in the Datura telescope is required to have exactly one hit in each of the six planes. The initial track candidate is built from track triplets formed independently in the upstream and downstream arms of the beam telescope (cf. Section 7.2). These track candidates with their initial residuals in each plane are then fitted using the GBL algorithm described in Section 3.3.2.

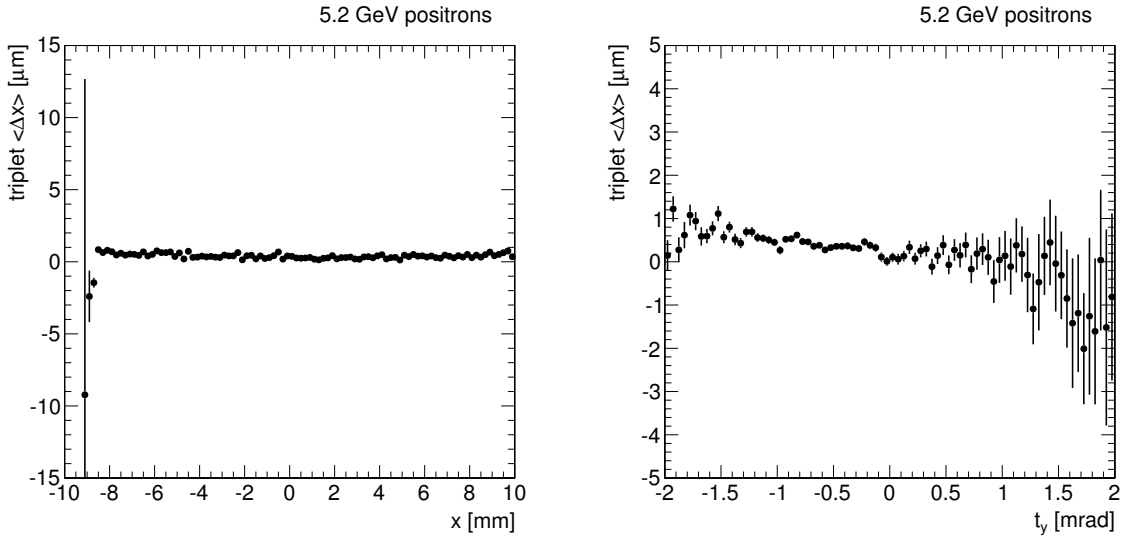

Figure 7.12: Triplet residual at telescope plane 1 as function of the triplet impact position in x (left) and the triplet slope t_y in y (right). Neither of the distributions show a significant dependence which would indicate a remaining telescope plane misalignment.

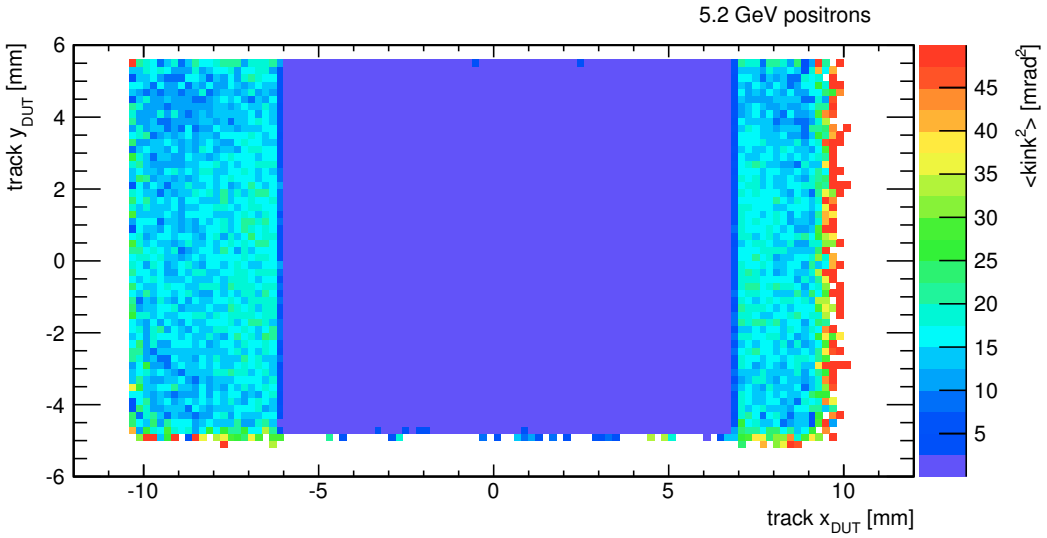

Figure 7.13: Average track kink angles at the z position of the DUT installation. The cut-out in the copper cooling block is clearly visible. The DUT is mounted in the central part with low material budget.

Triplets in the upstream telescope arm are formed by first only regarding hits in the telescope planes 0 and 2. For all possible hit combinations, the straight line connecting the two measurements is interpolated at the position of telescope plane 1. If a matching hit on plane 1 can be found within 200 µm of the interpolated impact point, the hit combination is accepted as track triplet. By correlating the residual distributions with the triplet impact point or slope, the telescope alignment can be confirmed as shown in Figure 7.12.

The same procedure is repeated for telescope planes 3 and 5, which require a matching hit in plane 4 within the same distance to the triplet candidate of 200 µm in order to be accepted as downstream triplet.

The two sets of triplets are then extrapolated to the nominal position of the DUT in the center of the telescope, and all combinations of upstream and downstream triplets are compared for possible intersection with two different matching scenarios available. For **tight telescope tracks**, the matching cut for triplet pairs is set to 100 µm, while **loose telescope tracks** only requires the two triplets to intersect within 300 µm. If an intersection point can be found, the triplet pair is accepted as track candidate. From the relative angles between up- and downstream triplets an estimate of the track kink angle and thus the material budget of the DUT installation can be made as shown in Figure 7.13. Here, the squared kink angle is defined as

$$\text{kink}^2 = \alpha_x^2 + \alpha_y^2,$$

where $\alpha_{x,y}$ denotes the kink angle between the upstream and downstream triplet in the x-z (y-z) plane at the position of the DUT.

GBL trajectories are built from the six track candidate measurements, while the upstream triplet is used as track seed. In addition to the actual measurements, scattering material for the telescope planes as well as the DUT are introduced to correctly account for multiple Coulomb scattering. Finally, the trajectory fit is performed by the GBL algorithm and the resulting track can be used as reference measurement to determine the DUT efficiency and resolution.

8. Qualification of the Phase I Readout Chip

The redesigned readout chip (ROC) is a key component of the Phase I Pixel Detector Upgrade, and its functionality, operational reliability, and performance are of paramount importance. The characteristics of every design iteration of the chip have been thoroughly tested at the DESY-II Test Beam Facility using the DATURA beam telescope as tracking reference. The tests provided valuable feedback to the chip designers and allowed to promptly identify design flaws and unexpected issues which were subsequently corrected for the final chip revision. In addition, the precision measurements allow to determine the behavior of the chip in a particle beam, and operational parameters, corrections, and expertise can be obtained from analyzing the test beam data.

This chapter describes the full data analysis including calibrations, corrections, and alignment procedures. The results obtained from the comprehensive studies performed for the final production version PSI46digV2.1-r of the ROC are presented. Similar measurements have been performed for the PSI46V2 ROC and sensors of the present pixel detector [181–183], and some results from the DESY-II test beams for prototype versions of the chip have been presented elsewhere [184, 185]. However, the new DAQ system described in Section 7.4.3 as well as the quasi-stationary setup at the DESY-II test beams allow for more extensive studies and user-friendly operation.

The chapter is structured as follows. Section 8.1 introduces the devices characterized and describes general conventions used throughout the chapter. The electrical pre-calibrations performed for the DUTs in the laboratory prior to the test beam measurements are described in Section 8.2. Section 8.3 details the cluster and hit reconstruction as well as the detector alignment, while the event selection criteria are introduced in Section 8.4. Statistical and systematic uncertainties on the performed measurements are discussed in Section 8.5, and control plots comparing data and simulation are presented in Section 8.6.

The results presented in this chapter are arranged in three sections. Measurements of the ROC tracking efficiency are presented in Section 8.7. Section 8.8 discusses intra-pixel effects such as efficiency or position resolution as a function of the track impact position within single pixel cells. The measurement of the spatial resolution of the ROC and the dependencies on the different chip orientations as well as the pixel threshold is presented in Section 8.9. Finally, the findings are summarized in Section 8.10.

8.1 Samples and Naming Conventions

Two samples have been used for the test beam studies presented in this chapter, both feature an unirradiated *gap30*-design single chip sensor (cf. Section 4.1) and the final PSI46digV2.1-r version of the ROC. The ROCs are thinned to about 170 µm thickness, the sensors have been measured to have a thickness of (285 ± 4) µm. Owing to constraints of the DUT mechanics described in Section 7.3.1 which only allows for rotation around one axis, the second single chip module (SCM) is mounted on a carrier rotated by 90°. This allows to study the sensor and chip properties in η (along rows) as well as in $r\phi$ direction (along columns). The two assemblies are shown in Appendix Figure A.4 and have been bump bonded, glued, and wire bonded at the DESY Phase I Production Center, and underwent the full qualification procedure described in Section 6.3. A pixel threshold of 1.7 ke (SCM 504) and 2.0 ke (SCM 506) is applied.

The following naming conventions will be used throughout the chapter. Unless otherwise noted, the local on-sensor coordinates x and y are synonymous for the row and column directions, respectively. The tilt angle α always denotes a rotation around the row axis, hence long clusters crossing several rows are produced and the row resolution along the 100 µm pixel pitch is measured. Whereas the angle ω indicates rotations around the column axis, and the column resolution with a pixel pitch of 150 µm is measured. Angles are always given relative to an incidence perpendicular to the sensor surface.

The so-called angle of *optimal charge sharing* is deduced from geometrical considerations. Exclusively two-pixel clusters are produced, if the particle crosses two pixel cells at an angle determined by the pixel pitch and the sensor thickness following the relation

$$p = \tan(\gamma)\, t, \tag{8.1}$$

where γ is the track incidence angle, t denotes the sensor thickness and p the implant pitch. Hence, for a pitch of $p = 150$ µm, the optimal charge sharing occurs at the track incidence angle $\omega \approx 27°$, assuming the nominal sensor thickness. For a pixel pitch of $p = 100$ µm, the optimal charge sharing is to be expected around $\alpha \approx 19°$.

The width of residual distributions is fitted using the generalized error function given in Equation 3.21, while in some cases the mean absolute difference (MAD) is employed for the sake of convenience. Cluster charge distributions are fitted using the Landau function convolved with a Gaussian distribution as will be described in Section 8.3.1.

8.2 Electrical Calibration, Trimming, and Operation Parameters

Trim parameters for several target thresholds have been determined to allow studies of e.g., spatial resolution as function of the pixel threshold as presented in Section 8.9.3. Gain calibrations for each of the threshold settings at different temperatures have been recorded since the ADC response is sensitive to temperature changes. The chips are either operated at room temperature or temperature-stabilized at 17 °C using the ethanol chiller (cf. Section 7.3.1).

Instead of the standard hyperbolic tangent fit for the pulse height response, a cumulative Weibull distribution [186] is used as it better describes the pulse height saturation. The cumulative distribution function is defined as

$$f(x) = p_4 + p_3 \left(1 - \exp\left(-\left|\frac{x - p_0}{p_1}\right|^{p_2}\right)\right), \tag{8.2}$$

with five free fit parameters p_0–p_4. The fit parameters obtained for every single PUC are stored in the calibration database and retrieved at reconstruction of the data where the ADC value of every pixel is translated to VCal units using the Weibull inverse function.

Pixels which exhibit an elevated hit rate in the test beam are not masked but their trimming is altered manually in order to slightly increase the charge threshold. This procedure is called *re-trimming* and has become a standard operation in the module testing procedure.

The WBC register is optimized in the test beam to match the trigger configuration described in Section 7.3.3. The value is chosen to roughly match the values to be expected in the CMS experiment, additionally required delays are compensated with the respective settings of the DTB [156].

The CMS Pixel SCMs are operated with a sensor bias voltage of $U = -200\,\mathrm{V}$ provided by a Keithley laboratory power supply. The analog (V_a) and digital (V_d) chip supply voltages from the DTB are set to $V_\mathrm{a} = 1.8\,\mathrm{V}$ and $V_\mathrm{d} = 2.6\,\mathrm{V}$, respectively. The full set of registers and DAC parameters for the DUT samples measured can be found in Tables B.1 and B.2 in the Appendix for reference.

8.3 Reconstruction

The particle impact point and the deposited charge in the CMS Pixel sensor have to be reconstructed from the raw detector data containing the encoded pixel addresses and the ADC charge information.

Decoding of the raw detector data is performed by the EUDAQ converter library as described in Section 7.4 at the same stage at which the telescope data are decoded. While the telescope tracks are reconstructed in the subsequent processing steps (cf. Section 7.5) the CMS Pixel chip information is stored as pixel coordinates with the original ADC value until the reference tracks are fully reconstructed and the telescope planes aligned.

Only for the final DUT analysis, the data from the CMS Pixel SCMs are clustered, aligned and matched with the telescope reference tracks. The following sections describe in detail the different steps of the reconstruction necessary to obtain three-dimensional space points with charge information in electrons from the raw pixel data, which subsequently can be analyzed. This involves several corrections to the data in order to account for systematic effects in the chip unveiled during the analysis, and comprises clustering and cluster center determination as well as detector alignment relative to the telescope.

8.3.1 Pixel and Cluster Charge Calibration

The CMS Pixel ROC provides 8 bit charge information for every single pixel via its internal ADC in the periphery (cf. Section 4.2). A typical ADC spectrum is shown in Figure 8.1 (left) with the noise of the lower ADC bits clearly visible as spikes in the spectrum. The noise pattern is unique per ROC but stays constant over time and is insensitive to temperature changes.

The pixel charge information is converted to internal VCal units by applying the inverse of Equation 8.2, viz.

$$x_\mathrm{vcal}\left(f_\mathrm{adc}\right) = p_0 + p_1 \left(-\ln\left(1 - \frac{f_\mathrm{adc} - p_4}{p_3}\right)\right)^{1/p_2}, \tag{8.3}$$

with the five parameters p_0–p_4 recorded for every pixel cell as described in Section 8.2. This calibration is temperature dependent and multiple sets of calibrations have been recorded at the different operating temperatures in order to match the respective ADC response.

The conversion factor from internal VCal units to electrons deposited in the sensor is uniform over the whole ROC but also varies with temperature. The absolute charge calibration relating VCal and electrons can be performed using X-ray measurements as described in Section 6.3.3,

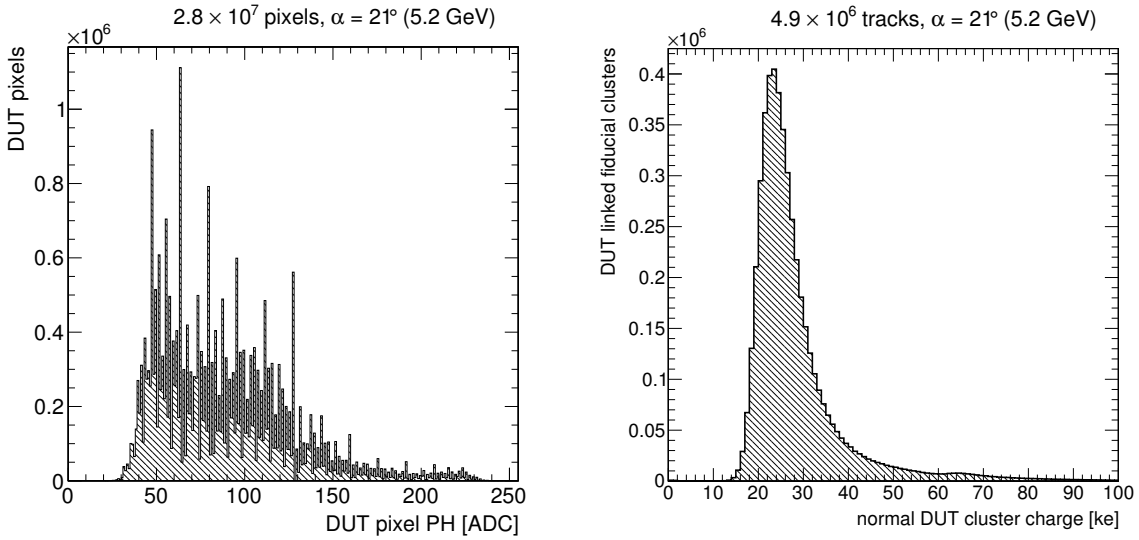

Figure 8.1: ADC distribution before calibration into VCAL units and electrons (left). The ADC noise is visible as spikes in the spectrum. Cluster charge distribution normalized to vertical track incidence (right). Shown are only DUT clusters in the fiducial volume which have been matched with a telescope reference track.

but a different method has been chosen for this analysis. The absolute charge calibration is obtained from simulation. The convolved Landau-Gauss distribution

$$f(x) = \frac{1}{\sqrt{2\pi}} \frac{p_2}{\sigma p_1} \int_{x_0-5\sigma}^{x_0+5\sigma} \text{Landau}\,(x, p_0, p_1) \times \text{Gauss}\,(x, x_0, \sigma)\, dx \tag{8.4}$$

is fitted to the cluster charge spectrum presented in Figure 8.1 (right). Here p_0 denotes the most probable value (MPV) and p_1 the width of the Landau distribution. The term p_2 is the total area for normalization, and σ represents the smearing parameter as width of the Gaussian distribution. The convolution extend is set to $\pm 5\sigma$ of the Gaussian distribution. The conversion factor is chosen such that the MPV of the cluster charge distribution matches the value obtained from fitting the same distribution to the simulation described in Chapter 5, and the Landau MPV is calibrated to 22 ke for vertical track incidence. An example for the final calibrated cluster charge distribution is shown in Figure 8.1 (right) for SCM 504, normalized to vertical track incidence.

This procedure is repeated for every new set of runs taken in order to account for temperature differences. If no data at vertical incidence are available, the cluster charge is normalized to vertical track incidence after the alignment has converged, using the relation

$$Q_0 = Q \cos\alpha \cos\omega, \tag{8.5}$$

where Q is the total cluster charge while α and ω are the Euler alignment angles described in Sections 8.3.5 and 8.3.6. A weak dependence of the normalized Landau peak value on the track incidence angle and thus on the total path length of the particle in the sensor has been found (cf. Appendix B). Thus, instead of using the MPV from simulation with vertical incidence, the normalized cluster charge from a simulation run with the same angle as found from alignment is taken as comparison.

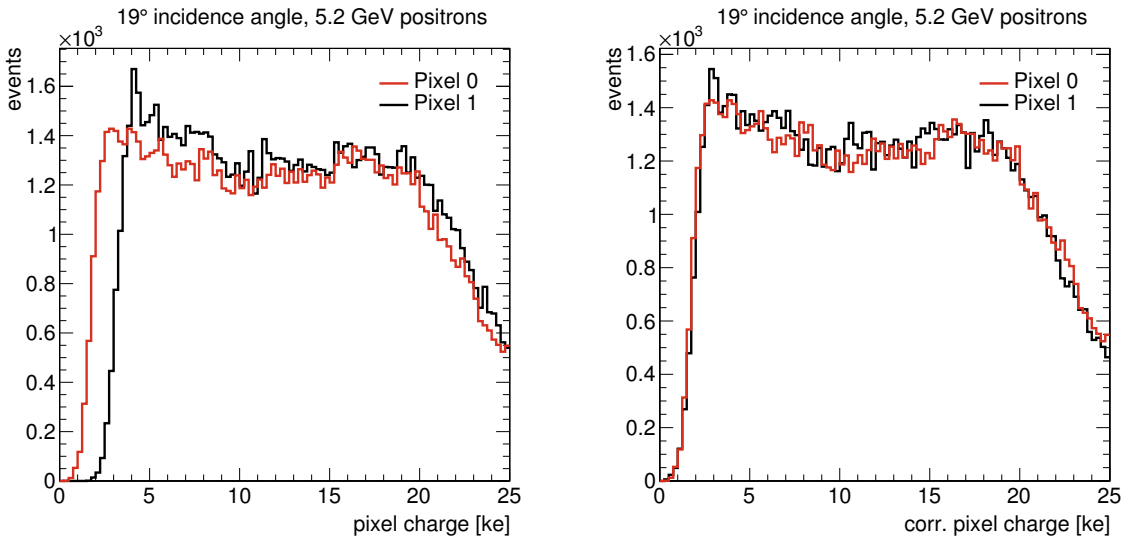

Figure 8.2: Charge distributions for the first and second pixel in two-pixel clusters only. Here, *first* refers to the readout order of the pixels. Shown in the calibrated charge distribution before (left) and after (right) the ADC correction.

8.3.2 Charging Effects in the DCol Transmission

When regarding the charge spectra of individual pixels a distinct effect can be seen. In Figure 8.2 (left), the two pixel charges from events only containing single two-pixel clusters are plotted, separating the pixel which has been read out first and last, according to the token flow described in Section 4.2.2. The left edge of the spectrum representing the pixel threshold is clearly shifted for the second pixel. The effect can be mitigated as shown in Figure 8.2 (right) by shifting the ADC value before performing the VCAL calibration. Here, every pulse height for the second pixel has been corrected by

$$f_{\text{adc}}^{\text{corr.}} = f_{\text{adc}} - 3.8 \tag{8.6}$$

to shift the distribution such that the two threshold edges match. The correction factor has been obtained from test beam data matching the spectra of the first and second pixel of two-pixel clusters as shown in Figure 8.2. These pixels are chosen as they are expected to exhibit very similar spectrum shapes due to symmetry, which facilitates the direct comparison. The shape of the corrected distribution changes slightly, since the correction is applied at the level of ADC values, before the conversion to electrons described in the previous section.

In order to evaluate whether this is an effect carried from one pixel to the next (memory or *tsunami* effect) or only introduces a constant offset starting from the second pixel in the token chain, the center pixels of four-pixel clusters are regarded as shown in Figure 8.3. The center pixels are chosen out of symmetry considerations for providing similar spectra. No difference in the threshold edge or spectral shape is visible before the correction. Thus, the effect constitutes a constant shift starting from the second pixel of every event. The spectral shapes are also presented after the correction of the charging effect for reference.

Since all gain calibration procedures are implemented such, that only a single pixel per event is calibrated and read out, the calibration is recorded for the lower ADC values. In events with multiple pixel hits, all pulse height values but the first have to be corrected in order to match the gain calibration constants. The source of this shift has been identified as charging of the pulse height transmission line from the double column (DCol) buffers to the ADC [187].

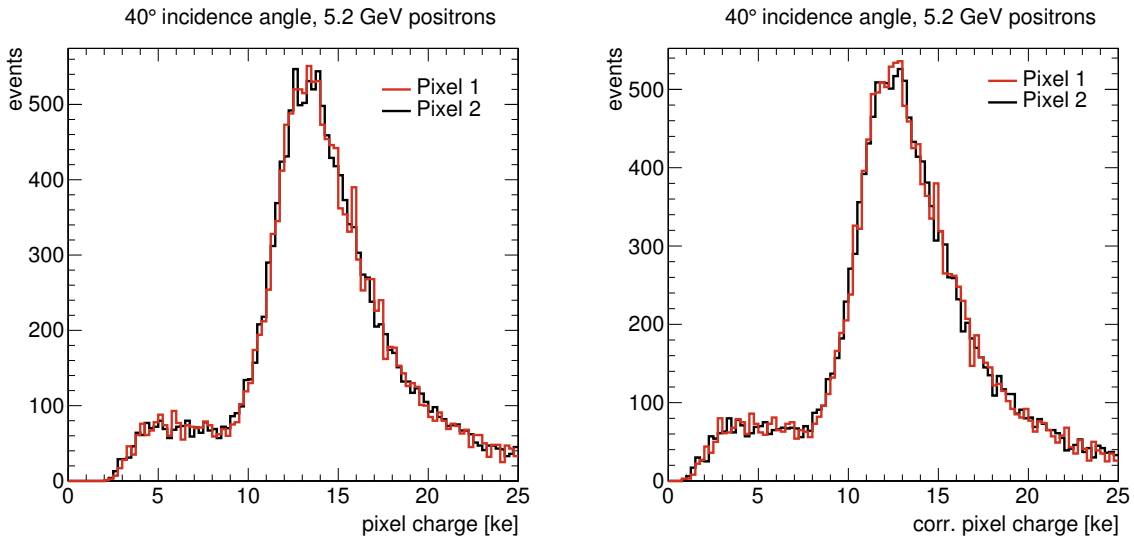

Figure 8.3: Charge distributions for the second and third pixel in four-pixel clusters only. Shown in the calibrated charge distribution before (left) and after (right) the ADC correction for the charging effect. No relative difference between the two spectra can be observed, neither before nor after the ADC correction.

8.3.3 Clustering and Cluster Center Interpolation

A sparse clustering algorithm is used to form clusters from the DUT and timing reference (REF) pixel hits. Starting from a seed pixel, the cluster is extended by calculating the distance of all remaining pixels to the pixels belonging to the cluster. Pixels found within a configurable distance are added to the cluster and removed from the list of remaining, unclustered pixel hits. If no more adjacent pixels can be found, the cluster is marked as complete, and a new seed pixel is selected.

The search range for new pixels to be added to the cluster is one pixel, i.e., only directly adjacent pixels are considered. For data with shallow track incidence angles and very long clusters, the search radius is set to two pixels, i.e., one missing pixel is allowed. However, the effect of this correction has shown to be negligible.

The position of the cluster center is calculated using the center of gravity (CoG) algorithm described in Section 3.3.1, which makes use of the available pixel charge information. The individual pixel charges in column and row direction are multiplied with the pixel position and summed up for the entire cluster. Finally, the column and row positions are divided by the full cluster charge for normalization. The seed pixel of the final cluster is defined as the pixel the CoG points to.

In some cases, the ADC value of a pixel hit does not allow for a correct conversion to electrons, e.g., for ADC values below the nominal threshold. The charge contribution of these pixel hits which failed the charge calibration and exhibit negative charge values is arbitrarily set to 1 ke in order to avoid strong effects on the CoG position of the cluster. In the rare case of a cluster charge of zero obtained from the conversion to electrons, the cluster position is identified with the coordinates of the seed pixel.

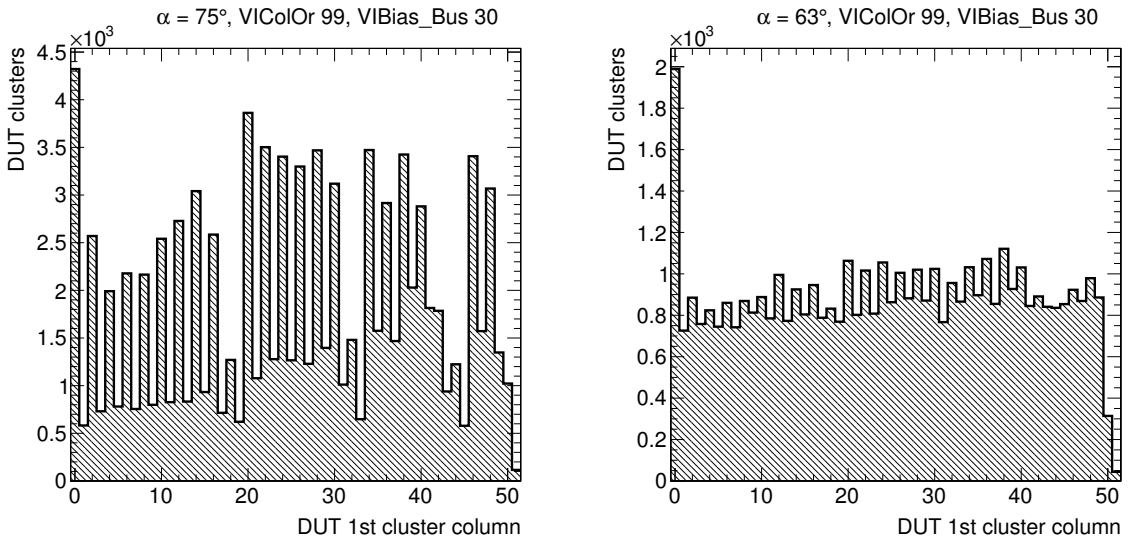

Figure 8.4: Column occupancy of the pixel at the cluster edge at different track incidence angles. At 75° (left) a distinct even/odd pattern can be observed, which is less pronounced at lower track incidence angles (shorter clusters, right).

8.3.4 Even/Odd Effect in the Column Occupancy

Another effect has been discovered when comparing the measured average cluster size with the expectation derived from the sensor geometry. Under certain circumstances, the average cluster size is smaller than expected and the column occupancy of the cluster edge shows a distinct even/odd pattern as displayed in Figure 8.4. Here, cluster edge refers to the first pixel of the cluster in the readout order. The plots show only events with clusters larger than two pixels and only contain the position of the first pixel of the cluster. The anomalies in the first and last column arise from clusters only partially contained in the sensor volume. The even/odd effect is only observed for clusters extending along rows of the ROC.

The data currently available do not allow for definite conclusions, but the effect appears to be related to whether a cluster occupies two pixels or only one pixel within the same DCol as sketched in Figure 8.5. The single pixels at the beginning or end of the clusters might not be able to notify the DCol periphery, and are not read out in the correct bunch crossing.

Three parameters have been identified, which influence the strength of the effect. The effect scales with the cluster length as indicated by the difference between Figures 8.4 (left) and (right). The longer the clusters, the more pronounced is the effect, and at track incidence angles below 45° no even/odd pattern can be observed. Moreover, the two DACs VIColOr, responsible for driving the fast-or signal (cf. Section 4.2.2), and VIBiasBus, controlling the digital bus receiver, have an influence on the DCol drain mechanism. Choosing higher values for either of them mitigates the effect, data with both parameters increased is presented in Figure 8.6.

However, there seems to be another, yet unknown dependency since runs have been observed where the settings of above parameters should have produced the even/odd pattern, but no effect could be observed in data. The exact timing of the ROC relative to the beam could be a candidate which can affect the timing of the PUC notification. As the effect only occurs for long clusters spanning multiple columns while clusters along columns do not seem to be affected, the DCol drain mechanism might be the source. For a more thorough understanding of the effect, more tests would have to be conducted, mapping the phase space outlined above.

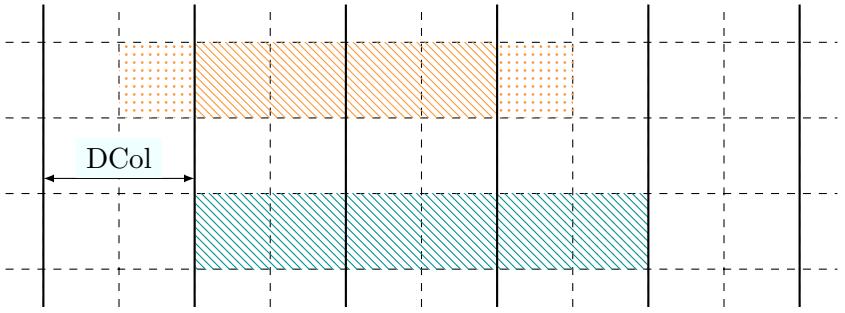

Figure 8.5: Lost pixels and the resulting even/odd column occupancy effect in long clusters. If a cluster starts in the left column of the DCol, two pixels initiate the DCI notification and all pixels are read out (lower cluster). In case of the cluster starting in the right column, the DCol might miss the notification from the single pixel, and the pixel hit is lost (upper cluster). The same holds true for the last pixel of the cluster.

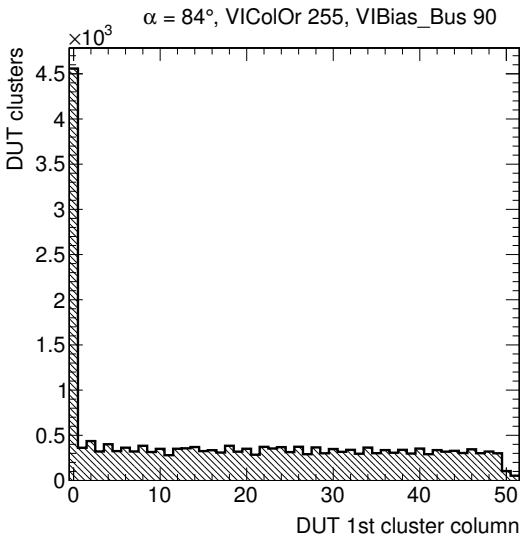

Figure 8.6: Column occupancy of the first pixel of a cluster. Increased settings for the VIColOr and VIBiasBus DACs allow to mitigate the even/odd effect. The effects in the first and last bin arise from clusters only partially contained in the sensor volume.

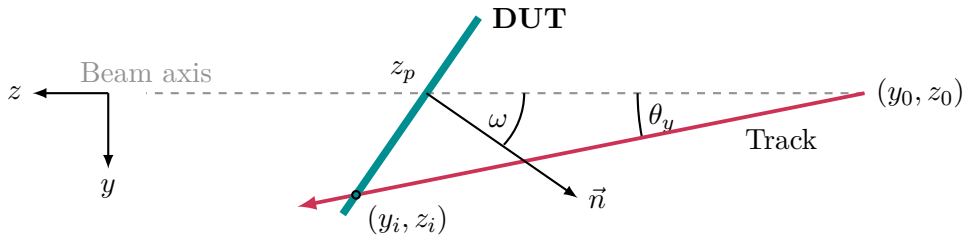

Figure 8.7: Sketch of the telescope reference track and the DUT sensor in the y-z plane.

8.3.5 Track Impact Reconstruction on the DUT

The reference tracks reconstructed from the beam telescope as described in Section 7.5 have to be transformed into the DUT reference coordinates for matching. A passive coordinate transformation is used in order to obtain the final coordinates in the DUT frame of reference. This facilitates the comparison with sensor features such as track impact positions relative to the pixel pitch. Figure 8.7 provides a sketch of the relevant quantities in two dimensions.

The track reconstructed from the telescope can be parametrized using a reference point of origin, here denoted as (x_0, y_0, z_0), and two slope parameters θ_x, θ_y for the track angle relative to the beam axis along z. The inclined track can then be described by the equations

$$\begin{aligned} x &= x_0 + (z - z_0) \tan \theta_x \\ y &= y_0 + (z - z_0) \tan \theta_y. \end{aligned} \tag{8.7}$$

The DUT sensor plane at position $\vec{r_p} = (0, 0, z_p)$ with the normal vector $\vec{n} = (n_x, n_y, n_z)$ satisfies the general plane equation

$$\{\vec{r} \mid \vec{n} \cdot (\vec{r} - \vec{r_p})\}\,. \tag{8.8}$$

Inserting the track coordinates from Equation 8.7 yields the z coordinate of the track intersection point $\vec{r_i} = (x_i, y_i, z_i)$ with the DUT plane

$$z_i - z_0 = \frac{n_z\,(z_p - z_0) - n_y y_0 - n_x x_0}{n_x \tan \theta_x + n_y \tan \theta_x + n_z}. \tag{8.9}$$

The x_i and y_i coordinates can be obtained by inserting z_i back into the track equations. The orientation of the DUT plane can be parametrized by rotating the plane normal vector $\vec{n}$ using Euler angles. For alignment, three shifts are required — a_x, a_y and a_z along the x, y and z axis, respectively — in addition to the angles ϕ, α, ω. With the rotation matrices $\mathcal{R}_x(\alpha)$, $\mathcal{R}_y(\omega)$, $\mathcal{R}_z(\phi)$ the transformation of the normal vector can be expressed by

$$\begin{pmatrix} n_x \\ n_y \\ n_z \end{pmatrix} = \mathcal{R}_y(\omega)\,\mathcal{R}_x(\alpha)\,\mathcal{R}_z(\phi) \begin{pmatrix} 0 \\ 0 \\ 1 \end{pmatrix}. \tag{8.10}$$

It is worthwhile noting that large rotations do not commute, and thus the order of application has to be preserved. The track intersection coordinates can be transformed into sensor coordinates using the passive rotation

$$\begin{pmatrix} x' \\ y' \\ z' \end{pmatrix} = \mathcal{R}_z(-\phi)\,\mathcal{R}_x(-\alpha)\,\mathcal{R}_y(-\omega) \begin{pmatrix} x_i \\ y_i \\ z_i \end{pmatrix} + \begin{pmatrix} a_x \\ a_y \\ 0 \end{pmatrix} \quad \text{where } z' = 0. \tag{8.11}$$

The rotation angle ϕ around the z axis is constrained by the DUT mechanics, and the associated rotation can usually be neglected. Due to the geometrical setup, the z coordinate is only weakly constrained by data, but with small track slopes θ_x, θ_y the influence on the track impact measurement vanishes.

8.3.6 Detector Alignment for DUT and REF

The alignment of the DUT and REF detectors is performed in their respective local reference frames using the coordinate transformation described in the previous section. The same iterative alignment procedure as for the beam telescope is employed, using a prealignment before the actual alignment step (cf. Section 7.5.3). Just as any fit, the alignment relies on reasonable starting values for rotation angles and shifts, preferably measured during data acquisition.

The prealignment consists of the simple histogramming method where the upstream and downstream telescope triplets are extrapolated to DUT and REF planes, respectively. The intersection with the rotated plane is obtained from Equation 8.9, and the residual between DUT or REF hits and the track impact is calculated. Only the shifts a_x and a_y of the planes are corrected for by determining the maximum of the residual distributions. This rough prealignment is sufficient for the timing reference plane, since the tagging of telescope tracks does not require high alignment precision.

In a second step, the DUT with the prealignment shifts applied is aligned using the MP-II algorithm (cf. Section 3.4) together with the GBL formalism described in Section 3.3.2. The GBL trajectories are built with the upstream telescope triplet as external seed, and include the upstream telescope arm and DUT measurements as well as the scattering material from DUT, telescope planes, and the surrounding air. This approach is taken since it excludes any multiple scattering contribution from the DUT support structure, cooling and mechanics downstream of the sensor. Seeding of the trajectory is performed by calculating the residual for the predicted track and the actual measurement for telescope and DUT alike with

$$x_{\text{gbl}} = x_{\text{meas}} - x_{trip}\left(z\right), \tag{8.12}$$

where x_{gbl} is the residual provided to GBL, x_{meas} is the measured hits position on the telescope planes or the DUT, and $x_{trip}\left(z\right)$ denotes the predicted hit position of the triplet at position z of the respective sensor. The measurements are weighted with their respective intrinsic resolution, where the telescope resolution is assumed to be $\sigma_{\text{tel}} = 3.4\,\mu\text{m}$ (cf. Section 7.2.2), the DUT resolution is estimated to $\mathcal{O}\left(10\,\mu\text{m}\right)$.

The DUT is aligned in all three spatial directions a_x, a_y and a_z, and the three rotations α, ω and ϕ as described in the previous section. Equation 7.1 is used to estimate the variance of the scattering angle in the thin scatterers. All alignment parameters are calculated relative to the position of the last upstream telescope plane. The GBL trajectories are collected and passed to the MP-II executable, which performs the matrix inversion and minimization. The alignment constants are retrieved from the MP-II output and stored in the run database. Upon the next execution of the analysis processor, the parameters are applied to the data. If necessary, the above procedure is repeated until the alignment constants have converged.

The alignment of the Datura beam telescope is changed whenever the telescope has been mechanically altered, or the environmental parameters such as temperature or humidity have changed, whereas the DUT is re-aligned for every run to maximize the alignment precision. The alignment constants for every run are monitored as shown in Figure 8.8 (left) for SCM 504 and Figure 8.9 (left) for SCM 506. Since the DUT alignment is calculated relative to the last upstream telescope plane, changes to the alignment parameters are expected whenever the telescope configuration has changed and a new telescope alignment has been prepared. In the figures, these runs are indicated with vertical dotted lines.

Within the series of runs for the same telescope configuration, the alignment parameters remain stable. The DUT seems to be mounted slightly off-center on the rotation axis since the alignment shift *dy* exhibits a slight dependence on the tilt angle along the x axis of the telescope as shown in Figures 8.8 (right) and 8.9 (right).

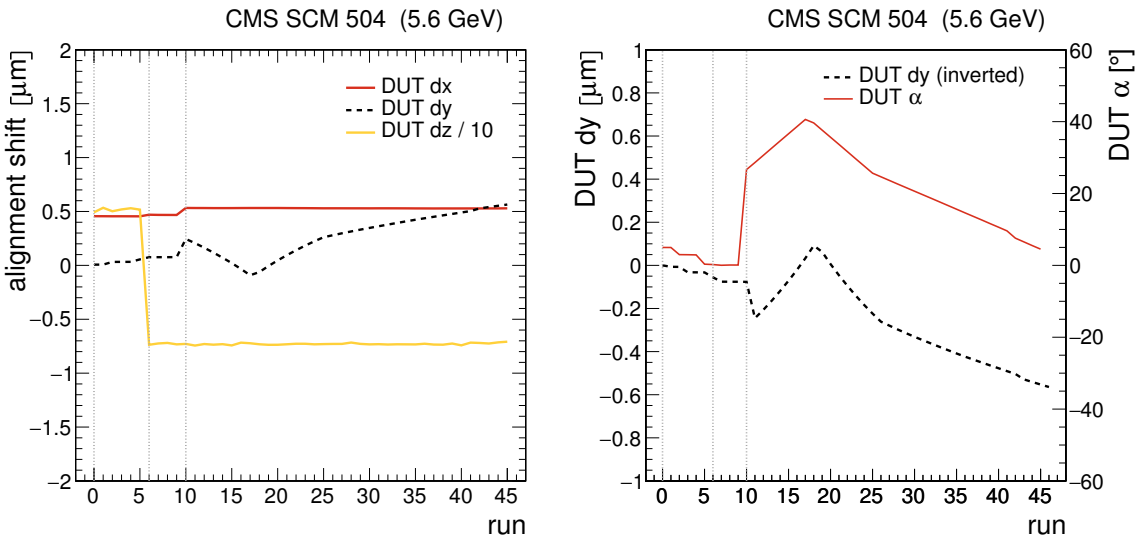

Figure 8.8: Alignment parameter evolution for SCM 504 over time, dotted vertical lines mark new telescope alignments. (left) shows the three alignment shifts dx, dy, dz. While dx and dz are stable within one telescope alignment section, a shift can be observed for dy. (right) shows the correlation of the parameters dy and the tilt angle α.

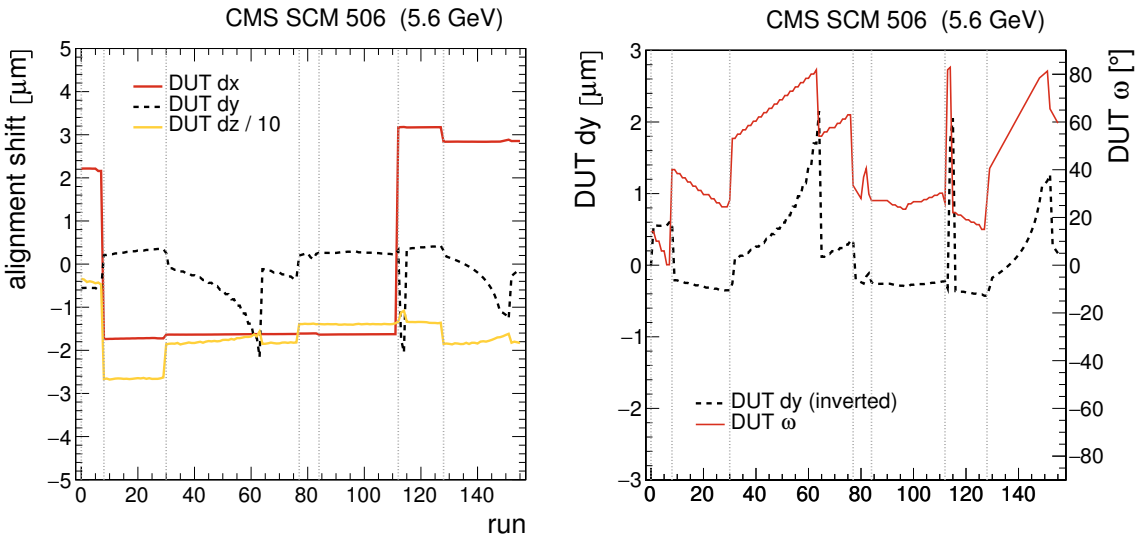

Figure 8.9: Alignment parameter evolution for SCM 506 over time, dotted vertical lines mark new telescope alignments. (left) shows the three alignment shifts dx, dy, dz. In addition to the correlation of dy and the tilt angle ω, also dz shows a slight dependence. (right) shows the correlation of the parameters dy and the tilt angle ω.

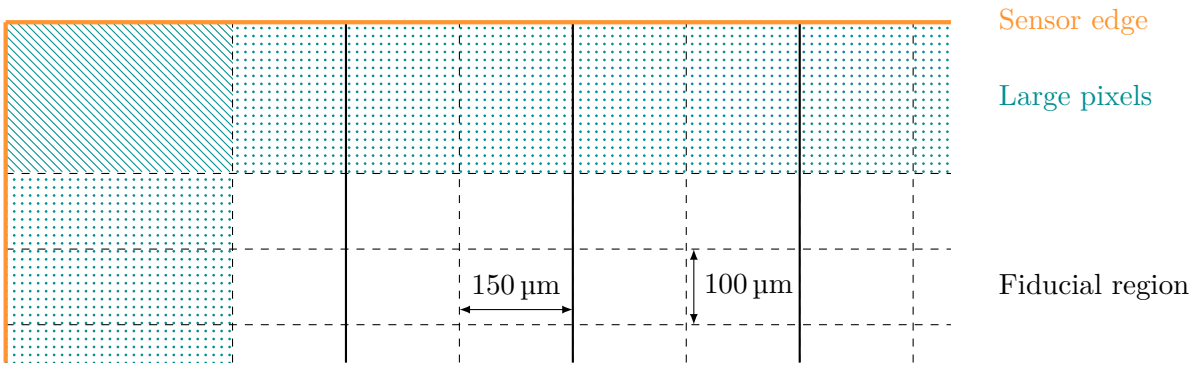

Figure 8.10: Fiducial volume of CMS SCM sensors. The pixels at the sensor edges are enlarged by a factor of two. The dotted areas correspond to pixels with double size, while the hatched area of the corner pixel has fourfold size. Thick lines indicate DCol boundaries.

8.4 Event Selection

Several selection criteria are imposed on the recorded test beam data in order to maximize the sensitivity of the analysis to the features of the ROC under test. The rejection criteria described in the following sections are adapted to the measurement performed. For instance, the resolution measurements are obtained with upstream telescope tracks only to avoid any influence of the larger material budget of the DUT mechanics. Efficiency measurements utilize full telescope tracks as the timing information and track tagging from the REF plane is required.

8.4.1 Geometric Constraints on the Sensor

The sensors of both the final CMS Pixel modules and the SCM assemblies contain enlarged edge pixels in order to accommodate the ROCs and add an additional placing margin between neighboring chips without creating insensitive areas. Since the electric field and charge collection behavior are different in these pixel cells, they are removed from the analysis, and the remaining pixel array indicated in Figure 8.10 is called the *fiducial region*. For resolution studies, clusters which extend into the edge region are excluded in their entirety in order not to influence the cluster center interpolation by removing single pixels from the cluster.

Due to limitations in the simulation, the biasing grid of the SCM sensor (cf. Figure 4.1) is not reproduced in the TCAD design (cf. Section 5.2), and thus has to be excluded from the data analysis in order to match the predictions. The region of the bias dot inside the PUC is excluded by cuts in x and y around the nominal position of the bias dot position for small tilt angles α and ω. In order to exclude the full region affected by the smeared effect of the bias dot at large tilt angles, only cuts in either x or y of the PUC are applied. Tracks intersecting the DUT sensor inside these regions are discarded.

The bias dots are not excluded from the analyses presented in Section 8.8 which are investigating the ROC characteristics depending on the particle impact position within the PUC.

8.4.2 Track Matching and Isolation Criteria

In the analysis presented, only clusters are accepted which can be matched to a telescope reference track. Depending on the analysis performed, a combination of the available telescope tracks described in Section 7.5.4 and two different DUT matching criteria can be selected, while

the acceptance cut for matching telescope tracks and REF plane hits is always set to 300 µm. The **loose DUT matching** requires the DUT hit to be within 500 µm of the reference telescope track for both dx_{match} and dy_{match}.

For the **tight DUT matching**, the matching cut dy_{match} is scaled as a function of the rotation angle with the expected resolution, and is set to about 10σ of the anticipated residual width. The scaling is implemented in rough steps and an extrapolation for large angles. For SCM 506 with a rotation around ω and a pitch of 150 µm along the telescope y axis, this translates to:

$$\begin{aligned} dy_{\text{match}} &= 400\,\mu\text{m} && \text{for } 0° < \omega < 14° \\ dy_{\text{match}} &= 250\,\mu\text{m} && \text{for } 14° < \omega < 19° \\ dy_{\text{match}} &= 100\,\mu\text{m} && \text{for } 19° < \omega < 35° \\ dy_{\text{match}} &= 100\,\mu\text{m} + 6.25\,\mu\text{m}/° \,(\omega - 35°) && \text{else.} \end{aligned} \tag{8.13}$$

Scaling is only required in the y coordinate of the telescope track, since the resolution in x is fixed due to the vertical track incidence arising from the mechanical constraints of the ROC mount (cf. Section 7.3.1). Here, the matching criterion applied is $dx_{\text{match}} = 150\,\mu\text{m}$. For SCM 504, matching criteria of 300 µm, 150 µm, and 50 µm are imposed for angles of $\alpha < 7°$, $\alpha < 15°$, and $\alpha < 25°$, respectively. For larger angles, a matching within $dy_{\text{match}} = 100\,\mu\text{m}$ is required.

Additional acceptance cuts on the telescope tracks help to significantly improve the achieved resolution, and are always applied, independent of the selected matching criterion. Some events contain several tracks due to the telescope track pile-up described in Section 7.3.2. The DUT clusters matched with telescope tracks are required to have a clearance of more than 300 µm in x and y on the sensor surface without another telescope track around them. This isolation requirement allows to reduce matching ambiguities. Tracks from particles which have undergone heavy scattering or do not originate from the original beam are filtered out using the track slope. The slope in θ_x and θ_y of the telescope upstream triplet are regarded, and tracks with a slope larger than $\theta > 2\,\text{mrad}$ are rejected. The impact of the fiducial volume restriction and track isolation on the background rejection and residual width is shown in Figure 8.11a.

8.4.3 Constraints on the Cluster Charge

Delta rays produced in the sensor severely affect the position resolution. The delta electron created at the position of the track incidence can travel significant distances inside the sensor volume, producing large clusters. The cluster CoG is thus shifted to the center of the delta electron track and does not provide information on the original particle track. Figure 8.11b shows the residual width (MAD) as a function of the cluster charge. A deterioration towards large cluster charges is visible, while the best resolution is achieved around the Landau MPV.

Therefore, the background stemming from delta rays can be efficiently rejected by imposing a quality cut on the cluster charge around the Landau MPV value. The deposited charge and thus the Landau MPV depend on the track incidence angle, hence the cut is applied to the cluster charge normalized to vertical track incidence, Q_0, as defined in Equation 8.5. The most restrictive cut, used for the resolution measurements, rejects all clusters outside of

$$16\,\text{ke} < Q_0 < 23\,\text{ke},$$

as indicated in Figure 8.11b. The fraction of clusters passing this cut is about 30 % of the isolated clusters inside the fiducial region. This corresponds to about 7 % of the total clusters recorded.

Figure 8.11a summarizes the effect of the various selection criteria on the DUT residual width. Both the track isolation requirements and the cut on the cluster charge greatly influence the background suppression.

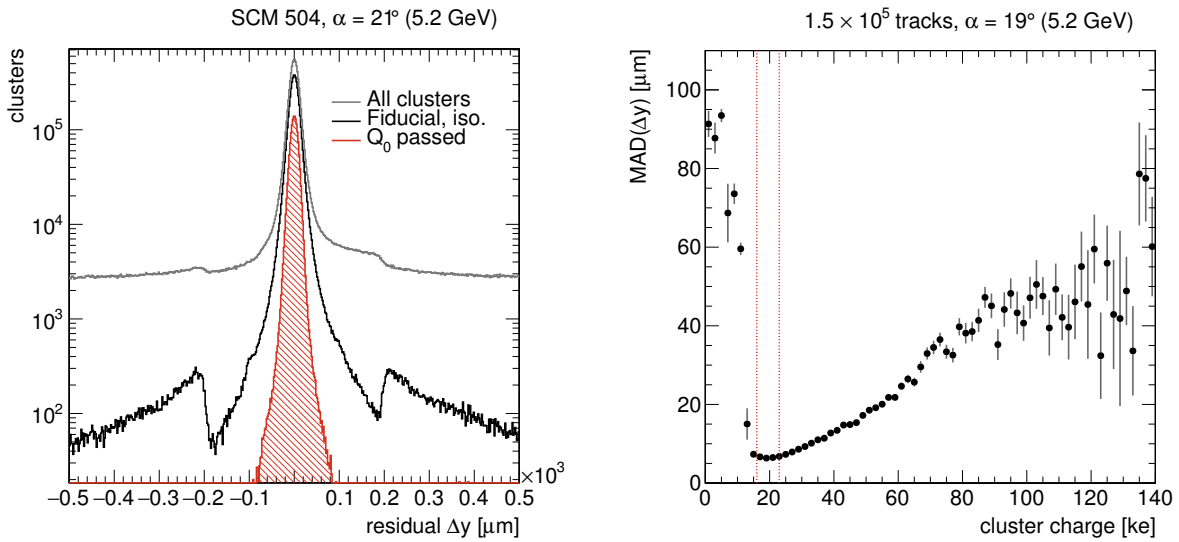

(a) Residual distribution for the different steps of the event selection procedure.

(b) Residual width as a function of the cluster charge. Dotted lines mark the Q_0 cut.

Figure 8.11: Influencing factors for the DUT residual distribution. The residual distribution at different stages in the event selection process is presented in (a), while (b) shows the residual width as a function of the cluster charge. The influence of delta rays on the residual distribution can be observed at large cluster charges.

8.5 Statistical and Systematic Uncertainties

The intrinsic detector resolution to be measured consists of two components as detailed in Equation 3.19. Thus, both statistical and systematic uncertainties on the individual components have to be propagated to the final intrinsic resolution via

$$(\Delta\sigma_{\text{int}})^2 = \left(\frac{\sigma_{\text{meas}}\Delta\sigma_{\text{meas}}}{\sqrt{\sigma^2_{\text{meas}} - \sigma^2_{\text{track}}}}\right)^2 + \left(\frac{\sigma_{\text{track}}\Delta\sigma_{\text{track}}}{\sqrt{\sigma^2_{\text{meas}} - \sigma^2_{\text{track}}}}\right)^2, \tag{8.14}$$

where σ denotes the component, and $\Delta\sigma$ its uncertainty, respectively.

The statistical uncertainty on the resolution measurements is calculated using pseudo-experiments. Every bin of the residual distribution under consideration is smeared with a Poisson distribution with the mean value being the original bin content. The resolution obtained from the smeared residual histogram is stored, and the pseudo-experiment repeated ten thousand times. The statistical uncertainty on the measured resolution is then taken as the width of the resulting resolution distribution (cf. Appendix B), and is propagated to the intrinsic resolution.

Systematic uncertainties for the measurements presented mostly concern environmental conditions during the test beam such as temperature or beam parameters, and the characteristics of the Datura beam telescope used for the reference tracks. Most systematic uncertainties enter the measurement via the calculated telescope track resolution, which is subtracted from the measured residual width in order to obtain the intrinsic resolution of the detector (cf. Equation 3.19). The track resolution to be subtracted is calculated using GBL as described in Section 7.2.1. Input parameters to the track model are the beam energy; the distance dz_{DUT} between the last upstream plane and the DUT detector; the intrinsic resolution and material budget of the telescope planes; and the material budget of the DUT installation itself.

From Figure 7.5 the uncertainty for both the beam energy and dz_{DUT} can be estimated. With the three-plane track configuration taken as upper limit, and a DUT distance around $dz_{\mathrm{DUT}} \approx 45\,\mathrm{mm}$, the uncertainty stemming from the beam energy is below $\pm 0.10\,\mu\mathrm{m}$ for measurements at 5.2 GeV. At beam energies of 5.6 GeV as used for some measurements, the uncertainty is expected to be even lower. With a rather conservative estimate of the uncertainty on the distance measurement between telescope upstream arm and the DUT of $\Delta dz_{\mathrm{DUT}} \approx 2\,\mathrm{mm}$, the effect on the extrapolated track resolution is estimated to be below $\pm 0.10\,\mu\mathrm{m}$.

The intrinsic telescope resolution is taken as $\sigma_{\mathrm{tel}} = 3.4\,\mu\mathrm{m}$ [166]. The systematic uncertainty arising from the effect of the intrinsic resolution on the track extrapolation can be estimated by repeating the GBL calculations using different values for the intrinsic plane resolution. A variation of the resolution by $\pm 5\,\%$ yields a track resolution uncertainty of about $\pm 0.16\,\mu\mathrm{m}$ for three-plane tracking, and about $\pm 0.11\,\mu\mathrm{m}$ for six planes used. The total systematic uncertainty on the predicted track resolution is calculated as the quadratic sum of the individual sources and amounts to

$$\Delta\sigma_{\mathrm{track}} = \pm 0.21\,\mu\mathrm{m}.$$

The material budget of the DUT is only relevant for the telescope track resolution calculated using all six planes. However, this is only necessary for efficiency measurements where track tagging with the REF detector is required, and resolution measurements are performed using three-plane telescope tracks only. For efficiency measurements, the track resolution is of no concern as the loose DUT matching criteria is applied (cf. Section 8.4).

Temperature changes of the ROC affect the response behavior of the ADC and thus the charge calibration. Since environmental temperature changes are rather slow, no changes are to be expected between runs, but rather for measurements taken on different days. The offset in the Landau MPV has been corrected by applying different calibration factors from internal VCal units to electrons to these sets of runs using the MPV of the charge distribution simulated by Pixelav as reference (cf. Section 8.3.1). In order to cover remanent dependencies and the uncertainty arising from the simulation, the rejection criteria for the cluster charge described in Section 8.4.3 are shifted by $\pm 1\,\mathrm{ke}$ and the resolution measurement is repeated. The uncertainty on the measured resolution width is found to be

$$\Delta\sigma_{\mathrm{meas}} = \pm 0.12\,\mu\mathrm{m},$$

averaging over all measurements at all track incidence angles.

Efficiency measurements are affected by the absolute particle rate and timing instabilities concerning the phase of trigger arrival relative to the detector clock. The particle rate influences the internal buffering mechanisms of the ROC and might lead to inefficiencies whenever buffer overflows occur (cf. Section 4.2.2). However, at the DESY-II test beam only rates of a few kHz can be achieved with the accelerator frequency being around 1 MHz (cf. Section 7.1). With the chip being designed for particle rates of $150\,\mathrm{MHz\,cm^{-2}}$, these inefficiencies can safely be neglected. The uncertainty arising from trigger timing instabilities are difficult to quantify, and are assumed to be of the order of the measured inefficiencies around 5‰.

The simulations do not enter the measurements by other means than the absolute charge calibration. However, it has to be noted that in order to match the angular dependence of data, different effective sensor thicknesses have to be assumed. While both sensors have been measured to comply with the nominal thickness of $(285 \pm 4)\,\mu\mathrm{m}$, the test beam measurements performed with SCM 504 require an effective simulated sensor thickness of 294 µm in order to correctly describe the shape. For SCM 506, a simulation performed with a sensor thickness of 308 µm is required. The different behaviors are under investigation but have not yet been fully understood.

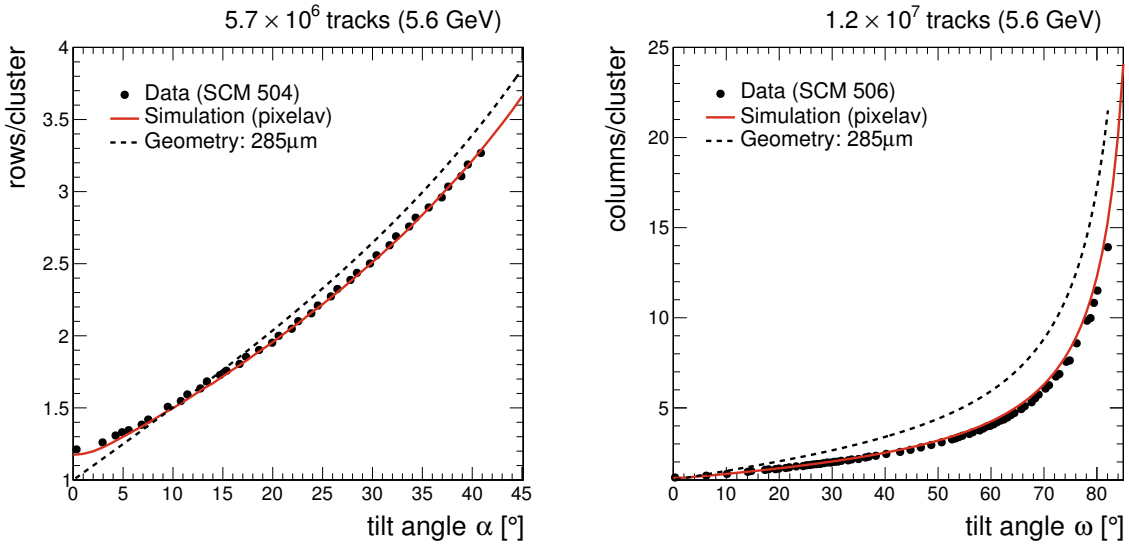

Figure 8.12: Cluster size versus tilt angles. While the simulation matches well for the tilt angle α of SCM 504 (left), the expected cluster size is slightly overestimated for SCM 506 (right) at large tilt angles ω.

8.6 Control Distributions

Geometrical considerations allow the comparison of charge deposition and collection in data and MC simulation. Particles traverse the sensor material and deposit charges along their path, which subsequently drift and are collected at the sensor implants by different PUCs of the ROC. As a result, both the size of the clusters as well as the total cluster charge scale with the incidence angle of the particles.

Figure 8.12 shows the cluster size for rotations in α (left) and in ω (right) as obtained from the test beam data, the PIXELAV simulation, and the geometric expectation. Geometrically, the cluster size is expected to be proportional to the tangent of the particle incidence angle. However, at small angles charge diffusion leads to a larger mean cluster size, while threshold effects reduce the measured cluster size at larger angles. The PIXELAV simulation and the subsequent digitization described in Chapter 5 correctly describe both effects and match well with the data obtained from SCM 504, while slightly overestimating the cluster size for SCM 506 at large tilt angles ω.

Charge carriers are deposited uniformly along the path of the traversing particle, which is why the absolute cluster charge is expected to scale linearly with the path length inside the sensor volume. The path length l is given by

$$l = t/\cos(\alpha)\,, \tag{8.15}$$

where t denotes the sensor thickness, and α the incidence angle. Figure 8.13 presents the Landau MPV of the absolute cluster charge as a function of the path length covered by the particle inside the sensor volume. Simulation and data match well for both DUT assemblies when taking the different effective sensor thicknesses of the simulation into account as described in the previous section.

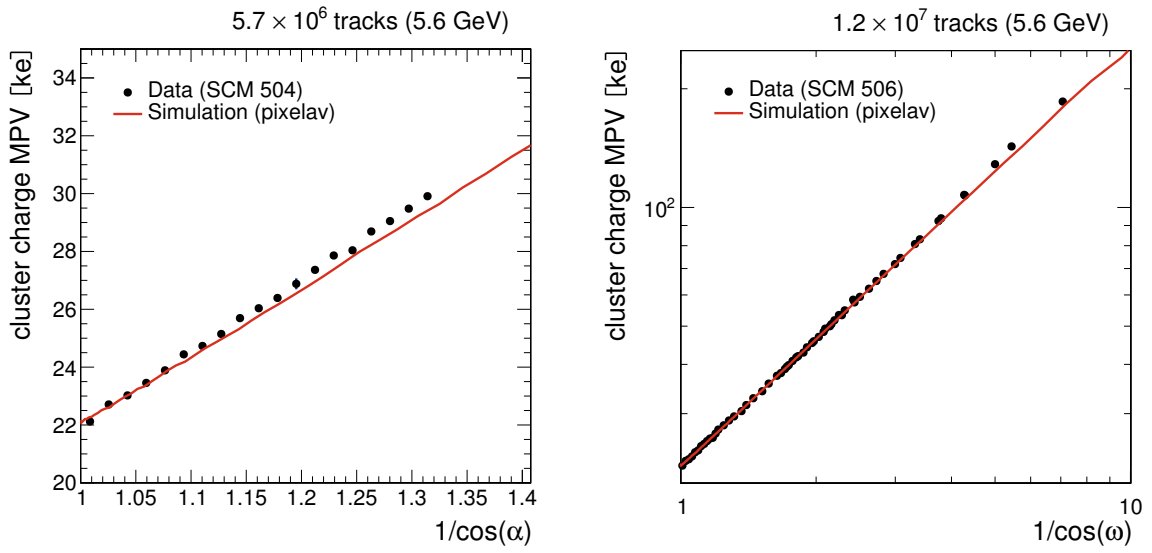

Figure 8.13: Landau MPV of the cluster charge distribution as a function of the path length of the incident particle in the sensor. The simulation matches well for both SCM 504 (left) and SCM 506 (right).

8.7 Tracking Efficiency

The tracking efficiency of the PSI46digV2.1-r ROC has been measured as a function of operation time and track position on the chip, and is calculated using only full six-planes telescope tracks which are referenced by the REF plane. By this, inefficiencies arising from particles arriving outside the trigger window as well as from limited geometrical acceptance are excluded. For this analysis, a combination of tight telescope tracks (cf. Section 7.5.4) and a loose DUT matching (cf. Section 8.4.2) is applied, an additional REF hit is required for the track to be accepted.

It is worth noting that operating the two PSI46 detectors synchronously using the same external clock is of particular importance, because otherwise hits of particle tracks will be lost and counted as inefficient which are inside the trigger window for the REF detector but not for the DUT. Furthermore, the timing of the chips relative to the beam trigger is of importance, since having a random trigger with respect to the ROC clock will yield a lower efficiency. However, this operation mode is not the intended scenario of the PSI46digV2.1-r chips, which will be operated with a beam-synchronous trigger at the LHC. In the test beam setup, the correct timing is ensured by the trigger setup described in Section 7.3.3.

With these preconditions fulfilled, the tracking efficiency is given by

$$\epsilon = \frac{\text{isolated track} \in \text{DUT} \cap \text{REF}}{\text{isolated track} \in \text{REF}}, \tag{8.16}$$

where the tracking efficiency ϵ is calculated as the fraction of tracks passing the isolation criteria, and have an associated hit in both the REF and DUT detectors, over the total number of isolated tracks with matching hits in the REF plane.

The tracking efficiency is depicted in Figure 8.14a as a map of the DUT chip. The chip shows a uniform efficiency with small variations stemming from statistical fluctuations and timing instabilities. A slightly reduced efficiency can be observed for a few pixels at the left edge of the sensor, which has its origin in shifted threshold values for the pixels in question. Figure 8.14b

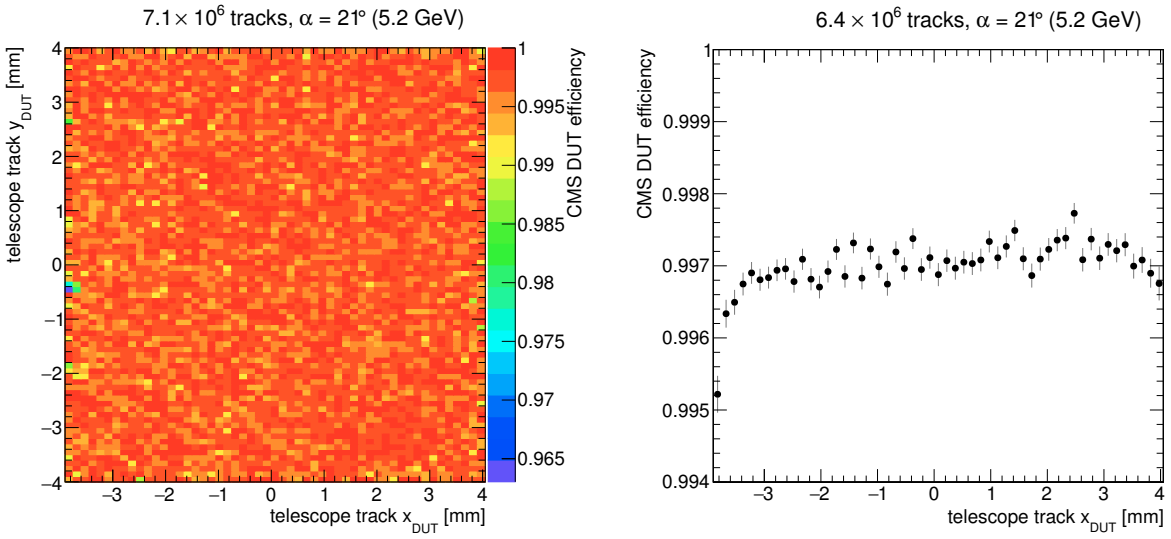

(a) DUT map indicating the tracking efficiency as a function of the track impact position.

(b) DUT tracking efficiency as a function of the track position on the chip along the x axis.

Figure 8.14: Tracking efficiency for the full fiducial volume of the DUT, shown as map (a) and as projection onto the track position along x (b). Both distributions show a uniform efficiency with minor effects from shifted pixel thresholds.

shows the projection of the map onto the columns of the DUT which allows the investigation of effects occurring on the DCol level. No significant pattern or dependency on even or odd columns can be observed.

The measured efficiency exhibits a mild dependency on the telescope track multiplicity due to matching ambiguities. Figure 8.15a plots the tracking efficiency achieved with the DUT versus the number of downstream triplets present in the telescope event. With eight telescope tracks present, an efficiency of 98.6 % can be reached, while restricting the selection to events with only a single telescope track yields an efficiency of about 99.9 %. No dependency on the running time has been observed, the efficiency is stable over a measurement time of about 20 min as shown in Figure 8.15b. The averaged efficiency over the full fiducial volume of the sensor including all selected events is evaluated to be

$$\epsilon = 99.70 \pm 0.01\,(\text{stat})\,^{+0.3}_{-0.5}\,(\text{syst})\,\%,$$

with the systematic uncertainties as estimated in Section 8.5. A cross-check measurement has been performed using the DUT detector as timing reference while measuring the tracking efficiency of the REF plane. Similar results as for the DUT measurement were achieved.

8.8 Intra-Pixel Resolution and Efficiency

Quantities such as spatial resolution, charge collection or tracking efficiency can be measured as a function of the intra-pixel position using the high-resolution reference tracks provided by the Datura beam telescope (cf. Section 7.2.2). The plots presented in this section always show a 2×2 pixel array matching the drawing presented in Figure 4.1. The measurements with matched tracks from the full fiducial volume are folded into these pixel cells in order to increase statistics.

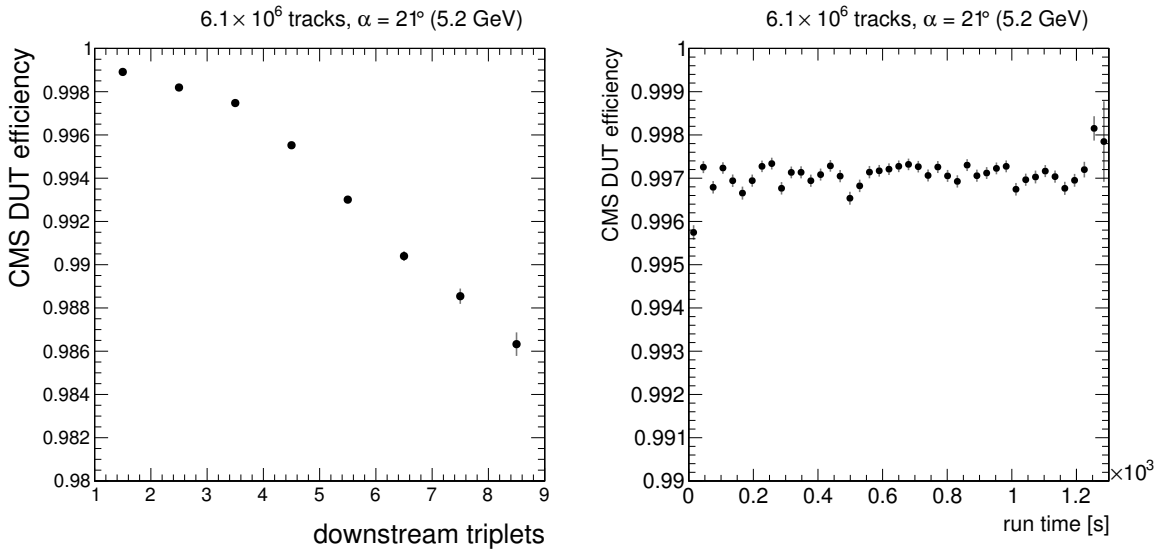

(a) DUT tracking efficiency as a function of the telescope reference track pile-up.

(b) DUT tracking efficiency as a function of the operation time.

Figure 8.15: DUT tracking efficiency as a function of track pile-up (a) and operation time (b). While no time dependency can be observed, the tracking efficiency is deteriorated with more telescope tracks present in the event due to matching ambiguities.

All effects are studied both at vertical track incidence $\alpha = 0°$ and around the angle of optimal two-pixel charge sharing, here for a tilt angle of $\alpha = 21°$. While the first provides interesting insights into the processes occurring in sensor and ROC, the latter allows to study the various quantities in a scenario closer to the expected operation conditions with charge drift induced by the external 3.8 T magnetic field in the CMS detector (cf. Section 2.2.3).

This analysis utilized the tight telescope track selection (cf. Section 7.5.4) as well as the tight DUT matching (cf. Section 8.4.2) for optimal position resolution. The additional REF matching is only required for the efficiency measurement presented in Section 8.8.2.

8.8.1 Charge Collection

The charge collection is an interesting quantity to be measured as a function as the track position within single pixel cells as it has a direct influence on the lifetime of the detector. It has to be pointed out that the plots presented here show the mean of the cluster charge instead of the Landau MPV and thus cannot be directly related to actual shifts of the Landau peak. However, they allow to qualitatively evaluate the effects of the sensor implant structure and the hereby altered electric field on the charge collection.

Figure 8.16 shows the mean total cluster charge as a function of the track impact position for the two different incidence angles. A strong effect around the bias dots can be observed for the vertical track incidence caused by the altered electric field in the sensor below the bias dots on ground potential. The cluster charge collection deficit for tracks incident vertically on the bias dot is about 35 %, while the effect is smeared out at inclined incidence where only 10 % of the charge is lost. In addition, threshold effects are visible at $\alpha = 21°$ as horizontal bars through the pixel cells with slightly reduced cluster charge. The scale differs for the two figures, and the mean total charge is higher for the measurement at $\alpha = 21°$ due to the longer path length of the particle traversing the sensor.

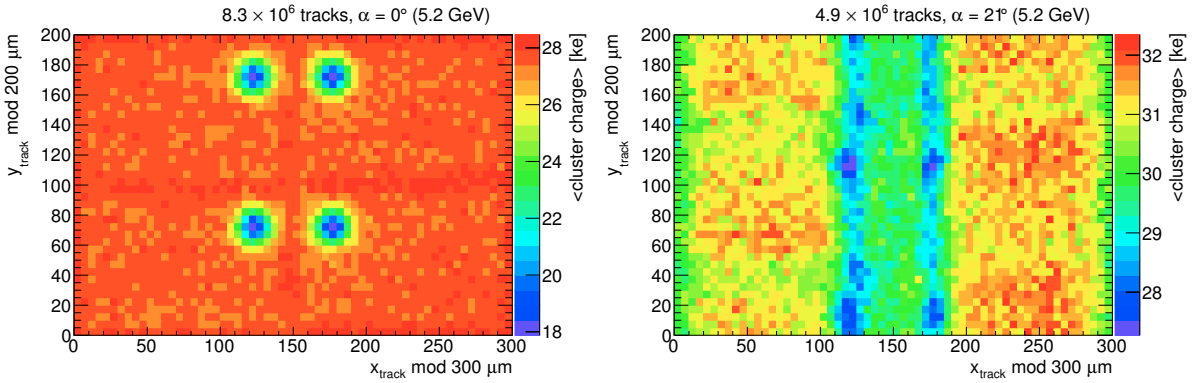

Figure 8.16: Charge collection in an array of 2×2 pixel cells. (left) shows the mean cluster charge collected at vertical track incidence. The bias dots are clearly visible and about 35 % of the total charge is locally lost. (right) shows the four pixel cells at a tilt angle of $\alpha = 21°$. The charge loss caused by the bias dots is smeared out and reduced in magnitude, only about 10 % of the charge is lost.

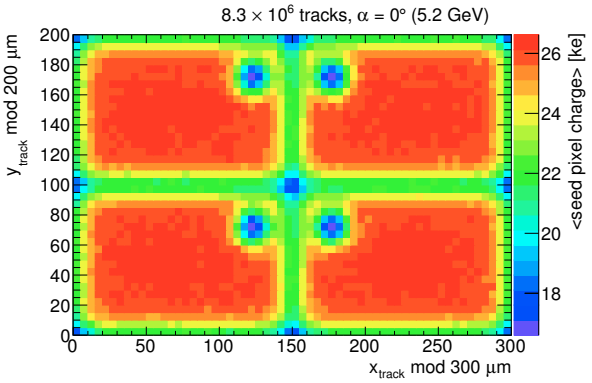

Figure 8.17: Mean charge of the cluster seed pixel as a function of the position within a 2×2 pixel array. The implant regions can be distinguished from the *p*-spray isolation and the bias dots.

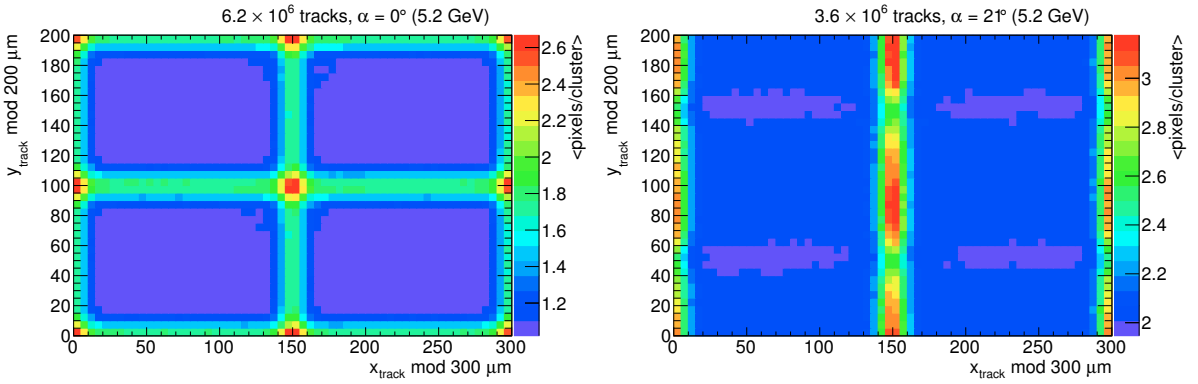

Figure 8.18: Mean cluster size as a function of the position within a 2×2 pixel array. (left) shows the distribution at vertical particle incidence. Around the pixel center, mostly one-pixel clusters are produced, while two-pixel clusters are dominant towards the edges. The pixel corners feature three- and four-pixel clusters. (right) shows the same quantity for a tilt angle of $\alpha = 21°$. Here, the average cluster size is larger due to the increased path length along the y axis as expected.

When plotting the seed pixel charge only instead of the full cluster charge, effects of the implant isolation structures on the charge collection can be observed as demonstrated in Figure 8.17. Here, the cluster seed pixel as defined in Section 8.3.3 is plotted against the intra-pixel track position, and the bias dots as well as the n^+ pixel implants are clearly visible and compare well with previous measurements of similar sensors [183]. While the full charge is collected when traversing the cluster center, the charge is shared between two pixels when approaching the pixel edges. With the p-spray isolation, the region of reduced charge collection extends into the pixel cell. The deposited charge is shared among three or four pixels when traversing the corner of a pixel cell, and the seed pixel charge drops accordingly.

8.8.2 Tracking Efficiency

The tracking efficiency measured for the full device in Section 8.7 can also be evaluated within the pixel cells. Since the average cluster size depends on the track incidence angle α as shown in Figure 8.18, the interpretation of the efficiency measurements for $\alpha = 0°$ and $\alpha = 21°$ is slightly different. At vertical incidence, the average cluster size is close to one, and the respective efficiency should be interpreted as single-hit efficiency rather than as tracking efficiency expected for operation in CMS. The measurement with inclined track incidence resembles the situation in the experiment more closely, where the mean cluster size is larger due to the Lorentz-induced charge sharing as well as the track dip angle.

Figure 8.19 shows the intra-pixel efficiencies for the different tilt angles. While both exhibit a very uniform efficiency distribution with a spread below 1 %, the tracking efficiency measured with the inclined sensor is slightly better than the single-hit efficiency obtained from the vertically incident particles. This is to be expected since the larger clusters increase the probability of recording at least one of the triggered pixels. However, the difference is marginal and the overall tracking and single-hit efficiencies are well above 99 %.

It is worthwhile pointing out that neither the comparatively large charge deficit at the bias dot for vertical track incidence, nor the smeared out bias dot structure around the Lorentz angle affect the tracking performance of the ROC. However, there is a small effect on the spatial resolution as will be presented in the subsequent section.

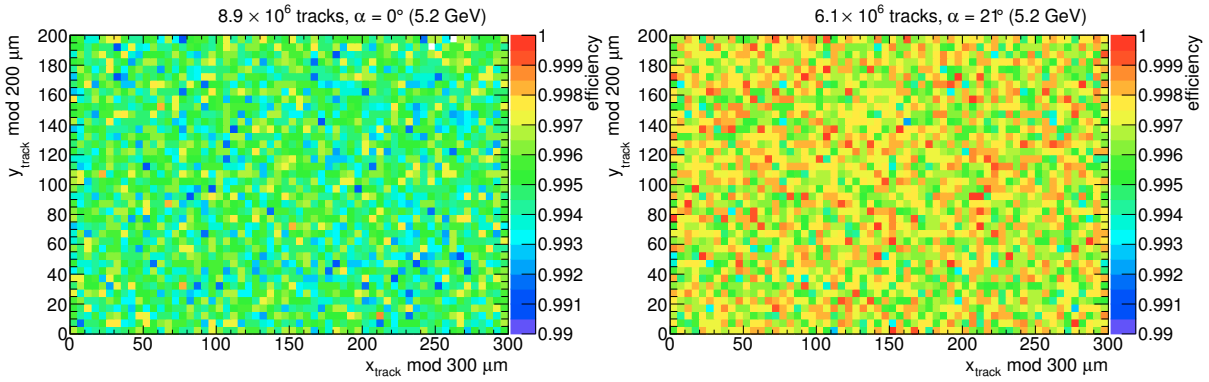

Figure 8.19: Tracking efficiency as a function of the intra-pixel position. Shown is a 2×2 pixel array at vertical incidence (left) and at a tilt angle of $\alpha = 21°$ (right). In neither of the situations any localized inefficiency can be observed, the charge deficit does not affect the tracking efficiency.

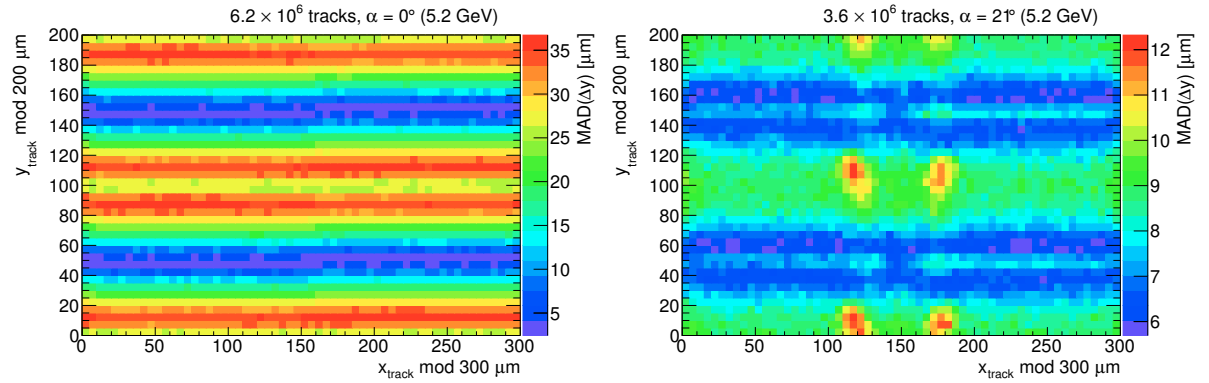

Figure 8.20: Intra-pixel resolution in y (residual MAD) for vertical and inclined incidence. (left) shows the resolution for vertical incidence, (right) for a tilt angle of $\alpha = 21°$. While at vertical incidence the resolution is dominated by effects at the pixel edges, the bias dot shows an effect in the resolution of the inclined measurement.

8.8.3 Intra-Pixel Spatial Resolution

The achieved position resolution depends on the track impact position within the pixel cell. The resolutions presented are not to be confused with the actual intrinsic detector resolution measured in Section 8.9, as no track uncertainty contribution has been subtracted, and the resolution is simply calculated as the MAD of the residual distributions for convenience. Nevertheless, interesting effects can be unveiled by correlating track impact position and residual width.

Figure 8.20 shows maps of a 2×2 pixel array with the column resolution in y as the colored z axis for both vertical incidence and incidence at $\alpha = 21°$. In both cases, variations of the y resolution can be observed, depending on the track impact position within the four pixels shown. For the measurement taken at $\alpha = 21°$, a slight deterioration of the resolution can be observed in the region of the smeared bias dots. Comparing to Figure 8.16, the effect occurs in the regions with about 10 % charge loss induced by the bias dots, while no effect can be seen at vertical incidence despite the larger charge loss. Here, the effects are overlain by the much larger variation in resolution imposed by the limited charge sharing at vertical incidence. In this case, the best resolution can be achieved if the track is incident in the center of the pixel cell, while tracks traversing the sensor close to the pixel edge produce broader residual distributions.

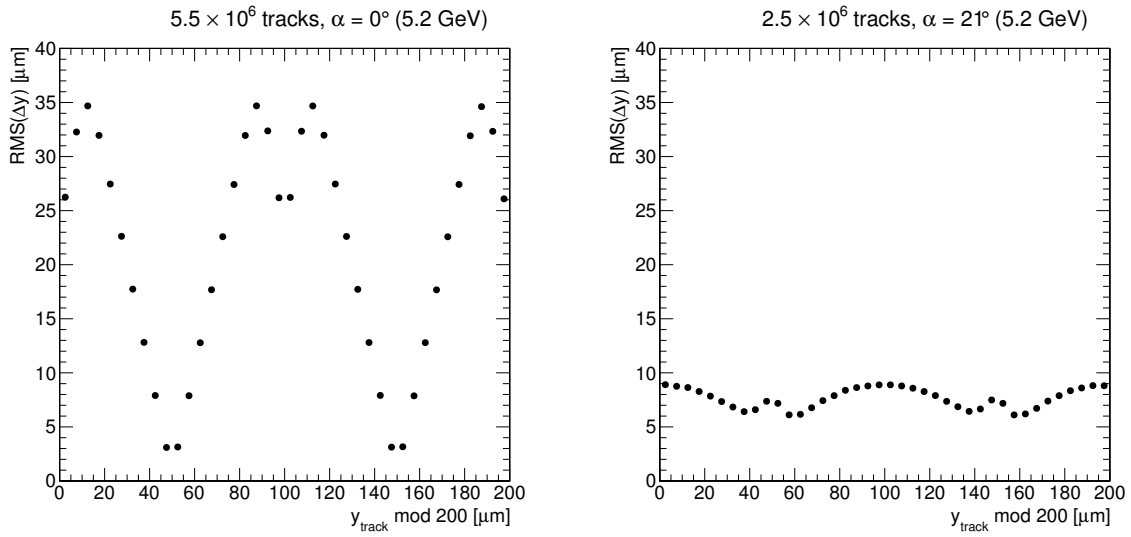

Figure 8.21: Projected intra-pixel resolution along the y axis. The y position shows a strong dependence of the position resolution at vertical incidence (left), while the magnitude of the variation is much reduced at $\alpha = 21°$ inclination.

The effect can also be studied in the projection of the maps onto the y axis as shown in Figure 8.21. While the left plot exhibits large variations from vertical incidence, the right plot shows a virtually flat RMS distribution with only small features visible around the pixel centers.

Figure 8.22a shows the x resolution which features similar but even stronger variations compared to the y resolution caused by the larger pixel pitch of 150 µm. Again, the pixel center yields the best resolution, while the regions towards the pixel edges exhibit a deterioration. When combining the x and y resolutions by adding them in quadrature as shown in Figure 8.22b, the two effects can be correlated. The best position resolution at vertical incidence can be achieved in the very center of the pixel, while the residuals are broader towards the edges, with a stronger effect in the x coordinate.

8.9 Intrinsic Spatial Resolution

Comprehensive studies and angular scans have been performed in order to quantify the achievable spatial resolution of the PSI46digV2.1-r ROC at the various positions in the barrel and endcap regions of the CMS Pixel Detector. The intrinsic resolution is measured by fitting the residual distribution with the generalized error function given in Equation 3.21, and by subtracting the telescope track pointing resolution in quadrature from the obtained distribution width as described in Section 3.5. With the distance dz_{DUT} from the last upstream telescope plane to the DUT given by the alignment, the telescope track resolution is obtained from the calculations presented in Section 7.2.1 for every run individually.

The analyses presented in the following sections require loose telescope track selection (cf. Section 7.5.4) and tight DUT matching (cf. Section 8.4.2) in order to obtain optimal position resolution. However, no downstream telescope tracks and matching with the REF plane is required, and only three-plane tracking is performed in order to exclude any effects from scattering in the DUT installation downstream of the sensor.

The intrinsic resolution is measured as a function of three parameters, namely the CMS Lorentz angle (α in the notation of this analysis), the position of the sensor along the barrel pixel

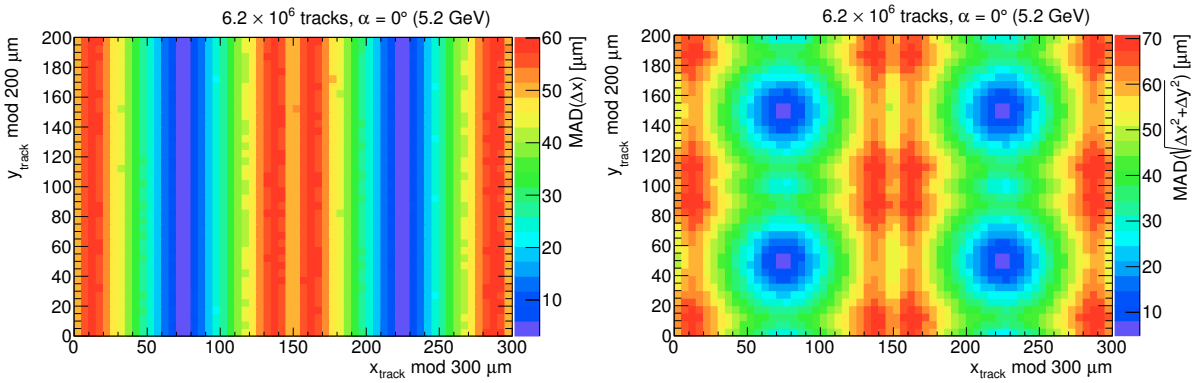

(a) Intra-pixel resolution in x (residual MAD) for vertical incidence.

(b) Combined intra-pixel resolution for vertical incidence, calculated as $\sqrt{\sigma_x^2 + \sigma_y^2}$.

Figure 8.22: Intra-pixel resolution in x (a), and combined x-y resolution (b) as a function of the track incidence position. Both plots show data taken at vertical incidence.

detector (η, or ω), and the pixel charge threshold. Data are compared to simulations where possible, and the best resolutions achieved are quoted.

8.9.1 Resolution as a Function of the Lorentz Angle

With the 3.8 T magnetic field present (cf. Section 2.2.3), the charges produced in the silicon sensor experience the Lorentz force in $r\phi$-direction while drifting to the pixel implants. The resulting Lorentz angle can be mimicked by tilting the sensor in α in order to spread the charge over several rows. The pixel pitch of the sensor has been designed such, that the initial Lorentz angle yields the optimal charge sharing, while increasing radiation induced damage and underdepletion will reduce the effective charge sharing.

The spatial resolution of the PSI46digV2.1-r ROC has been measured as a function of the Lorentz-equivalent tilt angle α using SCM 504 as DUT. Figure 8.23 shows three examples for residual distributions obtained at angles of around 0°, 19°, and 40°. The residuals exhibit the expected features: While the distribution is dominated by one-pixel clusters and thus resembles a box distribution at vertical incidence, the CoG interpolation works best at 19°, where almost exclusively two-pixel clusters are produced, yielding a very narrow residual distribution. Towards large tilt angles, the interpolation becomes more difficult, and noise fluctuations contribute to the broadening of the distribution.

Figure 8.24 presents the obtained position resolution for the full angular scan after subtraction of the telescope track resolution. The pronounced minimum at the optimal charge sharing angle is clearly visible, but also the minimum at three-pixel charge sharing can still be observed. The best resolution is obtained at $\alpha = 19.6°$ as

$$\sigma_x = 4.80 \pm 0.08\,(\text{stat}) \pm 0.28\,(\text{syst})\,\mu\text{m},$$

with the uncertainties calculated as detailed in Section 8.5. The Lorentz angle is expected to decrease with increasing radiation induced damage, and the achieved spatial resolution is thus subject to the steep rise visible for small angles α. However, in Chapter 9 methods are developed to at least partially mitigate this effect and to improve the position resolution for smaller Lorentz angles.

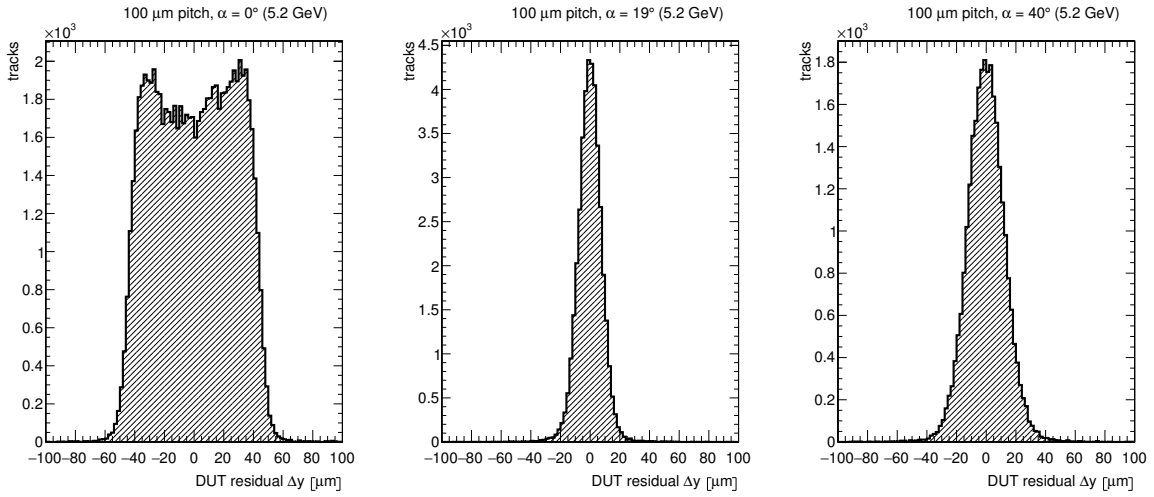

(a) Track angle $\alpha = 0.0°$, width $\sigma = 32.7\,\mu\text{m}$

(b) Track angle $\alpha = 19.6°$, width $\sigma = 6.8\,\mu\text{m}$

(c) Track angle $\alpha = 40.6°$, width $\sigma = 11.5\,\mu\text{m}$

Figure 8.23: Sample residual distributions for SCM 504 along the 100 µm pitch side for different tilt angles α. In addition, the residual width from a fit with the generalized error function is provided.

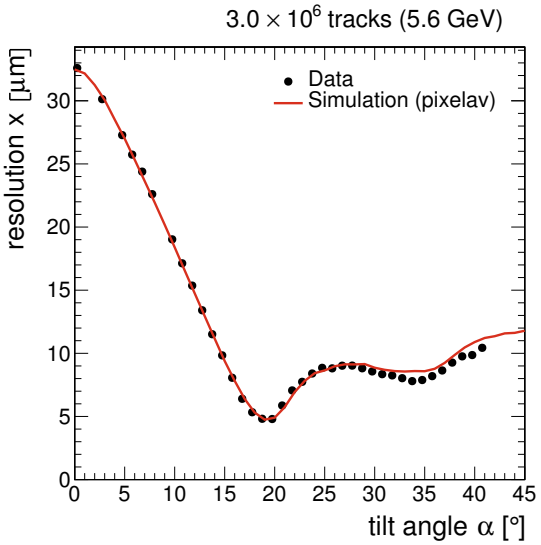

Figure 8.24: Position resolution as a function of the tilt angle α. In CMS, this angle denotes the $r\phi$-direction and is equivalent to the Lorentz angle induced by the magnetic field.

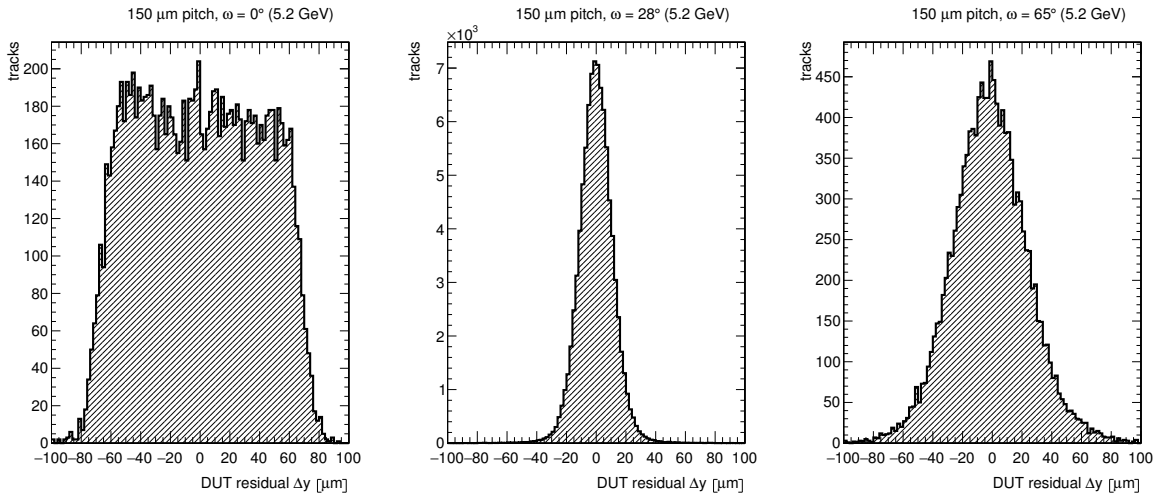

(a) Track angle $\omega = 0.0°$, width $\sigma = 50.2\,\mu\text{m}$

(b) Track angle $\omega = 28.1°$, width $\sigma = 9.7\,\mu\text{m}$

(c) Track angle $\omega = 65.7°$, width $\sigma = 23.0\,\mu\text{m}$

Figure 8.25: Sample residual distributions for SCM 506 along the 150 µm pitch side for different tilt angles ω. In addition, the residual width from a fit with the generalized error function is presented.

8.9.2 Resolution as a Function of the Pseudorapidity

The pixel detector barrel extends by almost 300 mm in both directions from the IP as discussed in Section 4.4, and the track dip angles in the sensors vary accordingly. The approximate maximum track dip angles expected for each of the detector layers can be taken from Figure 4.7. However, owing to the position uncertainty of the IP, these angles are expected to change significantly on an event-by-event basis. Rotating the DUT assembly in the test beam around the column direction as possible with SCM 506 allows to mimic different track dip angles ω, and provides the possibility of studying the expected detector performance at different positions along the barrel.

Figure 8.25 shows three sample residual distributions at vertical track incidence, at two-pixel charge sharing around $\omega = 28°$, and at high tilt angles of $\omega = 65°$, where very long clusters are expected. Again, the shape of the distributions follows the expectations, from a box shape at vertical incidence to a very narrow Gaussian distribution at two-pixel charge sharing, towards broader Gaussian shapes for long clusters.

The full angular scan up to $\omega = 82°$ is presented in Figure 8.26, plotted both as a function of the tilt angle ω and as a function of the pseudorapidity η as defined in Equation 2.3. The optimal resolution has been measured at a track dip angle of $\omega = 27.1°$ ($|\eta| = 0.49$) and yields

$$\sigma_y = 7.99 \pm 0.09\,(\text{stat}) \pm 0.21\,(\text{syst})\,\mu\text{m}.$$

It is worthwhile pointing out that the blades of the forward pixel detector are tilted such, that optimal charge sharing over two pixels with 150 µm pitch is ensured as discussed in Section 4.1. Thus, the position resolution of the forward detector modules is expected to be around this optimal value, independent of their position in the disks.

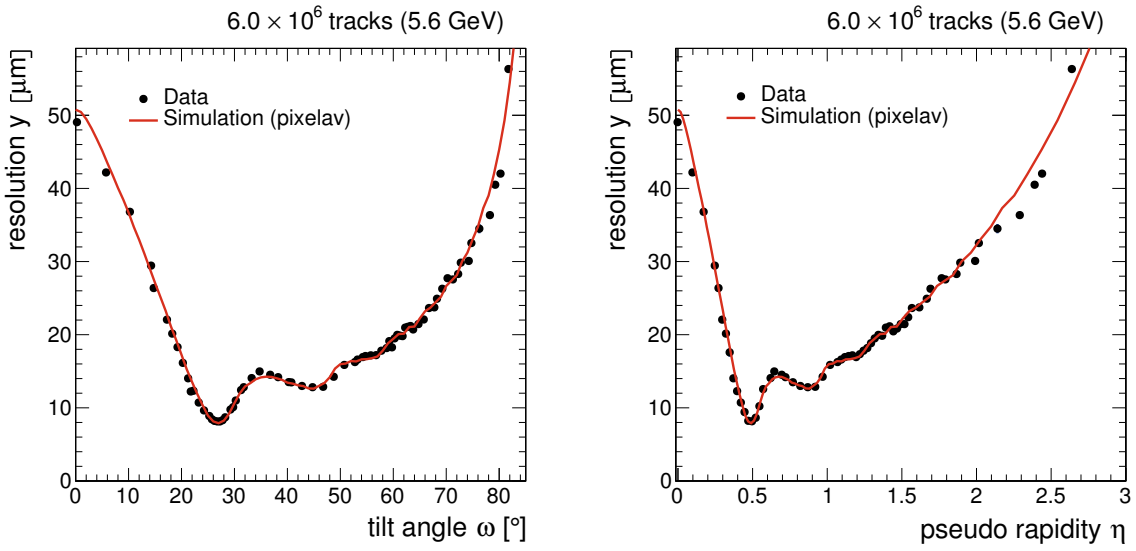

Figure 8.26: Position resolution as a function of the track dip angle ω (left) and the pseudorapidity η (right). The minima for two-pixel and three-pixel charge sharing can be distinguished, while higher order minima are diluted.

8.9.3 Resolution as a Function of the Pixel Threshold

The pixel charge threshold is a crucial parameter for the position resolution. With rising threshold, it is more likely that edge pixels of the cluster do not collect the required charge and thus do not pass the threshold. This has an impact on the interpolated cluster position and can be quantified by studying the chip behavior at different threshold settings. These threshold measurements have been performed using SCM 504 at a track incidence angle of $\alpha = 19.5°$, which is close to the optimum along the 100 µm pixel pitch (cf. Section 8.9.1). The trigger timing has been optimized for every comparator threshold setting independently, however, the threshold dependency on the timing is small for the PSI46digV2.1-r ROC as indicated in Figure 6.3b. The gain calibration described in Section 8.2 is repeated for each threshold setting.

The simulation shown in the following figures should be treated with caution. As described in Section 5.3, the digitization of the deposited charge is far from being sophisticated, and follows a rather simplistic model which has been tuned to test beam data. Simulations for different charge thresholds have been obtained by tuning the simulation to a threshold of 1.7 ke and then simply scaling it to the desired value.

Lost pixels at cluster edges can be visualized by comparing the mean cluster sizes measured at the same track incidence angle for different charge thresholds as demonstrated in Figure 8.27a. The mean cluster size slightly decreases with rising charge threshold, as expected. A similar behavior can be observed for the Landau MPV of the total cluster charge shown in Figure 8.27b, as more and more pixel charges do not pass the increasing threshold level.

Finally, the dependency of the position resolution on the charge threshold is shown in Figure 8.28. The spatial resolution is improved by about 20 % by reducing the pixel charge threshold from the operation value of the PSI46V2 ROC of 3.2 ke to a threshold of 1.7 ke achievable with the PSI46digV2.1-r ROC. The best resolution confirms the measurement from Section 8.9.1.

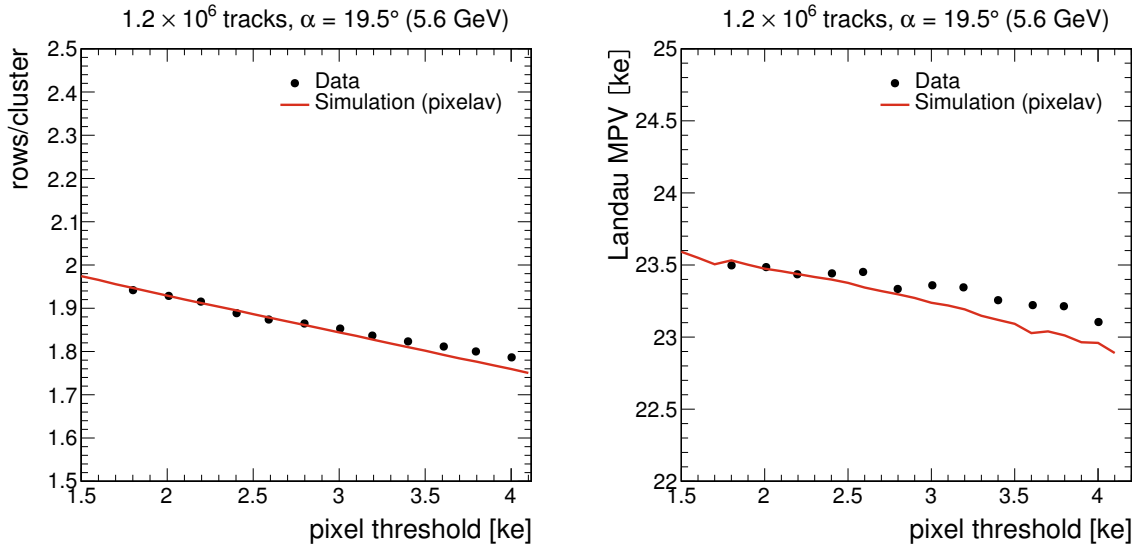

(a) Mean cluster size as a function of the ROC pixel threshold.

(b) Landau MPV as a function of the ROC pixel threshold.

Figure 8.27: Dependency of the mean cluster size (a) and the Landau MPV (b) on the pixel threshold of the ROC. Both show the expected slight reduction towards higher thresholds caused by charge signals at the cluster edges not passing the threshold.

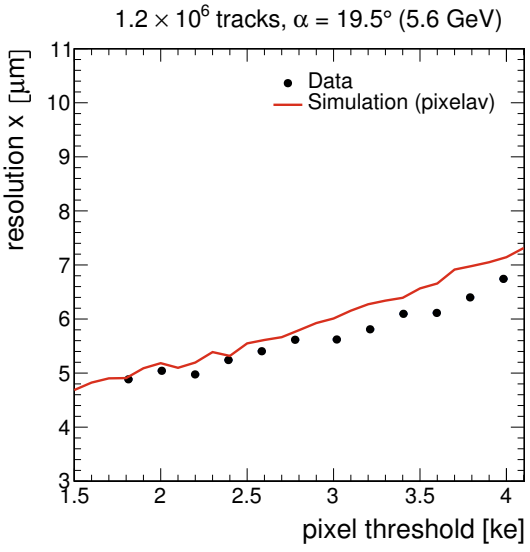

Figure 8.28: Spatial resolution as a function of the ROC pixel threshold, for a tilt angle of $\alpha = 19.5°$. The resolution improves with lower thresholds as expected.

8.10 Summary

Comprehensive test beam measurements have been performed at the DESY-II synchrotron in order to characterize the behavior of the PSI46digV2.1-r ROC under conditions close to the final deployment situation. The tracking efficiency is uniform over the full sensor volume and does not show a dependency on the operation time. The efficiency for tracks producing mostly two-pixel clusters ($\alpha = 21°$) has been measured to be $\epsilon = 99.70 \pm 0.01\,(\text{stat})\,^{+0.3}_{-0.5}\,(\text{syst})\,\%$.

Detailed studies of various intra-pixel quantities such as resolution and tracking efficiency have been performed. The quite distinct charge deficit at the bias dot at vertical track incidence is mitigated by rotating the sensor. This scenario resembles more closely the situation to be expected in the experiment, and the measured charge loss is only about 10 %. While the tracking efficiency does not seem to be influenced by the reduction in collected charge even at vertical incidence, small variations in the position resolution can be measured around the bias dots for track incidence angles around 20°. At vertical incidence, the resolution variations within the pixel cell are dominated by effects from single-pixel clusters and edge effects between the pixel cells.

The spatial resolution has been measured as a function of the angle along columns and rows. The minimal row resolution along the 100 µm pixel pitch is $\sigma_x = 4.80 \pm 0.08\,(\text{stat}) \pm 0.28\,(\text{syst})\,\mu\text{m}$. The equivalent orientation in the CMS experiment is $r\phi$, and the charge sharing is determined by the Lorentz angle. The optimal column resolution along the 150 µm pitch side, i.e., η in CMS, is determined to be $\sigma_y = 7.99 \pm 0.09\,(\text{stat}) \pm 0.21\,(\text{syst})\,\mu\text{m}$. Finally, the dependency of the position resolution on the pixel charge threshold has been measured. An improvement of 20 % can be observed when reducing the threshold from the present in-time threshold of the PSI46V2 ROC of 3.2 ke to a threshold of 1.7 ke as possible with the PSI46digV2.1-r ROC.

9. Improving the Position Resolution Using the Cluster Skewness

The position resolution achieved with segmented silicon detectors depends on a large set of parameters. The pixel or strip geometry plays a predominant role and defines the binary resolution of the sensor via the implant pitch. The signal formation in silicon sensors is influenced by diffusion, delta ray contributions as well as thermal noise. Additional impacts on the signal quality such as cross talk, threshold effects or inefficiencies arise from the front-end electronics. Depending on the operation mode, either a binary signal is emitted, or the actual pulse is amplified, shaped and sampled, which adds additional ADC noise. Finally, the cluster position is reconstructed in software. The algorithm can influence the effective position resolution by exploiting the full information available, and by correcting for certain characteristics of the detector. While some biases in the position determination are unavoidable owing to the finite pixel size, other systematic effects can be reduced significantly, e.g., by charge-weighted interpolation.

The center of gravity (CoG) algorithm employed in Chapter 8 for instance uses the mean of the pixel charge distribution to weight the contribution of every pixel cell to the track impact position. However, this algorithm has a strong dependence on the track incidence angle and only yields the best possible resolution at the optimal charge sharing angle for two-pixel clusters (cf. Sections 8.1 and 8.9). Around this minimum, steep slopes are present, deteriorating the position resolution already for angles deviating only slightly from the optimal incidence angle.

This chapter aims to explore the possibilities of improving the track impact interpolation by using a higher order moment of the charge distribution. Particular attention is paid to the position resolution around the track incidence angle of optimal charge sharing. First, the notion of central moments of distributions is discussed in Section 9.1. Section 9.2 provides details on the calculation of the cluster skewness from the third central moment. The position dependency of the cluster skewness can be parametrized, and parameters can be obtained from either data or independent simulations as demonstrated in Section 9.3. The improvement in spatial resolution is evaluated in Section 9.4 by applying the skew corrections to the results obtained in Chapter 8. Finally, Section 9.5 provides a brief summary of the findings.

9.1 Central Moments of a Distribution

Moments of a distribution are quantitative measures of its shape and can be used to investigate certain aspects of the contained random variable. The n-th moment of a distribution is defined as [188]

$$\mu_n = \int_{-\infty}^{+\infty} (x - c)^n f(x)\, dx, \tag{9.1}$$

where $f(x)$ denotes the probability density function. For raw moments, $c = 0$ is chosen and the zeroth moment yields the integral of the probability density function. The first raw moment ($n = 1$) is employed by the CoG algorithm described in Section 3.3.1, and represents the mean μ of the distribution.

Choosing this mean as the reference value for the random variable, $c = \mu$, allows to calculate the central moments of the distribution. Central moments are more useful for higher powers of n since they contain more information about the shape of the distribution rather than the absolute position. For binned distributions, Equation 9.1 can be rewritten for central moments as

$$\mu_n = \sum_i (x_i - \mu)^n f(x_i)\,. \tag{9.2}$$

The central moment μ_n can be interpreted as the expectation value of power n for the deviation from the mean μ. The low-order central moments do not carry any information owing to the reference value chosen, hence the zeroth central moment equals $\mu_0 = 1$, while the first central moment is $\mu_1 = 0$. Only the second central moment μ_2 has an informative value and represents the variance $\mathrm{Var}(x) = \sigma^2$ of the distribution and thus the resolution.

The lopsidedness or *skewness* of a distribution is described by the third central moment μ_3 [189]. Any symmetric distribution will have a third central moment equal to zero, for asymmetric distributions the skewness provides a measure for its imbalance. This sensitivity will be used in the following to correct for systematic effects observed in the position resolution within pixel cells.

9.2 The Cluster Skewness

The cluster skewness distribution is determined as a function of the track incidence angle in order to explore its sensitivity on the position resolution. Only clusters which fulfill the selection criteria and are fully contained within the fiducial volume of the sensor are considered (cf. Section 8.4). The skewness of a cluster is then calculated from the third central moment with additional normalization parameters, viz.

$$\mu_3 = \frac{1}{(N/2)^3} \cdot \frac{\sum_i (x_i - \mu)^3 Q(x_i)}{\sum_i Q(x_i)}, \tag{9.3}$$

where $Q(x_i)$ denotes the charge and x_i the position of pixel i, the term μ is the mean cluster position as determined from the CoG algorithm, and $\sum Q(x_i)$ is the total charge of the cluster. N represents the total number of pixels in the cluster, and the factor $(N/2)^3$ serves as normalization to the total cluster length. The cluster skewness is a dimensionless quantity since all measures of length are given in fractions of the pixel pitch.

The shape of the obtained distributions varies with the incidence angle as exemplified in Figure 9.1, but is always symmetric and centered around zero. For small track angles, the distribution is dominated by a sickle shape clearly visible in Figure 9.1a. With growing incidence angles

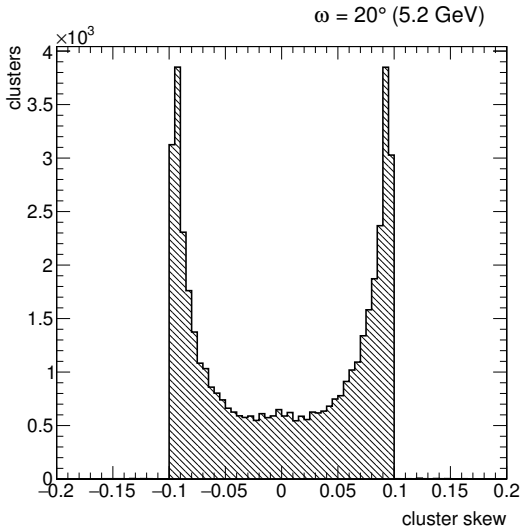

(a) Sickle shaped skewness distribution at small angles around $\omega = 20°$

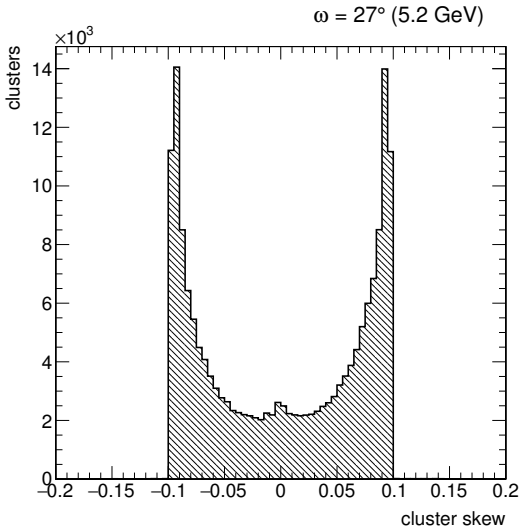

(b) Appearance of a central contribution around zero at $\omega = 27°$

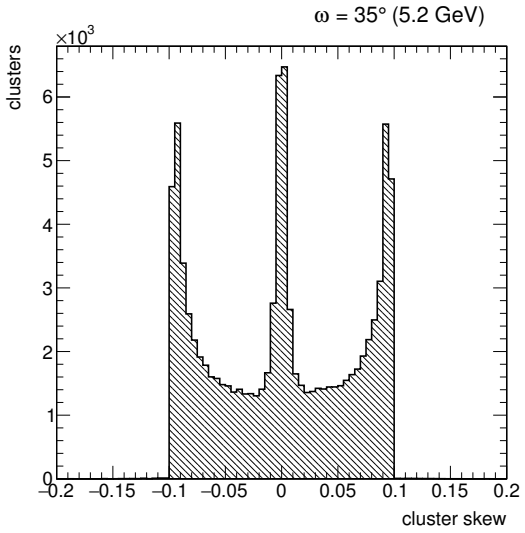

(c) Sickle and central part are of equal magnitude around $\omega = 35°$

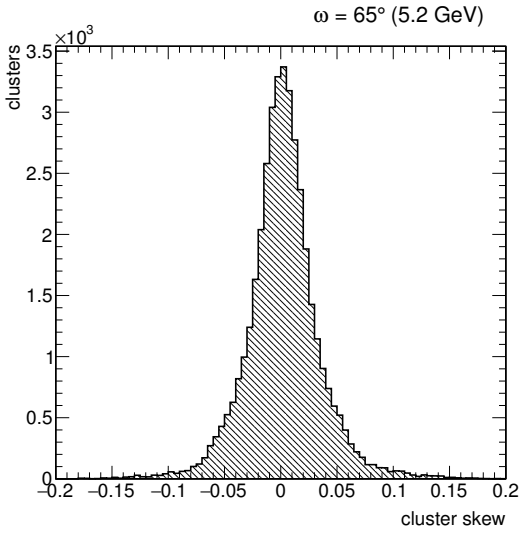

(d) Gaussian shape dominating the skewness for large angle $\omega = 65°$

Figure 9.1: Cluster skew μ_3 distributions for different track incidence angles. The shape changes with increasing angle. The limitation to $|\mu_3| < 0.1$ arises from the normalization to the total cluster charge, while entries exceeding this value can be identified with clusters with high charge.

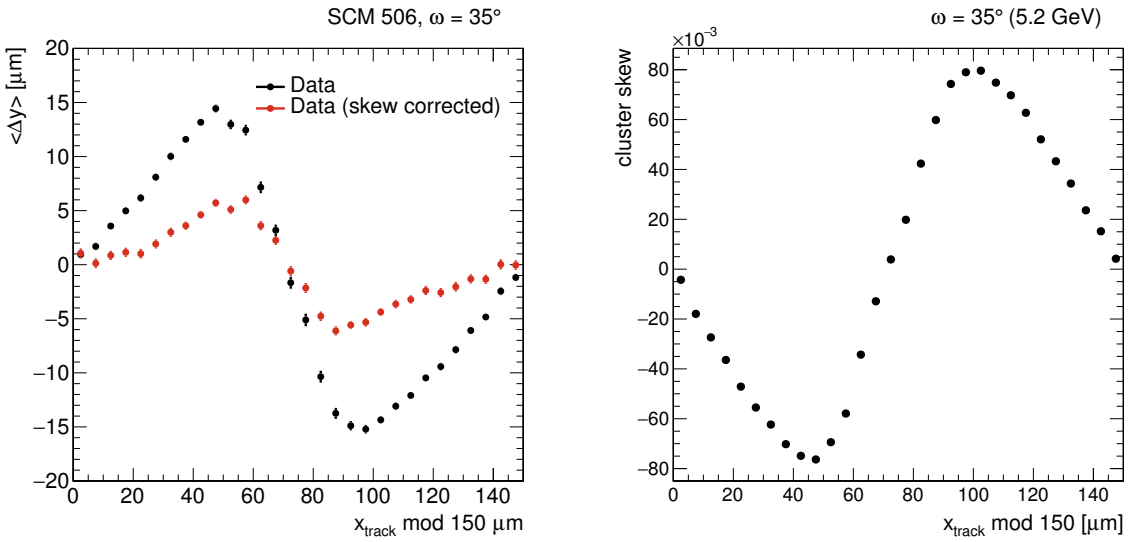

(a) Residual mean in y as a function of the track position along the x axis within the pixel.

(b) Cluster skewness as a function of the track impact position within the pixel.

Figure 9.2: Residual mean and skewness at $\omega = 35°$, between two- and three-pixel charge sharing. A strong effect can be seen in the residual mean and the cluster skewness.

of the particle track and thus longer clusters, a central contribution is added to the skewness distribution which is barely noticeable at $\omega = 27°$ (Figure 9.1b) but is of equal magnitude as the sickle at $\omega = 35°$ as shown in Figure 9.1c. A broadening of the central contribution can be observed for increasing track incidence angles. For large track angles the skewness distribution looses its distinct sickle shape and mostly resembles the Gaussian distribution presented in Figure 9.1d. The distributions shown are obtained from test beam data, but qualitatively the same shapes have also been extracted from Pixelav simulations as demonstrated in Figure C.1 in the Appendix. The limitation of the skewness distributions to the range $|\mu_3| \leq 0.1$ arises from the normalization to the total cluster charge. Further details on the normalization of the distribution are provided in Appendix C.

Both the mean of the track residual and the cluster skewness exhibit a dependency on the track impact position within the single PUC as shown in Figure 9.2. At the optimal angle, hardly any systematic shifts of the residual position can be noticed, while the large variations in Figure 9.2a broaden the distribution at other track impact angles. This systematic shift of the residual mean is a large contribution to the deterioration of the position resolution for angles differing from the angle of optimal charge sharing. The systematic dependency of the cluster skewness in Figure 9.2b exhibits the same shape as the residual dependence and suggests a correlation between the two parameters.

Figure 9.3 shows the mean residual position $\langle \Delta y \rangle$ as a function of the cluster skewness for different track incidence angles. A clear correlation can be observed, and the slope of the distribution scales as expected with the magnitude of the variations in $\langle \Delta y \rangle$: While the distribution is flat and shows no dependency around the optimal two-pixel charge sharing at $\omega = 27°$, steeper slopes are observed for other track angles. The outliers of the distributions at skew values $|\mu_3| > 0.1$ originate from clusters with large total cluster charges as detailed in Appendix C.

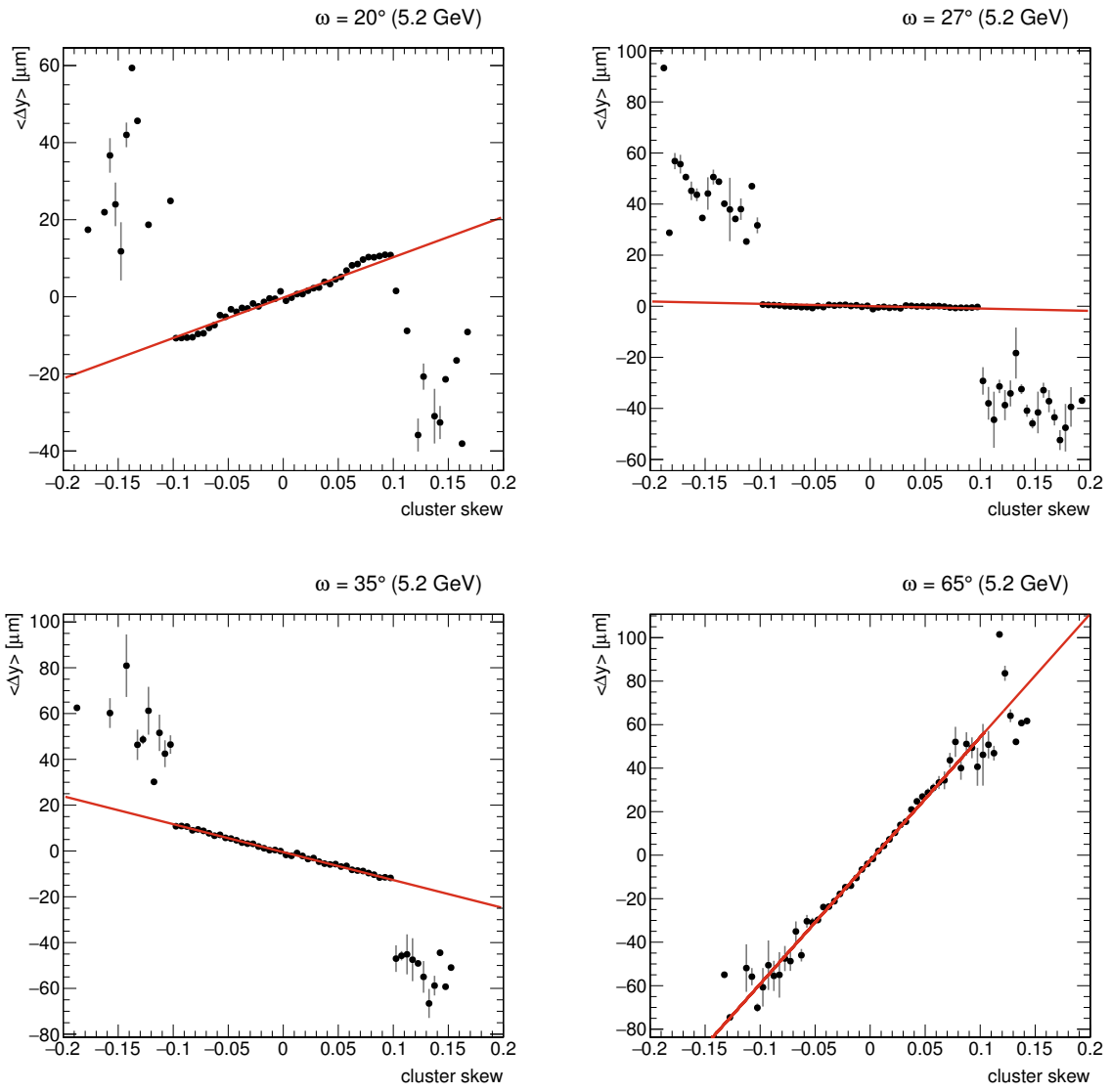

Figure 9.3: Residual mean position in y as function of the cluster skewness for different track incidence angles ω. Shown is the distribution as obtained from data as well as a linear fit to the central part of the distribution with $|\mu_3| \leq 0.1$.

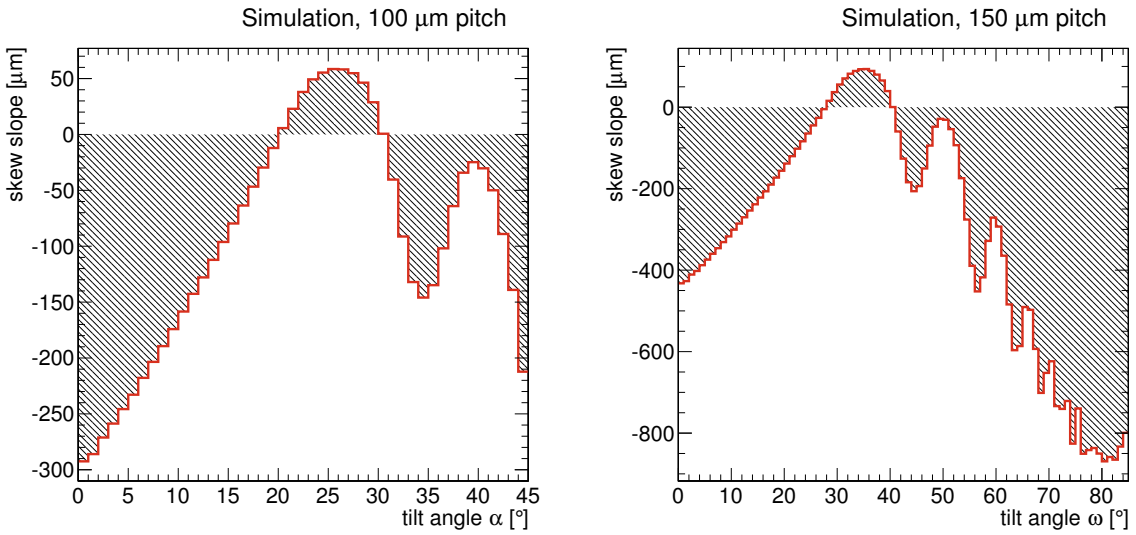

Figure 9.4: Slope of the linear fit to the residual shift vs. skewness distribution as obtained from simulations. (left) shows the slope parameter for a pixel pitch of 100 µm while (right) provides the same parameter for a pitch of 150 µm.

9.3 Skewness Parametrization and Cluster Position Correction

The cluster position can be corrected for the systematic effect observed in Figure 9.3 by parametrizing and correcting its dependency on the cluster skewness. A linear regression has been identified as the best compromise between accurate description of the distribution, stability of the fit and simplicity of the parametrization to be obtained for every angle. The dominant contribution stems from the slope p_1 of the linear regression, while the offset p_0 would constitute a global shift of the residual mean. Hence, the offset parameter should only show deviations in the sub-micron range as the global shift is accounted for by the alignment procedure.

The parameters have to be obtained for every track angle separately and can be retrieved either from data or from the Pixelav simulations, which exhibit very similar cluster skewness dependencies. The dominating slope parameter for the linear fit to simulated events is shown in Figure 9.4 as a function of the two tilt angles. The observed shape correlates with the expected minima in the position resolution from two-pixel, three-pixel, etc. charge sharing. Fit parameters for all angles are determined and stored in a lookup table, from where the correction factors can be retrieved depending on the individual track impact angle. The residuals are corrected by

$$\Delta y^{\text{corr.}} = \Delta y - (p_0 + p_1 \mu_3)\,, \tag{9.4}$$

where Δy is the uncorrected residual, p_0 and p_1 denote the parameters obtained from the linear regression, and μ_3 represents the cluster skewness calculated from Equation 9.3. Figure 9.5 shows the residual mean $\langle \Delta y \rangle$ as a function of the cluster skewness before and after the skewness correction for two different angles. While the original distributions exhibit slopes, the corrected distributions do not show a dependency on the cluster skewness. The correction allows to reduce the systematic shifts within the pixel cell as demonstrated by the skew-corrected curve in Figure 9.2a. The RMS as a function of the track position with and without skewness correction is compared in Figure 9.6, and an overall reduction of the RMS can be observed.

Other fit functions such as a third-order polynomial or a sine wave function have also been investigated but do not show significant improvements while adding additional complexity to the parametrization (cf. Appendix C).

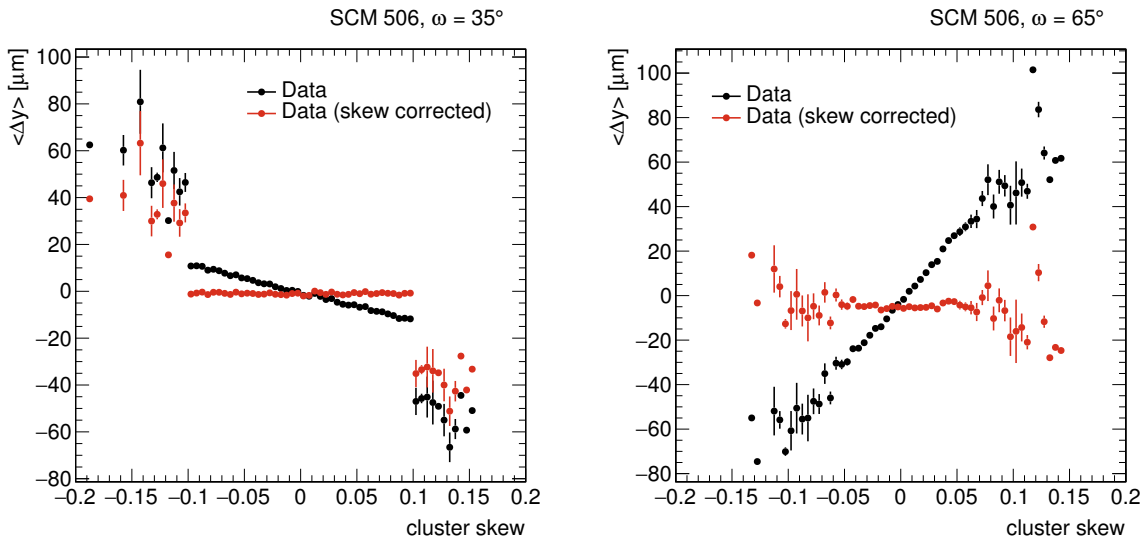

Figure 9.5: Residual mean as a function of the cluster skewness before and after applying the correction. The distributions are shown for the two different angles $\omega = 35°$ and $\omega = 65°$. After the correction, the residual mean position is independent of the cluster skewness.

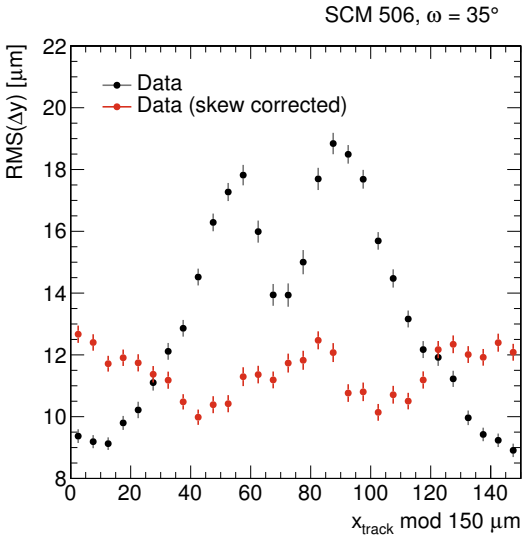

Figure 9.6: RMS of the residual distribution in y as a function of the track position along the x axis within one PUC. Shown are the curves before and after cluster skewness correction for a tilt angle of $\omega = 35°$. A unification and an overall improvement of the RMS can be observed.

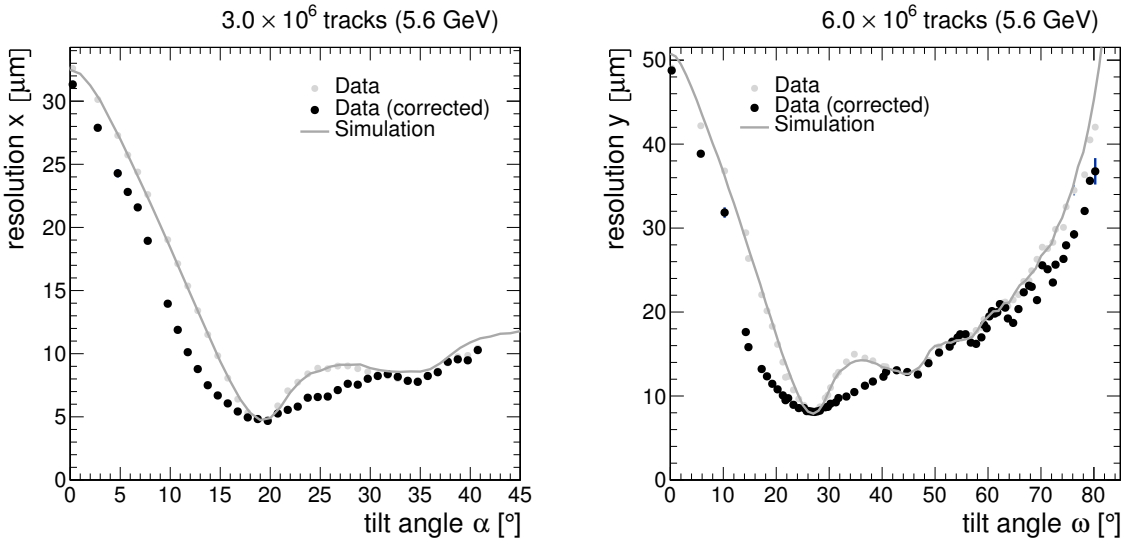

(a) Skewness corrected position resolution as a function of the tilt angle α.

(b) Skewness corrected position resolution as a function of the track dip angle ω.

Figure 9.7: Position resolution as function of the track incidence angles with and without skewness correction applied, shown are both data and simulation. The skewness parameters for the correction are derived from data.

9.4 Applying the Skew Correction to Test Beam Data

Applying the skew correction to the interpolated hit position allows to greatly reduce the systematic in-pixel shift of the residual mean and RMS as demonstrated in the previous section. In the following, the skewness correction factors are applied to the test beam results presented in Sections 8.9.1 and 8.9.2 in order to quantify the achievable improvement in position resolution for different track incidence angles. The results for correction factors obtained from data and from Pixelav simulations are compared.

The dependency of the skewness on the track incidence angle is rather strong and the angle has to be known precisely in order to select and apply the appropriate skewness correction parameters. Only with the correct parametrization, an improvement of the resolution can be achieved.

If the skewness parametrization is derived from data with good alignment as described in Section 9.4.1, the track angle is known sufficiently precise and the correction performs well. The correction using correction factors obtained from simulations as discussed in Section 9.4.2 requires exact matching of data and simulation in order to predict the exact charge sharing correctly.

9.4.1 Correction with Data Skewness

The test beam data presented in Chapter 8 were analyzed in two passes in order to correct for the systematic variation of the cluster skewness. In the first pass, no correction is applied but the cluster skewness is parametrized to obtain the correction factors. This correction is then applied to the same data in the second pass. While this does not allow statistically independent correction of the data due to the same samples being used twice, it can still be used to demonstrate the capabilities of the method.

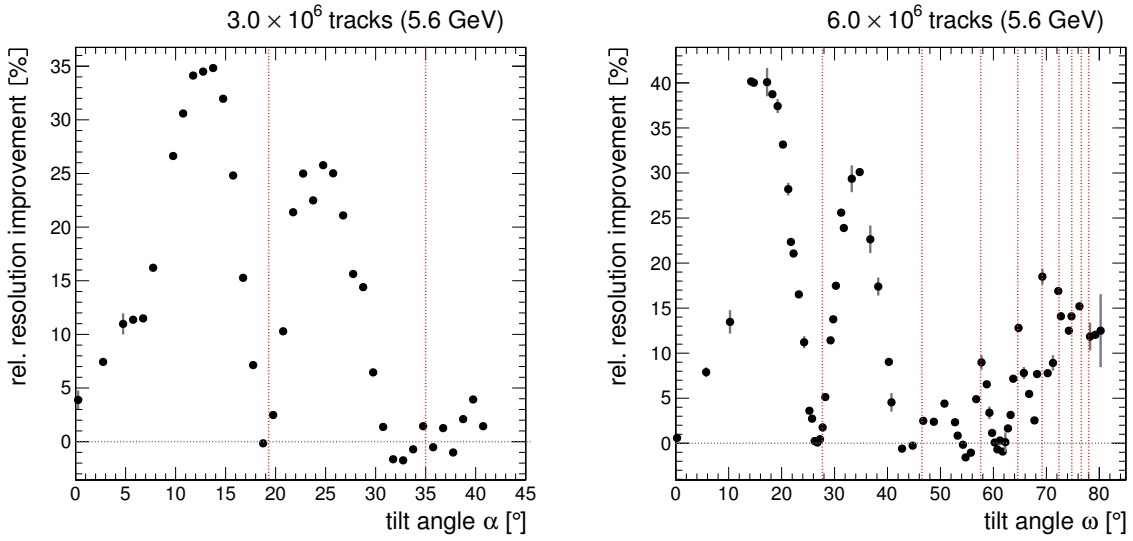

Figure 9.8: Relative improvement of the position resolution after the cluster skewness correction, plotted as a function of the track incidence angles. The red-dashed lines indicate the angles of two-pixel, three-pixel, etc. charge sharing. (left) shows the data for a pixel pitch of 100 µm, while (right) presents the improvements for 150 µm pixel pitch.

Figure 9.7 shows the original, uncorrected test beam data together with the data corrected for the cluster skewness for both tilt directions α (with 100 µm pixel pitch) and ω (pitch 150 µm). The impact of the skew correction is strongest in the vicinity of the minimum of optimal charge sharing while there is only a marginal improvement at the minimum itself. The charge distribution at this point is balanced and barely exhibits any skewness.

The strong correction towards lower angles α is of particular interest. With increasing radiation damage in the silicon sensor, the charge carriers are subject to trapping and reduced diffusion. Both effects lead to a decrease of the Lorentz charge sharing angle, and thus to a smaller average cluster size (cf. Section 3.1.5). Hence, the position resolution changes from the minimum at the optimal charge sharing angle towards higher values at lower track incidence angles.

The correction impact is particularly large at small angles but vanishes for vertical particle incidence because of the reduced fraction of two-pixel clusters. Since only clusters with charge sharing, i.e., with more than one pixel can be corrected, the contribution of corrected clusters to the total residual vanishes for small angles and the resolution is dominated by the box distribution of the binary pixel resolution. At larger angles the impact of the skewness correction is reduced despite the large correction parameters indicated in Figure 9.4. The charge distribution skewness seems to be diluted by the large cluster length and renders the distribution insensitive to corrections via the Gaussian-distributed skewness.

The relative enhancement of the position resolution at different track angles is shown in Figure 9.8. The skew correction yields a maximum improvement of up to 40 % over the resolution obtained from the CoG algorithm, which is achieved around $\omega = 20°$ track incidence along the 150 µm pitch. Up to 35 % improvement can be achieved at angles of around $\alpha = 12°$ for a pitch of 100 µm.

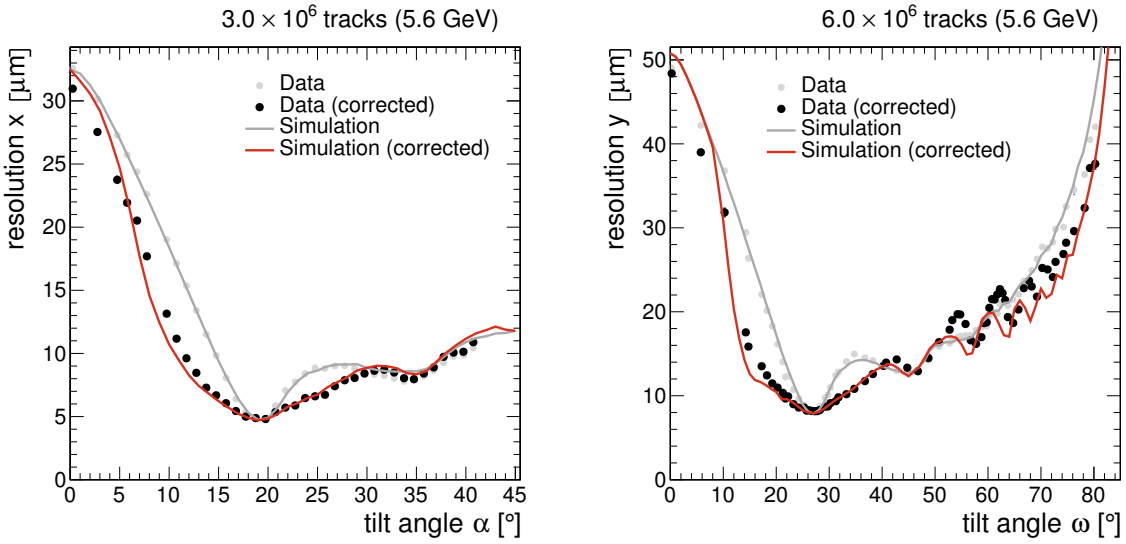

Figure 9.9: Position resolution as function of the track incidence angles with and without skewness correction applied, shown are both data and simulation. The skewness parameters applied to data and simulation are derived from simulation and produce similar results as for the correction with data.

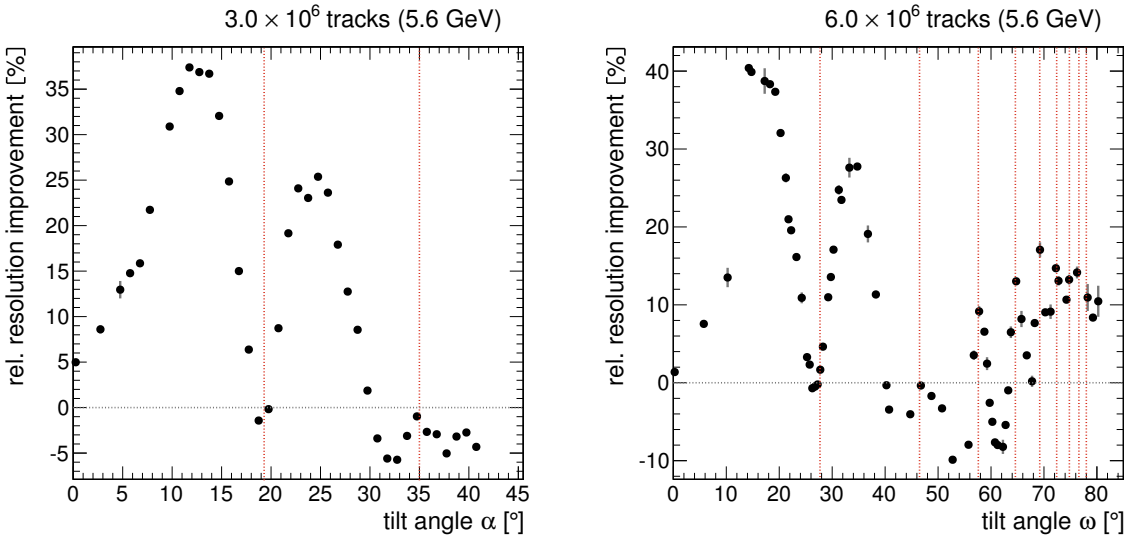

Figure 9.10: Relative improvement of the position resolution after correction with the simulated skewness. The red-dashed lines indicate the angles of two-pixel, three-pixel, etc. charge sharing. (left) shows the results for 100 µm pitch data, (right) for 150 µm pixel pitch. Especially at large angles some deterioration can be observed due to inaccurate description of the data by the simulation.

9.4.2 Correction with Simulation Skewness

A more independent approach is the correction of systematic effects via simulations. The cluster skewness is correctly described by the PIXELAV simulation and the extraction of the respective parametrization from simulations is well possible as shown in Section 9.3. The test beam data is thus analyzed using the correction factors obtained from the simulation.

Figure 9.9 presents the corrected position resolution as a function of the two track incidence angles. Similar results as for the correction with data parametrization can be achieved, however, some regions experience a deterioration of the resolution compared to the CoG algorithm. The broadening of the residual entails deviations from the original position resolution of up to 10 % as indicated in Figure 9.10 for tilt angles $\alpha \approx 55°$ along the 150 µm pitch side. The simulation for the short pitch side does seem to describe data better and only negative deviations of up to 5 % can be observed.

This effect originates from two features of the simulation. First, the matching between data and simulation for very long clusters is apparently not sufficiently precise. As a result, the skewness parametrization from the simulation at a given track angle does not describe the skewness distribution obtained from data at the same track angle, and thus the correction produces erroneous results.

Furthermore, some of the $\langle \Delta y \rangle$ versus skew distributions seem to deviate strongly from the linear form described in Section 9.3. Thus, a linear fit does not reproduce the features of the dependency, and the applied correction does not allow for a reduction of the systematic shifts. A non-linear fit function which correctly describes the cluster skewness dependency at these track angles might help to improve the obtained resolution but requires additional investigation. Some first ideas are presented in Appendix C.

9.5 Summary

The third central moment of the cluster charge distribution has shown to be sensitive to the mean value of the residual distribution as a function of the track impact position. Using this cluster skewness as parametrization for the residual mean shift allows to reduce the systematic variations within single pixel cells and thereby improve the position resolution significantly. The strongest impact has been observed for track incidence angles close to the optimal two-pixel charge sharing, where improvements of up to 40 % over the uncorrected CoG position resolution can be achieved.

The PIXELAV simulation is able to reproduce the cluster skewness, and correction parameters can thus either be derived from data or from simulations. Further investigation is needed for problematic regions with non-linear dependency of $\langle \Delta y \rangle$ on the cluster skewness, and for the correction of large clusters due to the reduced sensitivity on the skewness.

A possible application in the CMS experiment would require the approximate angle information from the correlation between track angle and location of the hit within the detector. The corresponding skewness correction would then be retrieved from a database and applied to the interpolated cluster center. Further research could be dedicated to combining the cluster skewness correction and the template matching algorithm [81, 119, 120] currently used by the CMS experiment (cf. Section 3.3.1). This would allow to significantly improve the performance of the detector, especially for the decreasing Lorentz charge sharing angle caused by radiation-induced defects in the silicon sensor (cf. Section 3.1.5).

Part II

Determination of the Normalized $\mathrm{t\bar{t}}$+jet Invariant Mass Distribution and Measurement of the Top Quark Mass

10. Introduction to Top Quark Physics and the Measurement

The third quark generation in the standard model (SM) of particle physics was predicted as an explanation for CP violation [26]. The lighter quark of the new generation, the bottom quark, was discovered in 1977 [190]. However, due to its large mass, the top quark was not measured until 1995, when the two Tevatron experiments Collision Detector at Fermilab (CDF) [9] and D0 [10] announced the discovery of a new quark in proton-antiproton collisions with a center-of-mass energy of $\sqrt{s} = 1.8\,\text{TeV}$. The Tevatron accelerator was the only source of top quarks until the start-up of the LHC machine in 2010. Then, already in Run 1 the LHC collisions produced more top quark events than all data collected by the Tevatron experiments, owing to the larger luminosity and cross section for the production of top quark pairs and single top quarks at the higher center-of-mass energy, as will be discussed in Section 10.1.

The top quark is a spin 1/2 fermion, carries color charge, and thus participates in the strong interaction. The top isospin is $I_3 = 1/2$ as the partner of the b quark, and being an *up*-type quark, its electrical charge is $Q_t = 2/3$, according to the SM. Due to its large mass, the top quark is an extremely elusive object and decays even before hadronization as will be described in Section 10.2. Its decay width Γ_t is smaller than the currently achievable experimental resolution and it thus cannot be measured directly at hadron colliders. However, indirect measurements are possible via the production cross sections of top-antitop quark pairs ($\text{t}\bar{\text{t}}$) and single top quarks (single-t). Section 10.3 gives a brief outlook on the relevance of the top quark for physics within and beyond the SM. Detailed reviews of top quark physics discussing its properties as well as implications for the potential discovery of new physics can be found in [191, 192].

The mass of top quark as the heaviest elementary particle known to date is of special interest and has thus been measured by all major collider experiments at both the Tevatron and the LHC. The measurements have been combined to a world average yielding a top quark mass of $m_t = 173.34 \pm 0.27\,(\text{stat}) \pm 0.71\,(\text{syst})\,\text{GeV}$ [193], while the most recent combination of direct measurements by the CMS experiment yields $m_t = 172.44 \pm 0.13\,(\text{stat}) \pm 0.41\,(\text{syst})\,\text{GeV}$ [11]. However, the relation of this measured mass to well-defined theoretical top quark masses is not entirely clear as will be discussed in Section 10.4. The measurement presented in this part of the thesis extracts a theoretically well-defined top quark mass from top quark pair events produced in association with an additional hard jet. The definition of the observable as well as further details on the analysis are given in Section 10.5.

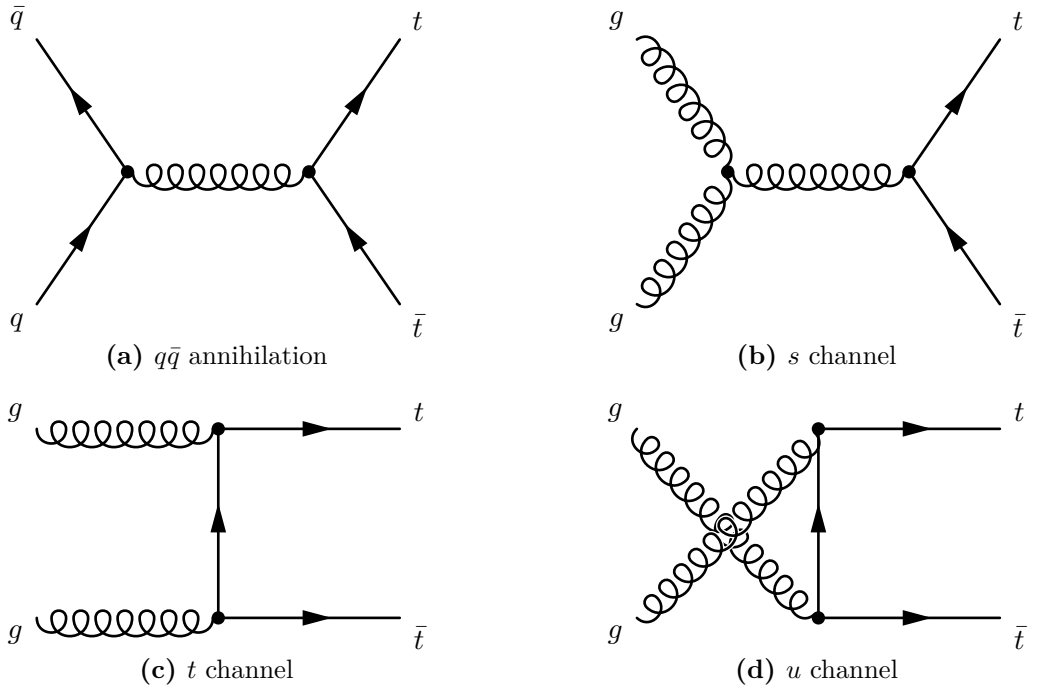

(a) $q\bar{q}$ annihilation **(b)** s channel **(c)** t channel **(d)** u channel

Figure 10.1: Production channels of top quark pairs via the strong interaction at leading order of perturbation QCD.

10.1 Top Quark Production Mechanisms

Top quarks are colored objects and can thus be produced either in pairs via the strong interaction preserving quark flavor, or individually via electroweak processes (cf. Section 1.1). The dominant contribution at hadron colliders stems from the strong pair production, which is the production mechanism considered for the analysis presented.

10.1.1 $t\bar{t}$ Production

At tree level in perturbation theory (cf. Section 1.1.2) $t\bar{t}$ are either produced via gluon-gluon fusion or quark-antiquark annihilation as shown in Figure 10.1. The production via quark-gluon scattering $qg \to t\bar{t}q'$ only appears at NLO level of the perturbative series expansion.

The production threshold for $t\bar{t}$ is $\sqrt{\hat{s}} = m_{t\bar{t}} = 2m_t \approx 346\,\text{GeV}$ where $\sqrt{\hat{s}} = \sqrt{x_1 x_2 s}$ denotes the partonic center-of-mass energy of the collision, $m_{t\bar{t}}$ and m_t are the invariant masses of the $t\bar{t}$ system and the top quark, respectively, and x_i are the momentum fractions of the two partons. For $t\bar{t}$ produced at central rapidity $y = 0$ at the LHC with a collision energy of 8 TeV this leads to momentum fractions of

$$x_1 = x_2 = \frac{2m_t}{\sqrt{s}} \approx 0.043. \tag{10.1}$$

At these values of x, the PDFs are dominated by gluons (cf. Figure 1.2) which makes the gluon-gluon fusion the predominant reaction around the production threshold. The contribution of quark-antiquark annihilation to the total production cross section rises with increasing invariant mass.

10.1.2 Single Top Quarks

Individual top quarks are produced in electroweak processes via three channels: The exchange of a virtual W boson in the t-channel and s-channel, and the associated production of the t quark in conjunction with a real W boson. The s-channel requires the production of a W boson via quark-antiquark annihilation and is thus suppressed at the LHC as no valence antiquarks are present in the initial state.

Since the cross sections are directly proportional to the respective CKM amplitude, single top quarks allow studies of charged weak interactions such as the direct measurement of the Wtb vertex coupling.

10.2 The Top Quark Decay

With three quark generations available, top quarks decay via electroweak interaction to W bosons plus either b, s, or d quarks. The branching fractions for different quark flavors are given by the squares of the CKM matrix elements $|V_{tq}|^2$ with $q = b, s, d$ as described in Section 1.1.1. Due to the unitarity of the CKM matrix and $|V_{tb}| \approx 1$, the decay is dominated by the process $\mathrm{t} \to \mathrm{bW}^+$ with a branching ratio of approximately 0.998. This is further enhanced since the decay into b quark and on-shell W boson is kinematically possible due to the high top quark mass. Within measurement uncertainties, the top quark can be regarded as decaying exclusively into W boson and bottom quark.

The lifetime of the top quark is extremely short with $\tau_\mathrm{t} = 1/\Gamma_\mathrm{t} \approx 5 \times 10^{-25}\,\mathrm{s}$ as the decay is a CKM allowed process. The time scale of hadronization, on which hadrons are formed from quarks and antiquarks, is about one order of magnitude larger than the top quark lifetime, with $\tau_\mathrm{had} = 1/\Lambda_\mathrm{QCD} \approx 3 \times 10^{-24}\,\mathrm{s}$. Thus, the top quark is unable to form hadrons and no bound top quark states can be observed. This allows to directly measure the bare quark properties such as spin correlations from the decay products without the dilution usually caused by hadronization.

In principle it would be necessary to describe both production and decay simultaneously in the same theoretical prediction. However, due to the small relative decay width $\Gamma_\mathrm{t}/m_\mathrm{t}$, the so-called *narrow width approximation* allows to factorize the process into the on-shell top quark or $\mathrm{t\bar{t}}$ production, and the subsequent decay of the individual quarks.

The $\mathrm{t\bar{t}}$ decay modes are classified according to the decay of the two W bosons, each of which either decays hadronically into two quarks, or leptonically including neutrinos. Having neutrinos as final state particles is challenging since they only interact via the weak force, and thus escape the detectors unnoticed. The only handle to detect the presence of neutrinos is the momentum they carry away, which is reflected in an imbalance of the total transverse energy in the event, which is quantified as missing transverse energy (E_T^miss).

Due to lepton universality all decay channels contribute with the same branching ratios, the hadronic channels have to be counted thrice owing to the additional degree of freedom arising from the quark color charge. For all decay channels, at least two jets are expected which originate from the b quarks of the $\mathrm{t\bar{t}}$ decay. Three $\mathrm{t\bar{t}}$ decay modes are distinguished.

In the **fully hadronic decay** both W bosons decay into quark pairs. This channel features at least six jets in the final state and has the largest branching ratio, but it is contaminated by large irreducible QCD multi-jet background contributions.

The **semi-leptonic decay**, where one W boson decays hadronically, and the other into a lepton and lepton-antineutrino, has the second largest branching ratio and a lower background contamination compared to the fully hadronic channel.

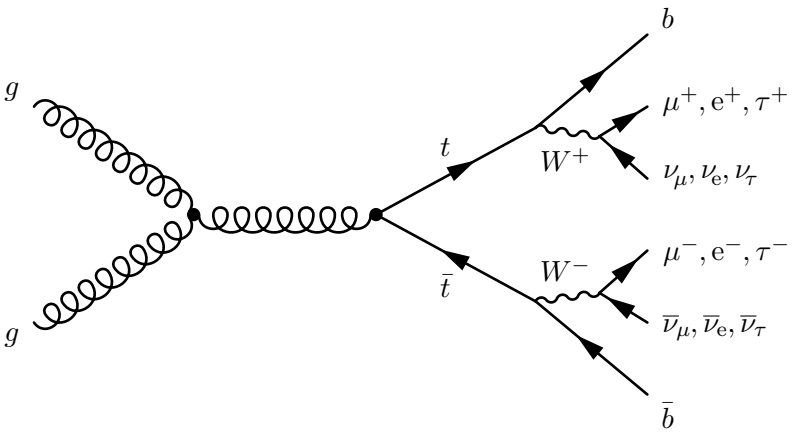

Figure 10.2: Signature of a $t\bar{t}$ event from gluon-gluon fusion with both W bosons decaying leptonically. The final state features two b jets, two oppositely charged leptons and their antineutrinos.

Table 10.1: Channels and branching ratios of $t\bar{t}$ decays, characterized by the decay channels of the two W bosons. The W branching ratios are taken from [15] assuming lepton universality. The decays into two leptons are colored in light orange, the dileptonic channels excluding τ decays in dark orange.

branching ratio [%]		W^+ decay			
		$u\bar{d}$, $c\bar{s}$	$\tau^+\nu_\tau$	$\mu^+\nu_\mu$	$e^+\nu_e$
W^- decay	$\bar{u}d$, $\bar{c}s$	45.7	7.3	7.3	7.3
	$\tau^-\bar{\nu}_\tau$	7.3	1.2	1.2	1.2
	$\mu^-\bar{\nu}_\mu$	7.3	1.2	1.2	1.2
	$e^-\bar{\nu}_e$	7.3	1.2	1.2	1.2

Finally, the **dileptonic decay** is characterized by both W bosons decaying leptonically as exemplified in Figure 10.2. The signature of this decay channel features two high-p_T, oppositely charged leptons, two neutrinos, and the b jets:

$$pp \to t\bar{t} \to b\ell^+\nu_\ell + \bar{b}\ell^-\bar{\nu}_\ell, \quad \text{with } \ell = e, \mu, \tau. \tag{10.2}$$

Tau leptons decay further into neutrinos and either hadrons with a branching ratio of 2/3 or to a lighter lepton, i.e., electron or muon, with a branching ratio of 1/6 each. The branching fractions for the different combinations of W decays are listed in Table 10.1.

10.3 Relevance of Top Quark Physics

Since the production and decay of the top quark involve both the strong and the electroweak force, it provides ample opportunities to measure properties of the SM. Measuring the $t\bar{t}$ production cross section allows precise tests of QCD, and higher-order effects arising from NLO processes can be studied, e.g., via charge asymmetry. Both differential and inclusive cross section measurements provide observables with sensitivity for other QCD parameters such as α_s or PDF distributions.

The electroweak sector is strongly influenced by the top quark via its large mass. With the mass being close to the scale of EWSB, and with a Yukawa coupling of the order of 1 (cf. Section 1.1.3),

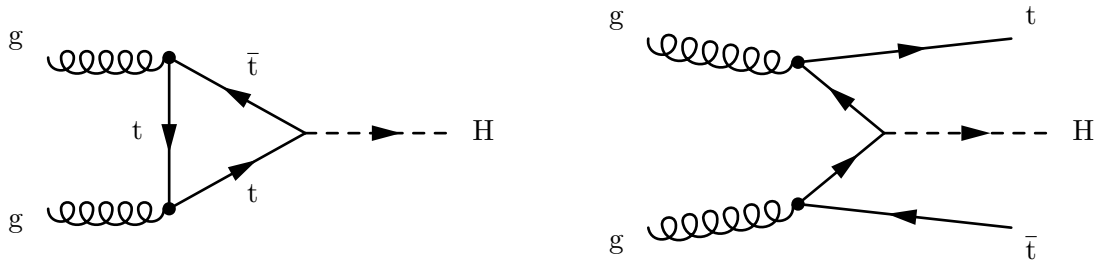

(a) H production via t loop

(b) Associated $t\bar{t}$ H production

Figure 10.3: Higgs production via gluon fusion through a top quark loop (a), and associated $t\bar{t}H$ production (b).

the SM Higgs boson couples strongest to the top quark. Due to the large abundance of gluons in LHC collisions (cf. Section 1.2.1) the Higgs boson production is dominated by gluon-gluon fusion through a top quark loop as depicted in Figure 10.3a, and the associated production of H and $t\bar{t}$ shown in Figure 10.3b. Using the known Higgs, W and top quark masses, the electroweak sector of the SM can be tested for consistency since the three parameters are linked. Higher order corrections to the W boson mass depend quadratically on m_t, while the Higgs boson mass contributes logarithmic corrections. Figure 10.4a shows a global fit to electroweak parameters comparing W and t mass predictions with and without inclusion of the latest measurements of the Higgs boson mass. Direct mass measurements are compared to the prediction, and a good agreement is found.

Also the stability of the electroweak vacuum depends on the top quark mass. The spontaneously broken symmetry yields a non-zero vacuum expectation value as described in Section 1.1.3. The relation between top quark mass and Higgs boson mass allows to determine whether this minimum is stable at all energy scales, or if a phase transition into a global minimum is possible at high energies. Three possibilities are distinguished as shown in Figure 10.4b. Either the electroweak vacuum and thus the minimum of the Higgs potential are stable; the vacuum is metastable and the probability for tunneling to the global minimum exceeds the age of the universe; or the tunneling probability is smaller yielding an unstable vacuum. The latter would be interpreted as a sign of physics beyond the SM as its occurrence would render the existence of the universe purely accidental [195].

Even in direct observations, top quark measurements might assist in unraveling new physics such as the models discussed in Section 1.1.4. SM $t\bar{t}$ event signatures might be resembled by new physics processes, and the precise measurement of quantities such as differential cross sections could help to constrain these new effects.

10.4 The Top Quark Mass and its Interpretation

The top quark participates in all interactions and thus couples to all elementary particles. Its mass is a fundamental parameter of the SM and plays a central role both in top quark physics due to the production and decay characteristics of the quark, and in predictions of electroweak processes as described above. A summary of recent discussions concerning the interpretation and measurement of the top quark mass can be found, e.g., in [196].

Top quark mass measurements are typically either based on the kinematic reconstruction of the mass from the decay products of the quark, or on the mass dependency of the inclusive

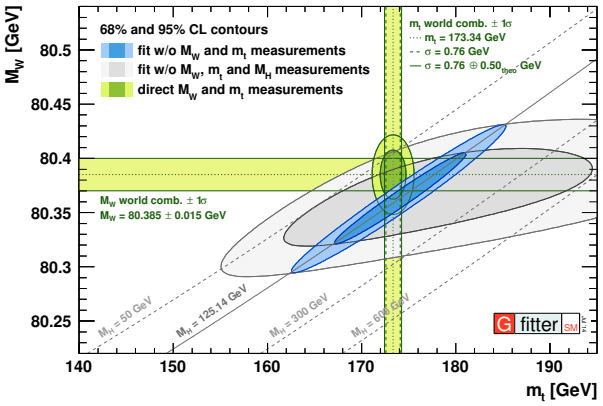

(a) Test of the consistency of the SM by studying the dependencies of the masses of H, W and t. From [194].

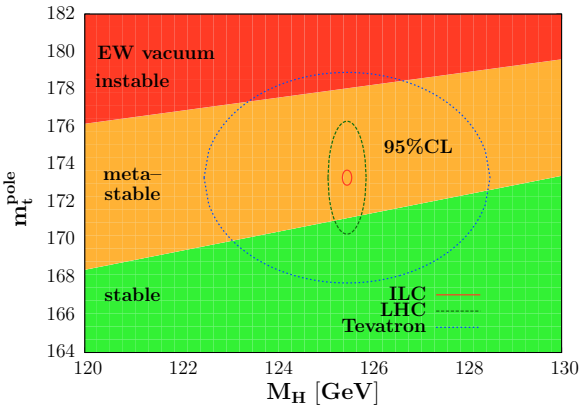

(b) Stability of the electroweak vacuum as function of the top quark pole mass and the Higgs boson mass. From [195].

Figure 10.4: Testing the consistency of the electroweak sector of the SM using top quark mass measurements. (a) shows a comparison of a global electroweak fit with and without the use of the measured Higgs boson mass to the directly measured W and t masses, while (b) indicates the regions of stability of the electroweak vacuum at the Planck scale.

$t\bar{t}$ production cross section [197, 198]. Current mass measurements such as the world average [193] provide m_t with a precision of less than 1 %. At a future linear e^+e^- collider, the top quark mass could be determined with unprecedented precision by a conceptually simple counting experiment. By scanning the cross section through the $t\bar{t}$ production threshold, the shape of the turn-on curve could be fitted to theoretical predictions resulting in a total uncertainty on the top quark mass of $\delta m_t \approx \mathcal{O}(150\,\text{MeV})$.

However, the top quark mass is a convention-dependent parameter. The relation of the extracted top quark mass to a well-defined Lagrangian parameter is not entirely clear, and different concepts for theoretically defining the top quark mass exist. When measuring the mass parameter from kinematic properties, the renormalization scheme is usually not well-defined [196], while extractions from the $t\bar{t}$ production cross section feature an unambiguously defined relation to a Lagrangian parameter.

In principle, the bare top quark is not observable due to the color confinement, and its full propagator does not have a pole. However, in finite-order perturbation theory the propagator exhibits a pole at the complex value

$$S_t(p) = \sqrt{p^2} = m_t^{\text{pole}} - i\Gamma_t/2, \tag{10.3}$$

where the real part m_t^{pole} is defined as the pole mass, and Γ_t represents the decay width of the top quark. In this purely perturbative concept, the on-shell or pole mass of the top quark can be defined due to the very short life time which prevents hadronization.

Other theoretically well-defined mass concepts are short-distance masses such as $\overline{m}_t(\mu)$ in the modified minimal subtraction ($\overline{MS}$) renormalization scheme [199]. Here, μ denotes the renormalization scale. The relation between the top quark pole mass and the $\overline{MS}$ mass can be perturbatively calculated and is known to $\mathcal{O}(\alpha_s^4)$ [200]. The $\overline{MS}$ mass is expected to be around 10 GeV lower than the pole mass.

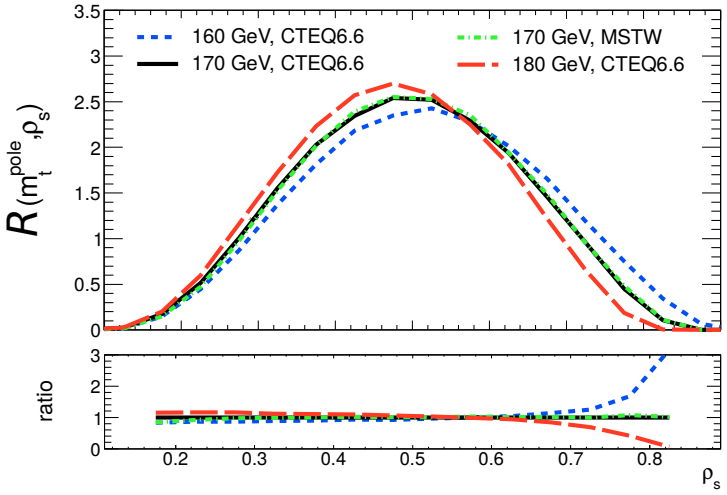

Figure 10.5: $\mathcal{R}$ distribution as a function of ρ_S for different top quark pole masses. Shown are NLO accuracy calculations for $m_t^{pole} = 160\,\text{GeV}$, 170 GeV, and 180 GeV. The lower plot shows the ratio with respect to a mass of $m_t^{pole} = 170\,\text{GeV}$ [12].

Since kinematic measurements of the top quark mass usually involve fits to predictions produced by MC event generators (cf. Chapter 11) the mass extracted from these measurements is usually referred to as the *MC mass* m_t^{MC}. In order to relate the experimental value to a well-defined Lagrangian mass parameter, appropriate observables have to be defined. The analysis presented in this thesis extracts the top quark mass from an observable which can be calculated perturbatively at NLO and relates to the pole mass of the top quark as will be discussed in the subsequent section.

10.5 Measurement of the Invariant Mass of the $t\bar{t}$+jet System and Extraction of the Top Quark Pole Mass

The analysis presented in this thesis provides an alternative approach to the standard direct measurements of the top quark mass, following the methodology proposed in [12]. The top quark mass is measured from the normalized differential cross section as a function of the inverse invariant mass of the $t\bar{t}$ system including the leading additional jet of the event. The observable is defined as

$$\rho_S = \frac{2m_0}{\sqrt{s_{t\bar{t}+\text{jet}}}}, \tag{10.4}$$

where m_0 is an arbitrary scale of the order of the top quark mass, and $\sqrt{s_{t\bar{t}+\text{jet}}}$ denotes the invariant mass of the $t\bar{t}$ candidate system and the leading additional jet. Here, a value of $m_0 = 170\,\text{GeV}$ is chosen without loss of generality, following the suggestion in [12]. The normalized differential $t\bar{t}$+jet production cross section $\mathcal{R}$ as a function of ρ_S is defined as

$$\mathcal{R}\left(m_t^{pole}, \rho_S\right) = \frac{1}{\sigma_{t\bar{t}+\text{jet}}} \frac{d\sigma_{t\bar{t}+\text{jet}}}{d\rho_S}\left(m_t^{pole}, \rho_S\right), \tag{10.5}$$

and is depicted in Figure 10.5. The different curves represent NLO calculations assuming different top quark pole masses, and are indicating a strong sensitivity of the distribution on the mass hypothesis. The intersection originates from the normalization of the cross section integrals.

In this work, the top quark mass is measured from data collected by the CMS experiment in 2012 at $\sqrt{s} = 8\,\text{TeV}$. The mass is extracted both at reconstruction level, and at generator level, i.e., after correction for detector effects, to compare the achievable precision. Furthermore, the data corrected to generator level is used to extract a theoretically well-defined top quark mass using calculations at NLO precision [13]. A similar measurement has been performed by the ATLAS experiment [201] in the semi-leptonic $\mathrm{t\bar{t}}$ decay channel.

In the subsequent chapters, the analysis is presented. The simulation of events, the event selection and analysis strategy, and the systematic uncertainties are described in Chapters 11–13, respectively. The measurements are presented in Chapters 14 and 15.

11. Simulation of Collision Events

Monte Carlo (MC) simulations as used in Chapter 5 to describe the response of a detector are also a highly important tool for the understanding and modeling of collision events. The interpretation of data recorded by the detectors and the extraction of physical parameters heavily rely on a well-understood theoretical modeling of the outcome of the scattering experiment. Due to the stochastic nature of quantum physics, the MC method described in Section 1.4 is a perfectly suited tool to simulate collision events, and is explored by a plethora of different event generators available to date.

By modeling the processes under investigation, it is possible to predict the behavior of observables, and to extract information which is not directly accessible from the final event signature recorded by the detectors. Furthermore, some quantities such as the detector acceptance need to be entirely estimated from MC simulations. Simulated events can also be used to guideline the development of new measurement techniques, and to study event selection criteria.

Especially hadron collisions pose a complex problem to simulation owing to the non-trivial initial state and to the nature of QCD (cf. Sections 1.1 and 1.2). The event generation process is based on the factorization theorem separating the event into independent phases, and will be discussed in Section 11.1. The relevant $t\bar{t}$ signal samples and their production are described in Section 11.2, while Section 11.3 lists the background samples used in the measurement, and briefly describes the deployed tools. Further information concerning MC event generation in particle physics, the different phases of event simulation, and the MC generator tools available can be found in literature [202, 203].

11.1 Event Generation

The MC event generation is based on the factorization theorem described in Section 1.2.2 which allows to split the overall event into sequential phases, separated by the factorization scale. The simulation starts with the matrix element calculation of the hard scattering process using perturbative QCD. The momenta of the initial state partons are provided by a PDF set. The high-energetic partons emerging from the hard scattering undergo radiation processes which are described by the parton shower using approximate implementations of the responsible QCD processes. Finally, the energy of the partons reaches the factorization scale where perturbative calculations break down, and where color confinement forms color-neutral hadrons. The following sections describe these processes in more detail and also provide information on some of the available tools.

11.1.1 Matrix Element Simulation

The matrix element of the hard scattering process is calculated at fixed order of α_s in perturbation theory (cf. Section 1.1.2), while higher order terms are approximated using the parton shower described in the following section. The initial state of the collision is predetermined by the PDF distribution, from which the momenta of the incoming partons are randomly chosen. The definition of the final state depends on the process, but also on supplemental features provided by the generator tool such as the additional emission of partons at matrix element level or different behavior concerning the decay of particles. The outgoing partons are randomly distributed in the available phase space.

Event generators for matrix element simulation can coarsely be divided into two categories, dedicated and general purpose generators. General purpose generators usually provide calculations for all SM processes as well as for selected processes from theories beyond the SM. The MadGraph generator [204] is used for the simulation of the signal $\mathrm{t\bar{t}}$ samples employed in this analysis as will be described in Section 11.2.1. It is a so-called *multi-leg* generator providing matrix elements at tree level, and allows up to nine particles in the final state. Tree level denotes that no virtual loop corrections are taken into account, but higher-order real emissions are included in the calculations. With six particles required for the dileptonic final state of the $\mathrm{t\bar{t}}$ decay, up to three additional partons can be produced by MadGraph at tree level. For MadGraph, the renormalization scale μ_R and factorization scale μ_F are combined in the hard-scattering Q^2 scale, defined as

$$\mu_R^2 = \mu_F^2 = \mathrm{Q}^2 = m_{\mathrm{t}}^2 + \sum p_T^2\,(\mathrm{jet})\,, \tag{11.1}$$

where m_{t} represents the top quark mass and the p_T sum is calculated from all additionally radiated partons from the matrix element. Other multipurpose generators are Pythia [205, 206] and Herwig [207], which do not only provide tools for matrix element event generation but also implement the subsequent steps of parton showering and hadronization.

Dedicated generators include precise calculations of specific processes such as $\mathrm{t\bar{t}}$ production, and are usually optimized for a certain analysis. Examples for dedicated process generators are mc@nlo [208] or Powheg [209–211] which implement calculations up to NLO including virtual loops and corrections as well as real emissions for a limited set of processes. Powheg is used to generate the predictions for the analysis presented as described in Section 11.2.2. The renormalization and factorization scales in Powheg are defined as $\mu_R^2 = \mu_F^2 = m_{\mathrm{t}}^2$.

Generated events are stored in so-called *Les Houches Event* files [212, 213], a format standardizing the exchange of simulation event information between different MC generator tools, containing the four-momenta of initial and final state particles and possible decay products as well as initial collision energy and additional process parameters.

11.1.2 The Parton Shower

Higher-order QCD effects such as radiation of additional gluons from the matrix element final state partons cannot be computed from first principles of the underlying theory, since the number of possible processes increases exponentially with each order in perturbative expansion. Hence, parton shower simulations implement a probabilistic approximation to describe the distribution of additional partons added to the event topology. The parton shower starts at a certain virtuality of the process, $\mathrm{Q}^2_{\mathrm{max}}$. Depending on the interface between matrix element calculation and parton shower tool, this is either defined by the PDF distributions used, or set explicitly by the hard scattering process. Especially when generating events with NLO accuracy at matrix element level, it is important to correctly inherit the scale. Otherwise, double-counting

can occur, when the parton shower radiates gluons above the scale already covered by the NLO calculations (cf. Section 11.2.2).

The emissions in the parton shower are usually ordered in Q^2 using the Sudakov form factor [214], which allows to calculate the probability of not emitting a parton between Q^2_{max} and Q^2. The available shower algorithms differ in the selection of the evolution variable. Pythia orders all emissions according to the scale $Q^2 = p_T^2$ in decreasing transverse momentum of the parent parton, while Herwig implements an angular ordered shower algorithm choosing $Q^2 = 2E^2\,(1 - \cos\theta)$ as evolution variable. Here, E denotes the energy of the parent parton, and θ the angle between the parent and the emitted parton. The shower evolution can be simulated for both final and initial state. While the virtuality Q^2 of radiated partons decreases for the space-like final state radiation, the shower is reversely ordered for the time-like initial state radiation, where the shower starts at the hard interaction and partons are radiated with increasing Q^2.

As the parent partons continue to radiate new daughter entities, the energy scale of the process decreases until color confinement becomes the dominant QCD characteristic.

11.1.3 Hadronization and Decay

The process of hadronization describes the combination of the produced partons into color-neutral hadronic objects which either decay or are stable on the timescale of QCD, and can be detected by the experiment. The description of parton hadronization is purely phenomenological since the event entered the non-perturbative regime at scales of Λ_{QCD}, and is dominated by color confinement. The process can be described independently from the hard process due to the factorization theorem, and the different models available are tuned to experimental data.

The Lund string hadronization model [215] implemented by Pythia regards color strings between quark-antiquark pairs. As the distance between the partons grows, the energy of the color potential represented by the string increases and the formation of a new hadron becomes favorable. A new quark pair is formed, which is again connected to the initial quarks via color strings. The evolution reaches its terminus as no more hadrons can be produced from the string energy. Herwig utilizes the cluster fragmentation approach [216, 217] which is based on the color pre-confinement assumption [218] assigning color connections between partons already early on in the parton shower. Quarks are clustered to colorless objects which are formed to hadrons via decay, while gluons are forced to produce $q\overline{q}$ pairs which are then assigned to a cluster.

An important effect in the description of the event final state is the so-called color reconnection (CR) [219, 220]. It has been found, that the color assignment provided by the perturbative calculations can be modified by non-perturbative effects. Many different models describing the observed effects coexist, and allow tuning to data. In Pythia, the CR is modeled by limiting the total color string length within the event, and by assigning reconnection probabilities in order to select candidate partons for the reconnection. The top quark is directly affected by the CR phenomenon since it decays within the proton radius, and thus in a dense environment of quarks and gluons available for reconnection.

At this stage of the event simulation, also the effects of multiple partonic interactions and the production of the underlying event (UE) are taken into account (cf. Section 1.2.3), since their description heavily depends on the hadronization model chosen. Finally, the decay of unstable hadrons is simulated in order to produce the event particle content recorded by the experiment. These particles emerging from the hadronization process are referred to as *hadron-level* or *generator-level* particles and can be used to define cross sections.

11.1.4 Detector Simulation

Simulating the exact detector response facilitates direct comparison of the recorded data and MC predictions. The interaction of the final state particles at generator level with the CMS detector is simulated using the GEANT4 software package [221]. GEANT4 implements an accurate simulation of particle interactions with the detector material, which is based on hadron-level information obtained from experimental data. The characteristics of the interaction are parametrized for every individual subsystem using test beam data. In addition, the electronic response of the readout electronics, noise and cross talk, malfunctioning detector channels, and calibrations from the CMS detector conditions database are taken into account to retrieve a realistic event signature. Finally, a full emulation of the L1 and HLT is added (cf. Section 2.2.5) to mimic the event selection process of the CMS experiment. This simulation of the detector is very computationally intense.

The same algorithms are used in simulation and data to reconstruct the event signatures from the detector response. These events are commonly referred to as *reconstruction level*. Understanding the effects of the detector simulation allows to correct the data for the effects introduced by the experimental apparatus, and to unfold the measurements to generator level as will be described in Section 15.1. This facilitates the comparison of physical quantities such as cross sections independently of the experiment, and allows to directly compare with theoretical calculations.

11.2 Simulation of $\mathrm{t\bar{t}}$ Events

Several $\mathrm{t\bar{t}}$ signal simulations are used to measure the top quark mass, to perform the unfolding from reconstructed particles to the generator level, and to assess systematic uncertainties.

11.2.1 Central $\mathrm{t\bar{t}}$ Samples from MadGraph

The central $\mathrm{t\bar{t}}$ sample is simulated using the MadGraph [204] event generator and the MadSpin [222] package to account for spin correlations. The top quark mass for this reference sample is chosen to be $m_{\mathrm{t}}^{\mathrm{MC}} = 172.5\,\mathrm{GeV}$, and the CTEQ6L1 PDF set [53] is used for the description of the initial state of the collision. The MadGraph generator is interfaced with Pythia6 [205] to simulate the parton shower and the hadronization, referred to as MadGraph + Pythia6 in the following. Matching of matrix element radiations with the parton shower is implemented using the MLM prescription [223] in order to avoid double counting of parton emissions. The UE activity is described using the Pythia Z2* tune [224].

Additional $\mathrm{t\bar{t}}$ samples with different values of $m_{\mathrm{t}}^{\mathrm{MC}}$ are used as predictions to determine the top quark mass. The samples are generated using the same MadGraph + Pythia6 configuration as the central sample with top quark masses of

$$m_{\mathrm{t}}^{\mathrm{MC}} = 166.5\,\mathrm{GeV},\ 169.5\,\mathrm{GeV},\ 171.5\,\mathrm{GeV},\ 173.5\,\mathrm{GeV},\ 175.5\,\mathrm{GeV},\ \text{and}\ 178.5\,\mathrm{GeV}.$$

The same configuration is also used to evaluate the systematic uncertainties arising from model dependencies on the renormalization and factorization scales as well as the jet/parton matching threshold as will be detailed in Chapter 13.

All simulated samples are normalized to the total integrated luminosity of $19.7\,\mathrm{fb}^{-1}$, according to the theoretical inclusive $\mathrm{t\bar{t}}$ cross section, calculated with next-to-next-to-leading order (NNLO) precision [225] for the corresponding value of m_{t}.

11.2.2 Production of Powheg *ttJ* Samples

The simulation of the $t\bar{t}$+jet process is implemented at NLO precision using PowhegBox [13]. In order to facilitate the measurement of the top quark mass, seven samples have been produced, assuming different top quark masses spanning the ranges $\pm 1\,\text{GeV}$, $\pm 3\,\text{GeV}$, and $\pm 6\,\text{GeV}$ around the nominal top quark mass of $m_t^{\text{MC}} = 172.5\,\text{GeV}$. These predictions are used to compare with the differential $t\bar{t}$+jet production cross section as will be described in Chapter 15, and have been generated as part of this thesis. The required configuration is detailed in this section.

Event Generation

The matrix element simulation is performed by the PowhegBox *ttJ* process. Jets are formed by the FastJet package, while LHAPDF serves as interface to the CT10 PDF set [54] used to describe the hadronic initial state. The configuration used to produce the $t\bar{t}$+jet samples can be found in Appendix E for reference. The robustness of the obtained simulation has been tested by modifying different parameters of the *ttJ* event generation.

The minimum p_T of the additional final state jet is set to $p_T^{\text{min}} = 40\,\text{GeV}$ in order to avoid possible conflicts when imposing the requirement of $p_T > 50\,\text{GeV}$ during event selection (cf. Section 12.5). The `hdamp` parameter, which regulates the high-p_T radiation, is set to the selected top quark mass in order to better describe the event kinematics measured in data. The Powheg *ttJ* process requires a non-zero value for the `bornktmin` input parameter to allow integration [226]. As a result, a large fraction of events with negative weights is produced as shown in Figure 11.1a which necessitates the generation of large samples. Samples with 2.5 million events have been produced for each of the top quark mass values. For the evaluation of the systematic uncertainty arising from the renormalization and factorization scales, additional samples for every top quark mass have been produced with the scales varied coherently by a factor 2 and 0.5.

Parton Shower Matching

The Powheg *ttJ* process is calculated at full NLO precision, including virtual loops and possible additional radiations. Thus, radiated partons at virtualities lower than the Q^2_{max} predicted by the PDF might already be accounted for by the matrix element simulation, and the matching between the perturbative QCD calculation and the parton shower has to correctly obtain the scale set by the hard scattering process (cf. Section 11.1.2). Otherwise, the parton shower might radiate partons above the scale set by the Powheg process, and therefore lead to double-counting effects.

Figure 11.1b demonstrates the influence of the double-counting effect on the p_T of the additionally generated jet. The shower matching implemented in Pythia6 is not able to correctly account for the NLO emissions provided by Powheg *ttJ*, and radiates partons at higher scales than required, leading to the pronounced deviation. The additional jet is significantly harder compared to the standard MadGraph simulation. When interfacing the NLO calculation to Pythia8 using the `ptHard = 2` parameter, the scale is correctly inferred from the events, and the p_T distribution of the additionally radiated partons are correctly described.

11.3 Simulation of Background Processes

For the presented analysis, the signal events originate from the decay of top quark pairs in the dileptonic channels in association with an additional jet as detailed in Section 10.2. Their signature, two leptons, two b jets, E_T^{miss} and the additional jet, can be mimicked by a plethora

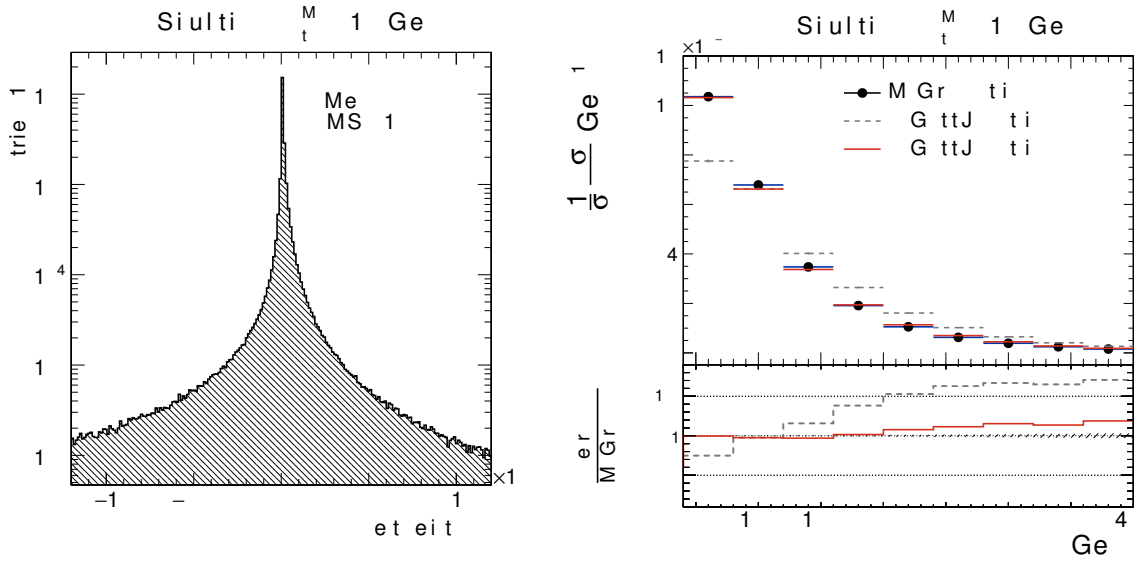

(a) Generator event weight distribution for the $t\bar{t}$+jet process implemented in POWHEG.

(b) Leading additional jet p_T for MADGRAPH and POWHEG, interfaced with PYTHIA6, and PYTHIA8 with correct shower matching.

Figure 11.1: POWHEG *ttJ* event weight distribution (a), and comparison of the leading jet p_T from POWHEG *ttJ* for different parton shower matching algorithms (b).

of background processes with similar particles in the final state, which need to be simulated accordingly.

In the same-flavor channels of the $t\bar{t}$ decay, the Drell-Yan (DY) process [55]

$$Z/\gamma^* \to \ell\bar{\ell} \tag{11.2}$$

has a large contribution. The process describes the production of a virtual photon or Z boson which subsequently decays into a pair of high-energetic oppositely charged leptons. This process as well as the $t\bar{t}$ production in association with a W, Z or γ boson ($t\bar{t} + Z/W/\gamma$), and events containing Z or W bosons accompanied by additional partons ($Z + \text{jets}$, $W + \text{jets}$) are simulated using the MADGRAPH + PYTHIA6 configuration also employed for the $t\bar{t}$ samples.

The associated single-t production channel tW described in Section 10.1.2 contributes to the $t\bar{t}$ dilepton channel background if the W boson decays leptonically, and is simulated using POWHEG [227] interfaced with PYTHIA6. Other background contributions arise from diboson production (WW, WZ and ZZ), and QCD multi-jet events. These events are generated and hadronized using the PYTHIA generator.

The simulated background samples are normalized to the total integrated luminosity of $19.7\,\text{fb}^{-1}$, according to their respective theoretical cross section predictions. The predictions are taken from the most precise calculations available, either at NNLO (for the $W + \text{jets}$ [228] and DY processes [229]), NLO+NNLL (tW [230]), NLO (diboson [231], $t\bar{t} + W$ [232]) or LO (QCD multi-jet [205]).

Additional hadronic interactions are added to the simulated events in order to reproduce the pile-up conditions in the CMS experiment. Furthermore, correction factors for lepton identification and trigger efficiencies as well as b-tagging are applied in order to match the efficiencies measured in data.

12. Object Reconstruction and Event Selection

The first step towards a measurement is the reconstruction of the final state objects of the interaction such as electrons, muons, or jets from the raw data recorded by the detectors. These reconstructed objects are the starting point for the quest of separating the signal events of interest from additional background contributions by applying an optimized selection, yielding a high purity sample of $\mathrm{t\bar{t}}$+jet events.

This analysis is performed with the data collected by the CMS experiment during the 2012 LHC run at $\sqrt{s} = 8\,\mathrm{TeV}$. The total integrated luminosity of the data sample amounts to $19.7 \pm 0.9\,\mathrm{fb}^{-1}$ [70] (cf. Section 2.1.1), and only data from certified runs passing the data quality criteria are considered.

This chapter provides an overview of the object reconstruction and event selection criteria applied. Section 12.1 introduces the selected triggers, while a description of the general approach of particle reconstruction is given in Section 12.2. Subsequently, the event selection criteria for the primary vertex, leptons, jets, and E_T^{miss} are reviewed in Sections 12.3 to 12.6. Section 12.7 describes the kinematic reconstruction of $\mathrm{t\bar{t}}$ events. Finally, the selection criteria are summarized, and control distributions are presented in Section 12.9.

12.1 Trigger Selection

The events used in this analysis are pre-selected based on several paths of the high level trigger (HLT) described in Section 2.2.5. The selected paths are listed in Table F.1 in the Appendix, and events are selected if at least one of the HLT path requirements is met, effectively combining the paths with a logical *OR*. All paths require the presence of at least two leptons with transverse momenta larger than 17 GeV for one lepton, and 8 GeV for the other.

Further pre-selection criteria are applied to the data in order to remove background events. Beam scraping events are proton interactions with residual gas particles or the beam collimators, and produce showers of secondary particles which have to be identified as machine-induced background. These events are rejected by requiring a fraction of high-purity tracks of at least 25 %, and at least 10 tracks present in the event. In addition, events with a significant noise contribution in the HCAL are removed. The hereby selected events are subsequently relayed to the reconstruction algorithm described in the following section.

12.2 The Particle Flow Algorithm

CMS employs the particle flow (PF) algorithm [233] in order to reconstruct the identity and energy-momenta four-vectors of all stable particles in the event by combining the available information from all subdetector systems. The PF algorithm aims for providing a complete representation of all particles traversing the detector. The high-precision tracking detectors, the high granularity of the ECAL, and the hermetic calorimetric coverage for both charged and neutral hadrons are key elements for the performance of the CMS PF algorithm.

The basic building blocks for the PF algorithm are tracks from the inner tracking system (cf. Section 2.2.1), calorimeter clusters (cf. Section 2.2.2), and muon candidates (cf. Section 2.2.4). The reconstruction starts with the identification of charged particles in the event using a combination of the tracks from the inner tracking system and the muon systems. In the calorimeters, clusters are formed from the deposited energy in adjacent calorimeter cells. The charged particle tracks are then extrapolated to the calorimeters and matched to the clusters while taking into account both deflection from multiple Coulomb scattering in the detector material and the typical longitudinal shower profile (cf. Section 1.3). The combination of this information is referred to as *block*.

The particle candidates are subsequently reconstructed from these blocks by applying quality criteria. Owing to the clean signal from the muon systems, muons are identified first, and their contribution to the PF block is removed. Subsequently, electrons are reconstructed from the block information, and photons stemming from bremsstrahlung processes are assigned to the electron candidates. These bremsstrahlung photons are identified by extrapolating tangents of the electron tracks to the calorimeters and matching them to calorimeter clusters. After removing the electron tracks and clusters, the remaining tracks are considered to originate from charged hadrons. The hadron momenta are reconstructed from the combined track momentum information and the matched calorimeter cluster energy. Excess energy in these clusters as well as the total energy of calorimeter clusters without linked particle tracks are attributed to neutral hadrons and photons. Taking the characteristics of the jet composition into account, the excess energy in the ECAL is completely assigned to photons, since neutral hadrons contribute only about 3 % of the overall energy deposited in the ECAL, while about 25 % of the total jet energy is carried by photons.

Significant corrections of the order of 20–30 % have to be applied to the calorimetry clusters originating from hadrons due to the energy dependent HCAL response, complications stemming from the characteristics of hadronic showers (cf. Section 1.3.2), and effects from the readout electronics. Since the ECAL is specifically calibrated for electrons and photons, these clusters only require small corrections of the order of 1 %. The calibration constants are obtained from simulation and have been validated using collision data [234, 235].

The particle candidates obtained from the PF algorithm are further processed, e.g., by combining them to jets, by identifying E_T^{miss}, and by reconstructing secondary particles in the collision.

12.3 Primary Vertex Reconstruction

The primary vertex corresponds to the interaction point (IP) at which the hard scattering takes place, and needs to be reconstructed for every event. Its position varies due to the extent of the colliding proton bunches, and event pile-up results in more than one primary vertex being present (cf. Section 1.2.3). This necessitates a detailed reconstruction of the vertex of interest, and requires high-resolution tracks from the inner tracking system described in Section 2.2.1.

Primary vertices are reconstructed from tracks fulfilling a set of quality criteria such as the total number of associated hits in the inner tracking system, the normalized χ^2 of the combinatorial Kalman filter (CKF) trajectory fit, and the impact parameter with respect to the nominal beam spot position [81]. A set of well-reconstructed tracks with a maximum longitudinal distance of 1 cm to each other at their point of closest approach to the beamline form a vertex candidate and enter the adaptive vertex fit [236]. The vertex corresponding to the hard interaction is selected as the candidate with highest p_T^2 sum over all associated tracks, and which satisfies the additional requirements of being close to the nominal IP with $|z| < 24\,\text{cm}$, and close to the beam axis with $|r| < 2\,\text{cm}$ in the transverse plane.

All other vertices in the event are attributed to pile-up collisions. Charged PF hadron candidates originating from these pile-up vertices are removed before jet clustering on an event by event basis by the so-called charged hadron subtraction algorithm. The remaining pile-up contribution from neutral particle candidates is subtracted at the level of jet energy corrections as will be described in Section 12.5.

12.4 Lepton Reconstruction and Selection

The **muon reconstruction** is performed in two stages. A stand-alone local pattern recognition in the muon systems is applied, and the hits are fitted with a Kalman filter. These tracks are then extrapolated to the primary vertex. The global reconstruction matches the muon tracks with the track information from the inner tracking system. The resulting global tracks are checked for ambiguities and only the best global fit per muon candidate is selected. This approach allows to improve the spatial resolution of the reconstructed muon tracks. Especially for low momentum muons, the tracker information is crucial since the uncertainties are dominated by multiple scattering in the material in front of the muon stations up to an energy of 200 GeV [237].

The **electron reconstruction** uses information from the inner tracking system and the energy clusters from the ECAL subdetector [238]. Without a distinct signal as available for the muons, the particle identification is more difficult and the low electron mass leads to a significant amount of bremsstrahlung photons emitted when traversing detector material. A *Gaussian sum filter* [239] is employed as reconstruction algorithm, and takes additional photon radiation as well as broken trajectories from Coulomb scattering into account. Furthermore, electrons from identified photon conversions are rejected.

The signature of dileptonic $\mathrm{t\bar{t}}$ events is characterized by two leptons present in the event as described in Section 10.2. Thus, two oppositely charged, well-reconstructed and identified leptons with a transverse momentum of $p_T > 20\,\text{GeV}$ are required to be found within $|\eta| < 2.4$.

The relative lepton isolation I_{rel} represents an estimator for additional energy around the actual particle track, and is defined as energy sum relative to the p_T of the regarded lepton. All photons, charged and neutral hadrons are summed inside a cone of the size ΔR in the $\eta \times \phi$ space around the lepton track, with

$$\Delta R = \sqrt{(\Delta\eta)^2 + (\Delta\phi)^2}. \tag{12.1}$$

The cone size is set to $\Delta R = 0.3$, and a value of $I_{\text{rel}} \leq 0.15$ is required for the lepton to be accepted. This criterion contributes to the rejection of W + jets and QCD multi-jet events.

Of all accepted leptons, the two opposite-sign leptons with the highest combined p_T are selected as the pair originating from the $\mathrm{t\bar{t}}$ decay. This allows to remove ambiguities in events with more than two leptons, and also assigns the event to one of the decay channels $\mathrm{e^+e^-}$, $\mathrm{e^\pm\mu^\mp}$, or $\mu^+\mu^-$.

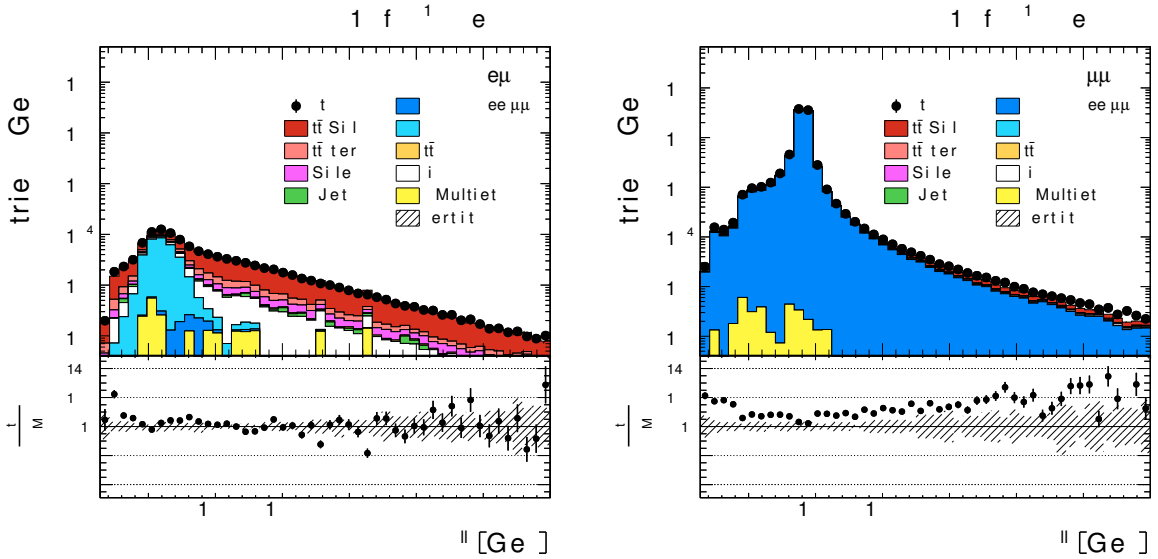

(a) Dilepton mass in the $e^{\pm}\mu^{\mp}$ channel after requiring two oppositely charged leptons.

(b) Dilepton mass before rejection of events in the Z peak, shown for the $\mu^{+}\mu^{-}$ channel.

Figure 12.1: Dilepton mass distribution after requiring two oppositely signed leptons for the $e^{\pm}\mu^{\mp}$ channel (a), and the $\mu^{+}\mu^{-}$ channel (b). The hatched bands represent the sum of all shape uncertainties on the $t\bar{t}$ signal events (cf. Chapter 13).

After applying these criteria, about 45 % of the selected events in the different-flavor lepton channel $e^{\pm}\mu^{\mp}$ correspond to $t\bar{t}$ decays (cf. Figure 12.1a), while the same-flavor channels $e^{+}e^{-}$ and $\mu^{+}\mu^{-}$ are dominated by DY events which contribute about 98 % of the events as depicted in Figure 12.1b for the $\mu^{+}\mu^{-}$ channel. Thus, an additional rejection criterion on the dilepton mass $m^{\ell\bar{\ell}}$ is applied for the same-flavor channels around the Z boson resonance:

$$76\,\text{GeV} \leq m^{\ell\bar{\ell}} \leq 106\,\text{GeV}.$$

Events with a dilepton invariant mass within this window are rejected.

12.5 Jet Reconstruction

At low energies, partons emitted by the hard interaction are subject to hadronization and form color-neutral hadrons due to the color confinement of the strong interaction (cf. Section 1.1.1). These hadrons are emitted in a narrow, collimated cone around the direction of the original parton and can be grouped to single objects referred to as *jet*. Jet algorithms allow to reconstruct these objects and their properties such as the four-momentum of the original parton, and thus provide crucial information for the description of the hard scattering process.

Several jet reconstruction algorithms have been developed and can be assigned to two main classes. **Cone algorithms** implement a top-down approach by finding and separating coarse regions of energy flow. The jet cone is declared stable, if the cone axis coincides with the sum of the momenta of the contained particles. By contrast, **sequential algorithms** follow a bottom-up approach and are building jets starting from an initial seed, iterating, and adding more particles to the jet until a cut-off criterion is reached. The cut-off criterion controlling the extension of the jet is often chosen to be the cone radius or so-called distance parameter R. The

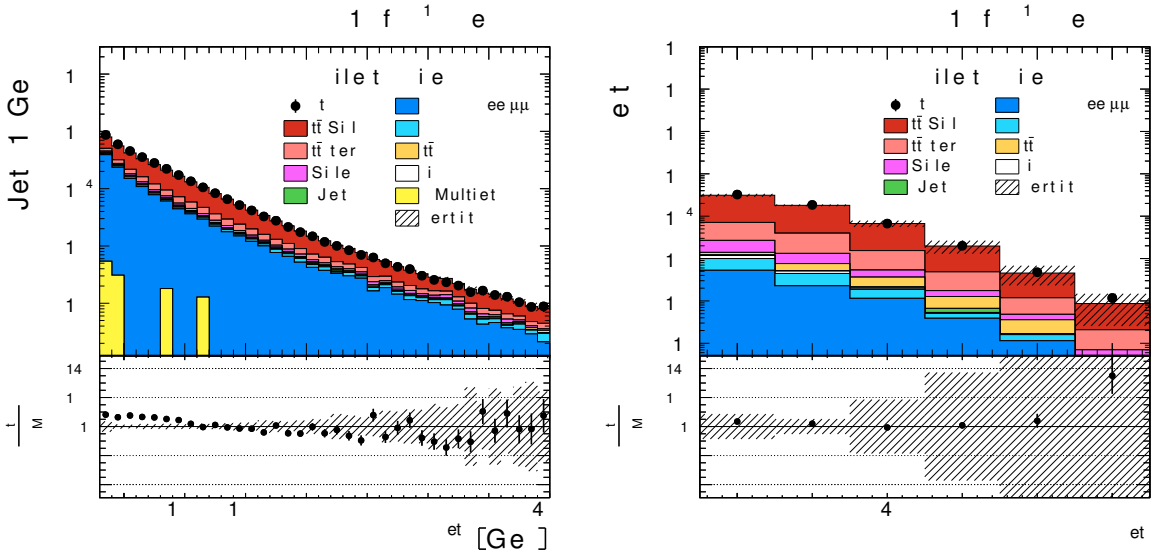

(a) Jet p_T distribution for events passing the lepton and jet selection criteria.

(b) Jet multiplicity distribution for events with solution for the kinematic reconstruction.

Figure 12.2: p_T distribution for all selected jets before the kinematic reconstruction (a), and jet multiplicity distribution of events with a valid solution for the kinematic reconstruction (b). The hatched bands represent the sum of all shape uncertainties on the $t\bar{t}$ signal events (cf. Chapter 13).

jet is built following the variables d_{ij}, denoting the distance between all pairs of objects i and j, and the distance d_{iB} between object i and the beam, which are defined as

$$d_{ij} = \min\left(p_{T,i}^{2p}, p_{T,j}^{2p}\right) \frac{\Delta R_{ij}^2}{R^2} \tag{12.2}$$

$$d_{iB} = p_{T,i}^{2p}, \tag{12.3}$$

where ΔR_{ij} is the distance of object i and j in the $\eta \times \phi$ space (cf. Equation 12.1), the term $p_{T,i(j)}$ denotes the transverse momentum of particle $i\,(j)$, and the relative power p allows to select different algorithms as described below. Object refers to either single particles or jet candidates containing multiple particles. The jet object grows by calculating and comparing all distances d_{ij} and d_{iB}. If d_{ij} is the smallest quantity, the two objects i and j are merged, and the four-momentum vector of the new object is calculated. However, if d_{iB} is the smallest distance, object i is considered a complete jet and removed from further jet searches. This procedure is repeated until all objects are clustered. Different algorithms can be distinguished, based on their relative powers p [240, 241]. CMS employs the anti-k_T algorithm [242] with $p = -1$, and reconstructs jets by clustering the PF particle candidates with a distance parameter of $R = 0.5$.

The jet energy is calibrated to account for remnant neutral hadrons from pile-up activity and non-linear calorimeter responses using data-driven corrections derived from minimum bias data (cf. Section 2.2.5) and DY events as described in [243]. In addition, the simulation is corrected for differences in the jet energy resolution compared to data.

Isolated leptons are removed from the jet candidates in order to avoid double counting. This analysis requires at least two jets within the pseudorapidity interval $|\eta| < 2.4$ and with a transverse momentum of $p_T > 30\,\text{GeV}$. The sample composition after imposing these requirements is shown in Figure 12.2a as a function of the jet p_T for the combination of the three dilepton channels.

12.5.1 Identification of b Jets

Since the lifetime of b quarks is about 1.6 ps, the feasible travel distance from the primary vertex before their decay is approximately 500 µm. This characteristic can be exploited to identify jets originating from b quarks. Owing to the high precision of the pixel detector, particle trajectories can be extrapolated backwards, and the occurrence of a secondary vertex dislocated from the primary vertex can be measured. This method is usually referred to as b-tagging.

For the analysis presented, the so-called combined secondary vertex algorithm for b-tagging [244] is employed, which provides a multivariate discriminant distinguishing between jets originating from b quarks and light-flavor jets. Jets are identified as b-tagged jets using a discriminant value yielding about 80–85 % b-tagging efficiency, and a mis-tag rate of around 10 %.

12.6 Missing Transverse Energy

The missing transverse energy $\vec{E}_T^{\text{miss}}$ arising from the undetected neutrinos allows to determine their contribution to the overall event, and is defined as the negative p_T sum of all PF candidates in the event, viz.

$$\vec{E}_T^{\text{miss}} = -\sum_i p_{T,i} \qquad E_T^{\text{miss}} = \left|\vec{E}_T^{\text{miss}}\right|, \tag{12.4}$$

where E_T^{miss} is the vector magnitude. E_T^{miss} is a critical parameter to many analyses and very sensitive to mis-identified or -reconstructed particles in the PF. Thus, several corrections are applied, and a multivariate analysis is used to reconstruct the final value with a typical resolution of 20 GeV [245].

The signal events regarded in this analysis are expected to feature a significant amount of missing transverse energy owing to the two neutrinos from the dileptonic $\mathrm{t\bar{t}}$ decay. Therefore, a requirement of $E_T^{\text{miss}} > 40\,\text{GeV}$ is imposed to suppress background events. Since this constraint mostly rejects DY events which contribute to the $\mathrm{e^+e^-}$ and $\mu^+\mu^-$ channels, the requirement is only imposed on the same-flavor channels.

12.7 Kinematic Reconstruction of the Event Topology

In order to study the kinematic properties of the $\mathrm{t\bar{t}}$+jet system, the jets originating from the $\mathrm{t\bar{t}}$ decay have to be identified and the top quarks reconstructed from their decay products. The individual contributions of the two neutrinos, reconstructed as E_T^{miss}, cannot be disentangled.

A kinematic reconstruction algorithm [246, 247] is used to solve the system of equations of the neutrino momenta. Owing to these unmeasured momenta, this system is underconstrained and requires the introduction of additional constraints. First, the measured E_T^{miss} is entirely attributed to the neutrinos. Furthermore, equality between the $\mathrm{W^\pm}$ masses is assumed, and the mass is fixed to 80.4 GeV [15]. Also the masses of the top and antitop quarks are assumed to be equal, and possible initial p_T of the interacting partons are neglected. With the additional condition $m_\mu^2 \ll m_\mathrm{b}^2 \ll m_\mathrm{t}^2$, the problem can be reformulated as fourth-order polynomial in one of the neutrino momentum components as

$$0 = \sum_{i=0}^{4} c_i \left(m_\mathrm{t}, p_\ell, p_{\bar{\ell}}, p_\mathrm{b}, p_{\bar{\mathrm{b}}}\right) p_x^i\left(\nu\right), \tag{12.5}$$

where $p_x\left(\nu\right)$ has been chosen as variable without loss of generality. The equation only depends on the four-momenta of the observed particles and the top quark mass, which is varied in the

Table 12.1: Number of expected signal and background events in the MC samples, compared to the number of observed events in 19.7 fb^{-1} of luminosity after the final event selection.

Channel	$\mu^+\mu^-$	e^+e^-	$e^\pm\mu^\mp$	combined	
$t\bar{t}$ signal	3227	2425	8882	14534	77 %
$t\bar{t}$ other	629	472	1726	2828	15 %
other	455	343	723	1516	8 %
Sum MC	4312	3240	11332	18880	
Data	4549	3226	11443	19218	

range from 100–300 GeV in steps of 1 GeV to account for the limited detector resolution. This procedure also ensures that the kinematic reconstruction does not favor a certain top quark mass.

Combinations with two b-tagged jets are preferred over the ones using only one b-tagged jet, while solutions without a b-tagged jet assigned are discarded. If more than one physical solution with the preferred b-tagging combination exist, the one with the most probable neutrino energy according to a simulated neutrino energy spectrum is chosen. The efficiency of this kinematic reconstruction method is about 90 % and events without a valid solution are excluded from the further analysis. Figure 12.2b shows the jet multiplicity in events passing the lepton and jet selection criteria and for which a valid solutions for the kinematic reconstruction could be obtained.

12.8 Leading Additional Jet

For this analysis, the presence of at least one additional jet in the event is required to form the invariant mass of the $t\bar{t}$+jet system. The additional jet is selected from all jets with $p_T > 50$ GeV and $|\eta| < 2.4$ which have not been selected by the kinematic reconstruction described above. The leading additional jet is then defined as the jet with the highest p_T among the ones passing the selection criteria. The fraction of events containing additional jet activity which meets the above requirements is about 30 % as can be inferred from Table F.2 in the Appendix.

12.9 Summary and Control Distributions

Events are selected for the analysis if two oppositely signed, isolated leptons fulfill the requirements $p_T > 20$ GeV and $|\eta| < 2.4$. In order to reject DY events in the same-flavor channels, the Z boson resonance window is excluded within ± 15 GeV around the Z mass. Further background events are removed by imposing a requirement of $E_T^{\text{miss}} > 40$ GeV in the same-flavor channels. The events are required to contain at least two jets with a $p_T > 30$ GeV, and at least one b-tagged jet in order to reject W + jets and tauonic DY events. A kinematic reconstruction is used to identify the jets originating from the top quarks and to reconstruct the $t\bar{t}$ system. Only events with a valid solution for the kinematic reconstruction and an additional jet not selected for the $t\bar{t}$ system with $p_T > 50$ GeV are accepted.

This event selection yields a total of around 19 200 events for the combination of all three dileptonic decay channels as shown in Table 12.1. About 77 % of the selected events are $t\bar{t}$ signal events from dileptonic $t\bar{t}$ decays to electrons and muons with additional jet activity, while $t\bar{t}$ decays via τ leptons are classified as background. The full summary table with event numbers

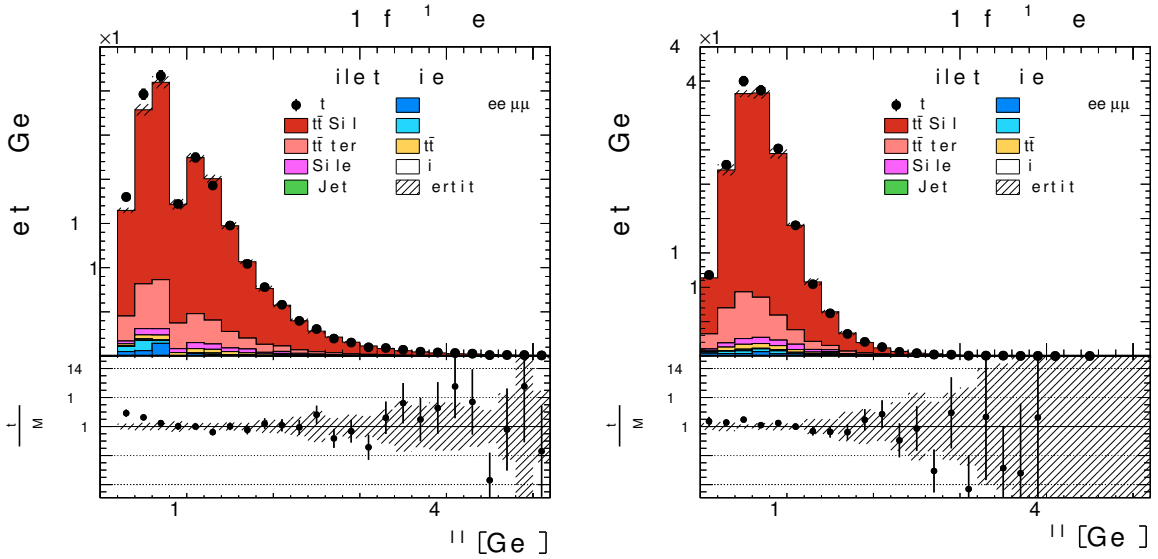

(a) Dilepton invariant mass distribution **(b)** Dilepton p_T distribution

Figure 12.3: Invariant mass (a) and p_T (b) distributions of the dilepton system for the combination of the three channels. The sum of all shape uncertainties on the $t\bar{t}$ signal events is represented by the hatched bands (cf. Chapter 13).

provided for every selection step, separated for the individual channels, can be found in Table F.2 in the Appendix. The main background originates from $t\bar{t}$ decays other than the dilepton channel, and is almost completely constituted by $t\bar{t}$ decays via $W \to \tau\bar{\nu}_\tau$. In the following figures, this background is indicated as *$t\bar{t}$ other*. The contribution from DY events to the remaining background is estimated from data using the $R_{\text{out/in}}$ method described in [248, 249].

Subsequently, control distributions for selected quantities are presented. The distributions are shown for the combination of all dilepton channels, while distributions for the individual channels as well as for additional quantities can be found in Appendix F. Both the data and the total expected events from simulation are shown, and their ratio is given in order to facilitate the comparison. The MadGraph simulation with $m_t^{\text{MC}} = 172.5\,\text{GeV}$ is used as reference for the $t\bar{t}$ signal contribution. The simulation is scaled to the luminosity of $19.7\,\text{fb}^{-1}$. Hatched bands represent the sum of all shape uncertainties on the $t\bar{t}$ signal events (cf. Chapter 13).

Figure 12.3a shows the dilepton invariant mass distribution after all selection criteria have been applied. Only a minor contamination of the sample with background events can be observed, and the simulation describes data well within the uncertainties. The p_T distribution of the dilepton system presented in Figure 12.3b exhibits a similar agreement. Some quantities for the reconstructed $t\bar{t}$ system are provided in Figure 12.4: Figure 12.4a shows the combined invariant mass distribution of the system, while the p_T distribution of the system is presented in Figure 12.4b. For both distributions, the simulation is in agreement with data within the uncertainties, and no significant deviations can be observed. The p_T and η distributions of the leading additional jet are depicted in Figure 12.5, which shows good agreement between data and the simulation. The p_T spectrum of the $t\bar{t}$ system peaks at about 80 GeV due to the recoil from the additional jet, which reaches its maximum at similar p_T values.

Finally, the distributions of the observable of interest, ρ_S, are presented in Figure 12.6 for each channel separately and for the combination of all three channels. The distributions show good agreement between data and simulation for all channels.

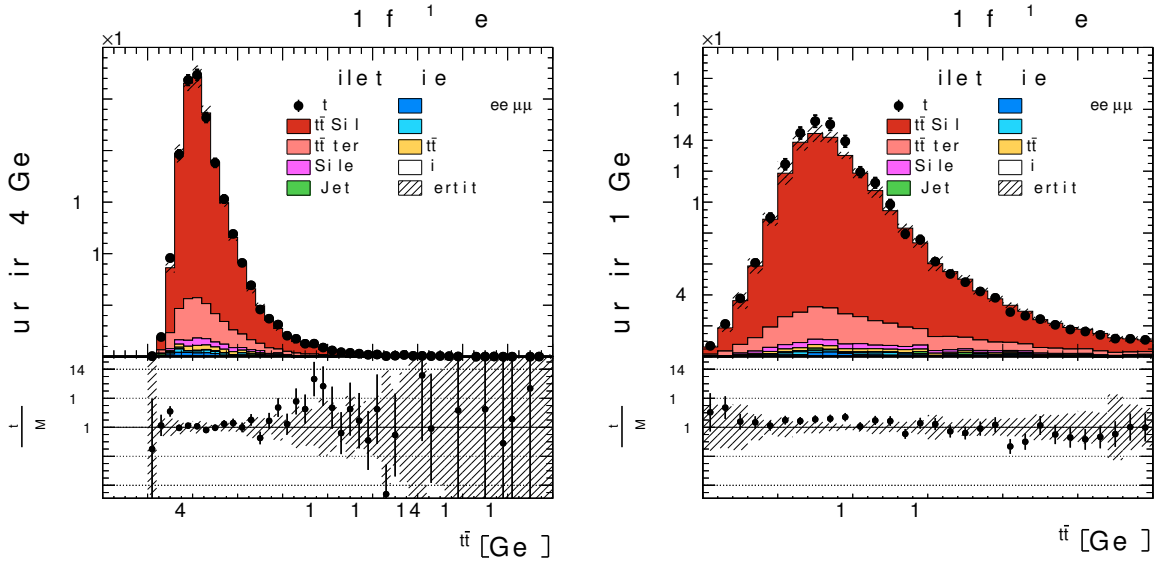

(a) Invariant mass of the $t\bar{t}$ system **(b)** p_T distribution of the $t\bar{t}$ system

Figure 12.4: Invariant mass (a) and p_T (b) distributions of the $t\bar{t}$ system for the combination of the three dileptonic channels. The sum of all shape uncertainties on the $t\bar{t}$ signal events is represented by the hatched bands (cf. Chapter 13).

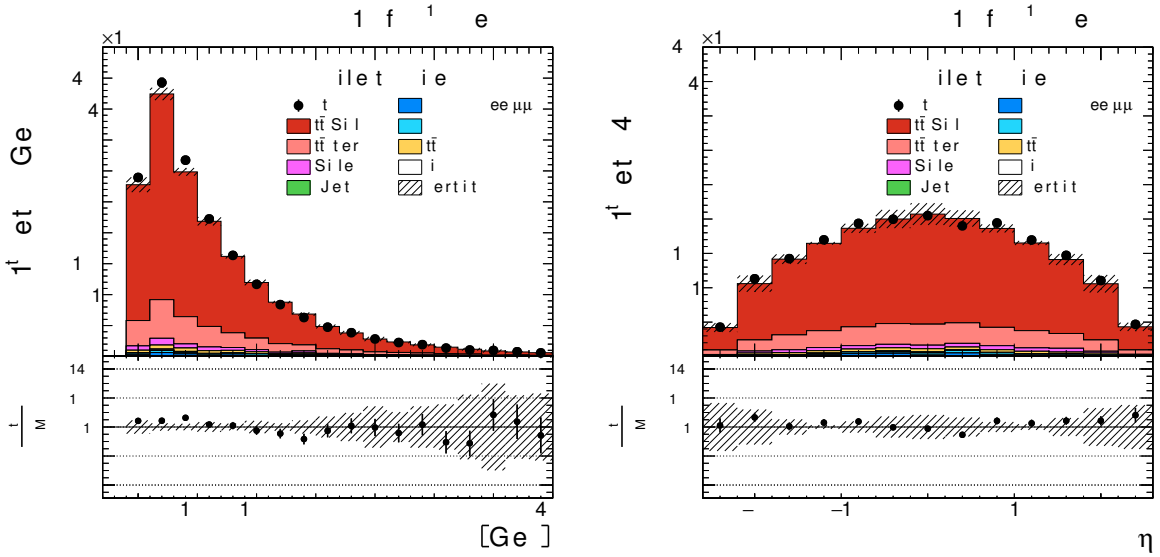

(a) Leading additional jet p_T **(b)** Leading additional jet η

Figure 12.5: p_T (a) and η (b) distributions of the leading additional jet for the combination of the three dileptonic channels. The sum of all shape uncertainties on the $t\bar{t}$ signal events is represented by the hatched bands (cf. Chapter 13).

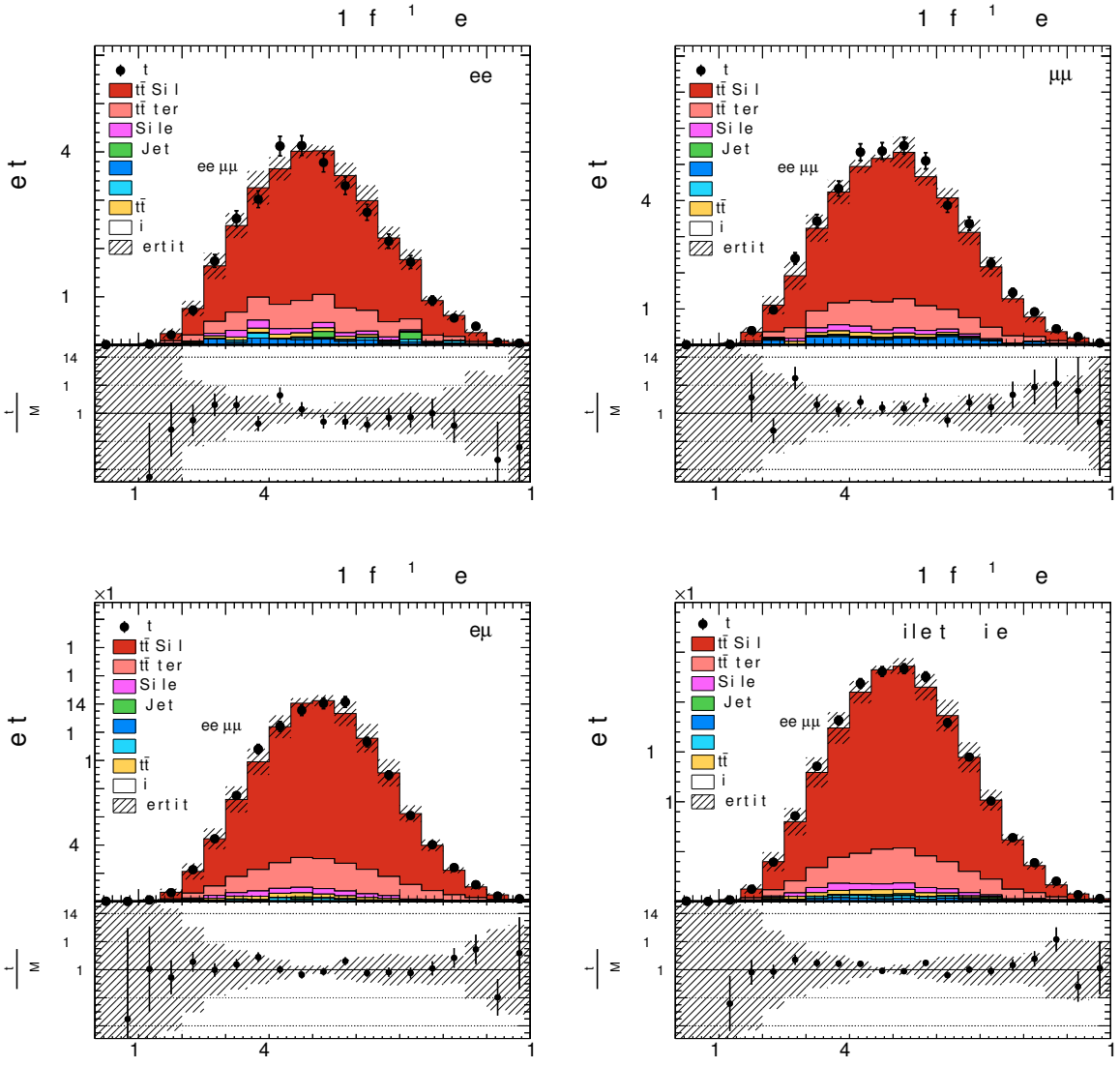

Figure 12.6: Distributions of ρ_s for the three dileptonic final states e^+e^- (top left), $\mu^+\mu^-$ (top right), $e^\pm\mu^\mp$ (bottom left) and the combination of the three channels (bottom right). The sum of all shape uncertainties on the $t\bar{t}$ signal events is represented by the hatched bands (cf. Chapter 13).

13. Systematic Uncertainties

The precision of a measurement is limited by both statistical and systematic uncertainties. While statistical uncertainties arise from stochastic fluctuations in the finite-statistics measurement, systematic uncertainties relate to permanent sources such as calibrations applied to all measurements, and to limited knowledge of the underlying theory.

This chapter introduces the sources of systematic uncertainties relevant to the performed measurements. The sources can be divided into two groups. Experimental uncertainties arise from detector effects such as limited resolution and efficiencies, while modeling uncertainties stem from assumptions made in the theoretical framework. These uncertainties affect the measurement due to inaccuracies in the acceptance calculations, estimation of efficiencies, or calibrations. A detailed study of the influence of the different sources of uncertainty on the measurement is a key element of every analysis, as it defines the precision of the result.

Section 13.1 introduces the uncertainties stemming from the experimental sources, while Section 13.2 summarizes the modeling uncertainties originating from theoretical assumptions. The propagation of systematic uncertainties to the measured quantities is described in Section 13.3.

13.1 Experimental Uncertainties

The sources of experimental uncertainty originate from the finite resolution and efficiency of the CMS detector. The MC simulations are corrected for the finite accuracy of particle reconstruction and four-momenta determination in order to correctly reproduce the measured quantities. The uncertainties on these calibrations are propagated to the measurement. The following section describes the individual contributions to the experimental uncertainty.

Lepton Trigger and Selection Efficiencies

The dilepton trigger efficiency is evaluated using samples selected with triggers that require a certain minimum E_T^{miss} or number of jets in the event, and which are only weakly correlated with the employed dilepton triggers as described in [250]. The trigger efficiency can be evaluated by comparing the number of events passing the weakly correlated triggers and the $\mathrm{t\bar{t}}$+jet event selection criteria with the number of events additionally passing the dilepton trigger criteria. The efficiency obtained from simulation is then corrected to the one measured in data. The

uncertainty on the correction factors, which are about 0.93–0.99 depending on the channel, is estimated to about 1 %.

The lepton isolation and identification efficiencies are determined using a tag-and-probe method, which exploits the Drell-Yan (DY) event topology. Z boson events are selected by requiring two leptons with their invariant mass $m^{\ell\ell}$ close to the Z boson resonance. One lepton serves as *tag*, and is required to fulfill a stringent selection to ensure a high purity sample. The second lepton is used as *probe* to determine the selection efficiency. The differences between data and simulation are accounted for with scale factors in p_T and $|\eta|$, which are of the order of 0.97–0.99. The systematic uncertainty on these factors is assessed by varying the selected window around the Z boson resonance and the requirements on the tag selection, and by re-evaluating the measured efficiencies. While this yields an uncertainty of about 0.3 %, the total uncertainty of 1 % also accounts for differences in the DY and $\mathrm{t\bar{t}}$ event topologies [250].

Jet Energy Scale and Resolution

The jet energy scale (JES) is evaluated double-differentially as a function of the transverse momentum p_T and the pseudorapidity $|\eta|$ of the jet to account for the position and energy dependence of the measurement, and to correct the simulation accordingly [243]. The systematic uncertainty attributed to the JES is evaluated by varying the reconstructed jet energy within the achieved experimental resolution in the different p_T and $|\eta|$ regions. The E_T^{miss} value is adapted according to the modifications of the jet energy values for consistency.

Similarly, the uncertainty on the jet energy resolution (JER) is determined by a variation of the scale factors derived from simulation as described in [243, 251]. The JER corrections are obtained for different regions of pseudorapidity, and are measured with an accuracy of ±2.5 %, ±4 %, and ±5 %, for the pseudorapidity regions $|\eta| < 1.7$, $1.7 < |\eta| < 2.3$ and $2.3 < |\eta| < 2.5$, respectively. The impact on the measurement is evaluated by varying the scale factors up and down according to the respective correction uncertainty.

b-Tagging Efficiency

Efficiency corrections are applied to account for differences in the b-tagging performance between data and simulation. These correction factors are subject to normalization and shape uncertainties which are evaluated in two regions of the b jet p_T and $|\eta|$ distributions. The normalization uncertainty is evaluated by shifting the distributions up and down within the uncertainty attributed to the correction factors. For the assessment of the shape uncertainty, the distributions are divided at the median of the quantity, yielding two equally populated bins. While the b jet correction factors of the first bin are increased by half of the uncertainty, the correction factors in the second bin are decreased accordingly, and vice versa in order to maximally alter the shape of the distribution. The two distributions are assumed to be uncorrelated, and the resulting uncertainties are added in quadrature. The uncertainties on the correction factors are obtained from [252].

Background Normalization

The uncertainty due to the background normalization is determined by variation of the number of selected background events as described in [249, 253]. For the same-flavor dilepton channels $\mathrm{e^+e^-}$ and $\mu^+\mu^-$, the dominating background originates from DY events, and can be estimated from data yielding an uncertainty of 30 % [254]. Background contributions from processes other than DY are inferred from simulation. The total number of selected background events is varied by ±30 % which includes the systematic uncertainties on the background estimated from modeling uncertainties as well as PDF and shape variations.

Simulated samples of the tW and $t\bar{t} + Z/W/\gamma$ processes were not available for all top quark masses considered, but only for the nominal value of $m_t^{MC} = 172.5\,\text{GeV}$. However, the effects on the total number of events and the shape of the distributions have been found to be negligible and well below the associated uncertainty of 30 %.

Kinematic Reconstruction

The event topology of the signal process is obtained using the kinematic reconstruction method described in Section 12.7. The efficiencies of the reconstruction are very similar in data and simulation, and only a small correction factor has to be applied to account for the difference. The uncertainty arising from the correction factor is found to be below 1 % [247].

Luminosity and Pile-up

The luminosity is measured centrally by the CMS experiment using the pixel counting method as described in Section 2.1.1. The overall uncertainty on the measured integrated luminosity is estimated to be 0.5 % (stat) + 2.5 % (syst) as stated in [70]. Since the presented measurements are performed using normalized distributions, the effect of the luminosity uncertainty cancels out.

The effect of pile-up (cf. Section 1.2.3) on the measurements is evaluated by weighting the simulation using the total inelastic proton-proton cross section measured from minimum bias data. The average vertex multiplicity in the data set used in this analysis is estimated to 20 interactions per event, based on a total inelastic proton-proton cross section of $\sigma = 69.4\,\text{mb}$ [255]. The systematic uncertainty arising from this pile-up correction is determined by varying the total cross section within its uncertainty of ±5 %.

13.2 Modeling Uncertainties

Modeling uncertainties arise from theoretical assumptions in the simulation. This affects, e.g., the hard scattering process or the modeling chosen for the description of the subsequent parton shower. The impact of these assumptions on the measurements is determined by repeating the full analysis while replacing the nominal MadGraph $t\bar{t}$ signal sample by dedicated simulations.

Parton Distribution Functions

The uncertainty from the PDFs is evaluated as follows. The simulated $t\bar{t}$ signal events are reweighted using the full uncertainty eigenvalue vector provided with the CT10 PDF set [54] at 68 % confidence level, and the difference between the envelope of all variations and the result obtained using the central PDF eigenvalue is taken as the systematic uncertainty.

Renormalization and Factorization Scales

In MadGraph, the renormalization and factorization scales are combined into the hard-scattering scale $Q^2 = \mu_R^2 = \mu_F^2$ as described in Section 11.1. The impact of the selected Q^2 scale is assessed by repeating the measurement using dedicated MadGraph $t\bar{t}$ samples with corresponding scale values of $4Q^2$ and $Q^2/4$ and comparing the result to the value obtained with the nominal MadGraph sample.

Jet/Parton Matching Threshold

The effect of additional jet production in MadGraph is evaluated by varying the jet/parton matching scale, i.e., the threshold between jet production on matrix element level and via parton showering in Pythia. For the nominal MadGraph sample, a matching threshold of 20 GeV is selected, while the systematic uncertainty is evaluated using samples with a threshold of 40 GeV and 10 GeV, respectively.

Parton Shower Model, Color Reconnection, and Underlying Event

Different parton shower models are available as discussed in Section 11.1.2. The uncertainty arising from the selection of a particular model are evaluated by comparing two samples with different shower implementations. The samples are generated by POWHEG and MC@NLO, interfaced with PYTHIA6 and HERWIG [207] for the parton shower and hadronization, respectively.

The effects of different descriptions of the underlying event (UE) and the modeling of color reconnection (CR) are estimated using different tunes for PYTHIA. The uncertainty arising from the CR model is evaluated by comparing the *Perugia 2011* and *Perugia 2011 noCR* tunes described in [206]. Two different Perugia 2011 PYTHIA tunes are available for the UE description, and the influence of the *mpHi* and *TeV* tunes is compared to the standard Perugia 2011 tune.

Top Quark Mass Hypothesis

The uncertainty stemming from the top quark mass hypothesis of the central MADGRAPH simulation used to measure the differential cross section is found to be negligible as will be discussed in Section 15.3.

13.3 Propagation of Systematic Uncertainties

Systematic uncertainties from modeling sources are propagated to the final measurement by replacing the reference MADGRAPH simulation by the corresponding dedicated sample, and repeating the measurement. Experimental uncertainty sources are evaluated by varying the corresponding efficiencies up and down within the respective uncertainties. The difference between the variation and the nominal measurement is taken as the quoted uncertainty, viz.

$$\Delta_k^{\text{syst}} = x_k^{\text{syst}} - x^{\text{nominal}}, \tag{13.1}$$

where k denotes the uncertainty source, while x_k^{syst} and x^{nominal} are the measured quantities for the systematic variation and the nominal measurement, respectively. Some systematic uncertainties are assessed by comparing two different models without referencing the nominal measurement, and thus only a single uncertainty value is provided by

$$\Delta_k^{\text{syst}} = \pm \left| x_k^{\text{model A}} - x_k^{\text{model B}} \right|, \tag{13.2}$$

where x_k is the variable evaluated for models A and B, e.g., the two different PYTHIA tunes used to evaluate the UE uncertainty.

For differential measurements with several bins, every systematic uncertainty is determined individually in each bin of the measurement. For the top quark mass measurements presented in Chapters 14 and 15, the systematic uncertainties are propagated to the mass by repeating the extraction, and by obtaining the top quark mass for each source of uncertainty. The difference between the top quark mass measured from the variation and the nominal value is taken as systematic uncertainty. More details will be given in the corresponding chapters.

The systematic uncertainties are assumed to be uncorrelated, and the total uncertainty on the measurement is thus calculated as the quadratic sum of all contributions as

$$\Delta_{\text{tot}}^2 = \sum_k \Delta_k^2, \tag{13.3}$$

where k runs over all considered uncertainty sources. Owing to the normalization of the distributions and cross sections used in this analysis, only uncertainties relevant to the shape of the regarded distributions are of concern, while uncertainties affecting the total event rate, such as luminosity, lepton and trigger related uncertainties and the kinematic reconstruction cancel out.

14. Measurement of the Top Quark Mass from the ρ_S Distribution of $t\bar{t}$+jet Events

The measurement presented in this chapter determines the top quark mass from the differential ρ_S distribution of observed $t\bar{t}$+jet events, and thus provides an alternative method to the standard mass measurements discussed in Section 10.4. The large top quark pair production cross section and the correspondingly high number of $t\bar{t}$ events produced at the LHC facilitate the determination of differential distributions of dileptonic $t\bar{t}$ events.

The following notation will be used throughout the subsequent chapters. $N^{t\bar{t}\text{ signal}}$ describes the simulated $t\bar{t}$ signal sample containing only events from prompt dileptonic decays of the $t\bar{t}$ system. Here, prompt refers to the $W^{\pm}$ bosons decaying directly into either electrons or muons. The $N^{t\bar{t}\text{ BG}}$ sample comprises all other simulated events stemming from $t\bar{t}$ decays, e.g., the tauonic dilepton channel, where the final state leptons are only produced via intermediate τ decays. All other background contributions such as single-t production or DY events are attributed to the $N^{\text{other BG}}$ sample. N^{data} corresponds to the number of events in data obtained after applying all selection criteria.

The extraction technique using a global χ^2 template fit is described in Section 14.1, while Section 14.2 discusses the tests performed to evaluate the robustness of the measurement method. Finally, the result of the measurement is presented in Section 14.3.

14.1 Global χ^2 Template Fit

The top quark mass is determined by comparing the number of events observed in the individual bins of the normalized ρ_S distribution with the predicted number of events for different top quark hypotheses. The observable ρ_S follows the definition given in Equation 10.4 and the measurement is performed for the sum of all three dileptonic $t\bar{t}$ decay channels. The binning chosen for the ρ_S distribution corresponds to the one presented in Figure 12.6 (bottom right), and only the lowest four and highest three bins are integrated to form the bins $\rho_S < 0.2$ and $\rho_S > 0.85$, respectively.

The predictions for the seven different top quark masses are obtained at reconstruction level from the simulations described in Section 11.2.1. Owing to the remaining background in data,

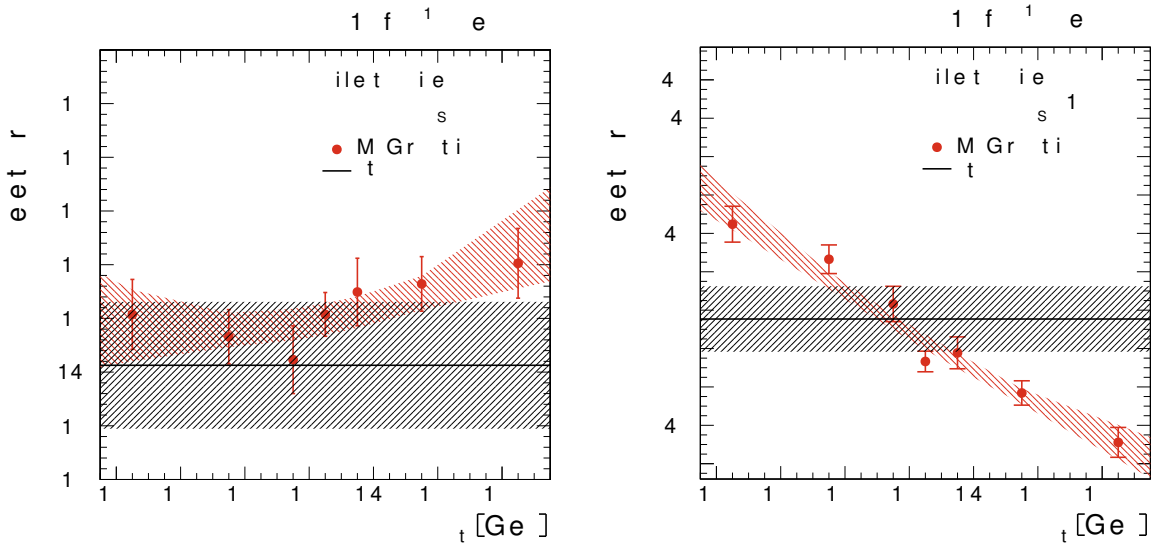

(a) Observed events and MadGraph predictions for the lowest bin, $0.0 < \rho_S < 0.2$.

(b) Observed events and MadGraph predictions for the highest bin, $0.85 < \rho_S < 1.0$.

Figure 14.1: Observed and expected events in the lowermost (b) and uppermost (a) bins of the ρ_S distribution for the combination of all dileptonic channels, normalized to the total number of events. The hatched bands represent the statistical uncertainty of data and of the fit to the simulations, respectively. While the highest bin shows a significant top quark mass dependence, the lowest bin is insensitive within the statistical uncertainty.

the $t\bar{t}$ and non-$t\bar{t}$ backgrounds are added to the MC signal events as

$$N_i^{\mathrm{MC}} = (N_i^{t\bar{t}\ \mathrm{signal}} + N_i^{t\bar{t}\ \mathrm{BG}})\Delta^{t\bar{t}} + N_i^{\mathrm{other\ BG}}, \tag{14.1}$$

with $\Delta^{t\bar{t}}$ being the scaling factor to normalize the MC prediction to the total number of events in data, i.e., $N^{\mathrm{MC}} \equiv N^{\mathrm{data}}$. The scaling factor is calculated from the integrals of the ρ_S distribution in simulation and data as

$$\Delta^{t\bar{t}} = \frac{N^{t\bar{t}\ \mathrm{signal}} + N^{t\bar{t}\ \mathrm{BG}}}{N^{\mathrm{data}} - N^{\mathrm{other\ BG}}}. \tag{14.2}$$

The statistical uncertainty on the MC prediction calculated in Equation 14.1 is estimated from the $t\bar{t}$ signal sample and scaled to the full bin content with

$$\delta N_i^{\mathrm{MC}} = \delta N_i^{t\bar{t}\ \mathrm{signal}} \frac{N_i^{\mathrm{MC}}}{N_i^{t\bar{t}\ \mathrm{signal}}}, \tag{14.3}$$

in order to preserve the relative statistical uncertainty. Finally, both the prediction distributions and data are normalized such that their integrals are equal to unity in order to suppress systematic uncertainties which are mostly rate-dependent and do not affect the distribution shape.

The content of each of the individual bins of data is compared to the expected contributions from simulation with $m_{\mathrm{t}}^{\mathrm{MC}} = 172.5\,\mathrm{GeV} \pm 1, 3, 6\,\mathrm{GeV}$ as shown in Figure 14.1 for two bins. The measured number of events in these bins, normalized to the total number of observed events, is shown as black line with the hatched area representing the statistical uncertainty. The seven

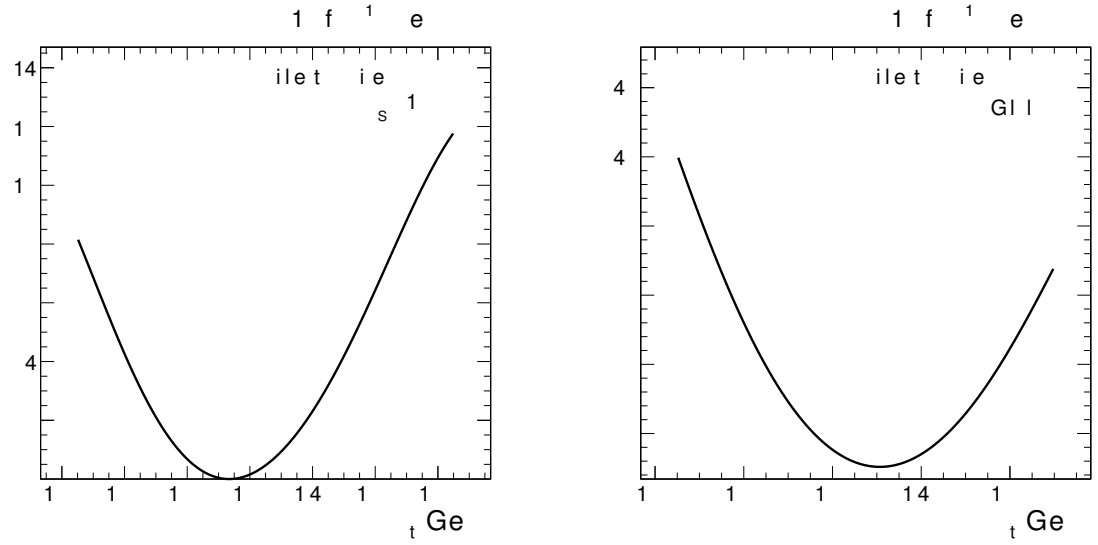

(a) Local χ_i^2 distribution calculated from the the ρ_S bin presented in Figure 14.1b.

(b) Global χ^2 distribution as a function of the top quark mass hypothesis.

Figure 14.2: Local χ_i^2 estimator for the highest bin in ρ_S (a), and global χ^2 distribution from all bins for the combination of the dileptonic channels (b). The top quark mass is obtained from the minimum, the statistical uncertainties from a $\chi^2_{\text{min}} + 1$ variation.

simulated samples with different m_{t}^{MC} mass hypotheses are shown in red, and indicate a distinct dependency on the top quark mass. This dependency is parametrized for each bin i as a function of the top quark mass hypothesis, $f_i^{\text{MC}}(m_{\text{t}})$, obtained from a fit to the seven mass points. The fit is performed using a χ^2 estimator for the second order polynomial function

$$f_i^{\text{MC}}(m_{\text{t}}) = f_{0,i} + f_{1,i}\,(m_{\text{t}} - 172.5\,\text{GeV}) + f_{2,i}\,(m_{\text{t}} - 172.5\,\text{GeV})^2\,, \tag{14.4}$$

where $f_{0\ldots2,i}$ are free parameters to the fit, while m_{t} represents the abscissa. The distributions are shifted to zero for a better convergence of the fit. The second order polynomial has been chosen as the most simplistic function providing a good description of the simulations. The statistical uncertainty δf_i^{MC} is obtained from the confidence interval of the fit at 68 % confidence level, and is shown as red hatched band in Figure 14.1.

The impact of the individual bins on the measurement can be directly deduced from the shape of the fit to the predictions. While the bin depicted in Figure 14.1a shows little sensitivity on the top quark mass and is subject to large statistical uncertainties, the bin shown in Figure 14.1b exhibits a steep slope, and is thus very sensitive on the mass. An overview of all fifteen bins considered is provided in Figure G.1 in the Appendix.

With the continuous parametrization available, the local χ_i^2 estimator for each bin i of the measurement can be calculated as

$$\chi_i^2(m_t) = \frac{(N_i^{\text{data}} - f_i^{\text{MC}}(m_{\text{t}}))^2}{(\delta N_i^{\text{data}})^2 + (\delta f_i^{\text{MC}}(m_{\text{t}}))^2}, \tag{14.5}$$

where N_i^{data} is the number of selected events in each bin with δN_i^{data} being the corresponding statistical uncertainty. The polynomial fit to the simulation distributions is denoted as $f_i^{\text{MC}}(m_{\text{t}})$, and δf_i^{MC} corresponds to the statistical uncertainties as obtained from the confidence interval.

An example for a χ_i^2 distribution obtained from a single bin is shown in Figure 14.2a for the highest bin of the ρ_S distribution in the combination of the dileptonic channels. The slight deviation from the parabola shape arises from the larger statistical uncertainties of the polynomial fit at the edges of the m_t spectrum. The local χ_i^2 distributions for all fifteen bins are provided in Figure G.2 of the Appendix for reference.

The data in the individual bins are statistically uncorrelated, as no overlap in events exists. Thus, the local χ_i^2 estimators can be calculated independently for every bin, and all bins of the measurement are combined in the global χ^2 by calculating the sum of the per-bin χ_i^2 distributions obtained from Equation 14.5 as

$$\chi^2\left(m_t\right) = \sum_i \chi_i^2\left(m_t\right). \tag{14.6}$$

The number of degrees of freedom is reduced by one owing to the normalization of the utilized distributions. In order to accommodate for this in the global χ^2, the bin with the lowest statistical significance is removed from the calculation, i.e., the first bin of the ρ_S distribution. The impact of choosing a different bin for removal has been studied. The statistical uncertainty of the measurement result scales with the statistical uncertainty of the removed bin as expected, while no shift of the central value can be observed. The resulting global χ^2 for the combination of the dilepton channels is shown in Figure 14.2b.

The most probable value of the top quark mass is extracted from the minimum of the global χ^2 distribution. The goodness of fit can be inferred from the minimal χ^2 value and the total number of degrees of freedom. With fourteen bins considered, the value of $\chi^2_{\text{min}}/\text{ndof} = 1.2$ indicates a good agreement of model and observation.

14.1.1 Statistical Uncertainty

The statistical uncertainty of the measured top quark mass is computed as the $\pm 1\sigma$ deviation from the minimum of the global χ^2 distribution by evaluating the curve at $\chi^2_{\text{min}} + 1$ and by calculating the difference to the minimum, viz.

$$\delta m_t = m_t(\chi^2_{\text{min}}) \pm m_t(\chi^2_{\text{min}} + 1). \tag{14.7}$$

This method allows to correctly estimate the magnitude of the statistical uncertainties since the shape of the χ^2 distribution is well-described by a parabola in the vicinity of the minimum up to $\chi^2_{\text{min}} + 4$ [188].

14.1.2 Systematic Uncertainties

The systematic uncertainties described in Chapter 13 are treated as external parameters to the measurement, following the methodology applied in previous analyses in the same $t\bar{t}$ decay channel [247, 254, 256, 257]. Consequently, the individual components are summed in quadrature in order to obtain the total systematic uncertainty.

Uncertainties are propagated to the mass measurement by repeating the extraction for each source of uncertainty with varied predictions. The difference between the top quark mass measured for each simulation and the nominal mass is taken as the systematic uncertainty as described in Section 13.3. The propagation of the individual uncertainties to the top quark mass is detailed in the following.

For all experimental sources of uncertainty described in Section 13.1, the scale factors and variations are applied individually to all MadGraph + Pythia6 samples with the different top quark masses, and the resulting ρ_S distributions are used to perform the mass measurement.

For the PDF uncertainty, scale factors are calculated for every bin of the ρ_S distribution from the variations obtained using the CT10 uncertainty eigenvalue set (cf. Section 13.2). The $\mathrm{t\bar{t}}$ samples are reweighted as

$$N_i^{\mathrm{t\bar{t}},\,\mathrm{PDF}} = (1 \pm p_i)\, N^{\mathrm{t\bar{t}}}, \tag{14.8}$$

where p_i is the PDF scale factor for bin i. The MC distribution is recalculated, and the top quark mass is extracted from the varied distribution.

The background normalization uncertainty is evaluated by scaling the non-$\mathrm{t\bar{t}}$ background contributions $N^{\mathrm{other\ BG}}$ up and down by 30 %, and by repeating the measurement.

For other uncertainties, dedicated simulations are employed. Since these systematically varied predictions are only provided for the central $m_{\mathrm{t}}^{\mathrm{MC}}$ point, absolute differences in event numbers are calculated at $m_{\mathrm{t}}^{\mathrm{MC}} = 172.5\,\mathrm{GeV}$ for each uncertainty, and applied to all different top quark mass MadGraph simulations. Two cases have to be distinguished: Modeling uncertainties related to the MadGraph simulation, and effects related to the parton shower or to a different generator.

The jet/parton matching threshold as well as the renormalization and factorization scale uncertainties constitute the first case, and the difference between the respective predictions and the reference MadGraph simulation are calculated.

The second case applies for the remaining modeling uncertainties. The uncertainty on the parton shower modeling is evaluated by calculating the difference between Powheg + Pythia and mc@nlo + Herwig. Uncertainties on the CR and the UE description are obtained similarly by computing the differences between several Perugia 2011 tunes for the Pythia generator as described in Section 13.2. The obtained difference in event numbers are split to

$$\Delta N_i^{\mathrm{syst}} = \pm \left| \frac{N_i^{\mathrm{A}} - N_i^{\mathrm{B}}}{2} \right|, \tag{14.9}$$

and the MadGraph predictions are varied up and down accordingly. Here, A and B indicate the different Pythia tunes.

14.2 Tests of the Extraction Technique using Pseudo-Data

In order to prove the robustness and stability of the method and to ensure the absence of preferred values for the assumed top quark mass in the simulation, the following studies were performed by replacing the data with simulated samples (*pseudo-data*). The pseudo-data have been obtained as

$$N_i^{\mathrm{pseudo}} = \left(N_i^{\mathrm{t\bar{t}\ signal}} + N_i^{\mathrm{t\bar{t}\ BG}}\right) + N_i^{\mathrm{other\ BG}} \tag{14.10}$$

from the different MadGraph samples, and are normalized to the luminosity of data using the corresponding cross section for the chosen MC top quark mass. The statistical uncertainty of the pseudo-data is inferred from the $\mathrm{t\bar{t}}$ signal sample $N^{\mathrm{t\bar{t}\ signal}}$.

The sensitivity of the measurement method has been studied with pseudo-data obtained from each of the available MadGraph simulations with different top quark masses, and the measured top quark masses have been compared to the mass used to generate the input samples (*true* m_{t}). Figure 14.3 shows that the measured masses agree with the simulated masses within the statistical uncertainty of the samples, and indicates that the method does not favor certain values of the mass or introduces a trend toward higher or lower masses. A linear regression with $m_{\mathrm{t}}^{\mathrm{meas}} = p_0 + p_1 m_{\mathrm{t}}^{\mathrm{true}}$ yields a slope of $p_1 = 1.10 \pm 0.14$, which is compatible with the diagonal

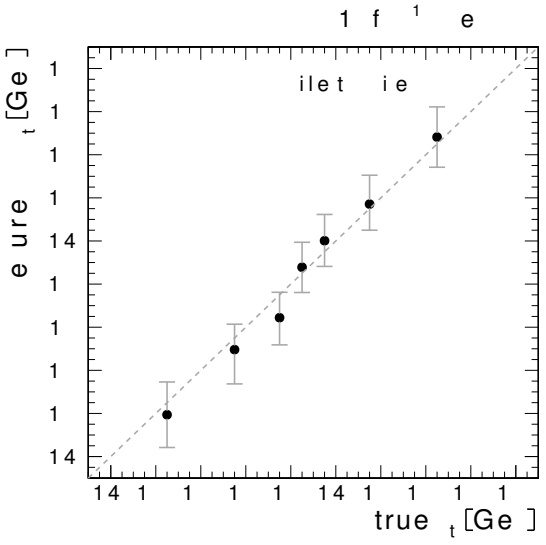

Figure 14.3: Comparison of the measured top quark mass from pseudo-data produced with different top quark masses (*true* m_t). The dashed line represents the diagonal. No trend or preferred value can be observed, and the performance of the extraction method is independent of the top quark mass in the pseudo-data sample.

within the statistical uncertainty of the fit. Propagating this uncertainty to the measured top quark mass would yield an additional uncertainty below 0.1 GeV for a mass shift of 1 GeV, and is negligible compared to the total uncertainty of the measurement as will be discussed in the following section.

Furthermore, the performance of the mass measurement without normalization of the distributions, or only from single bins of the ρ_S distribution has been evaluated. The results behave as expected: Omitting the normalization introduces additional systematic uncertainties from rate dependent sources and increases the total systematic uncertainty by about 1.5 GeV. Extracting the top quark mass only from the bin with the highest sensitivity neglects information available in the other bins of the distribution and thus yields larger statistical uncertainties of about 2 GeV, depending on the bin size and position.

14.3 Measurement of the Top Quark Mass

The top quark mass is measured from the combination of the dileptonic channels using the method outlined above. The analysis was first developed using pseudo-data. This so-called *blinding* of the analysis avoids influencing the measurement method to favor certain outcomes and ensures objectivity in the analysis design. Additionally, the uncertainties obtained from the measurement with data have been found to agree with the expected uncertainties derived from the blinded analysis, which indicates a good performance of the method.

The breakdown of all considered systematic uncertainties on the top quark mass measurement is presented in Table 14.1. The dominating uncertainties arise from modeling sources, namely the jet/parton matching threshold and the uncertainty on the renormalization and factorization scales. The measurement yields a slightly larger systematic uncertainty towards higher top quark masses because of the asymmetric behavior of the uncertainty on the jet/parton matching. For uncertainty sources affecting the shape of a distribution, there is no a priori reason for the

Table 14.1: Breakdown of the systematic uncertainties for the top quark mass measured from the normalized ρ_S distribution at reconstruction level for the combination of all dilepton channels.

Source	Δm_t[GeV]
Jet/Parton matching threshold	$^{+1.3}_{-0.1}$
Q^2 scale	± 2.0
Parton shower model	$^{+0.3}_{-0.2}$
Color reconnection	< 0.1
Underlying event	± 0.1
PDF	± 0.1
Background normalization	± 0.4
Jet energy scale	± 0.1
Jet energy resolution	± 0.1
Pile-up	± 0.1
Dilepton trigger efficiency	< 0.1
Kinematic reconstruction	< 0.1
Lepton selection efficiency	< 0.1
b-tagging efficiency	± 0.2
Systematic uncertainty	$^{+2.3}_{-2.0}$
Statistical uncertainty	$^{+1.0}_{-1.0}$
Total uncertainty	$^{+2.5}_{-2.2}$

systematic uncertainty to be symmetric, and similar effects have been observed before for the same uncertainty source [254].

Relevant experimental contributions stem from the background normalization and the uncertainty on b-tagging. The averaged total systematic uncertainty amounts to $\pm 2.2\,\text{GeV}$, corresponding to a relative uncertainty of 1.2 %. The statistical significance of the systematic uncertainties has been verified.

Measuring the central value of top quark mass from the global χ^2 distribution yields

$$m_t^{MC} = 173.1\,^{+1.0}_{-1.0}\,(\text{stat})\,^{+2.3}_{-2.0}\,(\text{syst})\,\text{GeV},$$

including the statistical uncertainties of both data and the MadGraph predictions as well as all systematic uncertainties discussed in Chapter 13. The measured mass can be identified with the Monte Carlo top quark mass.

The obtained result is in agreement with other measurements. The achieved precision is of the order 2.4 GeV (1.3 %) an is thus of similar size as the precision of the top quark mass measurement based on the inclusive $t\bar{t}$ cross section [258], but larger than the one obtained from direct measurements via the kinematic properties of the $t\bar{t}$ system.

To increase the precision of the measurement, the statistical uncertainty as well as the systematic uncertainties arising from modeling sources have to be addressed. In particular, the modeling uncertainties could be reduced by using reference simulations calculated at NLO. Moreover, with the increased collision energy of $\sqrt{s} = 13\,\text{TeV}$ of the LHC in Run 2, the increased cross section for $t\bar{t}$ production allows to collect a larger sample of dileptonic $t\bar{t}$ decays and will thus allow to reduce the statistical uncertainty of the measurement.

In order to facilitate the comparison with theoretical predictions, the measurement is also performed correcting for detector effects, and the top quark mass is determined from unfolded distributions at generator level as presented in Chapter 15. However, the measurement from the same quantity at reconstruction level does not suffer from bin-to-bin correlations introduced by the unfolding, features smaller statistical uncertainties, and serves as a cross-check.

15. Measurement of the Top Quark Mass from Differential $t\bar{t}$+jet Cross Sections

In this chapter, the top quark mass is measured from the normalized differential $t\bar{t}$+jet production cross section, which facilitates the direct comparison of the measurement with theoretical calculations without the need of a dedicated detector simulation or folding of the simulations to reconstruction level. The ρ_S distribution is corrected for detector effects, and the normalized differential cross section as a function of ρ_S (cf. Equation 10.5) is calculated. Differential cross sections of other observables of the $t\bar{t}$ system have been previously measured at both $\sqrt{s} = 7\,\text{TeV}$ and 8 TeV using a similar procedure, and are presented in [247, 254, 256, 257].

First, Section 15.1 describes the unfolding of the ρ_S distributions and the measurement of the differential cross sections. The global χ^2 method for the mass measurement including bin-to-bin correlations is described in Section 15.2, while Section 15.3 introduces the tests performed to evaluate the robustness of the unfolding and the measurement method. The results of the top quark mass measurements from the differential cross section are presented in Section 15.4, and the findings are summarized in Section 15.5.

15.1 Measurement of the Differential $t\bar{t}$+jet Cross Section

Differential cross sections describe the production cross section of a given process as a function of the selected observable. The measured number of events has to be corrected for detector effects in order to represent the actual cross sections which can be directly related to the matrix elements of the processes under investigation. In the following, the definition of the differential cross section is given and the effect of bin migrations is described. Finally, the method of regularized unfolding is presented and applied to the data.

15.1.1 Cross Section Definition

The differential cross section as a function of ρ_S is measured by evaluating the observed number of events in a defined segment of the phase space. The segments are realized as bins in the ρ_S distribution, and each bin is divided by the inclusive cross section for normalization. Hence, the normalized differential $t\bar{t}$+jet production cross section as a function of ρ_S is given by

$$\frac{1}{\sigma}\frac{d\sigma}{d\rho_S} = \frac{1}{\sigma}\frac{x_i}{\Delta_i^{\text{bin}}\mathcal{L}}, \tag{15.1}$$

where $\mathcal{L}$ denotes the luminosity, the term Δ_i^{bin} is the bin width, and x_i represents the number of signal events in data after background subtraction and correction for detector effects. The expression is normalized using the total inclusive cross section σ measured in the same phase space.

The measurement is performed in the visible phase space, i.e., the phase space geometrically and kinematically accessible by the experiment. Restricting the measurement to the visible phase space avoids additional model uncertainty which would arise from the extrapolation to the full phase space available in simulation. Kinematic requirements similar to the ones applied to data and detailed in Chapter 12 are imposed on the simulations.

The criteria are applied at generator level, i.e., after hadronization (cf. Section 11.1.3). At this level, jets are defined by applying the anti-k_T clustering algorithm (cf. Section 12.5) to all stable particles apart from the leptons and neutrinos of the W boson decays. b jets are defined as the jets containing at least one b hadron which is associated to the original b quark from the $t\bar{t}$ decay. The additional jet is selected as the jet with the highest p_T, excluding the previously identified b jets.

Only events are accepted, where pseudorapidities and transverse momenta of the leptons satisfy the requirements $|\eta| < 2.4$ and $p_T > 20\,\text{GeV}$, respectively. Furthermore, jets are selected with $|\eta| < 2.4$ and $p_T > 30\,\text{GeV}$, and the leading additional jet is required to fulfill the criterion of $p_T > 50\,\text{GeV}$.

Background events are subtracted from the ρ_S distributions for the cross section calculation. The contribution of non-$t\bar{t}$ background events is estimated from simulation as $N^{\text{other BG}}$, and directly subtracted from data. The expected number of $t\bar{t}$ background events, denoted as $N^{t\bar{t}\text{ BG}}$, is accounted for by correcting the remaining events by the signal fraction f^{sig}, which is defined as

$$f^{\text{sig}} = \frac{N^{t\bar{t}\text{ signal}}}{N^{t\bar{t}\text{ signal}} + N^{t\bar{t}\text{ BG}}}, \tag{15.2}$$

and is determined from simulation. This approach avoids a dependency on the inclusive $t\bar{t}$ production cross section. The final number of signal events in data is calculated as

$$N_i^{\text{sig}} = f^{\text{sig}} \left(N_i^{\text{data}} - N_i^{\text{other BG}} \right), \tag{15.3}$$

separately for each bin i of the distribution.

15.1.2 Migration and Binning

Events which are reconstructed from the detector responses are subject to migration effects, i.e., events which are generated in one bin of the observable might be reconstructed in another because of the limited resolution of the detector and finite bin sizes of the distribution. Furthermore, only a fraction of the total number of events generated in the collision are detected and correctly reconstructed due to limited efficiencies. These effects are described by the so-called response matrix $\boldsymbol{A}^{\text{resp}}$ given by

$$A_{ij}^{\text{resp}} = \frac{N_{i\to j}^{\text{rec}}}{N_i^{\text{gen}}}, \tag{15.4}$$

where $N_{i\to j}^{\text{rec}}$ describes the number of events generated in bin i and reconstructed in bin j, while N_i^{gen} denotes the total number of events generated in bin i. The response matrix contains all migration effects as well as the acceptance and efficiency factors for the experiment.

The probability of an event to migrate between different bins can be calculated from the response matrix, and is shown as migration matrix in Figure 15.1a for the $e^{\pm}\mu^{\mp}$ channel. Since migrations

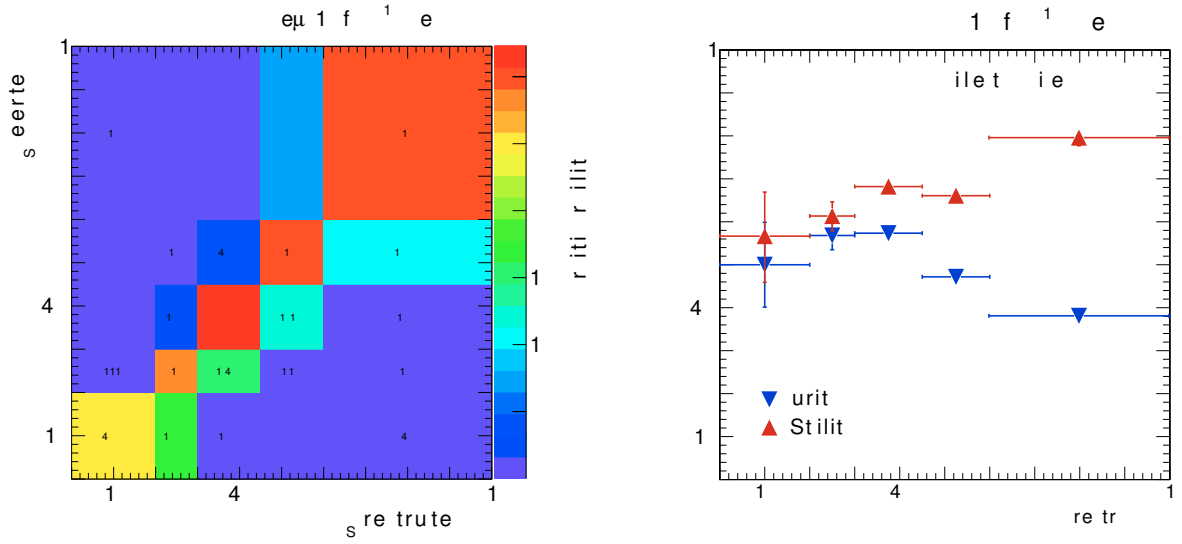

(a) Migration matrix showing the transition probability for the $e^{\pm}\mu^{\mp}$ channel.

(b) Purity and stability for all bins of the combination of the dileptonic channels.

Figure 15.1: Migration effects in the ρ_S distribution, presented as migration matrix (a), and as values of stability and purity for every bin (b). Both stability and purity show values above 40 %, with only the last bin exhibiting a smaller purity due to its size.

impair the precision of the measurement, an optimal binning of the distribution has to be determined in order to reduce the effects as much as possible. While small bins retain more information about the shape of the distribution, they contain fewer events and are subject to larger migration effects among them. The choice of binning is thus driven by finding a balance between the requirements described in the following.

Migrations can be quantified for a given bin i by the purity p_i and the stability s_i, defined as

$$p_i = \frac{N_i^{\text{rec\&gen}}}{N_i^{\text{rec}}}, \tag{15.5}$$

$$s_i = \frac{N_i^{\text{rec\&gen}}}{N_i^{\text{gen}}}. \tag{15.6}$$

Purity describes the fraction of all events reconstructed in one bin, N_i^{rec}, and the events which are both generated and reconstructed in the same bin, $N_i^{\text{rec\&gen}}$. It thus provides an estimate of the migrations into a given bin i. On the contrary, stability is defined as the fraction of events generated in one bin, which are reconstructed in the same bin and thus sheds light on the migration out of the bin under consideration. Without any migration effects, both purity and stability would be equal to unity. The number and size of bins is chosen such, that both stability and purity are above 40 % for all bins of the distribution as shown in Figure 15.1b.

For the measurements presented, an additional constraint has to be taken into account in order to optimize the sensitivity of the distribution on the top quark mass. The bin boundaries have to be chosen such, that the intersection point of the different cross section predictions depicted in Figure 10.5 aligns with a bin boundary. Otherwise, the shape differences in the bin containing the intersection cancel out and eliminate the mass sensitivity for the given bin. The size of the

last bin $0.6 < \rho_S < 1$ is driven by this requirement and thus exhibits a slightly lower purity owing to its size and the associated migration into the bin.

15.1.3 Regularized Unfolding

The effects from bin migrations and limited efficiencies can be removed from the measurement by inversely applying the detector response to the measured distribution. This yields the distribution $\vec{x}$ at generator level (*true* distribution), which relates with the measured signal distribution $\vec{N}^{\mathrm{sig}}$ via the response matrix as

$$\vec{N}^{\mathrm{sig}} = \boldsymbol{A}^{\mathrm{resp}} \vec{x}. \tag{15.7}$$

Hence, obtaining the true distribution from equation 15.7 requires the inversion of the response matrix

$$\vec{x} = \left(\boldsymbol{A}^{\mathrm{resp}}\right)^{-1} \vec{N}^{\mathrm{sig}}, \tag{15.8}$$

a situation commonly referred to as the *unfolding problem*. In general, this problem is ill-posed, as the results obtained from a direct inversion of $\boldsymbol{A}^{\mathrm{resp}}$ are usually unstable due to the spectral properties of the response matrix: The eigenvalues of response matrices generally span many orders of magnitude, with large values corresponding to significant and well defined contributions to the solution, and small eigenvalues originating from the correlations introduced by the migration effects discussed in the previous section. Small changes in the input distribution $\vec{N}^{\mathrm{sig}}$ can be amplified to large and unphysical oscillations in the solution for the true distribution $\vec{x}$.

The class of mathematical solutions to this problem is known as *regularized unfolding* which allows to evaluate the inversion by damping these oscillating solutions using *penalty terms*. A survey of different unfolding methods and their application in high energy particle physics is provided in [259], while [260–262] contain detailed descriptions of the singular value decomposition (SVD) regularization method deployed in this analysis.

Equation 15.7 can be solved for $\vec{x}$ using a minimum-χ^2 approach under inclusion of the penalty term $\tau \left(\boldsymbol{L}\vec{x}\right)^T \left(\boldsymbol{L}\vec{x}\right)$, also known as *Thikhonov* regularization [263]. This adds an additional a priori assumptions about the smoothness of the unfolded distribution to suppress high-frequency oscillations. The total χ^2 to be minimized is then given by

$$\chi^2\left(\vec{x}\right) = \left(\boldsymbol{A}^{\mathrm{resp}}\vec{x} - \vec{N}^{\mathrm{sig}}\right)^T \boldsymbol{COV}_{\mathrm{sig}}^{-1} \left(\boldsymbol{A}^{\mathrm{resp}}\vec{x} - \vec{N}^{\mathrm{sig}}\right) + \tau \left(\boldsymbol{L}\vec{x}\right)^T \left(\boldsymbol{L}\vec{x}\right), \tag{15.9}$$

where $\boldsymbol{L}$ defines the regularization matrix, and τ denotes the regularization parameter controlling the impact of the penalty term. The covariance matrix of the distribution at reconstruction level is represented by $\boldsymbol{COV}_{\mathrm{sig}}$.

The regularization matrix $\boldsymbol{L}$ for the penalty term is chosen as the curvature matrix

$$\boldsymbol{L}^2 = \begin{pmatrix} 1 & -1 & 0 & & \\ -1 & 2 & -1 & 0 & \\ & \ddots & \ddots & \ddots & \\ & 0 & -1 & 2 & -1 \\ & & 0 & -1 & 1 \end{pmatrix} \tag{15.10}$$

according to the SVD method described in [260].

Covariance matrices generalize the notion of variances. The relative uncertainty of two bins i and j of a distribution is represented by the covariance matrix element given by [188]

$$COV_{ij} = \mathrm{E}\left[\left(x_i - \mathrm{E}\left[x_i\right]\right)\left(x_j - \mathrm{E}\left[x_j\right]\right)\right], \tag{15.11}$$

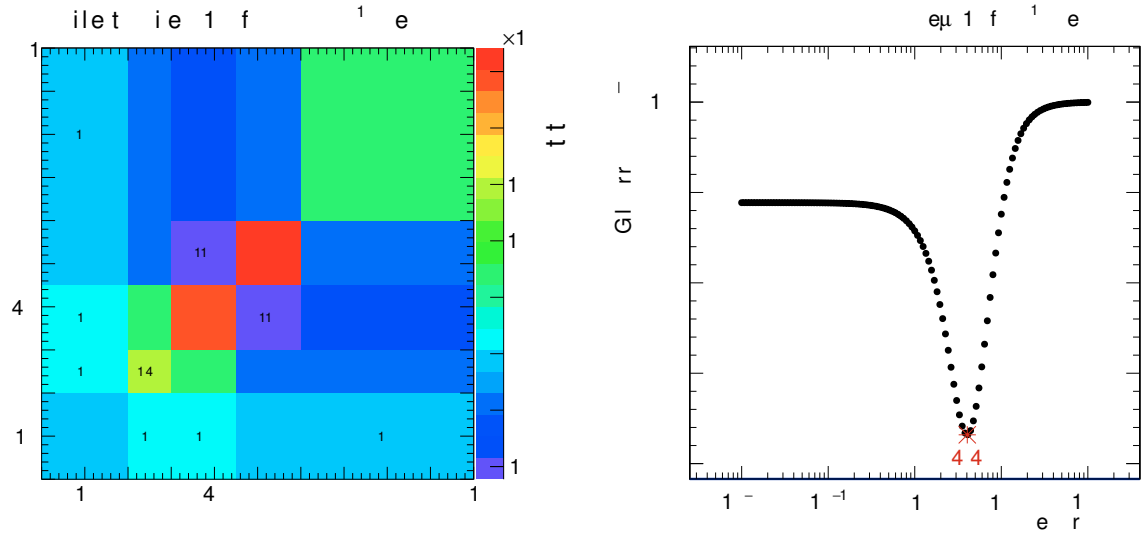

(a) Normalized statistical covariance matrix, combined for all dilepton channels.

(b) Scan of the average global correlation $\bar{\rho}$ over the regularization parameter τ for the $e^{\pm}\mu^{\mp}$ channel.

Figure 15.2: Statistical covariance matrix of the unfolded distribution for the combination of the decay channels (a), and regularization parameter scan for the $e^{\pm}\mu^{\mp}$ channel (b).

where E[x] denotes the expectation value of x. The diagonal elements correspond to the variances of the respective bins, and thus to their squared statistical uncertainty σ^2. Off-diagonal elements are only present for correlated bins and zero otherwise. For the measured distribution at reconstruction level, all bins are uncorrelated and the covariance matrix solely consists of the variances in the diagonal elements, viz.

$$COV_{ij}^{\text{sig}} = \delta_{ij} \left(\sigma_{\text{data}}^{i}\right)^2, \tag{15.12}$$

where δ_{ij} denotes the Kronecker delta. The inverse of the matrix can be calculated as the reciprocal of the individual elements if none of the variances is zero.

The statistical covariance matrix of the unfolded distribution $\boldsymbol{COV}^{\text{true}}$ can be obtained from $\boldsymbol{COV}^{\text{sig}}$ via propagation of uncertainties using pseudo-experiments. The measured event distribution is overlaid with random noise according to its statistical uncertainty and is unfolded to generator level. This procedure is repeated one thousand times in order to construct the covariance matrix of the unfolded distribution. Due to migrations, the bins are correlated, and thus the off-diagonal elements of the covariance matrix are non-vanishing. The normalized unfolded covariance matrices are calculated separately for the three dileptonic channels. The individual elements can then be combined by the inverse sum

$$\frac{1}{COV_{ij}^{\text{true}}} = \frac{1}{COV_{ij}^{\text{e}^+\text{e}^-}} + \frac{1}{COV_{ij}^{\mu^+\mu^-}} + \frac{1}{COV_{ij}^{\text{e}^{\pm}\mu^{\mp}}}, \tag{15.13}$$

to obtain the normalized covariance matrix for the combination of the three channels shown in Figure 15.2a.

The remaining difficulty is the determination of the optimal regularization strength. The regularization parameter τ is chosen such, that a robust and stable result is obtained. For $\tau = 0$,

no regularization is performed, and all high-frequency fluctuations are conserved. Large values of τ, on the other hand, might not only damp oscillations from statistical fluctuations, but also remove features of the true distribution itself and influence the result towards the simulation.

While there is no generally accepted and unique method to determine the regularization parameter τ, one possibility is demanding minimal correlations between the bins. This analysis uses the method of minimizing the average global correlation [188, 262]. The global correlation for bin i is defined as

$$\rho_i(\tau) = \sqrt{1 - \frac{1}{COV_{ii} COV^{-1}_{ii}}}, \tag{15.14}$$

where $\boldsymbol{COV} \equiv \boldsymbol{COV}^{\text{true}}$ represents the statistical covariance matrix of the unfolded distribution. The average global correlation is then calculated from all bins as

$$\bar{\rho}(\tau) = \frac{1}{n} \sum_i \rho_i(\tau), \tag{15.15}$$

where n is the total number of bins considered.

In order to find the optimal regularization strength, the parameter τ is scanned over a large range, the distribution is unfolded using the new regularization strength, and $\bar{\rho}$ is recalculated as shown in Figure 15.2b. Finally, the τ value with the minimum average global correlation is chosen as regularization strength for the unfolding. The τ parameter is optimized individually for each of the dileptonic decay channels.

15.1.4 Differential $t\bar{t}$+jet Production Cross Section as a function of ρ_S

The normalized differential $t\bar{t}$+jet production cross section is calculated individually for each of the three dileptonic channels, using the regularized unfolding method described previously. These measurements are then combined separately for each bin, according to their statistical significance. Since the channels are statistically independent, the combination is calculated as weighted mean. The MadGraph simulation with $m_t^{MC} = 172.5\,\text{GeV}$ has been chosen as reference sample for the calculation of the response matrix $\boldsymbol{A}^{\text{resp}}$ and the background estimation. The impact of this choice on the measured top quark mass is evaluated in Section 15.3.

Figure 15.3 presents the obtained differential cross section distributions for each channel individually as well as for their combination. Shown are the measured differential cross sections, compared to the predictions from MadGraph with $m_t^{MC} = 172.5\,\text{GeV}$, $m_t^{MC} = 166.5\,\text{GeV}$ and $m_t^{MC} = 178.5\,\text{GeV}$. The distribution exhibits a strong sensitivity on the top quark mass as expected (cf. Section 10.5). Especially the differential cross section in the bins $0.3 < \rho_S < 0.45$ and $\rho_S > 0.6$ depend on the top quark mass chosen, which conforms to the predictions presented in [12].

The systematic uncertainties on the measurement are assessed from variations of the cross section for each of the bins individually. The full analysis is repeated for every systematic variation, and the difference with respect to the nominal measurement is quoted as the corresponding uncertainty. A breakdown of the evaluated systematic uncertainties is presented in Table 15.1 for the combination of all dileptonic decay channels. Relative uncertainties for each uncertainty source as well as the total systematic uncertainty are given for each bin.

15.2 Global χ^2 Template Fit including Statistical Correlations

The mass measurement from the normalized differential cross sections follows the minimum-χ^2 estimation method described in Section 14.1 with the following modifications to account for the

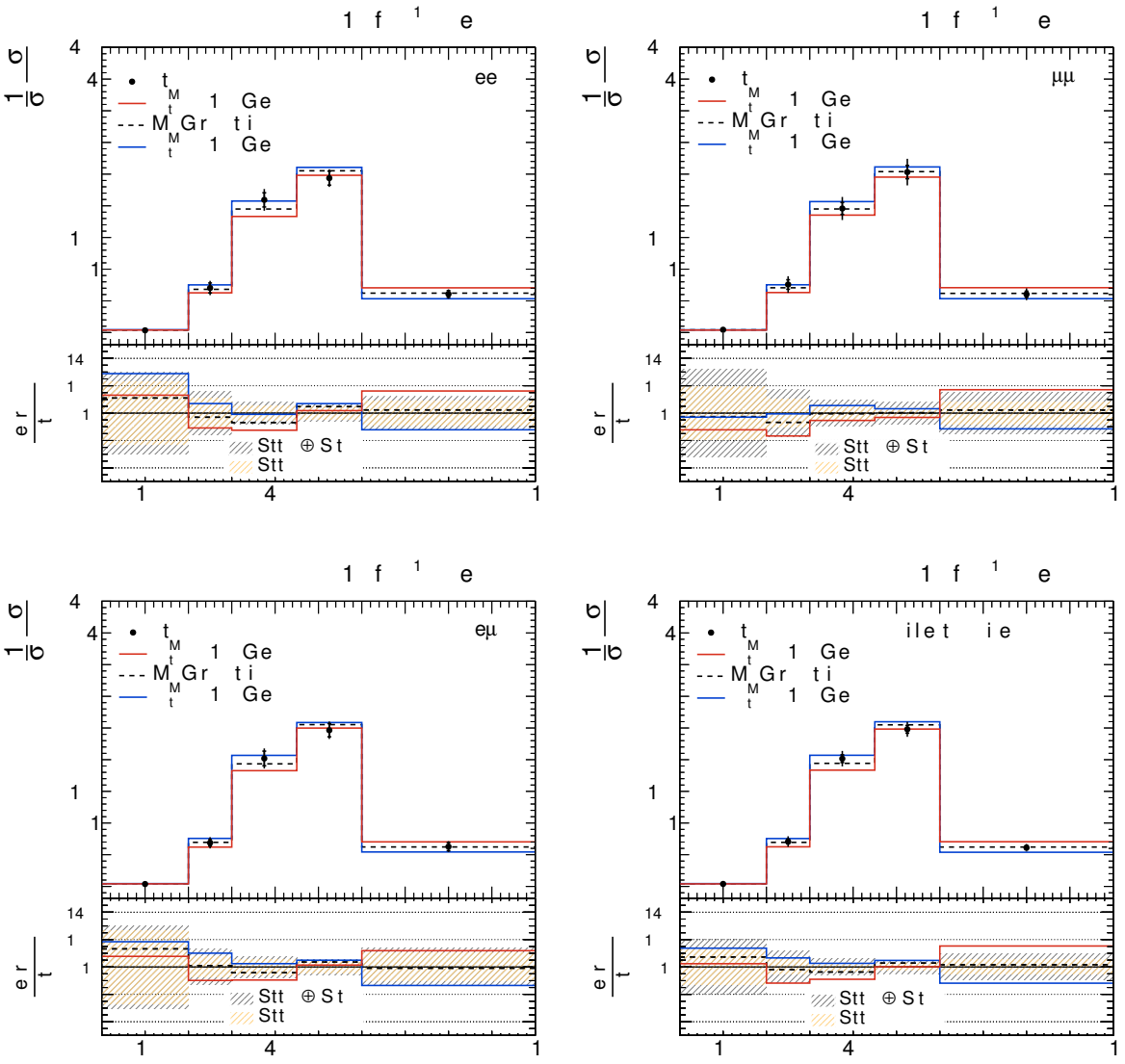

Figure 15.3: Normalized differential $\mathrm{t\bar{t}}$+jet production cross section as a function of ρ_S for the channels $\mathrm{e^+e^-}$ (top left), $\mu^+\mu^-$ (top right), and $\mathrm{e^{\pm}\mu^{\mp}}$ (bottom left) as well as for their combination (bottom right). Shown are the measured differential cross section together with the MadGraph prediction with $m_\mathrm{t}^\mathrm{MC} = 172.5\,\mathrm{GeV}$ used for unfolding (dashed), and two additional predictions with different top quark masses (red, blue). The hatched bands correspond to the statistical (yellow) and total uncertainty (gray).

Table 15.1: Breakdown of the systematic uncertainties for each bin of the cross section measurement for the combination of the three dileptonic channels. Results are given in percent.

Source	% uncertainty per bin in ρ_S				
	$(0, 0.2)$	$(0.2, 0.3)$	$(0.3, 0.45)$	$(0.45, 0.6)$	$(0.6, 1)$
Jet/parton matching thr.	4.8	3.0	0.5	0.6	1.5
Q^2 scale	6.3	2.6	2.4	0.9	4.4
Parton shower model	4.7	2.5	1.4	2.5	1.3
Color reconnection	5.6	5.0	0.7	1.0	1.1
Underlying event	2.4	4.0	0.5	2.1	2.6
PDF	9.6	6.5	4.2	1.9	5.7
Background normalization	2.7	1.9	1.0	0.3	1.9
Jet energy scale	0.5	0.2	0.2	< 0.1	0.2
Jet energy resolution	0.5	0.2	0.1	0.2	0.2
Pile-up	1.4	0.6	0.3	0.1	0.4
Dilepton trigger eff.	0.3	0.2	0.1	< 0.1	0.5
Kin. reconstruction	0.1	< 0.1	< 0.1	< 0.1	< 0.1
Lepton selection eff.	0.4	0.2	0.1	< 0.1	0.2
b-tagging eff.	0.3	0.1	0.1	< 0.1	0.1
Total syst.	15.0	10.4	5.2	4.1	8.2

fact that the individual bins of the ρ_S distribution cannot be treated as statistically independent owing to the unfolding.

The predicted differential cross sections are obtained at generator level in the visible phase space, following the definition given in Section 15.1.1. A vector $\boldsymbol{V}(m_\mathrm{t})$ with the difference between the measured and the predicted cross sections is calculated for each bin of the ρ_S distribution as

$$V_i(m_\mathrm{t}) = \left(\frac{1}{\sigma}\frac{d\sigma}{d\rho_S}\right)_i - f_i^{\mathrm{MC}}(m_\mathrm{t}), \tag{15.16}$$

where $(d\sigma/\sigma d\rho_S)_i$ denotes the measured normalized differential cross section in bin i of the ρ_S distribution, and $f_i^{\mathrm{MC}}(m_\mathrm{t})$ represents the continuous parametrization of the MC predictions obtained from the polynomial fit given in Equation 14.4. The statistical uncertainty of the MC predictions is obtained from the confidence interval of the polynomial fit, and is added to the diagonal of the normalized covariance matrix of the measurement as

$$COV_{ij}\left(m_\mathrm{t}\right) = COV_{ij}^{\mathrm{true}} + \delta_{ij}\left(\sigma_i^{\mathrm{MC}}\left(m_\mathrm{t}\right)\right)^2, \tag{15.17}$$

where σ_i^{MC} denotes the statistical uncertainty of the MC predictions, and δ_{ij} is the Kronecker delta. Adding the statistical uncertainty of the predictions removes the singularity of the normalized unfolding covariance matrix, and allows its inversion without additional measures. For the combination of all dileptonic channels, the covariance matrix is calculated from Equation 15.13.

After inversion, the reduced number of degrees of freedom from the normalization is accounted for by removing the least significant bin of the measurement from the covariance matrix and the vector $\boldsymbol{V}$, respectively. Finally, the global χ^2 is evaluated as the vector product

$$\chi^2\left(m_t\right) = \boldsymbol{V}^T\left(m_\mathrm{t}\right) \times \boldsymbol{COV}\left(m_\mathrm{t}\right)^{-1} \times \boldsymbol{V}\left(m_\mathrm{t}\right), \tag{15.18}$$

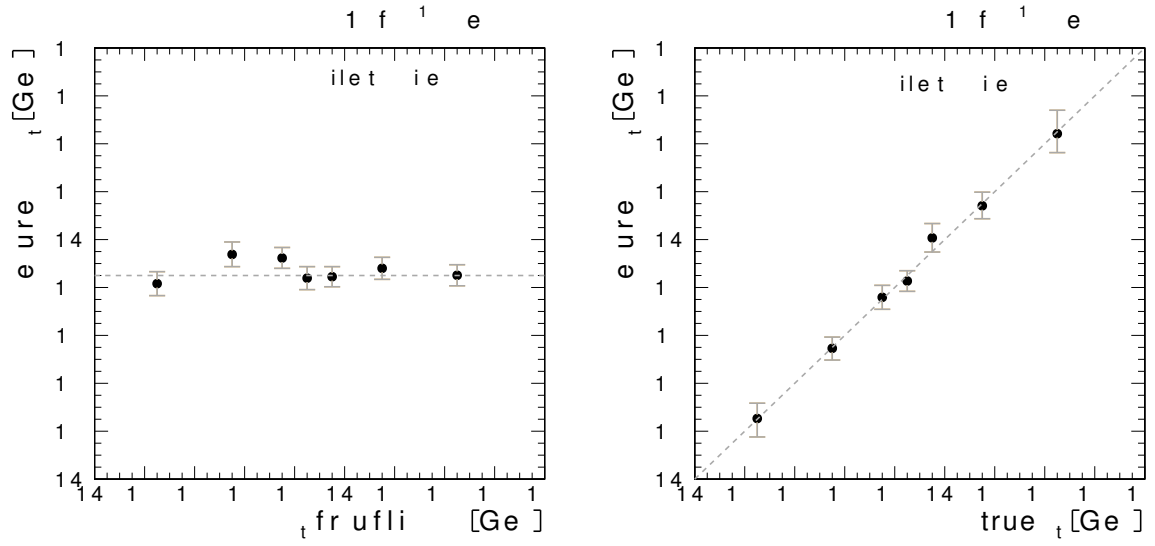

(a) Dependence of the measured top quark mass of the reference simulation. The mass of the pseudo-data is indicated as dashed line.

(b) Comparison of the measured top quark mass from pseudo-data sets with different masses. The dashed line represents the diagonal.

Figure 15.4: Measured top quark mass as a function of the mass of the MadGraph reference simulation for the measurement (a), and as a function of the assumed top quark masses of the pseudo-data (b). No trend or preferred value can be observed, and the performance of unfolding and mass measurement is independent of the top quark masses in the reference simulations.

where $\boldsymbol{COV}^{-1}$ represents the inverse statistical covariance matrix as calculated in Equation 15.17. The top quark mass is extracted from the minimum of the global χ^2 distribution, and the statistical and systematic uncertainties are obtained as described in Sections 14.1.1 and 14.1.2.

15.3 Tests of the Unfolding and Extraction Technique

The stability of the unfolding procedure and the mass measurement from the normalized differential cross section are tested using pseudo-data. The pseudo-data at reconstruction level described in Section 14.2 are unfolded to generator level using the same method as applied to data.

Figure 15.4a shows the measured top quark mass from pseudo-data with $m_{\mathrm{t}}^{\mathrm{MC}} = 172.5\,\mathrm{GeV}$ as a function of the mass of the reference simulation used for the measurement. The pseudo-data is unfolded using each of the MadGraph samples with varied top quark masses, and the mass measurement is repeated using the pseudo-data and the MadGraph predictions. No influence of the top quark mass assumption made for the reference simulation can be observed.

The second test, proving the robustness of the measurement, is performed using the same procedure as described in Section 14.2. The top quark mass is measured from several pseudo-data sets produced with different top quark masses. The results presented in Figure 15.4b demonstrate, that the measured top quark mass is in agreement with the simulated masses assumed for the pseudo-data, and no trend or favored top quark mass can be observed. A linear fit to the distribution with $m_{\mathrm{t}}^{\mathrm{meas}} = p_0 + p_1 m_{\mathrm{t}}^{\mathrm{true}}$ yields a slope of $p_1 = 1.04 \pm 0.07$, which is compatible with the diagonal within the fit uncertainty. Considering a variation of the top quark

mass by 1 GeV, the effect would translate to a ± 0.05 GeV deviation in the final result, which is well below the statistical uncertainty of the measurement.

15.4 Determination of the Top Quark Mass

Using the normalized differential cross sections calculated in the previous sections, the top quark mass is measured using two different predictions. The mass measurement presented in Section 15.4.1 uses the same MadGraph predictions as employed for the unfolding of the data and serves as direct comparison for the measurement conducted at reconstruction level. In Section 15.4.2, a first measurement is presented using the NLO Powheg $t\bar{t}$+jet simulations described in Section 11.2.2 to extract a theoretically well-defined top quark mass.

15.4.1 Measurement of m_t^{MC} from Differential Cross Sections

The top quark mass is measured from the normalized differential $t\bar{t}$+jet production cross section as a function of the ρ_S observable using the MadGraph predictions employed in Chapter 14. The measurement serves as direct comparison to the measurement at reconstruction level in order to evaluate the sensitivity of the two approaches. Figure 15.5 presents the measured differential cross section and the predictions with different top quark masses for the four bins considered in the global χ^2 minimization. The hatched bands represent the statistical uncertainties of the measured cross section and the fit to the predictions, respectively. The sensitivity of a given bin can be estimated by neglecting the bin correlations and by calculating the local χ_i^2 estimator following the methodology presented in Section 14.1 as demonstrated in Figure 15.6a for the highest bin of the ρ_S distribution. The global χ^2 including the bin correlations, calculated as described in Section 15.2 is presented in Figure 15.6b. The distributions features a distinct minimum for the mass extraction and the value of $\chi^2_{\text{min}}/\text{ndof} = 1.5$ indicates a good fit.

A breakdown of all systematic uncertainty sources is provided in Table 15.2. The uncertainties are dominated by modeling sources, as expected from the results presented in Chapter 14, namely jet/parton matching threshold and the MadGraph Q^2 hard-scattering scale. When measuring the top quark mass from differential cross sections, these uncertainties influence the result via the unfolding of the data distributions and via the predictions used for the mass determination. In order to avoid double counting of uncertainties when evaluating these effects individually, the jet/parton matching threshold and the Q^2 scale are varied coherently up and down for both the measurement of the differential cross section and the predictions. The systematic uncertainty attributed to the sources is taken as the difference between the measurement with both simulations varied and the nominal mass measurement.

The experimental uncertainties are compatible with the uncertainties of the measurement at reconstruction level presented in Table 14.1, with the dominant contribution arising from the background normalization. The averaged total systematic uncertainty amounts to ± 2.0 GeV, corresponding to a relative systematic uncertainty of 1.1 %. The top quark mass measured from the combination of the three dileptonic channels results to

$$m_t^{MC} = 173.8\,^{+1.1}_{-1.1}\,(\text{stat})\,^{+2.0}_{-1.9}\,(\text{syst})\,\text{GeV},$$

and represents the Monte Carlo top quark mass as defined by the MadGraph generator.

The number of events available from the MadGraph simulation in the visible phase space at generator level is about twice the number of events at reconstruction level because of the reconstruction efficiencies. Thus, the statistical uncertainty displayed as red band in Figure 15.5 is reduced compared to the uncertainty of the predictions presented in Figure 14.1 at reconstruction level. Furthermore, owing to the different sample sizes the two top quark masses are not expected to be the same. Nevertheless, both central values agree within 1σ of the statistical uncertainties.

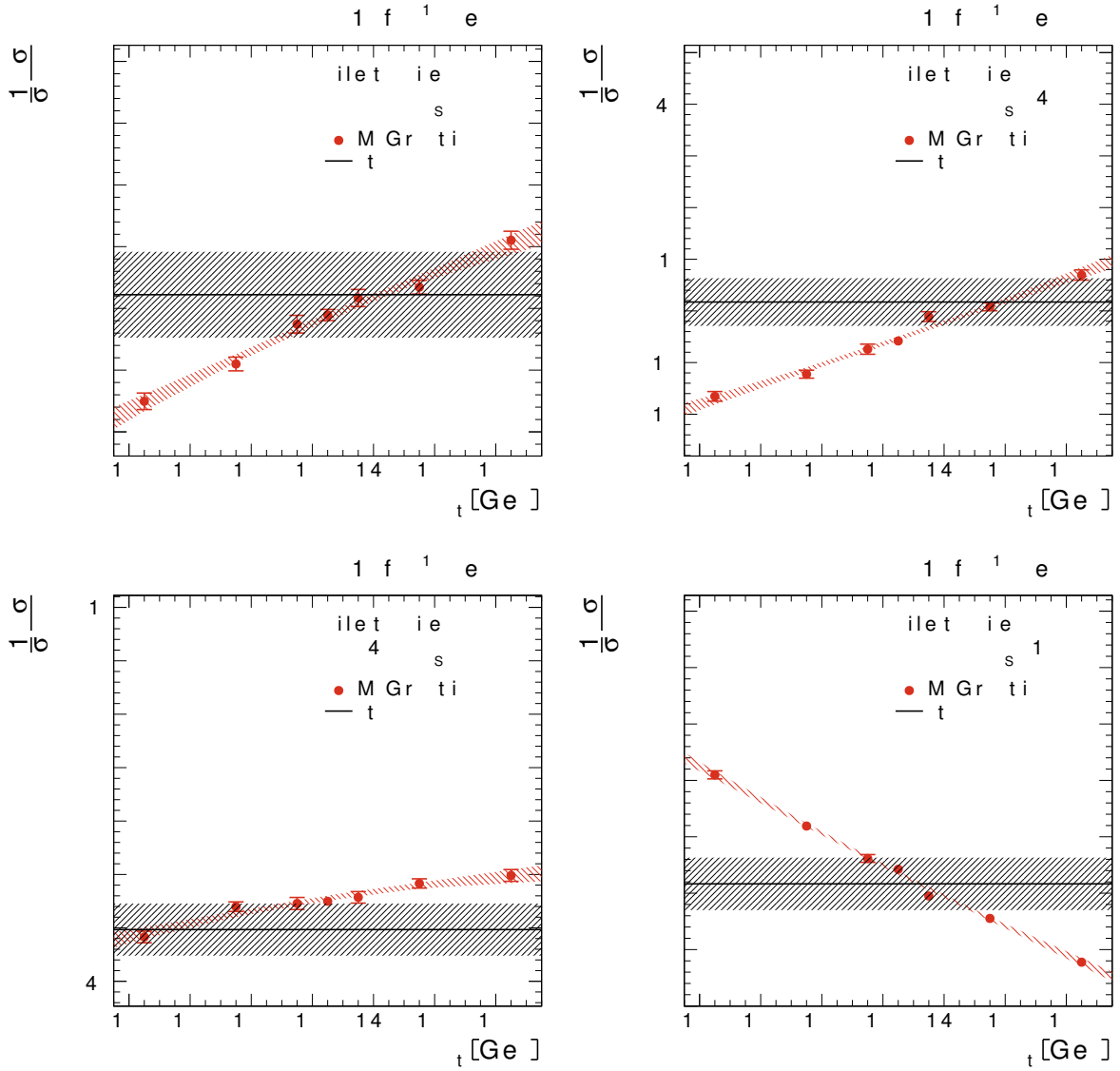

Figure 15.5: Observed and expected differential cross sections in the considered bins of the ρ_S distribution for the combination of the dileptonic channels. The predictions are obtained from MadGraph simulations. The hatched bands correspond to the statistical uncertainty of the measured cross section and the fit to the predictions, respectively.

Table 15.2: Breakdown of the systematic uncertainties for the top quark mass measured from the normalized differential $t\bar{t}$+jet production cross section and MadGraph predictions for the combination of all dilepton channels.

Source	Δm_t[GeV]
Jet/parton matching threshold	$^{+1.3}_{-0.1}$
Q^2 scale	$^{+0.5}_{-1.4}$
Parton shower model	± 0.4
Color reconnection	± 0.6
Underlying event	± 0.4
PDF	$^{+0.4}_{-0.3}$
Background normalization	± 0.9
Jet energy scale	$^{+0.1}_{-0.2}$
Jet energy resolution	± 0.1
Pile-up	± 0.3
Dilepton trigger efficiency	± 0.1
Kinematic reconstruction	< 0.1
Lepton selection efficiency	± 0.1
b-tagging efficiency	$^{+0.3}_{-0.2}$
Systematic uncertainty	$^{+2.0}_{-1.9}$
Statistical uncertainty	± 1.1
Total uncertainty	$^{+2.3}_{-2.2}$

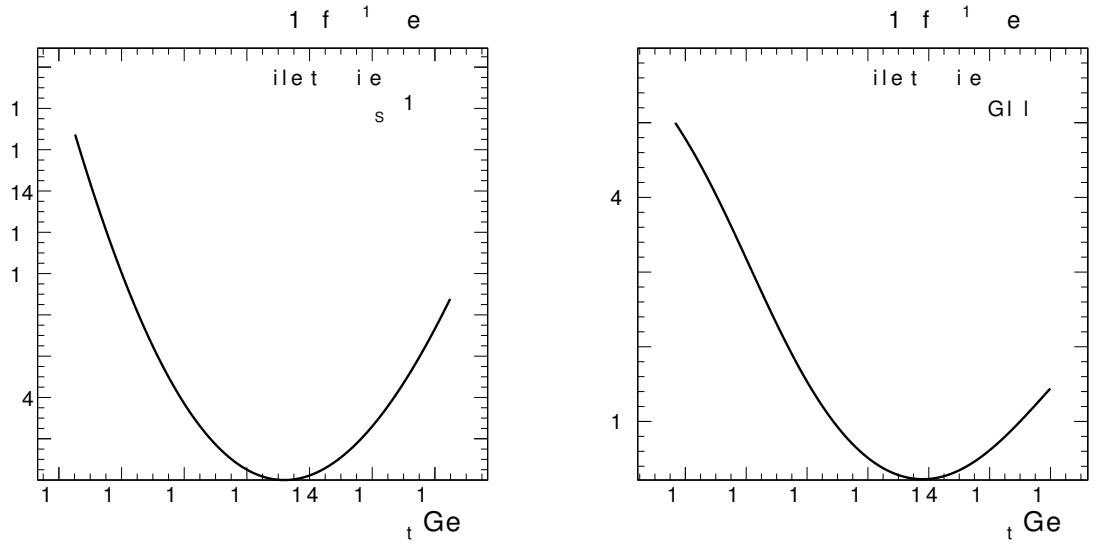

(a) Local χ^2_i distribution calculated from the distributions of the highest ρ_S bin.

(b) Global χ^2 distribution obtained from combining all relevant bins.

Figure 15.6: Local χ^2_i distribution for the highest bin in ρ_S (a), and global χ^2 distribution from all bins for the combination of the dileptonic channels (b).

15.4.2 Measurement of $m_{\mathrm{t}}^{\mathrm{pole}}$ from Differential Cross Sections

The main objective of this analysis is the measurement of a theoretically well-defined top quark mass from differential cross sections as a function of ρ_S as suggested in [12]. This pole mass determination is to be interpreted as exploratory measurement using a new observable and hence does not yet reach the optimal achievable precision.

The production of $\mathrm{t\bar{t}}$+jet events with NLO precision matrix element calculations and parton shower has been described in Section 11.2.2. Additionally, in order to validate the simulation, the predicted cross sections have been compared to other simulations as well as to the measurement. In Figure 15.7, the differential cross section for several observables is compared to the POWHEG $\mathrm{t\bar{t}}$+jet simulation as well as to the MADGRAPH prediction and to the official CMS POWHEG $\mathrm{t\bar{t}}$ simulation. All simulations have been produced using the nominal $m_{\mathrm{t}}^{\mathrm{MC}} = 172.5\,\mathrm{GeV}$, and the differential cross sections for the different observables have been obtained following the method described in Section 15.1 using the $m_{\mathrm{t}}^{\mathrm{MC}} = 172.5\,\mathrm{GeV}$ MADGRAPH prediction as reference. Shown are the normalized cross sections as functions of the lepton p_T, the invariant mass of the $\mathrm{t\bar{t}}$ system, the p_T of the leading additional jet, and the ρ_S observable. The hatched band represents the statistical uncertainty of the measured cross section.

For the lepton p_T distribution in Figure 15.7a, data is best described by the POWHEG $\mathrm{t\bar{t}}$+jet simulation, while the MADGRAPH simulation shows some deviation towards high values of p_T. The POWHEG $\mathrm{t\bar{t}}$+jet and MADGRAPH simulations provide very similar description of the invariant mass of the $\mathrm{t\bar{t}}$ system as shown in Figure 15.7b, and favor lower values of $m_{\mathrm{t\bar{t}}}$ compared to data. All simulations predict somewhat higher p_T values for the leading additional jet p_T, while this effect is most visible for the POWHEG $\mathrm{t\bar{t}}$+jet sample as depicted in Figure 15.7c. For the ρ_S observable presented in Figure 15.7d, reasonable agreement between data and all predictions can be observed for most of the range. Deviations are visible only in the lowest bin for both POWHEG simulations but are in agreement with data within 2σ of the total uncertainty. As this represents the bin to be removed from the global χ^2 calculation, the deviation is not

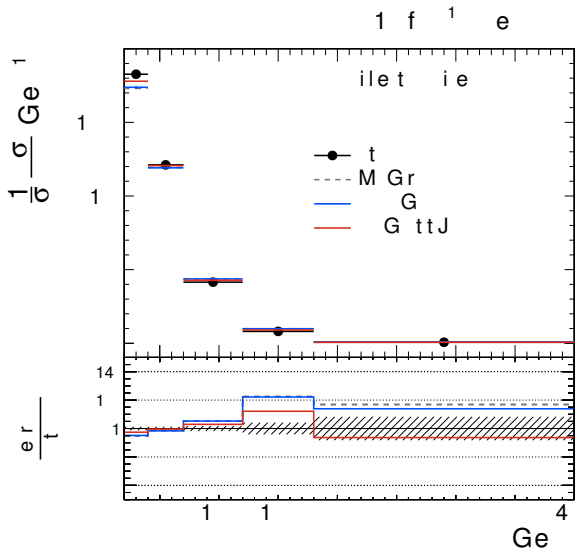

(a) Differential cross section as a function of the lepton p_T.

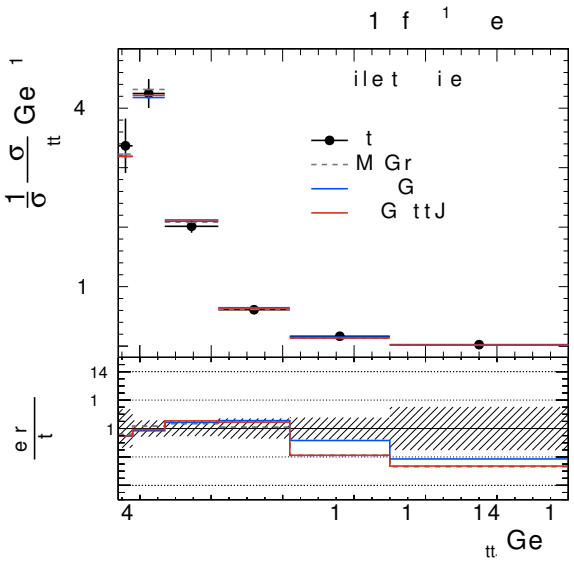

(b) Differential cross section as a function of the invariant mass of the $t\bar{t}$ system.

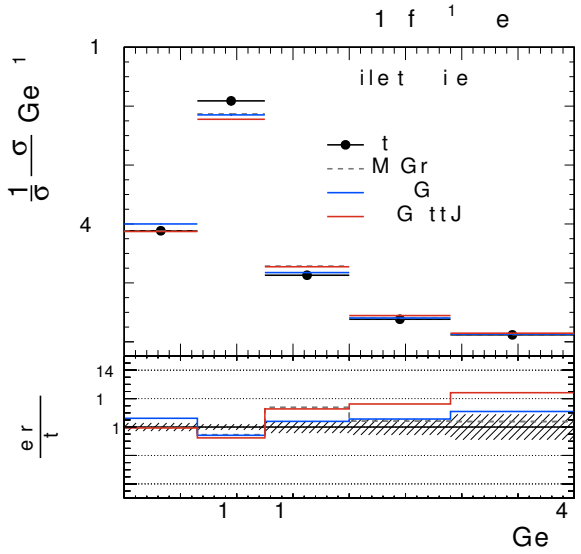

(c) Differential cross section as a function of the leading additional jet p_T. The lowest bin only contains jets with $p_T > 50\,\text{GeV}$.

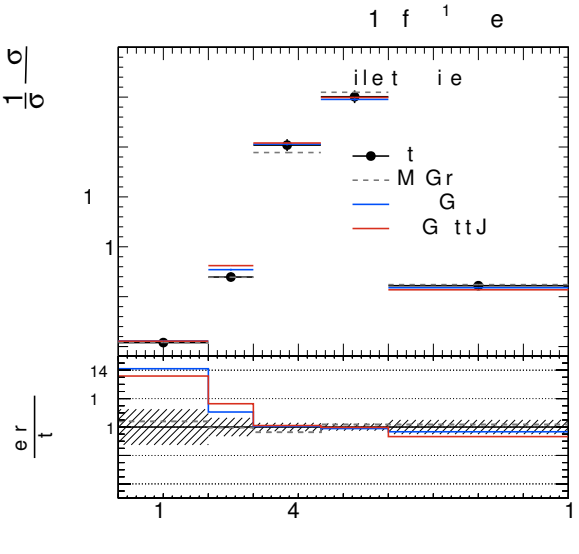

(d) Differential cross section as a function of ρ_S.

Figure 15.7: Comparison of the measured differential cross sections and different simulations with $m_t^{MC} = 172.5\,\text{GeV}$ by MadGraph (gray dashed), the reference CMS Powheg $t\bar{t}$ sample (blue), and the Powheg *ttJ* process (red). Shown is the combination of all dileptonic channels. The hatched bands represent the statistical uncertainty of the data.

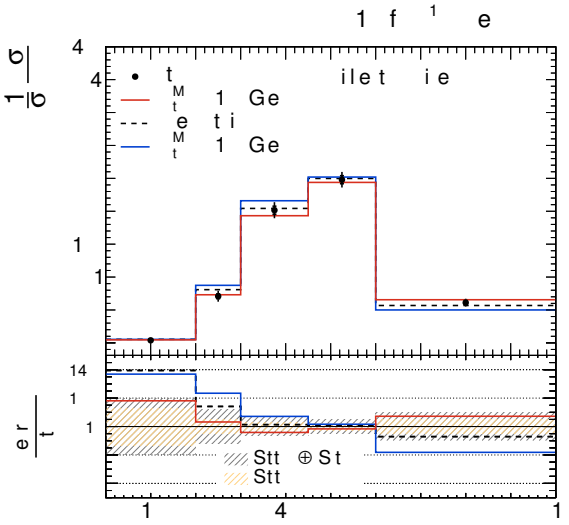

Figure 15.8: Normalized differential $t\bar{t}$+jet production cross section as a function of ρ_S for combination of all dileptonic channels. Shown are the measured differential cross section together with POWHEG $t\bar{t}$+jet predictions with $m_t^{MC} = 166.5\,\text{GeV}$ (red), $m_t^{MC} = 172.5\,\text{GeV}$ (dashed), and $m_t^{MC} = 178.5\,\text{GeV}$ (blue). The hatched bands correspond to the statistical (yellow) and total uncertainty (gray).

expected to have a strong influence on the top quark mass measurement.

Figure 15.8 shows the measured differential cross section compared to the NLO predictions obtained from POWHEG $t\bar{t}$+jet for three different assumed top quark masses. Especially the bins $0.3 < \rho_S < 0.45$ and $\rho_S > 0.6$ show a strong dependence on the top quark mass, which is in accordance with the results presented in Section 15.1.4. It can already be inferred from the figure that simulations with top quark masses lower than the nominal value of $m_t^{MC} = 172.5\,\text{GeV}$ provide a better description of the measured differential cross section.

The differential cross section and the NLO $t\bar{t}$+jet predictions in each of the relevant bins are presented in Figure 15.9 for illustration. The global χ^2 distribution including the statistical covariance is presented in Figure 15.10. The minimum of the distribution is shifted to lower values of m_t with respect to the measurement presented in the previous section using MADGRAPH predictions. The deviation from the parabolic shape arises from the larger fit uncertainties at the maximum and minimum values of m_t available as predictions. With the minimum of the global χ^2 close to the prediction with the lowest available top quark mass, the fit is not optimally constrained. This is also reflected in the goodness of fit estimate with $\chi^2_{min}/\text{ndof} \approx 2$. An additional prediction at $m_t = 163.5\,\text{GeV}$ might help to improve the fit.

Unlike for the measurement presented in the previous section, two different simulations are used for the measurement of the differential cross section and for the mass determination, and consequently, two independent model uncertainties need to be considered. Since POWHEG and MADGRAPH implement different definitions for the renormalization and factorization scales, and the hard-scattering Q^2 scale, respectively, the uncertainties arising from their variation have to be evaluated separately. The uncertainty arising from using MADGRAPH for the differential cross section measurement is evaluated by repeating the mass determination with the MADGRAPH simulations with varied Q^2 scales (cf. Section 11.2.1) and the POWHEG $t\bar{t}$+jet simulation. The

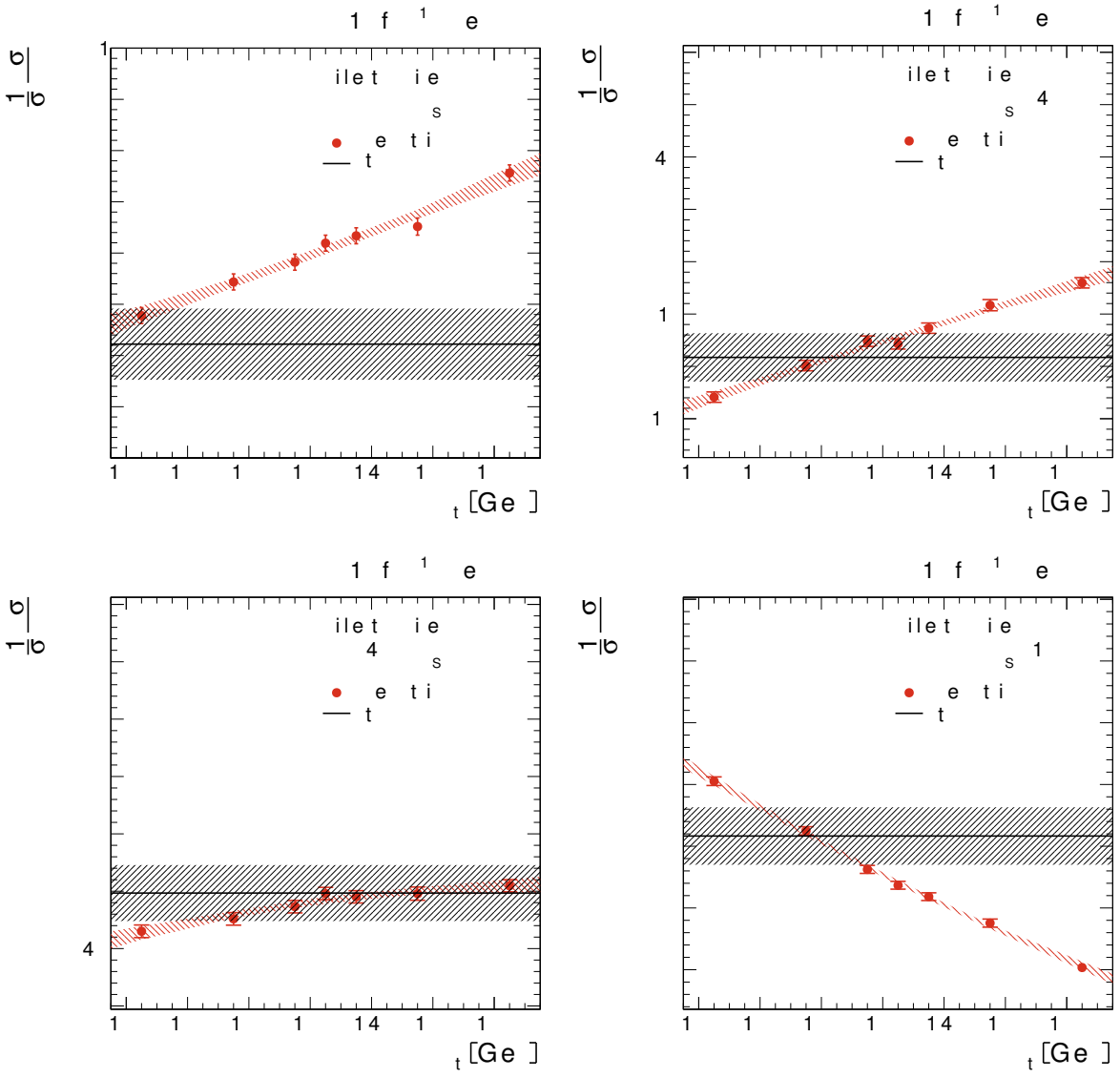

Figure 15.9: Observed and expected differential cross sections from the NLO POWHEG $t\bar{t}$+jet predictions for the considered bins of the ρ_S distribution for the combination of all dileptonic channels.

Table 15.3: Breakdown of the systematic uncertainties for the top quark mass measured from the normalized differential $t\bar{t}$+jet production cross section and POWHEG $t\bar{t}$+jet predictions at NLO for the combination of all dilepton channels.

Source	Δm_t[GeV]
POWHEG $t\bar{t}$+jet modeling	$^{+3.9}_{-0.4}$
Jet/parton matching threshold	$^{+1.5}_{-0.1}$
Q^2 scale	$^{+0.9}_{-1.7}$
Parton shower model	± 0.4
Color reconnection	± 0.6
Underlying event	± 0.4
PDF	$^{+1.4}_{-0.1}$
Background normalization	± 0.9
Jet energy scale	$^{+0.1}_{-0.2}$
Jet energy resolution	± 0.1
Pile-up	± 0.3
Dilepton trigger efficiency	± 0.1
Kinematic reconstruction	< 0.1
Lepton selection efficiency	± 0.1
b-tagging efficiency	$^{+0.3}_{-0.2}$
Systematic uncertainty	$^{+2.6}_{-2.1}$
Statistical uncertainty	± 1.1
Total uncertainty	$^{+4.7}_{-2.1}$

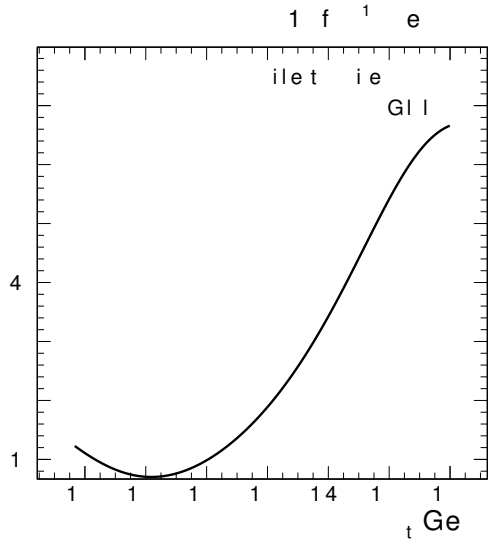

Figure 15.10: Global χ^2 distribution from all bins for the combination of all dileptonic channels, obtained with the NLO $t\bar{t}$+jet predictions.

renormalization and factorization scale uncertainties arising from the POWHEG predictions are evaluated by comparing the measured differential cross section to the dedicated POWHEG simulations with varied scales described in Section 11.2.2.

The breakdown of the uncertainties arising from the theoretical predictions and the differential cross section measurement is provided in Table 15.3. Similar to the measurement using the MADGRAPH predictions, the dominating systematic uncertainty from the differential cross section measurement corresponds to the jet/parton matching threshold and the Q^2 scale variations. The latter is slightly larger compared to the measurement using MADGRAPH simulations owing to the weakly constrained fit as outlined above. A larger mass range of the predictions would allow to better constrain the uncertainty of the fit. The systematic uncertainties arising from experimental sources are compatible with the values obtained from the measurement with MADGRAPH presented in Table 15.2.

The mass measurement is performed for the combination of all dileptonic channels and yields

$$m_t^{\text{pole}} = 168.2\,^{+1.1}_{-1.1}\,(\text{stat})\,^{+2.6}_{-2.1}\,(\text{syst})\,^{+3.9}_{-0.4}\,(\text{theory})\,\text{GeV}.$$

The result is in agreement with other m_t^{pole} measurements within the uncertainty, such as the ATLAS measurement in the semi-leptonic decay channel using the same observable and yielding $m_t^{\text{pole}} = 173.7\,^{+2.3}_{-2.1}\,\text{GeV}$ [201], or the most recent CMS measurement from the inclusive $t\bar{t}$ production cross section with $m_t^{\text{pole}} = 173.6\,^{+1.7}_{-1.8}\,\text{GeV}$ [198]. An overview of recent measurements of the top quark pole mass in comparison to the result obtained from this analysis is given in Figure 15.11.

15.5 Summary

The normalized differential $t\bar{t}$+jet production cross section has been measured as a function of ρ_S [12] in the visible phase space of the $t\bar{t}$ decay products and the additional jet. The total uncertainties range from 4 % to 15 %, depending on the bin of the measurement.

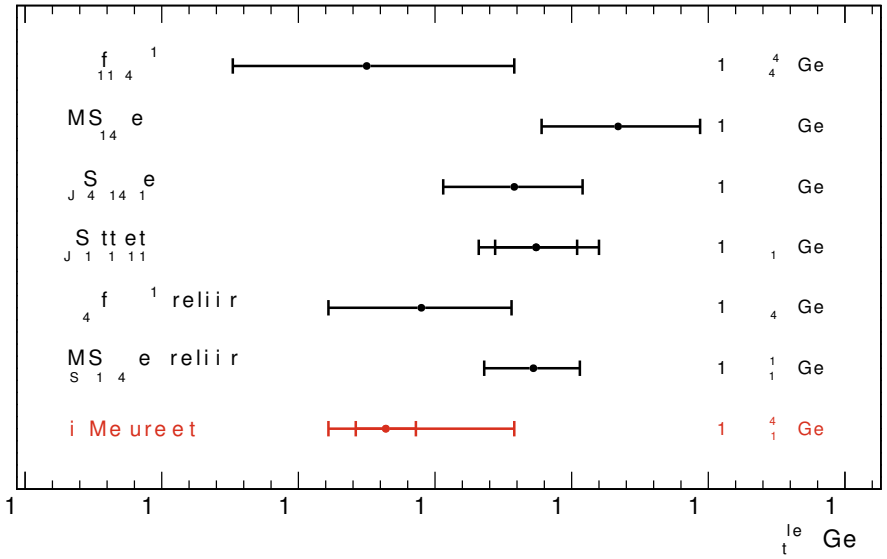

Figure 15.11: Comparison of recent $m_{\mathrm{t}}^{\mathrm{pole}}$ measurements by different experiments. The inner bars represent the statistical uncertainties if available, while the outer bars indicate the total uncertainty of the measurement. The value obtained from the presented analysis is marked in red.

This measurement has been used to determine the top quark mass using two different MC simulations as cross section prediction. The mass measured with the MadGraph predictions serves as direct comparison for the measurement conducted at reconstruction level and yields a total uncertainty of 2.3 GeV, which corresponds to a relative uncertainty on the top quark mass of 1.3 % and is in agreement with the precision achieved at reconstruction level. The dominating uncertainties are constituted by the modeling uncertainties arising from the jet/parton matching threshold and the Q^2 scale variations. The measured mass is compatible with other top quark mass measurements within the associated uncertainties.

A first measurement of the theoretically well-defined top quark pole mass is performed from the normalized differential cross sections using NLO precision calculations for the $\mathrm{t\bar{t}}$+jet cross section [13]. The systematic uncertainty of this measurement amounts to 2.3 GeV (1.4 %), while the uncertainty on the assumption of the renormalization and factorization scales in Powheg yields an additional uncertainty of 2.1 GeV (1.3 %) on average. In total, the measured top quark pole mass yields an uncertainty of 3.4 GeV, which corresponds to a relative uncertainty of 2.0 %. The measurement is in agreement with other $m_{\mathrm{t}}^{\mathrm{pole}}$ measurements within the assigned uncertainty.

The measurement of the top quark pole mass could be further improved by several measures. The modeling uncertainties could be reduced by performing the entire measurement with the Powheg + Pythia8 $\mathrm{t\bar{t}}$+jet simulation which was not possible for the analysis presented owing to the large computational effort required for the detector simulation. This would avoid the need for two independent simulations and would allow for a coherent evaluation of the scale uncertainties arising from the differential cross section measurement and the theory predictions. With simulations at NLO available at reconstruction level, an additional measurement of the same quantity could also be performed at the level of observed events avoiding the unfolding

and the accompanying statistical correlation of the different bins of the measurement.

Furthermore, the differential cross sections could be unfolded to parton level, i.e., after the parton shower. This would allow to remove effects stemming from the hadronization model and from the description of the UE and CR, and might lead to a reduced total uncertainty.

Summary and Prospects

Further deepening the knowledge about the fundamental properties of nature and pushing the limits in high energy particle physics requires a huge and interdisciplinary effort. Experiments and particle accelerators are planned and built on the timescale of decades, and experts in detector technology are needed just as are specialists in data analysis. This thesis covers a wide spectrum of aspects of modern particle physics experiments, ranging from the design and qualification of a new detector, to the aspects of data acquisition (DAQ) and calibration, to the first operation in a particle beam, and finally, to the analysis of collision data recorded by the experiment.

Test Beam Measurements for the CMS Pixel Detector Upgrade

The first part of this thesis is dedicated to studies and measurements for the Phase I upgrade of the pixel detector of the Compact Muon Solenoid (CMS) experiment. After consolidation of the Large Hadron Collider (LHC) at CERN during the Long Shutdown 1 (LS1), protons are now brought to collision at a center-of-mass energy of 13 TeV. The instantaneous luminosity will be continuously increased in the coming years and will likely exceed $\mathcal{L} = 2 \times 10^{34}\,\mathrm{cm}^{-2}\mathrm{s}^{-1}$ by 2023. At these luminosities and the corresponding particle flux, the current pixel detector would be subject to severe data losses and inefficiencies due to readout-induced dead time and limitations of the on-chip buffers. To overcome these limitations, the CMS collaboration has decided to build a new pixel detector, which is currently under construction and will be installed in the experiment during the LHC year-end technical stop 2016/2017. This so-called Phase I pixel detector constitutes an advancement of the present detector and comprises new front-end electronics, among other improvements. As part of this thesis, the pxarCore DAQ software has been developed in order to facilitate laboratory and test beam measurements with the new PSI46digV2.1-r readout chip (ROC), and to allow consistent calibration of the detector modules produced in the various institutes around the globe.

Comprehensive test beam measurements have been conducted at the DESY test beam facility in order to scrutinize the characteristics of the new ROC. The tracking efficiency of the chip has been measured to be $99.7\,^{+0.3}_{-0.5}\,\%$ uniformly over the full sensor volume. The charge collection efficiency, position resolution, and tracking efficiency have been studied as functions of the intra-pixel position of the particle trajectory, allowing detailed insights into the behavior of the signal formation in the sensor, and threshold effects in the ROC. The spatial resolution of the chip has been measured as a function of the track impact angles. The intrinsic resolution

along the 100 µm pitch of the pixels is found to be (4.80 ± 0.29) µm, while the resolution along the 150 µm pitch is measured to be (7.99 ± 0.23) µm. The reduced charge threshold of 1.7 ke achieved by the new chip provides an improvement in position resolution of about 20 % over an operation corresponding to the in-time threshold of 3.2 ke of the current PSI46V2 ROC. Simulations of the detector response have been performed in order to reproduce the test beam measurements and to provide further insight into the processes occurring in the silicon sensor.

It has been found that the third central moment of the cluster charge distribution, i.e., the cluster skewness, exhibits a strong sensitivity to the track impact position. Applying a skewness correction to the track residual allows to significantly reduce systematic in-pixel shifts of the reconstructed trajectory position, and by this, to improve the position resolution considerably. The new cluster center interpolation algorithm provides up to 40 % improvement in the position resolution in comparison to the standard center of gravity algorithm, especially at trajectory angles with charge sharing between two pixel cells. This is of special interest since this behavior is expected for smaller Lorentz angles after radiation-induced damage in the silicon sensor. Sensor and front-end simulations have shown to correctly reproduce these findings, and can be used to predict the necessary correction factors for the cluster skewness.

Measurement of the Top Quark Mass from Differential Cross Sections

The second part of the thesis focuses on the measurement of the top quark mass from normalized differential cross sections. The top quark is the heaviest known elementary particle, and its mass is a fundamental parameter to the standard model (SM) and plays a central role in many physics analyses and theoretical predictions. Top quark mass measurements are typically either based on the kinematic reconstruction of the mass from the quark decay products, or on the mass dependency of the inclusive top quark pair ($\mathrm{t\bar{t}}$) production cross section. While the former provide a high measurement precision, the relation of the measured top quark mass to well-defined theoretical mass definitions is ambiguous. Measurements from the cross section allow to unequivocally relate the measured top quark mass to a parameter of the Lagrangian, but suffer from larger systematic uncertainties.

The measurement presented provides an alternative approach to the standard methods by measuring the top quark mass from differential $\mathrm{t\bar{t}}$+jet production cross sections. The large cross section for $\mathrm{t\bar{t}}$ production at the collision energy of the LHC allows the collection of a large number of $\mathrm{t\bar{t}}$ events, and thus enables the measurement of differential distributions for observables of the $\mathrm{t\bar{t}}$ system. The measurement is based on the data recorded by the CMS experiment at $\sqrt{s} = 8\,\mathrm{TeV}$ in 2012, corresponding to an integrated luminosity of $19.7\,\mathrm{fb}^{-1}$, and is performed in the dileptonic decay channel of $\mathrm{t\bar{t}}$ events with additional jet activity ($\mathrm{t\bar{t}}$+jet). The observable considered is defined as the inverse of the invariant mass of the $\mathrm{t\bar{t}}$ system and the additional jet, i.e., $\rho_S = 2m_o/\sqrt{s_{\mathrm{t\bar{t}+jet}}}$, where m_0 is an arbitrary scale of the order of the top quark mass, and $s_{\mathrm{t\bar{t}+jet}}$ corresponds to the invariant mass regarded. The mass is extracted both at reconstruction level from the normalized ρ_S distributions, and at generator level, i.e., after correction for detector effects, from the normalized differential cross section as a function of ρ_S to compare the achievable precision.

The measurement at reconstruction level uses MadGraph + Pythia6 predictions with different assumed top quark masses in order to extract the top quark mass from a global χ^2 template fit. The mass obtained from the combination of all three dileptonic $\mathrm{t\bar{t}}$ decay channels amounts to $m_t = 173.1\,^{+1.0}_{-1.0}\,(\mathrm{stat})\,^{+2.3}_{-2.0}\,(\mathrm{syst})\,\mathrm{GeV}$, with the main contribution to the systematic uncertainty arising from modeling sources, namely the jet/parton matching threshold and the renormalization and factorization scales. The relative precision of this measurement is about 1.3 %.

In order to facilitate the comparison with theoretical calculations, the mass is also determined from the differential $\mathrm{t\bar{t}}$+jet production cross section at generator level using an unfolding procedure. First, the top quark mass is determined from the normalized differential cross section with the same MadGraph predictions at generator level, and using a similar χ^2 template fit, but taking into account the correlations between the bins introduced by the unfolding. The mass measurement yields $m_{\mathrm{t}}^{\mathrm{MC}} = 173.8\,^{+1.1}_{-1.1}\,(\mathrm{stat})\,^{+2.0}_{-1.9}\,(\mathrm{syst})\,\mathrm{GeV}$ for the combination of all dileptonic decay channels, and thus a precision of about 1.3 %. The dominating systematic uncertainties likewise arise from the jet/parton matching threshold and the renormalization and factorization scales. From the experimental uncertainties, the largest contribution stems from the uncertainty on the background estimate.

Finally, a first measurement of the top quark mass from the normalized differential cross sections is presented, using predictions at next-to-leading order (NLO) precision for the $\mathrm{t\bar{t}}$+jet process using Powheg for the matrix element calculation and Pythia8 for the parton shower and hadronization. This allows to measure a theoretically well-defined mass, which can be related to the pole mass of the top quark. The measurement yields $m_{\mathrm{t}}^{\mathrm{pole}} = 168.2\,^{+1.1}_{-1.1}\,(\mathrm{stat})\,^{+2.6}_{-2.1}\,(\mathrm{syst})\,^{+3.9}_{-0.4}\,(\mathrm{theory})\,\mathrm{GeV}$ with a precision of about 2.0 %. The additional theoretical uncertainty arises from the renormalization and factorization scale uncertainties of the Powheg $\mathrm{t\bar{t}}$+jet simulation used for the mass determination.

Prospects

The forthcoming year marks the final milestone for the Phase I upgrade of the CMS Pixel Detector. While the module production will be concluded, the detector layers will be assembled, and the entire detector commissioned and finally installed in the experiment. The design qualification of the recently submitted ROC for layer 1 requires further detailed test beam measurements in order to ensure a correct functionality of the redesigned buffering and readout scheme. Furthermore, test beam studies with irradiated samples of the PSI46digV2.1-r ROC will be performed to investigate the behavior of the chip under the influence of radiation-induced defects over the full lifetime of the detector. Additional work could be dedicated to combine the template matching algorithm for hit determination in the pixel detector currently in use by the CMS experiment with the cluster skewness correction presented in this thesis. This might allow to take advantage of the improved position resolution at particle trajectory angles corresponding to a decreased Lorentz angle, while retaining the excellent performance of the template algorithm in mitigating the effects of radiation damage.

The precision of the top quark measurement could be improved by specifically addressing the dominating systematic uncertainties by using predictions with NLO precision throughout the analysis. In particular, this would allow to remove the necessity of evaluating the renormalization and factorization scale uncertainties independently for two different predictions and thus significantly reduce the total uncertainty on the top quark pole mass measurement. Furthermore, the collision energy of $\sqrt{s} = 13\,\mathrm{TeV}$ of the LHC in Run 2 and the hereby increased $\mathrm{t\bar{t}}$ production cross section facilitates the collection of a larger sample of dileptonic $\mathrm{t\bar{t}}$ decays and will thus allow to reduce the statistical and systematic uncertainty of the measurement.

Appendix - Part I

A Photographs

In the following, some photographs are presented documenting the test beam equipment, telescope configuration, chip carriers, and samples used for the test beam measurements presented in this thesis.

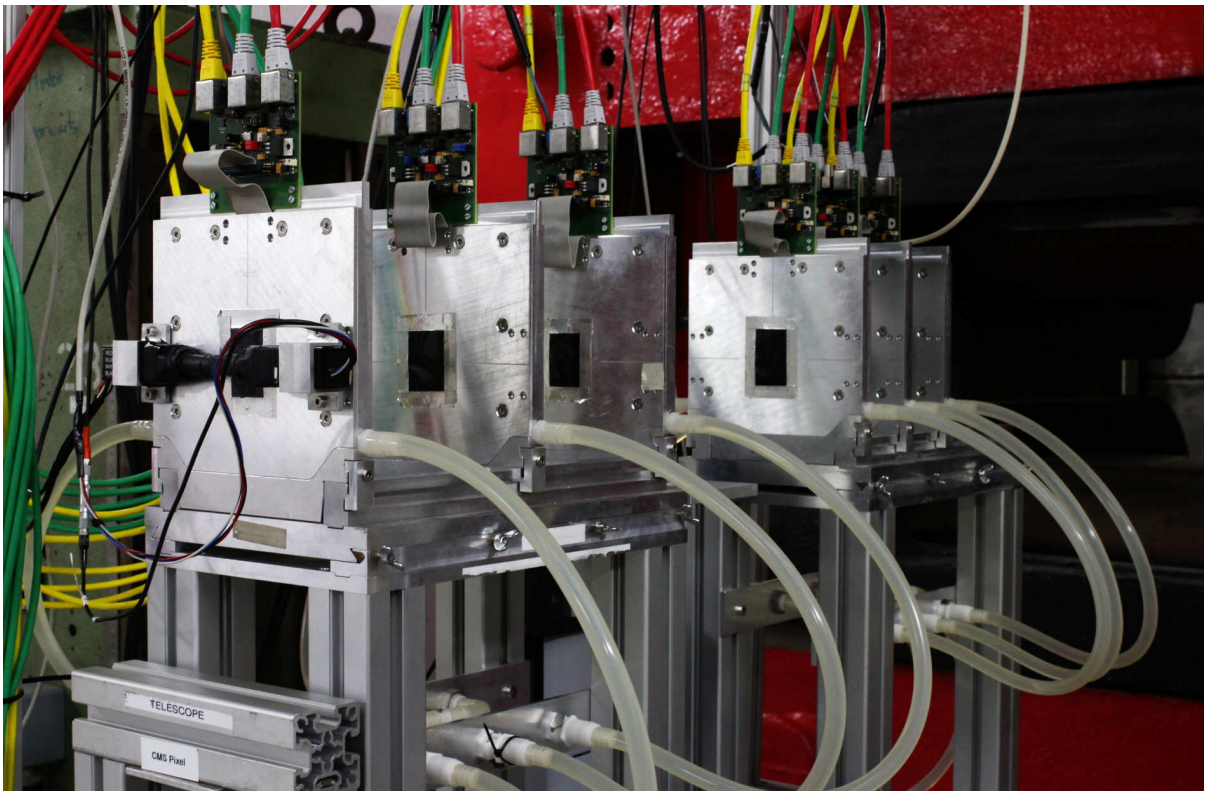

Figure A.1: The DATURA beam telescope with six MIMOSA26 (M26) sensor planes on aluminum rails. Auxiliary boards for clock, sensor configuration, and data connections are mounted on top of the planes. Two of the photomultiplier tubes (PMTs) as well as the tubing for cooling water are visible.

Photograph A.1 shows the DATURA beam telescope as deployed in the DESY test beam line 21. Shown are the six telescope planes with MIMOSA26 (M26) sensors mounted inside the aluminum boxes. Black Kapton foil covers the beam entry and exit windows to protect the sensors but retain a low material budget in the beam. The telescope planes are powered, triggered, and read out via the auxiliary boards mounted on top of the aluminum frames. The water-based chiller runs coolant through the aluminum boxes and allows temperature stabilization at 17 °C. The individual telescope planes are movable on the mounting rails, and the upstream and downstream arm can be shifted as a whole. The device under test (DUT) can be mounted in between the arms, but is not present in this picture.

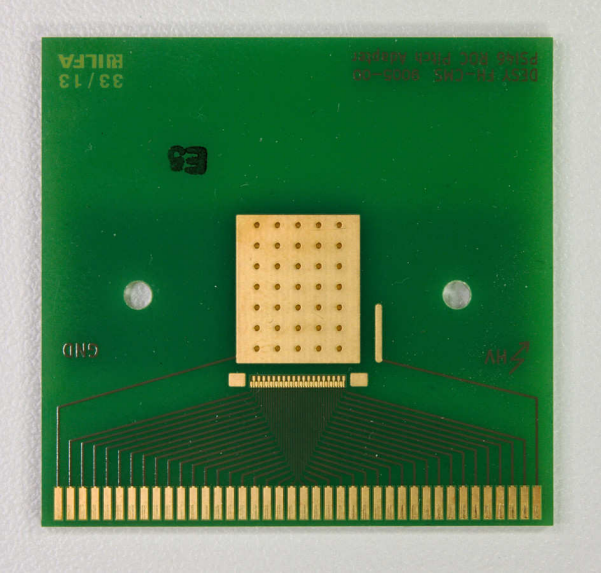

Figure A.2: CMS pixel ROC carrier PCB with reduced metal content for irradiation, copper metallization and vias for cooling contact below the ROC, and additional gold pads for trial wire bonding.

Picture A.2 presents a single chip module (SCM) carrier printed circuit board (PCB) which features a reduced metal content (DESY PCB number 9005-00). This PCB has been designed as part of this thesis in order to allow irradiation of samples without unnecessary activation and thus cool-down time of the mounting PCB. A metallization with vias to the backside is provided in the central region, where the ROC is mounted. This ensures good cooling contact to the metallization on the backside, which is in contact with the cooling block of the DUT assembly. The metal pad is set to ground potential. Additional pads are provided next to the wire bond pads of the fan-out, to allow test bonding without impairing the actual bond pads. An alternative carrier layout is available, featuring a rotated ROC mounting pad and wirebond fan-out (DESY PCB number 9006-00). However, on this PCB the ROC is located slightly off-center due to constraints from the signal routing.

The pictures presented in A.3 show the single ROC adapter used in the test beam measurements. It features a 68-pin half-pitch SCSI connector for the digital test board (DTB) ribbon cable connection, and a Samtech edge connector receiving the SCM carrier board. This version is shorter than the standard single ROC adapter used in laboratory tests and does not provide spy pads for oscilloscope measurements. However, it features an RTD network allowing for the connection of a PT10 000 temperature sensor which can be read out using the *slow ADC* of the DTB. The sensor is connected via a two-pin Molex connector, the fuse connects the 3.3 V power supply to the circuit. The four drill holes allow fixture of the PCB to the cooling block.

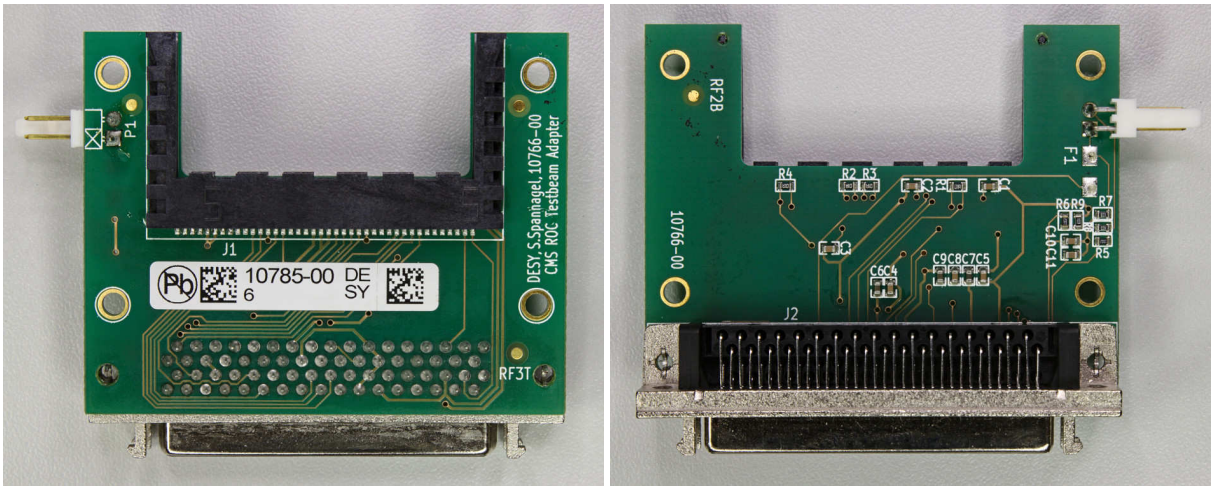

Figure A.3: The CMS pixel SingleROC adapter for test beams. This version of the adapter is shorter than the standard model and features an additional RTD network for temperature sensors which can be connected via the 2-pin Molex connector.

Figure A.4: CMS SCM assemblies for the test beam measurements. Due to mechanical constraints, one of the samples is mounted upright, the other one rotated by 90° to allow for tilting of the sensor plane in both column and row direction.

Photograph A.4 presents the CMS pixel SCMs characterized in the test beam. While SCM 504 is mounted in the upright position and allows measurements of the row resolution, SCM 506 is rotated by 90° for column resolution measurements.

The copper cooling block of the DUT installation is shown in Picture A.5. It features a cut-out in the center as beam window, a pipe for coolant, and mounting screws for the single ROC adapter described previously. Picture A.6 shows the full DUT assembly as mounted in between the arms of the DATURA beam telescope. The rotation stage allows remote tilting of the assembly. The installation is shown in the high-resolution configuration without the polyethylene cover for humidity control, and with very small distance to the up- and downstream telescope arms in order to reduce extrapolation uncertainties on the telescope tracks.

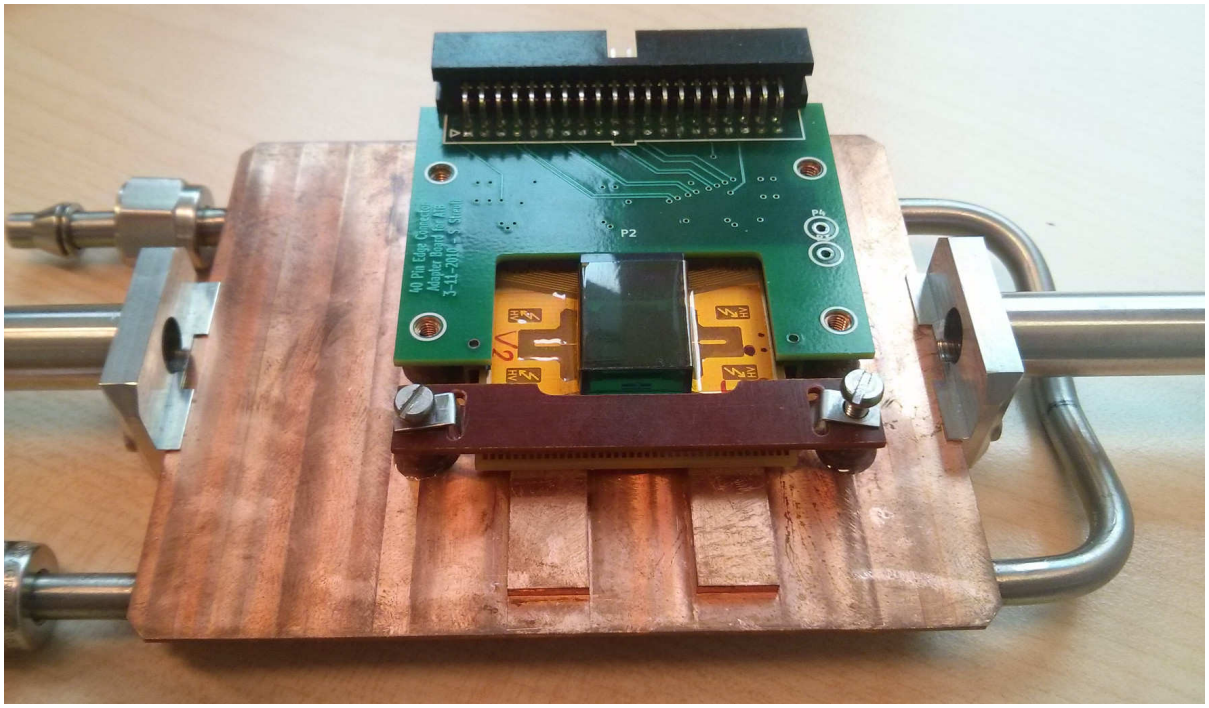

Figure A.5: Copper cooling block of the DUT with single ROC adapter installed. The single ROC adapter shown here is for analog PSI46V2 ROCs.

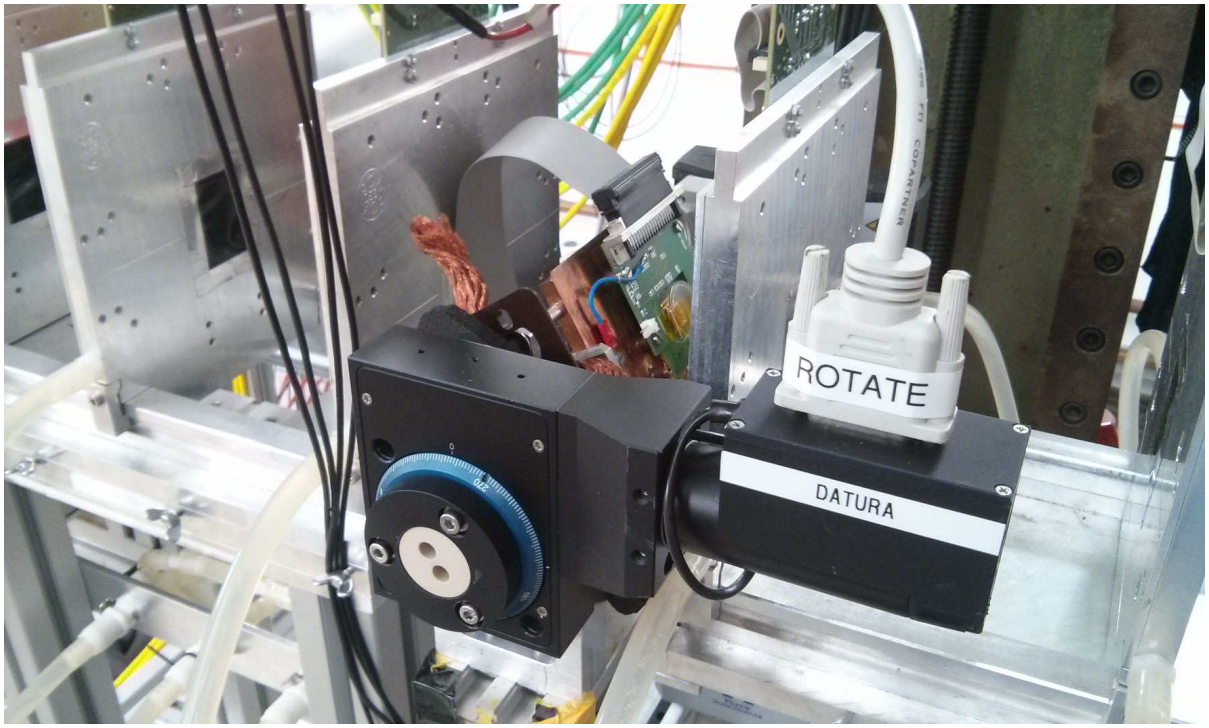

Figure A.6: CMS pixel DUT installation in the DATURA beam telescope, here shown in the high-resolution configuration.

B Test Beam Analysis: Supplemental Material

This section provides some additional material concerning the test beam analysis presented in Chapter 8.

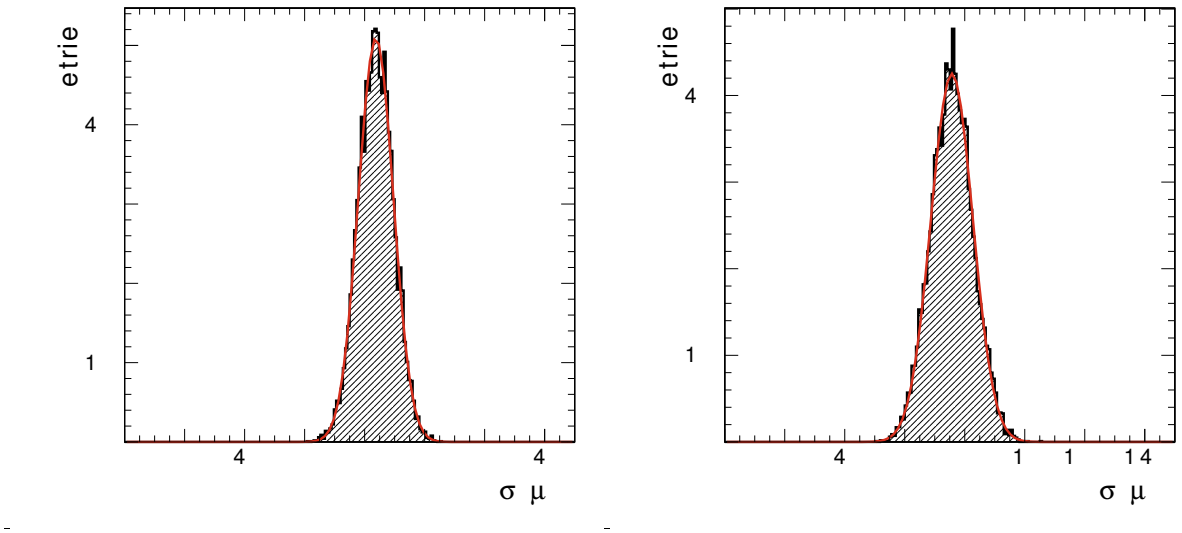

Figure B.1: Resolution distributions obtained from the pseudo-experiments performed for the statistical uncertainty. (left) shows the distribution of width for the minimum of Figure 8.24, (right) shows the distribution for the minimum of Figure 8.26.

Figure B.1 provides the distributions of smeared residual widths calculated for the evaluation of the statistical uncertainty of the position resolutions measured. The residual distribution is retrieved from the test beam data, and each bin is replaced by a random number drawn from a Poisson distribution with the original bin content as mean value. The resulting new histogram is fitted with the generalized error function presented in Equation 3.21, and the fit width is stored. This procedure is repeated 10 000 times, and the obtained distribution of residual width is fitted with a Gauss function, following the central limit theorem. The width of this fit is taken as the statistical uncertainty of the measured resolution.

In Figure B.2 the normalized most probable value (MPV) of the convolved Landau-Gauss function presented in Equation 8.4 is shown as a function of the tilt angle ω of SCM 506. Here, the total cluster charge is normalized to vertical incidence of the ionizing radiation. While the charge is calibrated to match simulation at vertical incidence, a slightly different behavior as a function of the tilt angle can be observed leading to about 1 ke higher cluster charges at incidence angles around 80°. The source of this mismatch with simulation is not yet understood and is still subject to investigations.

Tables B.1 and B.2 provide the digital-to-analog converter (DAC) parameters and register settings for the measured samples as reference. The WBC register value only represents a rough range of the values, since it has been tuned in the test beam to match the respective trigger configuration and SCM.

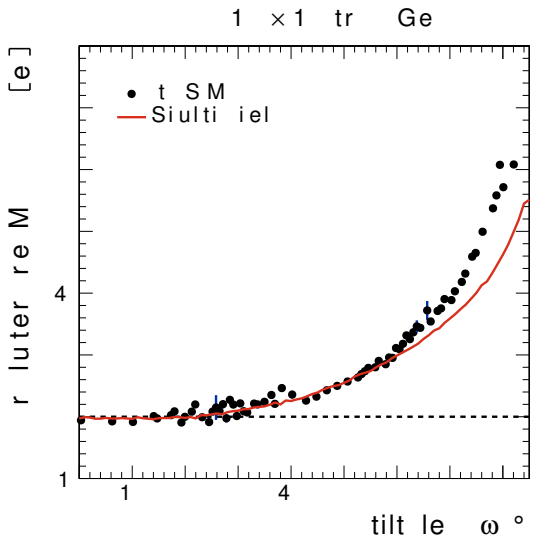

Figure B.2: Dependency of the normalized cluster charge on the tilt angle. Shown is the Landau most probable value (MPV) for SCM 506. A slight dependency can be observed.

Table B.1: DAC parameters and registers for SCM 504 at room temperature and stabilized to 17 °C using the ethanol chiller. Both parameter sets correspond to a threshold trimmed to 28 VCal units, corresponding to approx. 1.4 ke.

Room Temp.		Stabilized at 17 °C	
DAC/Reg.	Value	DAC/Reg.	Value
Vdig	9	Vdig	9
Vana	85	Vana	80
Vsh	33	Vsh	33
Vcomp	12	Vcomp	12
VwllPr	160	VwllPr	150
VwllSh	160	VwllSh	170
VhldDel	252	VhldDel	252
Vtrim	147	Vtrim	143
VthrComp	111	VthrComp	111
VIBias_Bus	90	VIBias_Bus	60
PHOffset	159	PHOffset	161
Vcomp_ADC	10	Vcomp_ADC	10
PHScale	112	PHScale	110
VIColOr	255	VIColOr	255
VCal	222	VCal	222
CalDel	151	CalDel	148
CtrlReg	4	CtrlReg	4
WBC	141	WBC	141
RBReg	12	RBReg	12

Table B.2: DAC parameters and registers for SCM 506 at room temperature. The first parameter set corresponds to a threshold trimmed to 28 VCal units, while the second set represents a threshold of 32 VCal.

28 VCal		32 VCal	
DAC/Reg.	Value	DAC/Reg.	Value
Vdig	9	Vdig	9
Vana	76	Vana	76
Vsh	33	Vsh	33
Vcomp	12	Vcomp	12
VwllPr	160	VwllPr	160
VwllSh	160	VwllSh	160
VhldDel	252	VhldDel	252
Vtrim	149	Vtrim	153
VthrComp	95	VthrComp	91
VIBias_Bus	30	VIBias_Bus	30
PHOffset	150	PHOffset	151
Vcomp_ADC	10	Vcomp_ADC	10
PHScale	112	PHScale	112
VIColOr	255	VIColOr	255
VCal	222	VCal	222
CalDel	157	CalDel	155
CtrlReg	4	CtrlReg	4
WBC	141	WBC	141
RBReg	12	RBReg	12

C Cluster Skewness: Supplemental Material

This section provides additional material concerning the cluster center interpolation algorithm using the cluster skewness presented in Chapter 9.

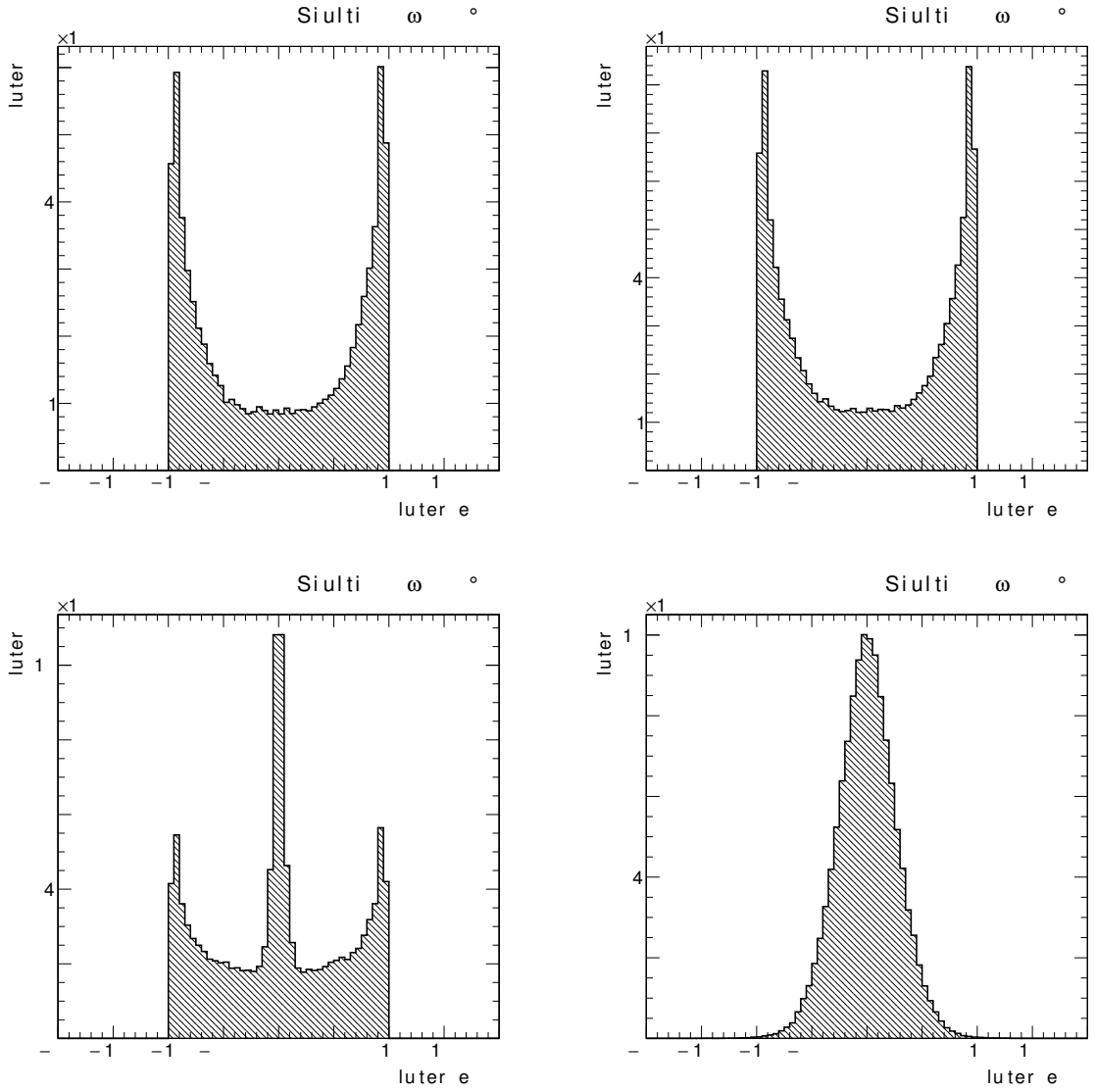

Figure C.1: Cluster skewness μ_3 distributions for different track incidence angles, obtained from simulation.

Figure C.1 presents the skewness distributions for different incidence angles as obtained from the PIXELAV simulation. Behavior and features very similar to the skewness obtained from test beam data as shown in Figure 9.1 can be observed. The distribution starts with a sickle shape at small incidence angles, and the central Gaussian distribution develops as the particle incidence angle, and thus the cluster size, increases. At large angles, only the Gaussian contribution is left.

The sharp edges of the skewness distribution arise from the normalization to the total cluster charge Q. When plotting the skew distribution without the normalization from Equation 9.3, namely

$$\mu_3 = \frac{1}{(N/2)^3} \cdot \sum_i (x_i - \mu)^3 \, Q(x_i) \,, \tag{.19}$$

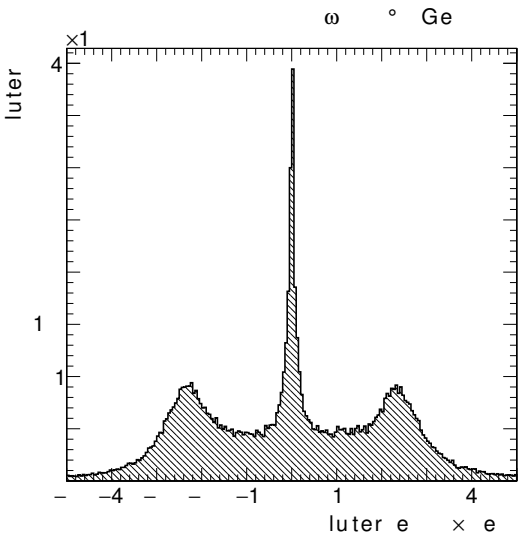

Figure C.2: Skewness distribution as shown in Figure 9.1c, but without normalization to the total cluster charge Q.

the distribution is smeared out and does not feature the sharp edges as demonstrated in Figure C.2. The large skew values outside the range $[-0.1, 0.1]$ arise from anomalous cluster charges as can be seen from Figure C.3 and C.4. Figure C.3 presents the (normalized) cluster skewness according to Equation 9.3 as a function of the total cluster charge, normalized to vertical incidence. While small cluster charges around the Landau MPV exhibit small skew values, some outliers at large total cluster charges exhibit larger skewness values. This can also be seen from Figure C.4, where the cluster charge Q is shown as a function of the associated cluster skewness. While clusters within the normal skewness range exhibit cluster charges close to the MPV of the Landau charge distribution, clusters with smaller or larger skew values tend to have larger charges. All cluster charges shown here are normalized to vertical particle incidence using the path length and the alignment angle ω.

An example for non-linear dependence of the residual mean position in y on the cluster skewness is shown in Figure C.5. The depicted distribution is obtained from a sample measured at a track incidence angle of 60°, and would allow fitting with a third-order polynomial function. However, due to the Gaussian shape of the skewness distribution at these large angles, no significant improvement is expected.

Figure C.6 presents the resolution obtained from simulation as a function of the tilt angle ω. The resolutions are corrected for the cluster skewness using two different parametrizations for the skewness determination. The turquois line presents the resolution achieved with the linear regression employed in Chapter 9, while the red curve represents a skew correction performed with a parametrization with a third order polynomial. At the maxima between the tree/four-pixel and four/five-pixel charge sharing minima, a small improvement is visible, while the methods yield the same results for the other track incidence angles.

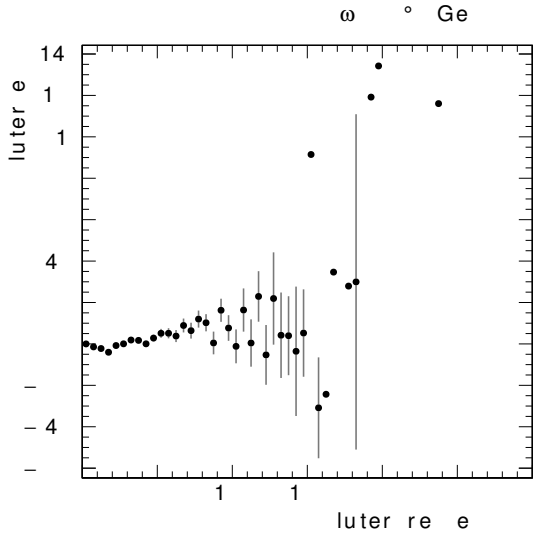

Figure C.3: Cluster skewness shown in Figure 9.1c as a function of the cluster charge.

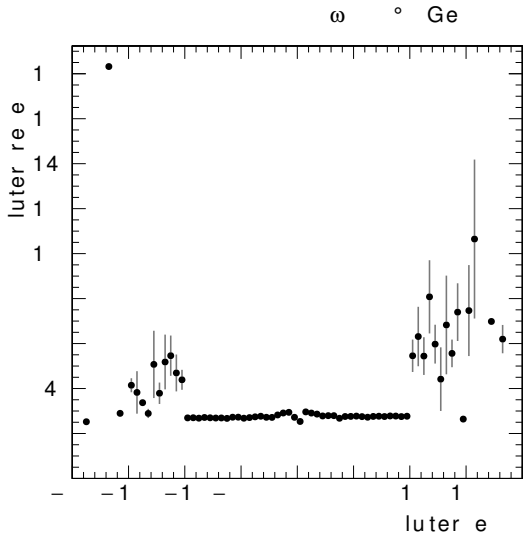

Figure C.4: Cluster charge as a function of the normalized cluster skewness, with the skew distribution taken from Figure 9.1c. Clusters with skew values outside the interval $[-0.1, 0.1]$ tend to have larger total cluster charges.

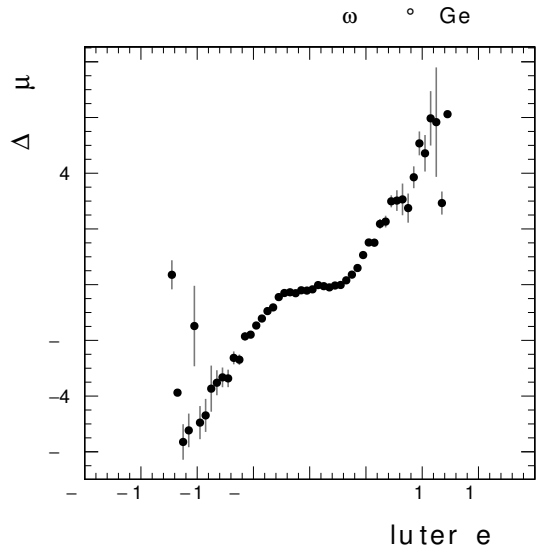

Figure C.5: Example for a track angle with non-linear cluster skewness distribution. This shape would allow the fitting of a third-order polynomial.

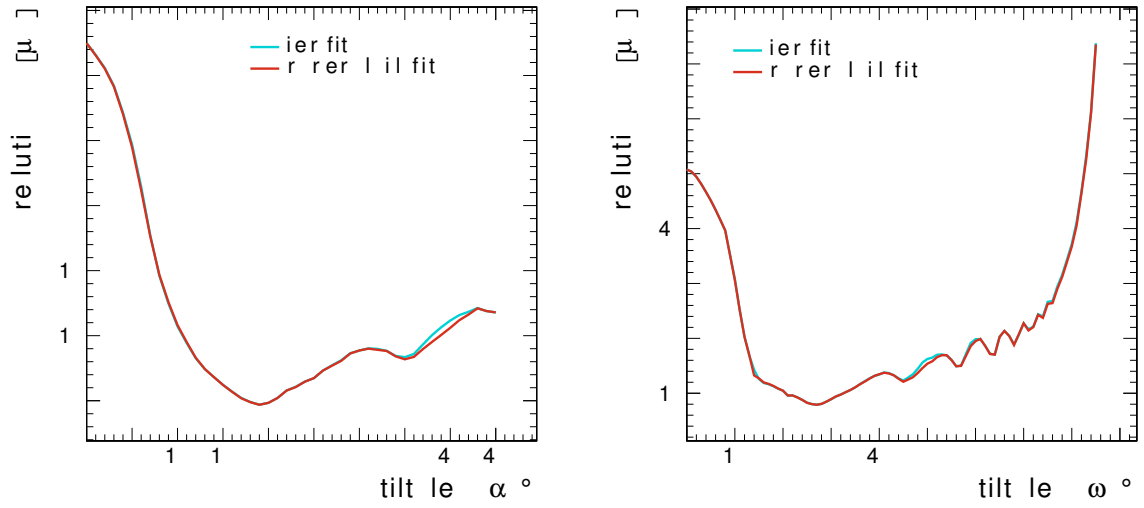

Figure C.6: Comparison of the skewness-corrected position resolution achieved with a linear and a third-order polynomial fit.

Figure D.1: Detector and trigger setup for in-plane tracking measurements. One CMS pixel module (center) is triggered by two scintillators in coincidence (top right) and readout out by the DTB (left). From [265].

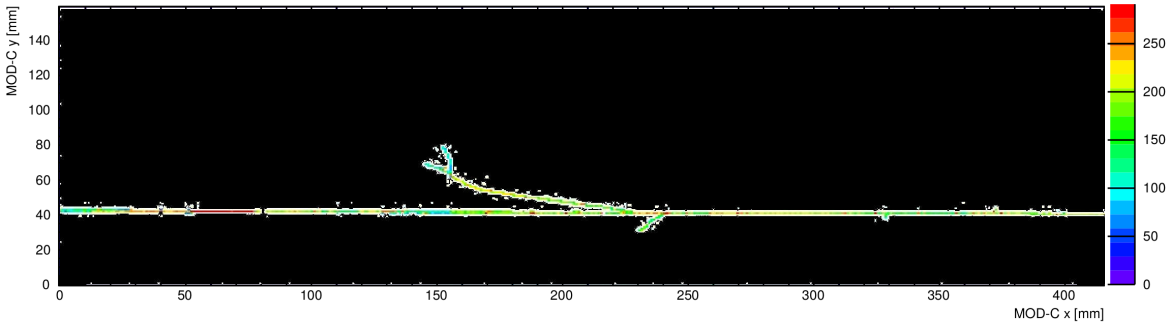

Figure D.2: Event display from in-plane tracking data. Shown is one particle crossing the silicon sensor along the long side of the module and producing delta rays. Modified from [265].

D Measurements with Phase I Detector Modules

The DAQ system described in Section 7.4.3 is also capable of operating multiple CMS pixel modules with sixteen ROCs each. The setup has been used to perform measurements with pixel modules produced in the DESY production center. The scripts used for the analysis of the data are based on the framework employed for the analysis presented in Chapter 8 and have been adapted in the context of a Summer Student Project [264]. Some of these measurements are briefly introduced in the following.

D.1 In-Plane Tracking with Edge-On Beam

In order to test the correlation of the multiple ROCs within one module, a single CMS module has been arranged such, that the electron beam of DESY test beam 24 enters the sensor from the short side and the particles travel inside the silicon sensor as long as possible as presented in Photograph D.1. The setup is triggered with two scintillators in coincidence visible in the top right corner of the photograph, the readout is performed using a DTB (cf. Section 6.1) and the pxarCore library (cf. Section 6.2) together with the EUDAQ integration (cf. Section 7.4.3).

Since the cross section of the sensor from the side is only about 16 mm × 0.3 mm, most of the triggered events are empty despite the small overlap of the scintillators. Events with a large number of pixels present are filtered and analyzed. Figure D.2 shows an event display with a particle track and additional production of delta rays. The data has also been used to perform

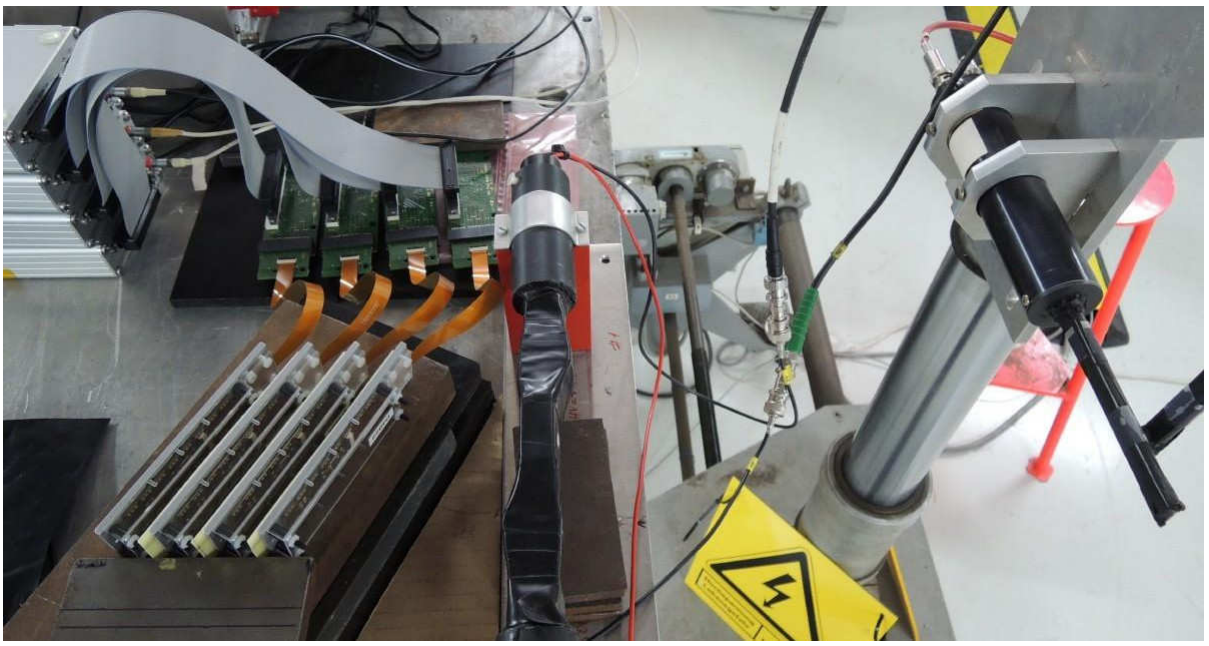

Figure D.3: Four CMS Pixel Detector modules operated in parallel. The modules are read out separately by four DTBs (top left) and triggered by two scintillators in coincidence (right). The planes are inclined for charge sharing. From [265].

in-plane tracking with the triplet method described in Section 3.3.2 using two columns of the sensor as reference measurements and the middle column to calculate the residual.

D.2 Tracking Efficiency

The tracking efficiency of the modules has been measured by operating multiple modules as telescope planes as depicted in Photograph D.3. Three modules serve as beam telescope providing the reference particle track, while the efficiency of the fourth module is determined as described for single ROCs in Section 8.7. The complication of requiring an additional timing reference is not necessary for these measurements, since all detectors have the same trigger window and are operated synchronously on the same external clock. The planes are inclined with respect to the beam direction in order to simulate the charge sharing expected from the Lorentz drift in the CMS experiment (cf. Section 3.1.5). The modules are numbered from A to D along the beam.

Figure D.4 shows the projected hit map of module C for columns and rows. The beam profile is clearly visible. In addition, the large pixels show up as expected with higher occupancies according to their area (cf. Section 8.4.1). Figure D.5 shows the same data as a 2D map of module C. Here, the beam spot as well as the separation of the different ROCs are visible via their edge pixels. The correlation between the different planes is exemplified in Figure D.6 for modules B and C. The plots indicate both correlation in time as well as a good spatial alignment (cf. Section 7.4.2 for more information about correlation plots).

Using this setup, the tracking efficiency of module C can be determined. Figure D.7 presents the measured tracking efficiency as a function of the track impact point on the module. The efficiency is uniform over the full module area. The region around the left edge is not completely covered by the beam spot and thus lacks reference particle tracks for the efficiency measurement. The efficiency as a function of the trigger number is depicted in Figure D.8. No dependency on time can be observed and the efficiency is constantly above 99.5 %. The tracking efficiency is

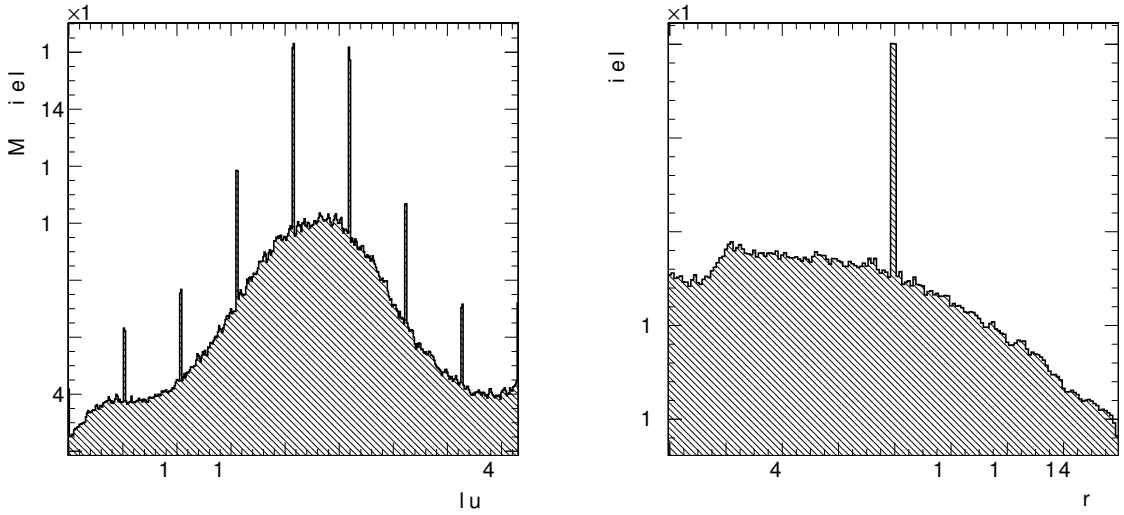

Figure D.4: Projected hit maps of module C along columns and rows. Both the shape of the particle beam and the features from the pixels with larger area are clearly visible.

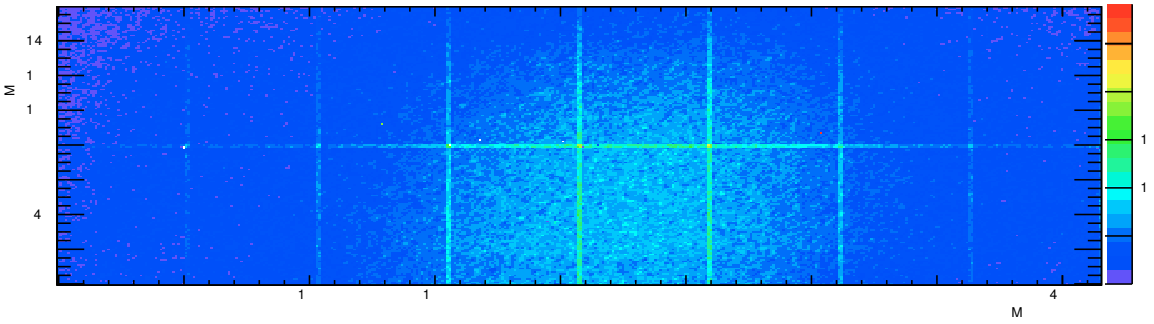

Figure D.5: 2D hit map of module C. The beam spot as well as the separation of the individual ROCs by their large edge pixels are visible.

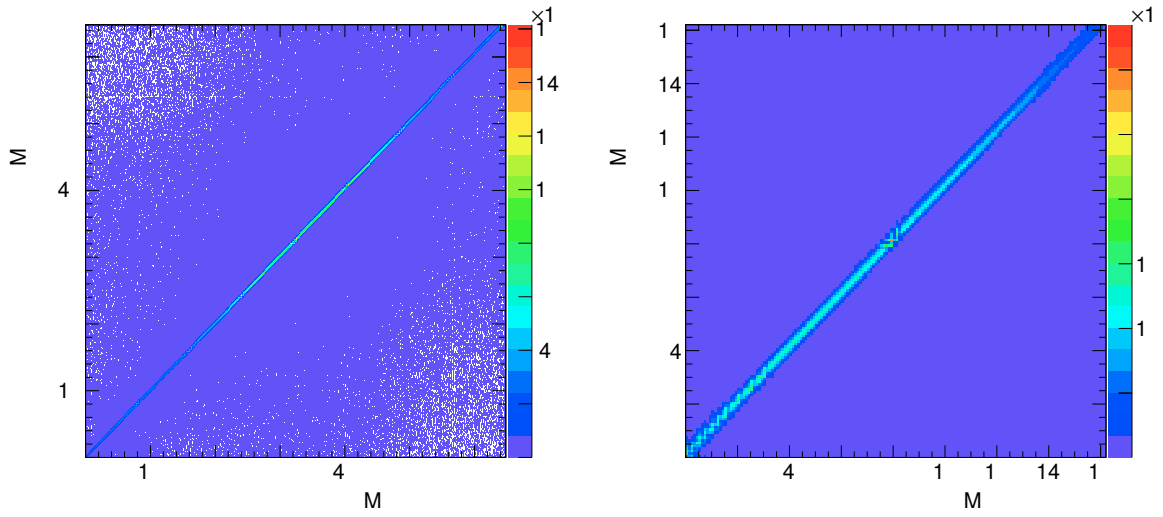

Figure D.6: Correlation histograms for the column and row coordinates of modules B and C. Both plots show a clear correlation and a good alignment.

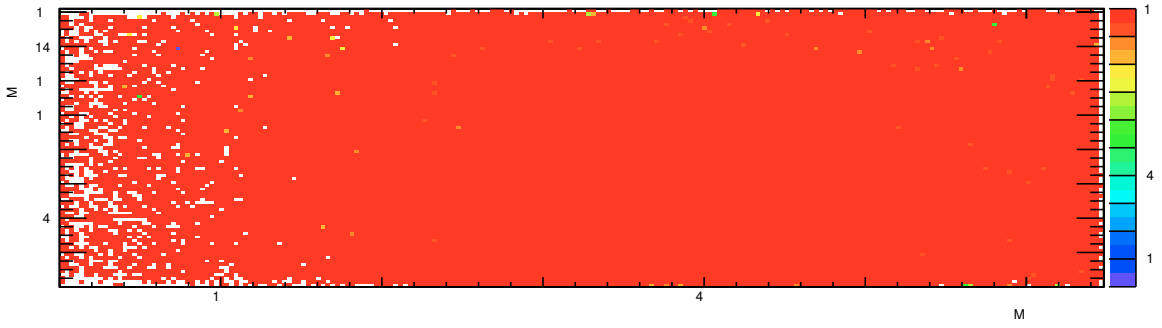

Figure D.7: Efficiency map of module C. The efficiency is above 99 % except for the left part of the module where no tracks have been registered due to the size of the beam spot.

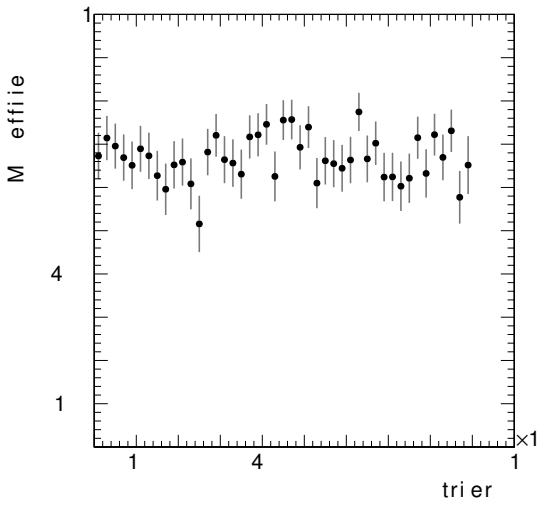

Figure D.8: Efficiency of module C as a function of the trigger number. The tracking efficiency is stable over time.

measured to be $(99.7 \pm 0.3)\,\%$, with the uncertainty representing the statistical uncertainty of the measurement. This value has been obtained from a single run, and the statistical uncertainty could be much reduced by taking into account more of the recorded data.

Appendix - Part II

E Powheg Monte Carlo Sample Production

POWHEG input card for the $t\bar{t}$+jet process. The parameter `##TOPMASS##` is replaced with the respective top quark mass of the sample produced. Unchanged default parameters of the regarded POWHEG user process are suppressed.

```
! ttbar+jet production
bornktmin  5d0      ! (default 0d0) kt min at Born level for jet in ttbar+jet
topmass ##TOPMASS## ! default: 172.5d0
R_jet 0.5d0
ptmin_jet 40d0      ! Minimum pT of the additional jet
topdecaymode 22000  ! Number of ttbar decay products for e,mu,tau,u,c

hdamp ##TOPMASS##
dampreweight 1 ! h_damp reweighting (mt/2, mt, mt*2)

numevts 10000    ! number of events to be generated
ih1   1           ! hadron 1 (1 for protons, -1 for antiprotons)
ih2   1           ! hadron 2 (1 for protons, -1 for antiprotons)
lhans1  10800         ! pdf set for hadron 1 (LHA numbering) -> CT10
lhans2  10800         ! pdf set for hadron 2 (LHA numbering) -> CT10

! Parameters to allow or not the use of stored data
use-old-grid    1 ! if 1 use old grid if file pwggrids.dat is present
                  ! (<> 1 regenerate)
use-old-ubound  1 ! if 1 use norm of upper bounding function stored in
                  ! pwgubound.dat, if present; <> 1 regenerate

ncall1 100000  ! number of calls for initializing the integration grid
itmx1    5     ! number of iterations for initializing integration grid
ncall2 100000  ! number of calls for computing the integral
               ! and finding upper bound
itmx2    5     ! number of iterations for computing the integral
```

```
               ! and finding upper bound
foldcsi   1    ! number of folds on csi integration
foldy     1    ! number of folds on  y  integration
foldphi   1    ! number of folds on phi integration
nubound 100000 ! number of bbarra calls to setup norm of upper
               ! bounding function
icsimax  3     ! <= 100, number of csi subdivision when computing
               ! the upper bounds
iymax    3     ! <= 100, number of y subdivision when computing the
               ! upper bounds
xupbound 2d0   ! increase upper bound for radiation generation

withnegweights 1   ! (default 0) if on (1) use negative weights
bornsuppfact 100d0 ! (default 0d0)  mass param for Born suppression factor
```

Additional samples with `hdamp = 0`, `bornsuppfact = 0`, `withnegweights = 0`, and different values for `ncall1, ncall2` as well as combinations of these parameters have been produced in order to test their influence on the measurement. The difference on the top quark mass has been found to be below the statistical uncertainty of the samples.

For the hadronization with PYTHIA8 the following configuration has been used. The parameter `pThard = 2` prevents double counting, and `nFinal = 3` is necessary for PYTHIA to correctly determine the lowest-Q^2 parton radiated at matrix element level. The influence of the different tunes `4C` and `CUEP8M1` has been evaluated and found to be negligible.

```
process.generator = cms.EDFilter("Pythia8HadronizerFilter",
  comEnergy = cms.double(8000.0),
  PythiaParameters = cms.PSet(
    pythia8PowhegEmissionVetoSettings = cms.vstring(
      'POWHEG:veto=1',
      'POWHEG:pTdef=1',
      'POWHEG:emitted=0',
      'POWHEG:pTemt=0',
      'POWHEG:pThard=2', # enable POWHEG veto user hook
      'POWHEG:nFinal=3', # three final state particles: tt+j
      'POWHEG:vetoCount=100',
      'SpaceShower:pTmaxMatch=2',
      'TimeShower:pTmaxMatch=2',),
    processParameters = cms.vstring(
      'ParticleDecays:limitTau0 = on',
      'ParticleDecays:tauMax = 10',
      'Tune:pp=14',
      'Tune:ee=7',
      '6:m0 = ##MASS##',
      'MultipartonInteractions:pT0Ref=2.4024',
      'MultipartonInteractions:ecmPow=0.25208',
      'MultipartonInteractions:expPow=1.6',),
    parameterSets = cms.vstring('pythia8PowhegEmissionVetoSettings',
      'processParameters')
))
```

F Trigger Paths, Event Yield, and Control Distributions

The following section provides some additional reference material for the event selection and analysis strategy of the top quark mass measurement.

Table F.1: high level trigger (HLT) paths used in data and simulation for the three dileptonic $t\bar{t}$ decay channels.

Channel	Trigger Path
$\mu^+\mu^-$	HLT_Mu17_Mu8_v*
$\mu^+\mu^-$	HLT_Mu17_TkMu8_v*
e^+e^-	HLT_Ele17_CaloIdT_CaloIsoVL_TrkIdVL_TrkIsoVL_ Ele8_CaloIdT_CaloIsoVL_TrkIdVL_TrkIsoVL_v*
$e^\pm\mu^\mp$	HLT_Mu17_Ele8_CaloIdT_CaloIsoVL_TrkIdVL_TrkIsoVL_v*
$e^\pm\mu^\mp$	HLT_Mu8_Ele17_CaloIdT_CaloIsoVL_TrkIdVL_TrkIsoVL_v*

Table F.1 presents the high level trigger (HLT) trigger paths used in the event pre-selection for dileptonic $t\bar{t}$ decays. All paths are dilepton triggers, requiring one lepton with $p_T > 17\,\text{GeV}$, and a second lepton with $p_T > 8\,\text{GeV}$. The same selection rules are applied for the simulated Monte Carlo (MC) samples.

Table F.2 provides a detailed overview of the number of events selected after each selection criterion. The numbers are given for data, and for the three simulation categories *$t\bar{t}$ signal*, *$t\bar{t}$ background*, and *other background* for each of the dileptonic channels individually as well as for their combination. The columns represent the subsequent steps of the selection process described in Chapter 12.

Finally, Figures F.1 – F.4 present control distributions for several observables of the $t\bar{t}$ system and the additional jet after the full event selection criteria have been applied. The distributions are presented for all three dileptonic channels as well as their combination, and in general show a good agreement between simulation and data. The hatched regions correspond to the sum of all shape uncertainties on the $t\bar{t}$ signal events (cf. Chapter 13).

Table F.2: Number of expected signal and background events in the MC samples, compared to the event yields in the 19.7 fb^{-1} of data. Shown are the number of events remaining after each selection step.

$\mu^+\mu^-$	2 leptons	2 jets	E_T^{miss}	b-tag	kin. reco.	add. jet
$\text{t}\bar{\text{t}}$ signal	20553	15859	12056	11262	9764	3227
$\text{t}\bar{\text{t}}$ background	3610	2765	2128	1973	1842	629
other background	758421	37095	3818	1897	1386	455
Sum MC	782586	55719	18003	15133	12993	4312
Data	851382	61025	18904	15837	13723	4549
$\text{e}^\pm\mu^\mp$	2 leptons	2 jets	E_T^{miss}	b-tag	kin. fit	add. jet
$\text{t}\bar{\text{t}}$ signal	44176	34120	34120	31905	28240	8882
$\text{t}\bar{\text{t}}$ background	7894	6074	6074	5645	5294	1726
other background	52891	5201	5198	3289	2577	723
Sum MC	104963	45397	45393	40840	36113	11332
Data	106955	45927	45927	41324	36787	11443
e^+e^-	2 leptons	2 jets	E_T^{miss}	b-tag	kin. fit	add. jet
$\text{t}\bar{\text{t}}$ signal	15693	12064	9151	8542	7245	2425
$\text{t}\bar{\text{t}}$ background	2643	2038	1577	1463	1339	472
other background	475498	23893	2444	1252	909	343
Sum MC	493835	37996	13173	11257	9494	3240
Data	503979	40117	13052	11062	9440	3226
combined	2 leptons	2 jets	E_T^{miss}	b-tag	kin. fit	add. jet
$\text{t}\bar{\text{t}}$ signal	80423	62043	55328	51710	45249	14534
$\text{t}\bar{\text{t}}$ background	14148	10878	9780	9082	8477	2828
other background	1286807	66191	11405	6415	4857	1516
Sum MC	1381380	139113	76514	67207	58583	18880
Data	1462320	147069	77883	68223	59950	19218

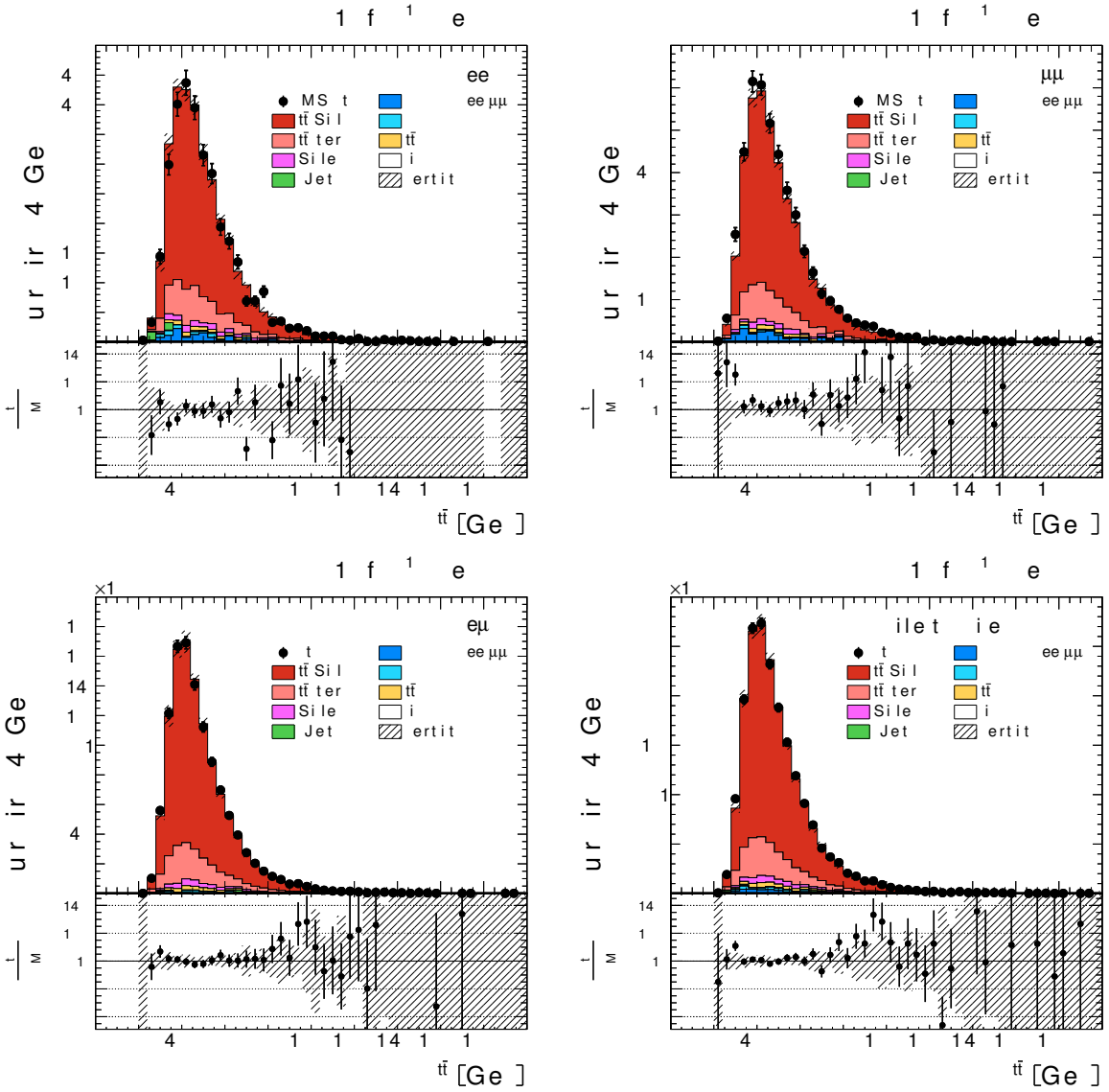

Figure F.1: Invariant mass of the $t\bar{t}$ system for the three individual dilepton final states e^+e^- (top left), $\mu^+\mu^-$ (top right), $e^\pm\mu^\mp$ (bottom left) and the three channels combined (bottom right). The hatched regions correspond to the sum of all shape uncertainties on the $t\bar{t}$ signal events (cf. Chapter 13).

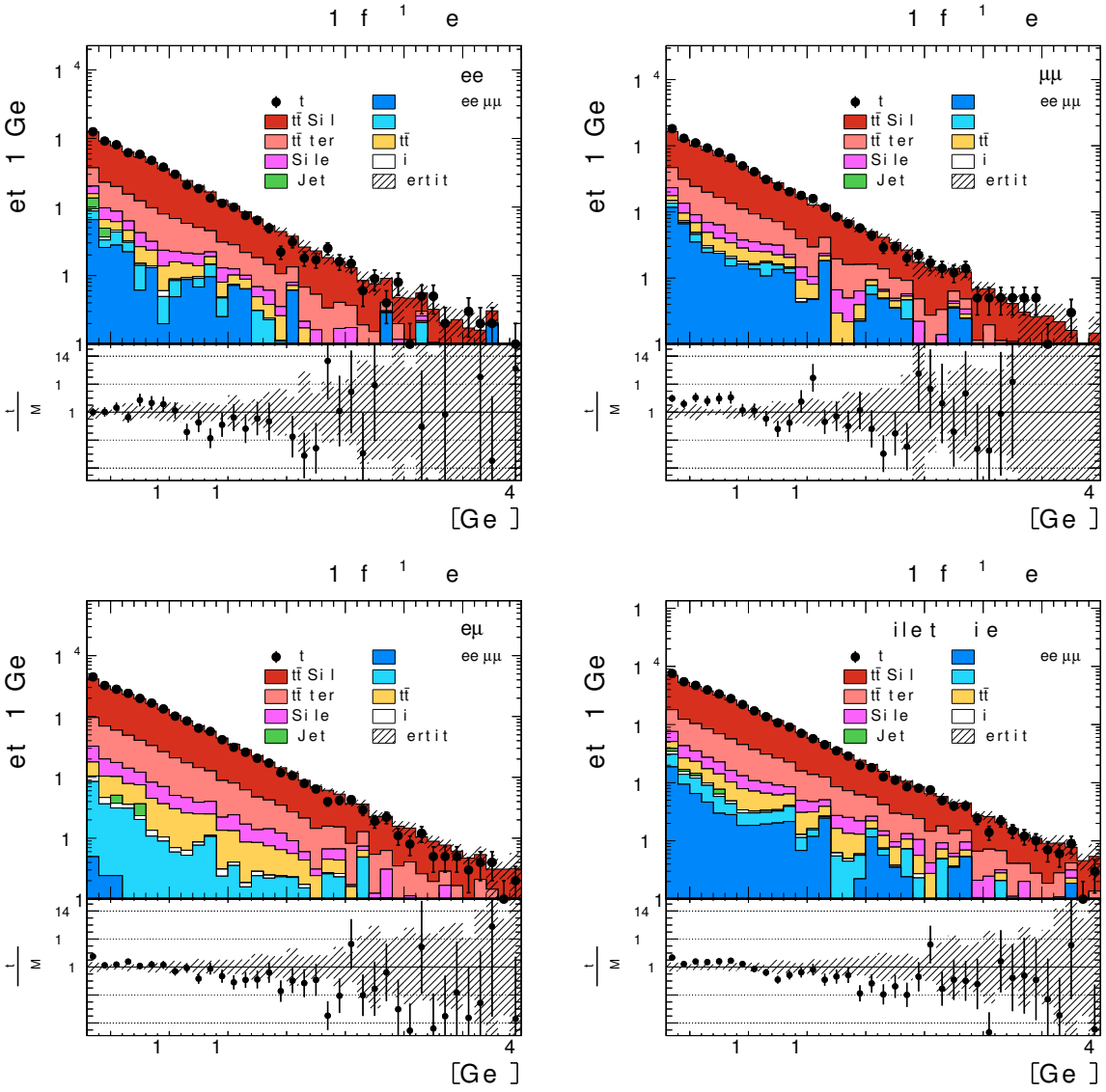

Figure F.2: p_T distribution of the b jets for the three individual dilepton final states e^+e^- (top left), $\mu^+\mu^-$ (top right), $e^\pm\mu^\mp$ (bottom left) and the three channels combined (bottom right). The hatched regions correspond to the sum of all shape uncertainties on the $t\bar{t}$ signal events (cf. Chapter 13).

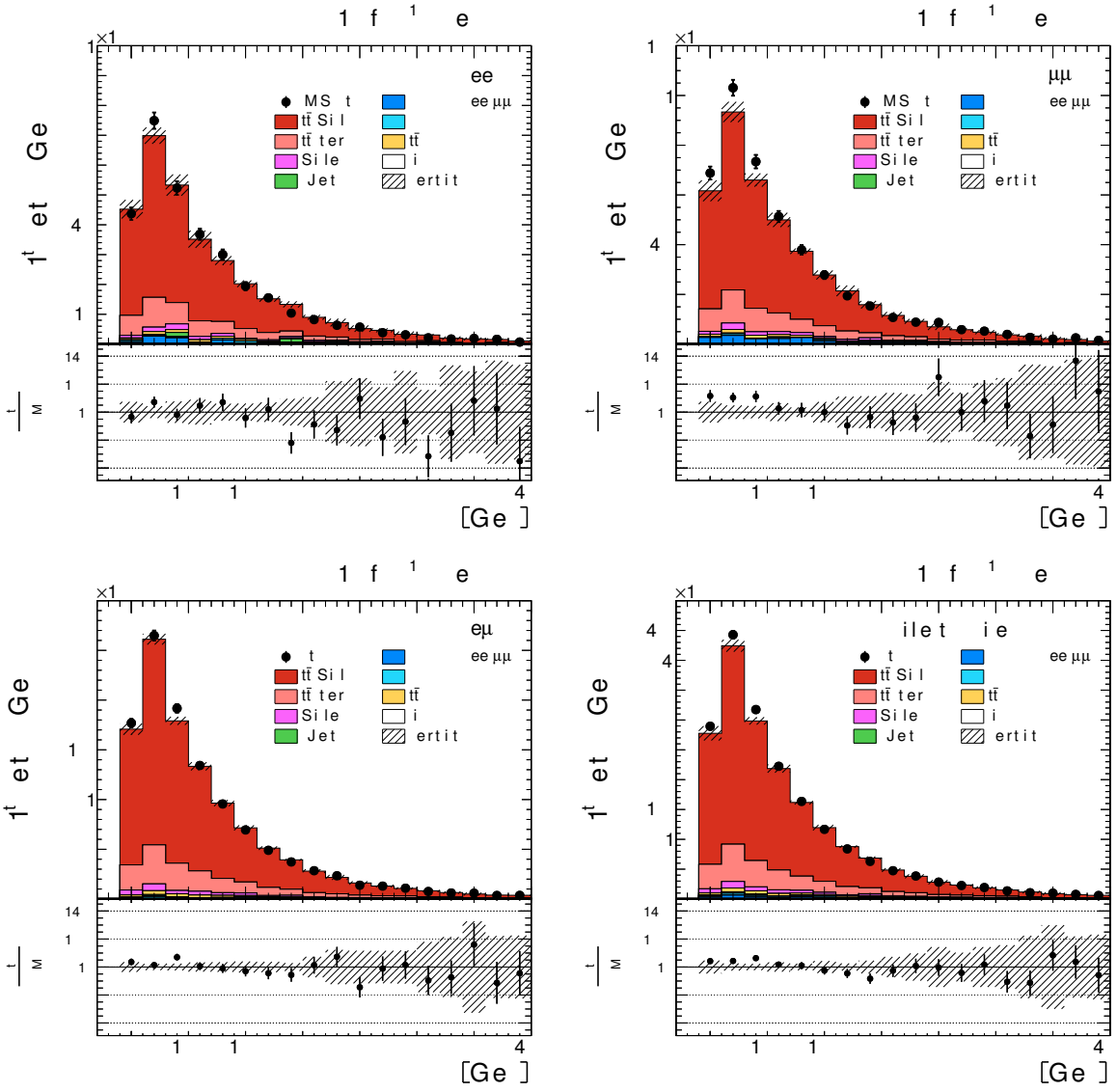

Figure F.3: Leading additional jet p_T distributions for the three dilepton final states e^+e^- (top left), $\mu^+\mu^-$ (top right), $e^\pm\mu^\mp$ (bottom left) and the three channels combined (bottom right). The hatched regions correspond to the sum of all shape uncertainties on the $t\bar{t}$ signal events (cf. Chapter 13).

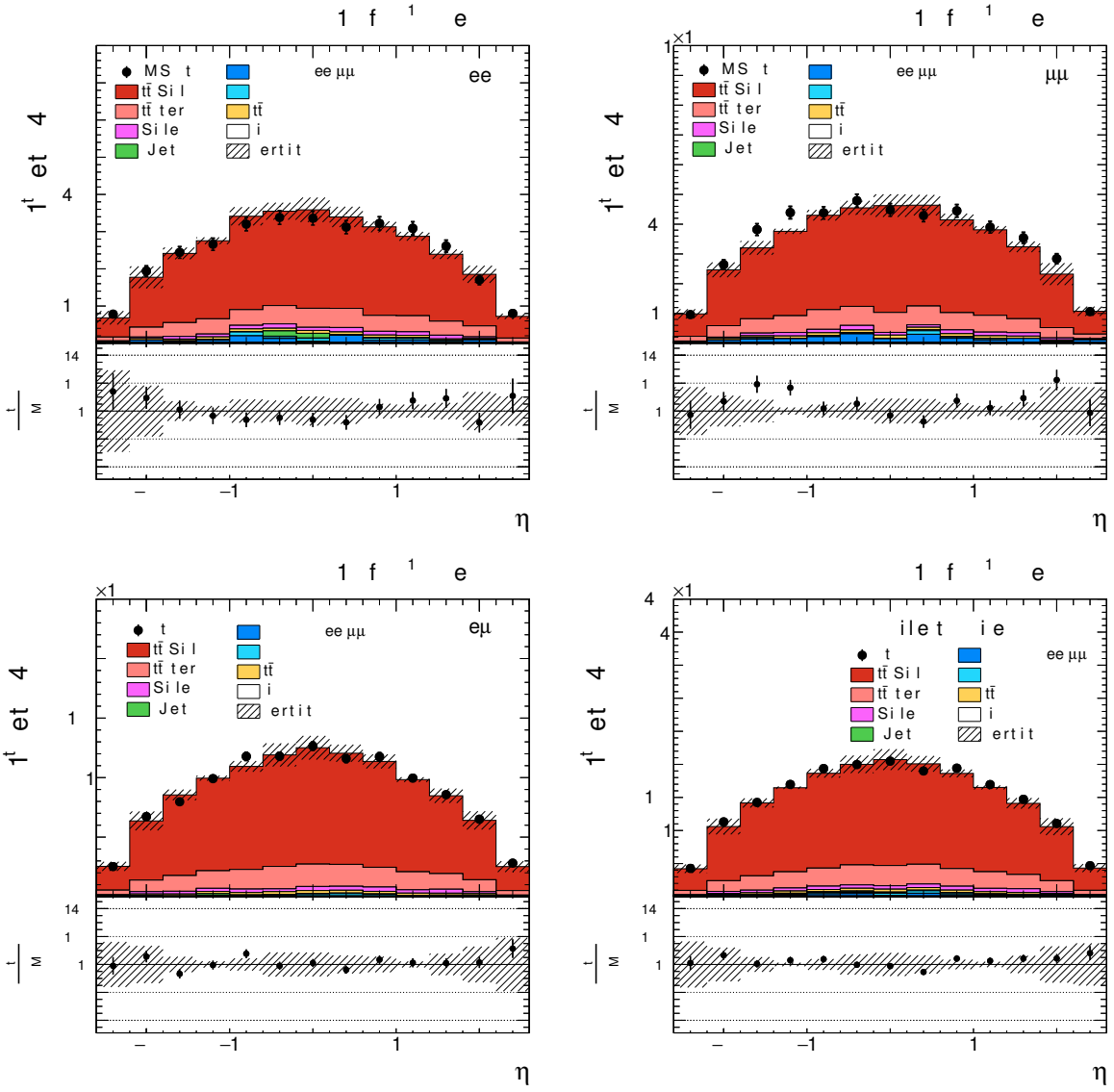

Figure F.4: Distribution of the leading additional jet η for the three dilepton final states e^+e^- (top left), $\mu^+\mu^-$ (top right), $e^\pm\mu^\mp$ (bottom left) and the three channels combined (bottom right). The hatched regions correspond to the sum of all shape uncertainties on the $t\bar{t}$ signal events (cf. Chapter 13).

G Bin Distributions and Local χ_i^2 Estimators for the Top Quark Mass Extraction

In the following, additional figures for the top quark mass extraction from the normalized ρ_S distribution are presented. The measurement is performed in 14 bins, the first bin of the distribution is not considered due to the reduced number of degrees of freedom arising from the normalization. Hence, in the subsequent figures the bin $0.00 < \rho_S < 0.20$ is only provided for illustration but does not enter the global χ^2 calculation.

Figure G.1 shows the measured number of events, normalized to the total number of events, and the MC predictions for every individual bin of the ρ_S distribution. The result from data is shown as black line, with the hatched band representing the statistical uncertainty for the respective bin. The seven MC samples with different assumed top quark masses are shown with red markers. Here, the red hatched band represents the confidence interval of the second-order polynomial fit to the different samples (cf. Equation 14.4). The slope of the MC simulations indicates the sensitivity of the respective bin on the top quark mass. While bins with small slopes are not sensitive and do not contribute much information to the global χ^2, bins such as $0.85 < \rho_S < 1.00$ with steep slopes provide a good sensitivity.

Figure G.2 presents the local χ_i^2 estimators for every bin, calculated from the distributions shown in Figure G.1 according to Equation 14.5. The different bins are summed to form the global χ^2 distribution to be minimized as detailed in Section 14.1.

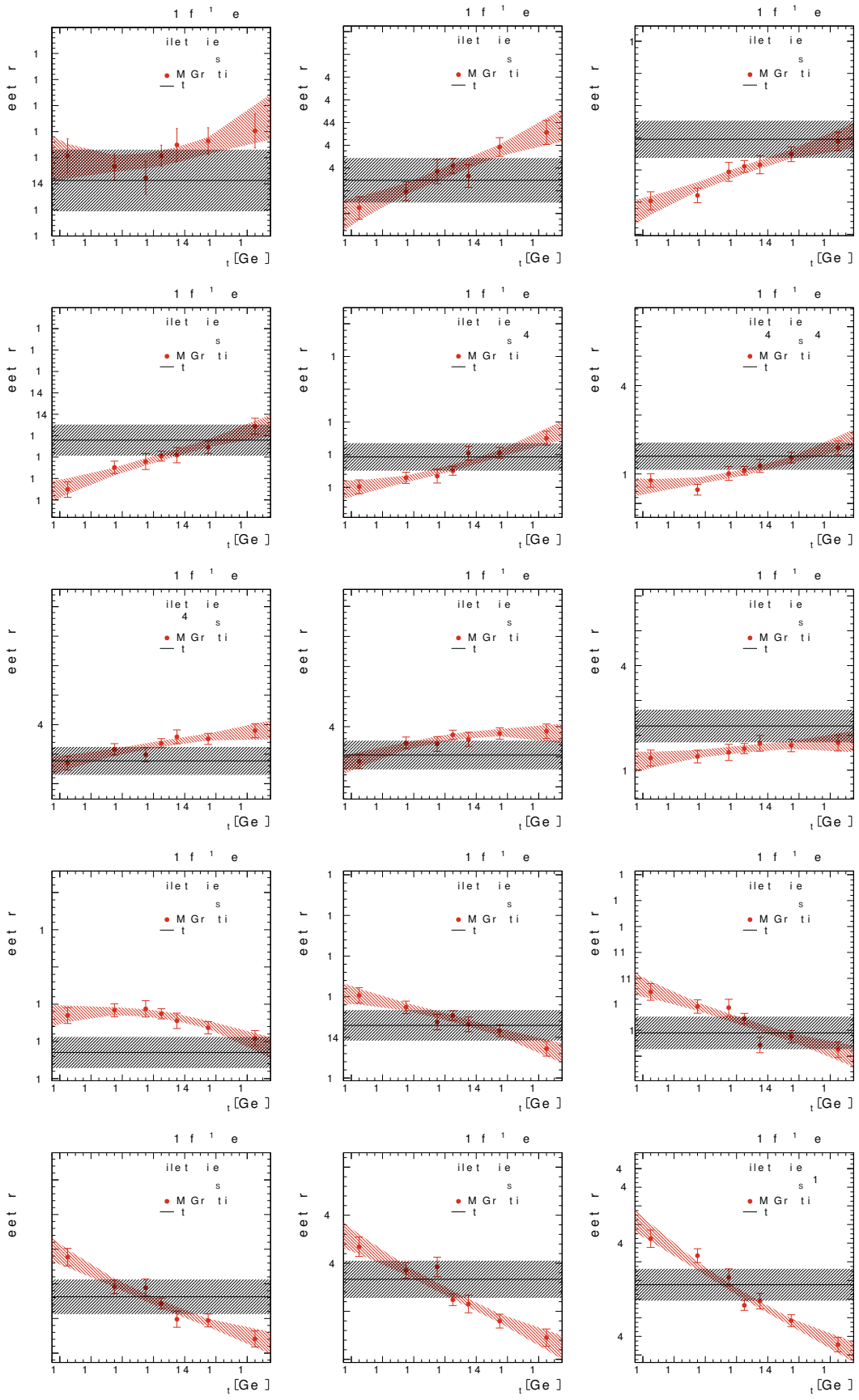

Figure G.1: Normalized ρ_S distributions for data and the simulations with different top quark masses in all individual bins, shown for the combination of all dilepton channels.

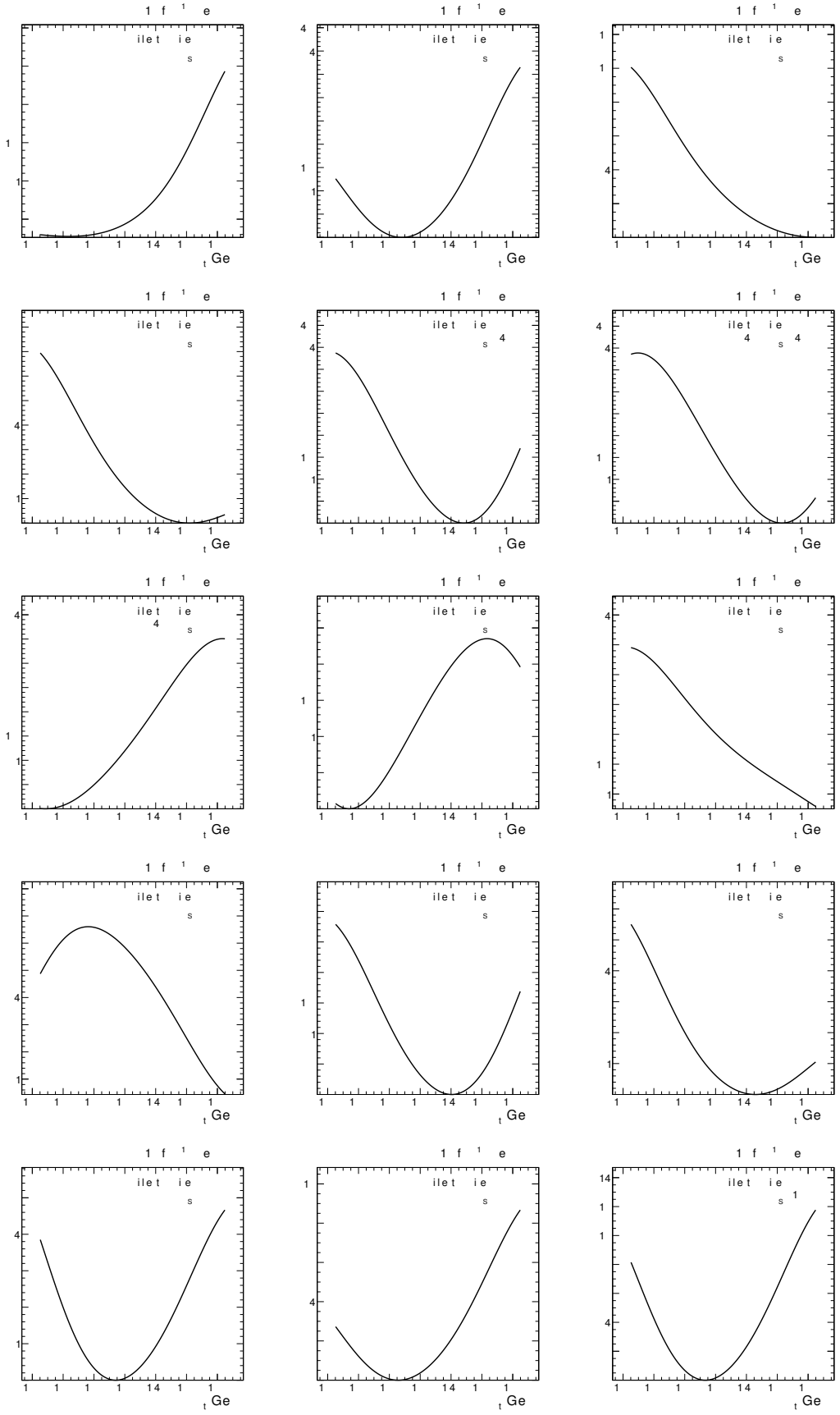

Figure G.2: Local χ_i^2 distributions for each individual bin of the ρ_s distribution in the combination of all dilepton channels. The χ_i^2 estimators are obtained from the distributions presented in Figure G.1.

H Differential Cross Section: Supplemental Material

The following section provides supplemental material for the differential cross section measurement presented in Section 15.1.

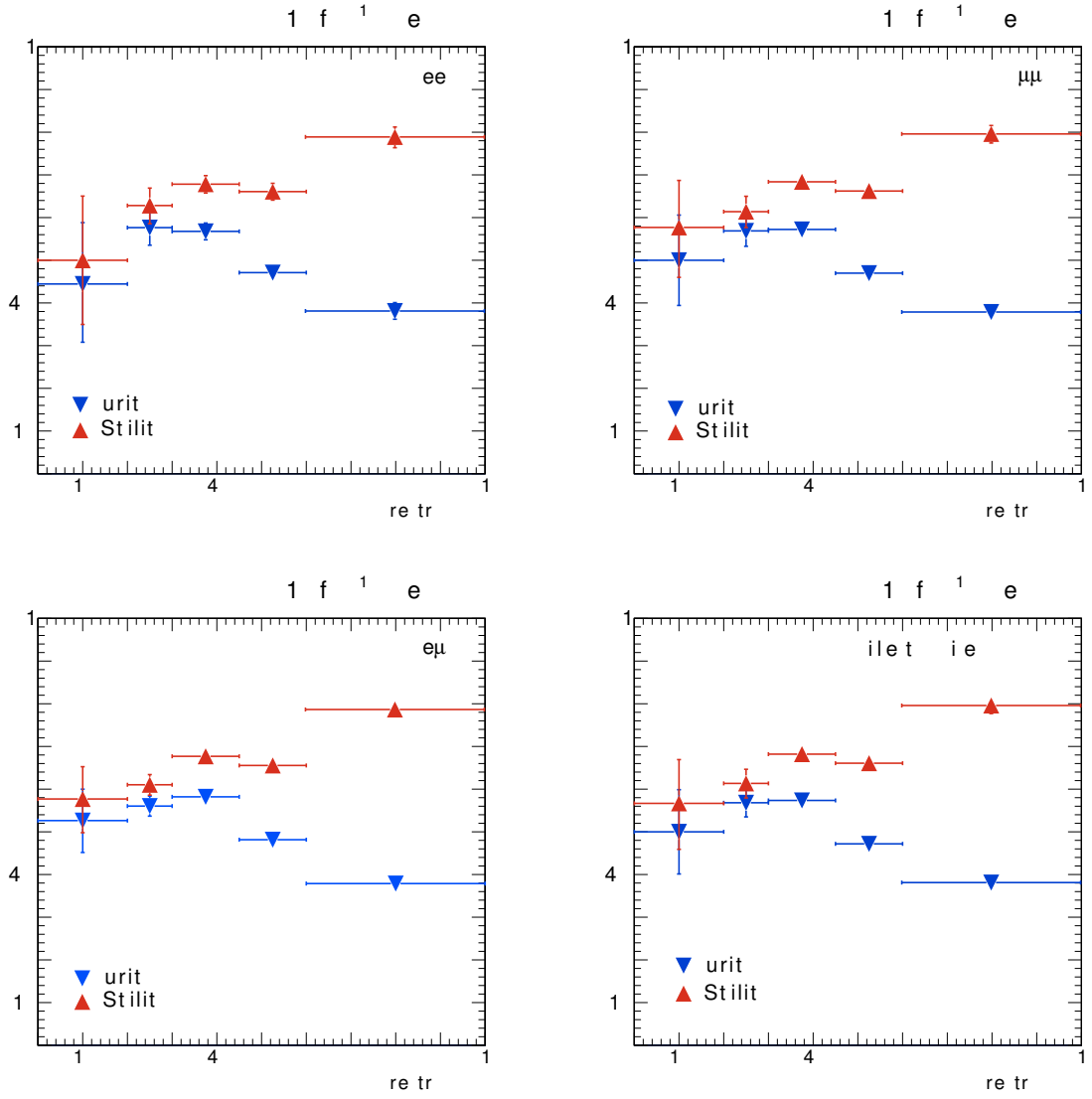

Figure H.1: Stability and purity of the bins of the ρ_S distribution, for the three dilepton final states e^+e^- (top left), $\mu^+\mu^-$ (top right), $e^\pm\mu^\mp$ (bottom left) and the three channels combined (bottom right).

Figure H.1 presents the stability and purity of the individual bins of the ρ_S distribution following the definition provided in Equation 15.5, for all dileptonic decay channels as well as for their combination. The binning has been chosen such, that both stability and purity are above 40 %, and the sensitivity on the top quark mass is maximized. The latter requires the last bin to span the range $0.60 < \rho_S < 1.00$, which leads to a slightly lower purity. The statistical correlation between the different bins of the unfolded ρ_S distribution is provided in Figure H.3 for all dileptonic decay channels as well as for their combination.

Figure H.2 provides the normalized statistical covariance matrices for the unfolded ρ_S distribu-

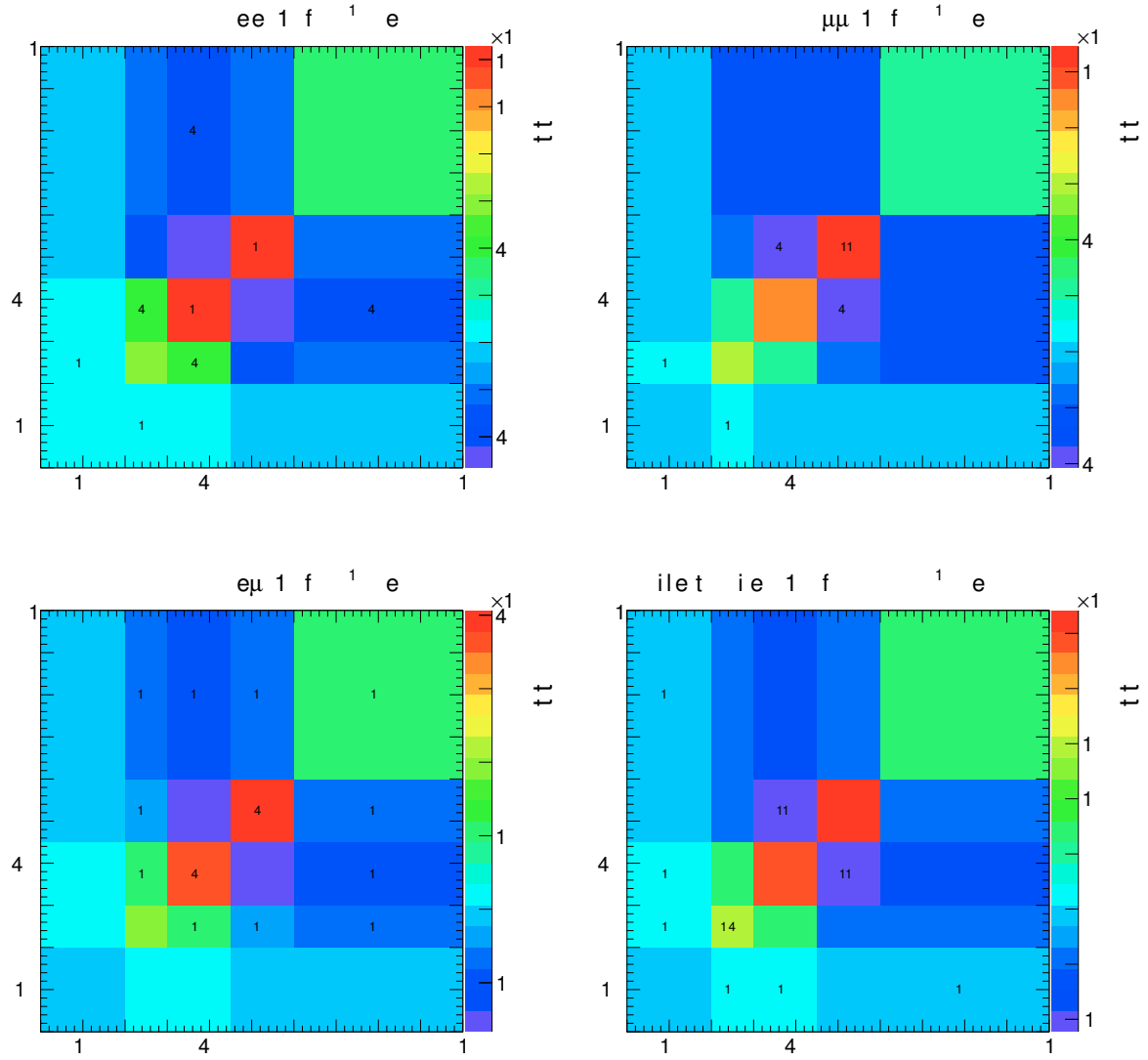

Figure H.2: Normalized statistical covariance matrices from unfolding for the three dilepton final states e^+e^- (top left), $\mu^+\mu^-$ (top right), $e^\pm\mu^\mp$ (bottom left) and the three channels combined (bottom right). The values are corrected for the corresponding bin width in both dimensions.

tions, for each dileptonic decay channel and their combination. The measured values for the normalized differential $\mathrm{t\bar{t}}$+jet cross section as a function of ρ_S are provided in Table H.1 for all bins and decay channels. The cross sections are presented together with the respective bin size as well as the relative statistical, systematic, and total uncertainties.

Table H.1: Normalized differential $\mathrm{t\bar{t}}$+jet cross sections as a function of ρ_S, provided for each bin and dileptonic decay channel, and for the combination of all channels.

Channel: $\mathrm{e}^{\pm}\mu^{\mp}$		Uncertainties %		
Bin range $[\rho_S]$	$\left(\frac{1}{\sigma}\frac{d\sigma}{d\rho_S}\right)$	Stat.	Syst.	Total
$0.00 \to 0.20$	0.03	26.6	14.5	30.3
$0.20 \to 0.30$	0.69	7.3	10.6	12.9
$0.30 \to 0.45$	2.02	5.7	5.4	7.8
$0.45 \to 0.60$	2.46	4.2	3.7	5.6
$0.60 \to 1.00$	0.63	10.2	8.9	13.6
Channel: $\mathrm{e}^{+}\mathrm{e}^{-}$		Uncertainties %		
Bin range $[\rho_S]$	$\left(\frac{1}{\sigma}\frac{d\sigma}{d\rho_S}\right)$	Stat.	Syst.	Total
$0.00 \to 0.20$	0.04	22.8	19.7	30.1
$0.20 \to 0.30$	0.70	11.2	11.5	16.0
$0.30 \to 0.45$	2.09	5.4	6.2	8.2
$0.45 \to 0.60$	2.44	4.5	3.5	5.7
$0.60 \to 1.00$	0.61	8.8	8.4	12.2
Channel: $\mu^{+}\mu^{-}$		Uncertainties %		
Bin range $[\rho_S]$	$\left(\frac{1}{\sigma}\frac{d\sigma}{d\rho_S}\right)$	Stat.	Syst.	Total
$0.00 \to 0.20$	0.04	19.5	25.7	32.2
$0.20 \to 0.30$	0.76	9.9	14.2	17.3
$0.30 \to 0.45$	1.96	4.8	7.9	9.3
$0.45 \to 0.60$	2.53	4.1	7.2	8.3
$0.60 \to 1.00$	0.61	8.1	13.1	15.4
Channel: Combined		Uncertainties %		
Bin range $[\rho_S]$	$\left(\frac{1}{\sigma}\frac{d\sigma}{d\rho_S}\right)$	Stat.	Syst.	Total
$0.00 \to 0.20$	0.04	13.0	15.0	19.9
$0.20 \to 0.30$	0.71	5.2	10.4	11.7
$0.30 \to 0.45$	2.02	3.0	5.2	6.1
$0.45 \to 0.60$	2.48	2.5	4.1	4.8
$0.60 \to 1.00$	0.61	5.1	8.2	9.7

Figure H.4 presents the measured differential cross section for all dileptonic channels as well as for their combination, and compares the measurement to predictions obtained form POWHEG $\mathrm{t\bar{t}}$+jet with assumed top quark masses of $m_{\mathrm{t}}^{\mathrm{MC}} = 166.5\,\mathrm{GeV}$, $m_{\mathrm{t}}^{\mathrm{MC}} = 172.5\,\mathrm{GeV}$, and $m_{\mathrm{t}}^{\mathrm{MC}} = 178.5\,\mathrm{GeV}$.

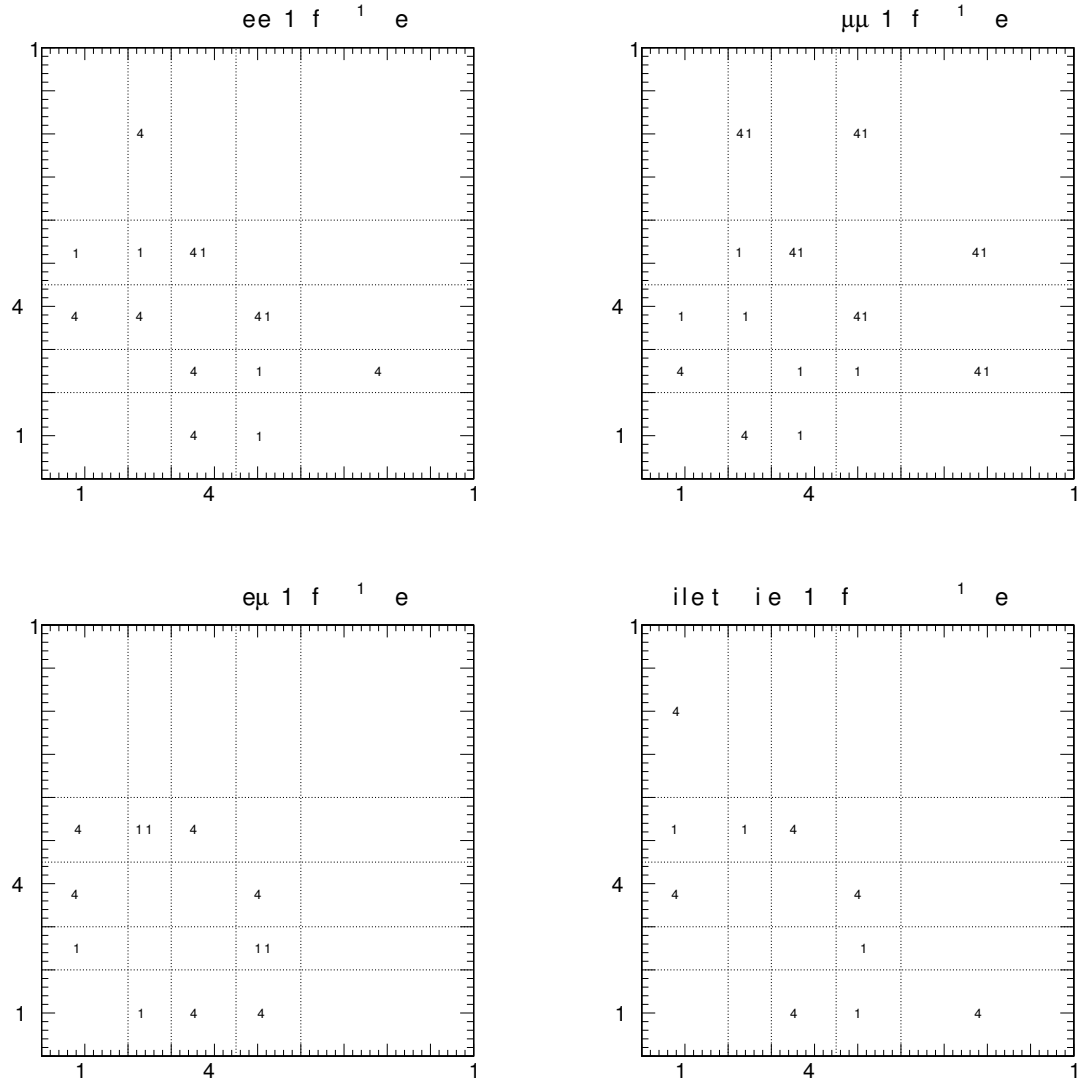

Figure H.3: Normalized statistical correlation matrices from unfolding for the three dilepton final states e^+e^- (top left), $\mu^+\mu^-$ (top right), $e^\pm\mu^\mp$ (bottom left) and the three channels combined (bottom right). The correlations are given in %.

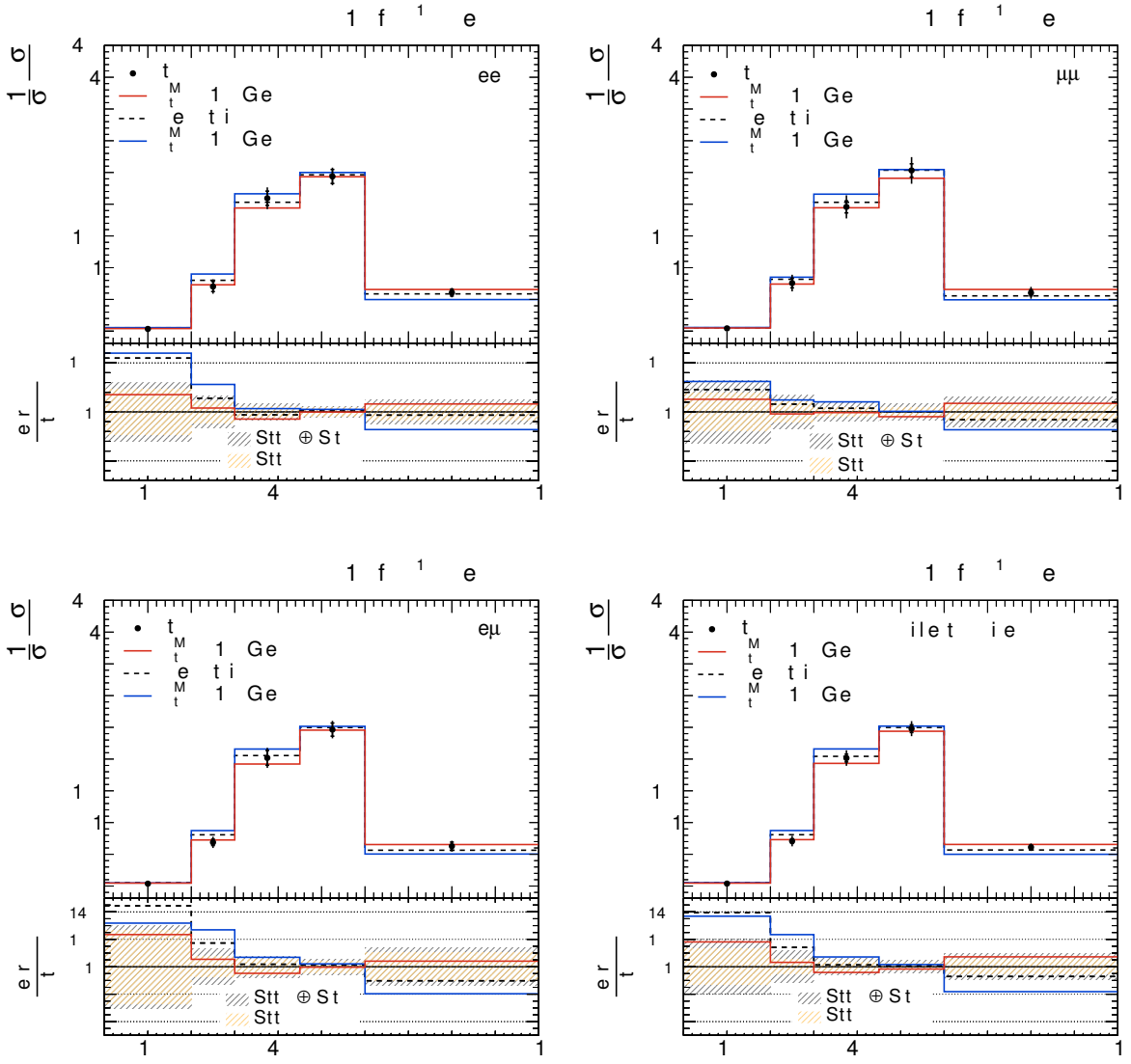

Figure H.4: Normalized differential $\mathrm{t\bar{t}}$+jet production cross section as a function of ρ_S for the channels $\mathrm{e^+e^-}$ (top left), $\mu^+\mu^-$ (top right), and $\mathrm{e^\pm\mu^\mp}$ (bottom left) as well as for their combination (bottom right). Shown are the measured differential cross section together with POWHEG $\mathrm{t\bar{t}}$+jet predictions with $m_\mathrm{t}^\mathrm{MC} = 166.5\,\mathrm{GeV}$ (red), $m_\mathrm{t}^\mathrm{MC} = 172.5\,\mathrm{GeV}$ (dashed), and $m_\mathrm{t}^\mathrm{MC} = 178.5\,\mathrm{GeV}$ (blue). The hatched bands correspond to the statistical (yellow) and total uncertainty (gray).

List of Acronyms

ADC	Analog-digital converter, pp. 21, 39, 48, 50 f., 60 f., 64, 72, 94 f., 97, 107, 123
API	Application programming interface, pp. 66 f.
ATLAS	A Toroidal LHC ApparatuS, pp. 19, 24, 144, 190
BC	Bunch crossing, pp. 49, 70
BORE	Begin-of-run event, pp. 85, 88
CCE	Charge collection efficiency, pp. 38, 48
CDS	Correlated double sampling, p. 80
CERN	European Organization for Nuclear Research, pp. 17, 26
PS	Proton Synchrotron, p. 17
CKF	Combinatorial Kalman filter, pp. 22, 153
CKM	Cabibbo-Kobayashi-Maskawa, pp. 8, 11, 139
CMB	Cosmic microwave background, p. 11
CMS	Compact Muon Solenoid, pp. IX, 2 f., 19 ff., 31, 41, 43, 45 ff., 54, 63 f., 66, 72, 79 f., 82 f., 87 f., 95, 104, 111, 113, 115, 121, 133, 137, 144, 148, 150 ff., 155, 161, 163, 185, 190, 193 ff., 199, 208 f.
CoG	Center of gravity, pp. 40, 61, 98, 105, 116, 123 f., 131, 133
CR	Color reconnection, pp. 147, 164, 169, 189, 192
CSC	Cathode strip chamber, pp. 25, 27
DAC	Digital-to-analog converter, pp. 47 ff., 51, 65, 67, 69 ff., 74, 88, 95, 99, 201
DAQ	Data acquisition, pp. 2, 21, 26, 39, 53, 67 f., 78, 83, 85 ff., 93, 102, 193, 208
DCol	Double column, pp. 47 ff., 97, 99, 110
DCI	Double column interface, pp. 48 f.
DESER160	160 MHz deserializer module, p. 64
DESER400	400 MHz deserializer module, pp. 64, 70
DESY	Deutsches Elektronen-Synchrotron, pp. 47, 54
DT	Drift tube, p. 25
DTB	Digital test board, pp. 63 ff., 72, 74, 81, 83, 88, 95, 198, 208
RPC	Remote procedure call, pp. 66, 68
DUT	Device under test, pp. 44, 67, 78 ff., 86, 88 ff., 98, 101 f., 104 ff., 115 f., 118, 198 f.

DY	Drell-Yan, pp. 150, 154 ff., 162, 165
EB	Barrel electromagnetic calorimeter, p. 23
ECAL	Electromagnetic Calorimeter, pp. 23 f., 152 f.
EE	Endcap electromagnetic calorimeter, p. 23
ES	Preshower electromagnetic calorimeter, p. 23
RC	Run Control, pp. 85 ff.
EWSB	Electroweak symmetry breaking, pp. 10, 19, 140
FED	Front end driver, pp. 21, 55, 64
FIFO	First-in first-out, pp. 50 f.
FPGA	Field Programmable Gate Array, pp. 25, 64 f.
FSM	Finite-state machine, p. 86
GBL	General Broken Lines, pp. 42 f., 61, 79, 90, 92, 102, 106 f.
GSW	Glashow-Salam-Weinberg, pp. 8, 10
HAL	Hardware abstraction layer, pp. 66, 68
HB	Barrel hadronic calorimeter, pp. 24, 27
HCAL	Hadron Calorimeter, pp. 24, 27, 151 f.
HDI	High density interconnect, p. 53
HE	Endcap hadronic calorimeter, pp. 24, 27 f.
HF	Forward hadronic calorimeter, pp. 24, 27
HL-LHC	High-Luminosity LHC, pp. 26 f.
HLT	High level trigger, pp. 26, 28, 148, 151, 215
HO	Outer hadronic calorimeter, p. 24
HPD	Hybrid photodetector, pp. 24, 27
I^2C	Inter-Integrated Circuit, pp. 47, 53, 65
IP	Interaction point, pp. 17 ff., 45, 54, 118, 152 f.
JER	Jet energy resolution, pp. 162, 189
JES	Jet energy scale, pp. 162, 189
L1	Level 1 Trigger, pp. 25 f., 28, 45, 48 ff., 53, 148
LHC	Large Hadron Collider, pp. 1 ff., 13, 17 ff., 25 ff., 31, 45, 47, 51, 82 f., 109, 137 ff., 141, 151, 165, 172, 193 f.
LHCb	Large Hadron Collider beauty, p. 19
LO	Leading order, pp. 9, 150
LS1	Long Shutdown 1, pp. 18 ff., 24 ff., 54, 193
MAD	Mean absolute difference, pp. 61, 94, 105, 114
MAPS	Monolithic active pixel sensor, pp. 36, 80
MC	Monte Carlo, pp. 3, 15, 108, 143, 145 f., 148, 157, 161, 166, 169, 172, 180, 182, 191, 215, 221
M26	Mimosa26, pp. 80 ff., 89, 198
MIP	Minimum ionizing particle, pp. 25, 31, 37, 72
MP-II	Millepede-II, pp. 43, 90, 102
MPV	Most probable value, pp. 37, 61, 96, 105, 107 f., 111, 119, 201, 205
NLO	Next-to-leading order, pp. VII, 3, 9, 138, 140, 143 f., 146 f., 149 f., 172, 182, 185, 187, 189, 191, 195
NNLO	Next-to-next-to-leading order, pp. 148, 150
PCB	Printed circuit board, pp. 79, 198
PDF	Parton distribution function, pp. 12 f., 138, 140, 145 f., 148 f., 162 f., 169, 189
PF	Particle flow, pp. 22 ff., 152 f., 155 f.
PLL	Phase-locked loop, pp. 50 f.
PMT	Photomultiplier tube, pp. 27, 78, 80, 82 f.

PUC	Pixel unit cell, pp. 47 ff., 60, 69 ff., 94, 99, 104, 108, 126
QCD	Quantum chromodynamics, pp. VII, 3, 7, 12 f., 20, 139 f., 145 ff., 149 f., 153
QFT	Quantum field theory, p. 6
RCI	ROC controller and interface, pp. 48, 50 f.
REF	Timing reference, pp. 80, 82, 89, 98, 102, 104 f., 107, 109 ff., 115
RMS	Root mean square, pp. 44, 72, 78, 80, 115, 128 ff.
ROC	Readout chip, pp. 2 f., 36, 45 ff., 53 f., 60, 63 f., 66 ff., 74, 81 ff., 88, 93 ff., 99, 104 f., 107 ff., 111, 113, 115 f., 119, 121, 193 ff., 198 f., 208 f.
RPC	Resistive plate chamber, p. 25
SCM	Single chip module, pp. 47, 57, 69, 79 ff., 87, 94 ff., 102, 104 f., 107 f., 116, 118 f., 198 f., 201 ff.
SCR	Space-charge region, pp. 34 f.
SEU	Single event upset, pp. 27, 47, 55
SiPM	Silicon photomultiplier, pp. 24, 27
SM	Standard model, pp. 1, 3, 5 ff., 15, 19, 137, 140 ff., 146, 194
SPS	Super Proton Synchrotron, p. 17
SVD	Singular value decomposition, p. 176
TBM	Token Bit Manager, pp. 46 f., 53 ff., 64, 66 f., 69 f., 88
TLU	Trigger logic unit, pp. 82 f.
UE	Underlying event, pp. 13, 147 f., 164, 169, 189, 192

Bibliography

[1] R. Lullus, "Arbor scientiæ". Lugdunum, 1515. https://opacplus.bsb-muenchen.de/metaopac/search?id=BV001437374.

[2] S. L. Glashow, "Partial-symmetries of weak interactions", *Nucl. Phys.* **22** (1961), no. 4, 579 – 588, doi:10.1016/0029-5582(61)90469-2.

[3] R. Wideröe, "Über ein neues Prinzip zur Herstellung hoher Spannungen", *Archiv für Elektrotechnik* **21** (1928), no. 4, 387–406, doi:10.1007/BF01656341.

[4] D. W. Kerst, "Acceleration of Electrons by Magnetic Induction", *Phys. Rev.* **58** (Nov, 1940) 841–841, doi:10.1103/PhysRev.58.841.

[5] E. Lawrence, "Method And Apparatus For The Acceleration Of Ions", 1934. US patent no. 1948384 A.

[6] ATLAS Collaboration, "Observation of a New Particle in the Search for the Standard Model Higgs Boson with the ATLAS Detector at the LHC", *Phys. Lett. B* **716** (2012), no. 1, 1 – 29, doi:10.1016/j.physletb.2012.08.020.

[7] CMS Collaboration, "Observation of a New Boson at a Mass of 125 GeV with the CMS Experiment at the LHC", *Phys. Lett. B* **716** (2012), no. 1, 30–61, doi:10.1016/j.physletb.2012.08.021.

[8] Nobel Media AB, "The 2013 Nobel Prize in Physics - Press Release, Nobelprize.org". Online, Dec. 2, 2015. http://www.nobelprize.org/nobel_prizes/physics/laureates/2013.

[9] CDF Collaboration, "Observation of Top Quark Production in $\overline{p}p$ Collisions with the Collider Detector at Fermilab", *Phys. Rev. Lett.* **74** (Apr, 1995) 2626–2631, doi:10.1103/PhysRevLett.74.2626, arXiv:hep-ex/9503002.

[10] D0 Collaboration, "Observation of the Top Quark", *Phys. Rev. Lett.* **74** (Apr, 1995) 2632–2637, doi:10.1103/PhysRevLett.74.2632, arXiv:hep-ex/9503003.

[11] CMS Collaboration, "Measurement of the top quark mass using proton-proton data at $\sqrt{s} = 7$ and 8 TeV", Technical Report CMS-TOP-14-022, CERN, 2015. arXiv:1509.04044.

[12] S. Alioli et al., "A new observable to measure the top-quark mass at hadron colliders", *Eur. Phys. J.* **C73** (2013) 2438, doi:10.1140/epjc/s10052-013-2438-2, arXiv:1303.6415.

[13] S. Alioli, S.-O. Moch, and P. Uwer, "Hadronic top-quark pair-production with one jet and parton showering", *J. High Energy Phys.* **01** (2012) 137, doi:10.1007/JHEP01(2012)137, arXiv:1110.5251.

[14] D. Griffiths, "Introduction to Elementary Particles". Wiley-VCH, 2008.

[15] K. Olive and Particle Data Group, "Review of Particle Physics", *Chin. Phys. C* **38** (2014), no. 9, 090001, doi:10.1088/1674-1137/38/9/090001.

[16] P. A. M. Dirac, "The quantum theory of the electron", *Proc. R. Soc. A* **117** (1928), no. 778, 610–624.

[17] C. D. Anderson, "The Positive Electron", *Phys. Rev.* **43** (Mar, 1933) 491–494, doi:10.1103/PhysRev.43.491.

[18] LHCb Collaboration, "Observation of $J/\psi p$ Resonances Consistent with Pentaquark States in $\Lambda_b^0 \to J/\psi K^- p$ Decays", *Phys. Rev. Lett.* **115** (Aug, 2015) 072001, doi:10.1103/PhysRevLett.115.072001, arXiv:1507.03414.

[19] E. Fermi, "Versuch einer Theorie der β-Strahlen. I", *Z. Phys.* **88** (1934), no. 3-4, 161–177, doi:10.1007/BF01351864.

[20] S. Weinberg, "A Model of Leptons", *Phys. Rev. Lett.* **19** (Nov, 1967) 1264–1266, doi:10.1103/PhysRevLett.19.1264.

[21] B. Naroska, "e^+e^- Physics with the Jade Detector at PETRA", *Physics Reports* **148** (1987), no. 2–3, 67 – 215, doi:10.1016/0370-1573(87)90031-7.

[22] ALEPH, DELPHI, L3, OPAL, SLD Collaborations, The LEP Electroweak Working Group, and The SLD Electroweak and Heavy Flavour Groups, "Precision electroweak measurements on the Z resonance", *Physics Reports* **427** (2006), no. 5–6, 257 – 454, doi:10.1016/j.physrep.2005.12.006, arXiv:hep-ex/0509008.

[23] C. S. Wu et al., "Experimental Test of Parity Conservation in Beta Decay", *Phys. Rev.* **105** (Feb, 1957) 1413–1415, doi:10.1103/PhysRev.105.1413.

[24] J. H. Christenson, J. W. Cronin, V. L. Fitch, and R. Turlay, "Evidence for the 2π Decay of the K_2^0 Meson", *Phys. Rev. Lett.* **13** (Jul, 1964) 138–140, doi:10.1103/PhysRevLett.13.138.

[25] N. Cabibbo, "Unitary Symmetry and Leptonic Decays", *Phys. Rev. Lett.* **10** (Jun, 1963) 531–533, doi:10.1103/PhysRevLett.10.531.

[26] M. Kobayashi and T. Maskawa, "CP-Violation in the Renormalizable Theory of Weak Interaction", *Progr. Theor. Phys.* **49** (1973), no. 2, 652–657, doi:10.1143/PTP.49.652.

[27] SNO Collaboration, "Measurement of the Rate of $\nu_e + d \to p + p + e^-$ Interactions Produced by ^8B Solar Neutrinos at the Sudbury Neutrino Observatory", *Phys. Rev. Lett.* **87** (Jul, 2001) 071301, doi:10.1103/PhysRevLett.87.071301, arXiv:nucl-ex/0106015.

[28] Super-Kamiokande Collaboration, "Evidence for Oscillation of Atmospheric Neutrinos", *Phys. Rev. Lett.* **81** (Aug, 1998) 1562–1567, doi:10.1103/PhysRevLett.81.1562, arXiv:hep-ex/9807003.

[29] Nobel Media AB, "The 2015 Nobel Prize in Physics - Press Release, Nobelprize.org". Online, Oct. 24, 2015. http://www.nobelprize.org/nobel_prizes/physics/laureates/2015.

[30] Z. Maki, M. Nakagawa, and S. Sakata, "Remarks on the Unified Model of Elementary Particles", *Progr. Theor. Phys.* **28** (1962), no. 5, 870–880, doi:10.1143/PTP.28.870, arXiv:http://ptp.oxfordjournals.org/content/28/5/870.full.pdf+html.

[31] B. Delamotte, "A hint of renormalization", *Am. J. Phys.* **72** (2004), no. 2, 170–184, doi:10.1119/1.1624112.

[32] F. Englert and R. Brout, "Broken Symmetry and the Mass of Gauge Vector Mesons", *Phys. Rev. Lett.* **13** (August, 1964) 321–323, doi:10.1103/PhysRevLett.13.321.

[33] P. Higgs, "Broken Symmetries and the Masses of Gauge Bosons", *Phys. Rev. Lett.* **13** (October, 1964) 508–509, doi:10.1103/PhysRevLett.13.508.

[34] G. Guralnik, C. Hagen, and T. Kibble, "Global Conservation Laws and Massless Particles", *Phys. Rev. Lett.* **13** (November, 1964) 585–587, doi:10.1103/PhysRevLett.13.585.

[35] J. Goldstone, A. Salam, and S. Weinberg, "Broken Symmetries", *Phys. Rev.* **127** (Aug, 1962) 965–970, doi:10.1103/PhysRev.127.965.

[36] ATLAS and CMS Collaborations, "Combined Measurement of the Higgs Boson Mass in pp Collisions at $\sqrt{s} = 7$ and 8 TeV with the ATLAS and CMS Experiments", *Phys. Rev. Lett.* **114** (May, 2015) 191803, doi:10.1103/PhysRevLett.114.191803, arXiv:1503.07589.

[37] D. Clowe et al., "A Direct Empirical Proof of the Existence of Dark Matter", *Astrophys. J.* **648** (2006), no. 2, L109, doi:10.1086/508162, arXiv:astro-ph/0608407.

[38] A. Refregier, "Weak Gravitational Lensing by Large-Scale Structure", *Annu. Rev. Astron. Astrophys.* **41** (2003), no. 1, 645–668, doi:10.1146/annurev.astro.41.111302.102207, arXiv:astro-ph/0307212.

[39] WMAP Collaboration, "Seven-year Wilkinson Microwave Anisotropy Probe (WMAP) Observations: Sky Maps, Systematic Errors, and Basic Results", *Astrophys. J. Suppl.* **192** (2011), no. 2, 14, doi:10.1088/0067-0049/192/2/14, arXiv:1001.4744.

[40] WMAP Collaboration, "Seven-year Wilkinson Microwave Anisotropy Probe (WMAP) Observations: Cosmological Interpretation", *Astrophys. J. Suppl.* **192** (2011), no. 2, 18, doi:10.1088/0067-0049/192/2/18, arXiv:1001.4538.

[41] Supernova Search Team Collaboration, "Observational Evidence from Supernovae for an Accelerating Universe and a Cosmological Constant", *Astron. J.* **116** (1998), no. 3, 1009, doi:10.1086/300499, arXiv:astro-ph/9805201.

[42] Supernova Cosmology Project Collaboration, "Measurements of Ω and Λ from 42 High-Redshift Supernovae", *Astrophys. J.* **517** (1999), no. 2, 565, doi:10.1086/307221, arXiv:astro-ph/9812133.

[43] Nobel Media AB, "The 2011 Nobel Prize in Physics - Press Release, Nobelprize.org". Online, Dec. 2, 2015. http://www.nobelprize.org/nobel_prizes/physics/laureates/2011.

[44] S. P. Martin, "A Supersymmetry Primer", ch. 1, pp. 1–153. World Scientific, 2011. arXiv:hep-ph/9709356. doi:10.1142/9789814307505_0001.

[45] M. Schmaltz and D. Tucker-Smith, "Little Higgs Theories", *Annu. Rev. Nucl. Part. Sci.* **55** (2005), no. 1, 229–270, doi:10.1146/annurev.nucl.55.090704.151502, arXiv:hep-ph/0502182.

[46] B. Gripaios, "Lectures on Physics Beyond the Standard Model", arXiv:1503.02636.

[47] J. Gao et al., "The CT10 NNLO Global Analysis of QCD", *Phys. Rev. D* **89** (Feb, 2014) 033009, doi:10.1103/PhysRevD.89.033009, arXiv:1302.6246.

[48] V. N. Gribov and L. N. Lipatov, "Deep inelastic *ep* scattering in perturbation theory", *Sov. J. Nucl. Phys.* **15** (1972) 438–450.

[49] G. Altarelli and G. Parisi, "Asymptotic freedom in parton language", *Nucl. Phys. B* **126** (1977), no. 2, 298 – 318, doi:10.1016/0550-3213(77)90384-4.

[50] Y. L. Dokshitzer, "Calculation of the Structure Functions for Deep Inelastic Scattering and e^+e^- Annihilation by Perturbation Theory in Quantum Chromodynamics.", *Sov. Phys. JETP* **46** (1977) 641–653.

[51] A. Martin, W. Stirling, R. Thorne, and G. Watt, "Parton distributions for the LHC", *Eur. Phys. J. C* **63** (2009), no. 2, 189–285, doi:10.1140/epjc/s10052-009-1072-5, arXiv:0901.0002.

[52] H1 and ZEUS Collaboration, "Combined measurement and QCD analysis of the inclusive $e^{\pm}p$ scattering cross sections at HERA", *J. High Energy Phys.* **2010** (2010), no. 1, doi:10.1007/JHEP01(2010)109, arXiv:0911.0884.

[53] J. Pumplin et al., "New Generation of Parton Distributions with Uncertainties from Global QCD Analysis", *J. High Energy Phys.* **2002** (2002), no. 07, 012, doi:10.1088/1126-6708/2002/07/012, arXiv:hep-ph/0201195.

[54] H.-L. Lai et al., "New parton distributions for collider physics", *Phys. Rev. D* **82** (Oct, 2010) 074024, doi:10.1103/PhysRevD.82.074024, arXiv:1007.2241.

[55] S. D. Drell and T.-M. Yan, "Massive Lepton-Pair Production in Hadron-Hadron Collisions at High Energies", *Phys. Rev. Lett.* **25** (Aug, 1970) 316–320, doi:10.1103/PhysRevLett.25.316.

[56] T. Sjöstrand and M. van Zijl, "A multiple-interaction model for the event structure in hadron collisions", *Phys. Rev. D* **36** (Oct, 1987) 2019–2041, doi:10.1103/PhysRevD.36.2019.

[57] R. Wigmans, "Calorimetry", *AIP Conf. Proc.* **674** (2003), no. 1, 144–168, doi:10.1063/1.1604077.

[58] N. Metropolis and S. Ulam, "The Monte Carlo Method", *JASA* **44** (1949), no. 247, 335–341, doi:10.1080/01621459.1949.10483310.

[59] E. Rutherford, "The scattering of α and β particles by matter and the structure of the atom", *Philos. Mag.* **21** (1911), no. 125, 669–688, doi:10.1080/14786440508637080.

[60] S. Myers and E. Picasso, "The design, construction and commissioning of the CERN large Electron–Positron collider", *Contemp. Phys.* **31** (1990), no. 6, 387–403, doi:10.1080/00107519008213789.

[61] NA62 Collaboration, "NA62: Technical Design Document", Technical Report NA62-10-07, CERN, Geneva, Dec, 2010.

[62] CMS Collaboration, "Pseudorapidity distribution of charged hadrons in proton-proton collisions at $\sqrt{s} = 13\,\text{TeV}$", *Phys. Lett. B* **751** (2015) 143–163, doi:10.1016/j.physletb.2015.10.004, arXiv:1507.05915.

[63] L. Evans and P. Bryant, "LHC Machine", *J. Instrum.* **3** (2008), no. 08, S08001, doi:10.1088/1748-0221/3/08/S08001.

[64] O. S. Brüning et al., "LHC Design Report". CERN, Geneva, 2004.

[65] M. Lamont, "Status of the LHC", *J. Phys. Conf. Ser.* **455** (2013), no. 1, 012001, doi:10.1088/1742-6596/455/1/012001.

[66] CMS Collaboration, "CMS Luminosity - Public Results", 2012. https://twiki.cern.ch/twiki/bin/view/CMSPublic/LumiPublicResults. Accessed: 09.08.2015.

[67] CMS Collaboration, "Public CMS Data Quality Information", 2013. https://twiki.cern.ch/twiki/bin/view/CMSPublic/DataQuality. Accessed: 06.12.2015.

[68] CMS Collaboration, "Measurement of CMS Luminosity", CMS Physics Analysis Summary CMS-PAS-EWK-10-004, CERN, Geneva, 2010.

[69] CMS Collaboration, "Absolute Calibration of the Luminosity Measurement at CMS: Winter 2012 Update", CMS Physics Analysis Summary CMS-PAS-SMP-12-008, CERN, Geneva, 2012.

[70] CMS Collaboration, "CMS Luminosity Based on Pixel Cluster Counting - Summer 2013 Update", CMS Physics Analysis Summary CMS-PAS-LUM-13-001, CERN, Geneva, 2013.

[71] S. van der Meer, "Calibration of the effective beam height in the ISR", Technical Report CERN-ISR-PO-68-31, CERN, Geneva, 1968.

[72] ATLAS Collaboration, "The ATLAS Experiment at the CERN Large Hadron Collider", *J. Instrum.* **3** (August, 2008) S08003, doi:10.1088/1748-0221/3/08/S08003.

[73] CMS Collaboration, "The CMS Experiment at the CERN Large Hadron Collider", *J. Instrum.* **3** (August, 2008) S08004, doi:10.1088/1748-0221/3/08/S08004.

[74] ALICE Collaboration, "The ALICE Experiment at the CERN Large Hadron Collider", *J. Instrum.* **3** (August, 2008) S08002, doi:10.1088/1748-0221/3/08/S08002.

[75] LHCb Collaboration, "The LHCb Detector at the Large Hadron Collider", *J. Instrum.* **3** (August, 2008) S08005, doi:10.1088/1748-0221/3/08/S08005.

[76] LHCf Collaboration et al., "The LHCf detector at the CERN Large Hadron Collider", *J. Instrum.* **3** (2008), no. 08, S08006, doi:10.1088/1748-0221/3/08/S08006.

[77] TOTEM Collaboration, "The TOTEM Experiment at the CERN Large Hadron Collider", *J. Instrum.* **3** (2008), no. 08, S08007, doi:10.1088/1748-0221/3/08/S08007.

[78] J. L. Pinfold, "The MoEDAL Experiment at the LHC", *EPJ Web Conf.* **71** (2014) 00111, doi:10.1051/epjconf/20147100111.

[79] CMS Collaboration, "CMS Physics Technical Design Report Volume I : Detector Performance and Software", Technical Design Report CERN-LHCC-2006-001, CERN, 2006.

[80] CMS Collaboration, "CMS Tracker Detector Performance Results", 2012. https://twiki.cern.ch/twiki/bin/view/CMSPublic/DPGResultsTRK. Accessed: 10.08.2015.

[81] CMS Collaboration, "Description and performance of track and primary-vertex reconstruction with the CMS tracker", *J. Instrum.* **9** (2014), no. 10, P10009, doi:10.1088/1748-0221/9/10/P10009, arXiv:1405.6569.

[82] R. Frühwirth, "Application of Kalman filtering to track and vertex fitting", *Nucl. Instr. Meth. Phys. A* **262** (1987), no. 2–3, 444 – 450, doi:10.1016/0168-9002(87)90887-4.

[83] T. Speer et al., "Track Reconstruction in the CMS Tracker", *Nucl. Instr. Meth. Phys. A* **559** (2006), no. 1, 143 – 147, doi:10.1016/j.nima.2005.11.207.

[84] D. del Re, "Timing performance of the CMS ECAL and prospects for the future", *J. Phys. Conf. Ser.* **587** (2015), no. 1, 012003, doi:10.1088/1742-6596/587/1/012003.

[85] S. Abdullin, V. Abramov, B. Acharya et al., "Design, performance, and calibration of CMS hadron-barrel calorimeter wedges", *EPJ C* **55** (2008), no. 1, 159–171, doi:10.1140/epjc/s10052-008-0573-y.

[86] S. Abdullin et al., "Design, performance, and calibration of the CMS hadron-outer calorimeter", *EPJ C* **57** (2008), no. 3, 653–663, doi:10.1140/epjc/s10052-008-0756-6.

[87] G. Anzivino et al., "Review of the hybrid photo diode tube (HPD) an advanced light detector for physics", *Nucl. Instr. Meth. Phys. A* **365** (1995), no. 1, 76 – 82, doi:10.1016/0168-9002(95)00486-6.

[88] A. Lobanov, "The CMS Outer HCAL SiPM Upgrade", *J. Phys. Conf. Ser.* **587** (2015), no. 1, 012005, doi:10.1088/1742-6596/587/1/012005.

[89] N. Akchurin and R. Wigmans, "Hadron Calorimetry", *Nucl. Instr. Meth. Phys. A* **666** (2012) 80–97, doi:10.1016/j.nima.2011.10.035.

[90] CMS Collaboration, "CMS TriDAS project: Technical Design Report, Volume 1: The Trigger Systems", Technical Design Report CERN-LHCC-2000-038, CERN, Geneva, 2002.

[91] CMS Collaboration, "CMS TriDAS Project: Technical Design Report, Volume 2: Data Acquisition and High-Level Trigger", Technical Design Report CERN-LHCC-2002-026, CERN, Geneva, 2002.

[92] CMS Collaboration, "CMS High Level Trigger", Technical Report CERN-LHCC-2007-021, CERN, Geneva, 2007.

[93] CMS Collaboration, "CMS Technical Design Report for the Level-1 Trigger Upgrade", Technical Report CERN-LHCC-2013-011. CMS-TDR-12, CERN, Geneva, Jun, 2013.

[94] CMS Collaboration, "CMS Technical Design Report for the Phase 1 Upgrade of the Hadron Calorimeter", Technical Report CERN-LHCC-2012-015. CMS-TDR-10, CERN, Geneva, Sep, 2012.

[95] CMS Collaboration, "Technical proposal for the upgrade of the CMS detector through 2020", Technical Report CERN-LHCC-2011-006, CERN, Geneva, Jun, 2011.

[96] CMS Collaboration, "Technical Proposal for the Phase-II Upgrade of the CMS Detector", Technical Report CERN-LHCC-2015-010, CERN, Geneva. Geneva, Jun, 2015.

[97] G. Lutz, "Semiconductor Radiation Detectors: Device Physics". Springer, 2007.

[98] H. Spieler, "Semiconductor Detector Systems (Series on Semiconductor Science and Technology)". Oxford Univ. Press, 2005.

[99] L. Rossi, P. Fischer, T. Rohe, and N. Wermes, "Pixel Detectors (Particle Acceleration and Detection)". Springer Berlin Heidelberg, 2006.

[100] F. Hartmann, "Evolution of Silicon Sensor Technology in Particle Physics". Springer, 2008.

[101] R. Mankel, "Pattern recognition and event reconstruction in particle physics experiments", *Rep. Prog. Phys.* **67** (2004), no. 4, 553, doi:10.1088/0034-4885/67/4/R03, arXiv:physics/0402039.

[102] M. Moll, "Radiation damage in silicon particle detectors: Microscopic defects and macroscopic properties". PhD thesis, Hamburg U., 1999.

[103] A. Junkes, "Influence of radiation induced defect clusters on silicon particle detectors". PhD thesis, Hamburg U., 2011.

[104] V. Van Lint, T. Flanagan, R. Leadon, and J. Naber, "Mechanisms of radiation effects in electronic materials Vol 1". Wiley-Interscience, United States, 1980.

[105] A. Chilingarov, "Temperature dependence of the current generated in Si bulk", *J. Instrum.* **8** (2013), no. 10, P10003, doi:10.1088/1748-0221/8/10/P10003.

[106] Y. Gornushkin et al., "Tracking performance and radiation tolerance of monolithic active pixel sensors", *Nucl. Instr. Meth. Phys. A* **513** (2003), no. 1–2, 291 – 295, doi:10.1016/j.nima.2003.08.050.

[107] H. Bichsel, "Straggling in thin silicon detectors", *Rev. Mod. Phys.* **60** (Jul, 1988) 663–699, doi:10.1103/RevModPhys.60.663.

[108] L. Landau, "On the energy loss of fast particles by ionization", *J. Phys.(USSR)* **8** (1944) 201–205.

[109] P. V. Vavilov, "Ionization losses of high-energy heavy particles", *J. Exp. Theor. Phys.* **5** (1957) 749–751. [Zh. Eksp. Teor. Fiz. 32, 920 (1957)].

[110] W. Shockley, "Currents to Conductors Induced by a Moving Point Charge", *J. Appl. Phys.* **9** (1938), no. 10, 635–636, doi:10.1063/1.1710367.

[111] S. Ramo, "Currents Induced by Electron Motion", *Proc. IRE* **27** (Sept, 1939) 584–585, doi:10.1109/JRPROC.1939.228757.

[112] C. Jacoboni, C. Canali, G. Ottaviani, and A. A. Quaranta, "A review of some charge transport properties of silicon", *Solid-State Electron.* **20** (1977), no. 2, 77 – 89, doi:10.1016/0038-1101(77)90054-5.

[113] "Silicon (Si), Hall scattering factor", in *Group IV Elements, IV-IV and III-V Compounds. Part b*, O. Madelung, U. Rössler, and M. Schulz, eds., volume 41A1b of *Landolt-Börnstein - Group III Condensed Matter*, pp. 1–4. Springer Berlin Heidelberg, 2002.

[114] R. Turchetta, "Spatial resolution of silicon microstrip detectors", *Nucl. Instr. Meth. Phys. A* **335** (1993), no. 1–2, 44 – 58, doi:10.1016/0168-9002(93)90255-G.

[115] E. Belau et al., "Charge collection in silicon strip detectors", *Nucl. Instr. Meth. Phys.* **214** (1983), no. 2–3, 253 – 260, doi:10.1016/0167-5087(83)90591-4.

[116] T. Kawasaki et al., "Measurement of the spatial resolution of wide-pitch silicon strip detectors with large incident angle", *IEEE T. Nucl. Sci.* **44** (Jun, 1997) 708–712, doi:10.1109/23.603738.

[117] S. Cucciarelli and D. Kotlinski, "Pixel Hit Reconstruction", CMS Internal Note CMS-IN-2004-014, CERN, Geneva, 2004.

[118] M. Swartz, "Reconstructing Pixel Hits with Large Pixels", CMS Internal Note, CERN, Geneva, 2006.

[119] V. Chiochia et al., "A novel technique for the reconstruction and simulation of hits in the CMS pixel detector", in *Nuclear Science Symposium Conference Record, 2008. NSS '08. IEEE*, pp. 1909–1912. Oct, 2008. doi:10.1109/NSSMIC.2008.4774762.

[120] M. Swartz et al., "A new technique for the reconstruction, validation, and simulation of hits in the CMS Pixel Detector", *PoS* **Vertex 2007** (Jul, 2007) 035. 37 p.

[121] V. Blobel, "A new fast track-fit algorithm based on broken lines", *Nucl. Instr. Meth. Phys. A* **566** (2006), no. 1, 14 – 17, doi:10.1016/j.nima.2006.05.156.

[122] C. Kleinwort, "General broken lines as advanced track fitting method", *Nucl. Instr. Meth. Phys. A* **673** (2012) 107 – 110, doi:10.1016/j.nima.2012.01.024.

[123] W. Hulsbergen, "The global covariance matrix of tracks fitted with a Kalman filter and an application in detector alignment", *Nucl. Instr. Meth. Phys. A* **600** (2009), no. 2, 471 – 477, doi:10.1016/j.nima.2008.11.094.

[124] V. Blobel, "Software alignment for tracking detectors", *Nucl. Instr. Meth. Phys. A* **566** (2006), no. 1, 5 – 13, doi:10.1016/j.nima.2006.05.157.

[125] V. Blobel, C. Kleinwort, and F. Meier, "Fast alignment of a complex tracking detector using advanced track models", *Comput. Phys. Commun.* **182** (2011), no. 9, 1760 – 1763, doi:10.1016/j.cpc.2011.03.017.

[126] C. C. Paige and M. A. Saunders, "Solution of Sparse Indefinite Systems of Linear Equations", *SIAM J. Numer. Anal.* **12** (1975), no. 4, 617–629, doi:10.1137/0712047.

[127] CMS Collaboration, "Alignment of the CMS tracker with LHC and cosmic ray data", *J. Instrum.* **9** (2014), no. 06, P06009, doi:10.1088/1748-0221/9/06/P06009, arXiv:1403.2286.

[128] D. Kotliński, "Status of the CMS Pixel detector", *J. Instrum.* **4** (2009), no. 03, P03019, doi:10.1088/1748-0221/4/03/P03019.

[129] F. Meier, "Physics Performance with the CMS Pixel Detector", in *Proceedings of PIXEL2014*. Niagara Falls, Canada, Sep, 2014. arXiv:1412.5628.

[130] CMS Collaboration, "The CMS tracker system project: Technical Design Report", Technical Design Report CERN-LHCC-98-006, CERN, Geneva, 1997.

[131] CMS Collaboration, "CMS Technical Design Report for the Pixel Detector Upgrade", Technical Report CERN-LHCC-2012-016. CMS-TDR-11, CERN, Geneva, Sep, 2012.

[132] W. Erdmann et al., "Upgrade plans for the CMS pixel barrel detector", *Nucl. Instr. Meth. Phys. A* **617** (2010), no. 1–3, 534 – 537, doi:10.1016/j.nima.2009.10.029.

[133] T. Rohe, "Drawings of the CMS barrel pixel sensor cells". private communication, 2015.

[134] D. Pitzl et al., "Type inversion in silicon detectors", *Nucl. Instr. Meth. Phys. A* **311** (1992), no. 1, 98 – 104, doi:10.1016/0168-9002(92)90854-W.

[135] W. Erdmann, "The CMS Pixel Detector", *Int. J. Mod. Phys. A* **25** (2010), no. 07, 1315–1337, doi:10.1142/S0217751X10049098.

[136] H. Kästli et al., "Design and performance of the CMS pixel detector readout chip", *Nucl. Instr. Meth. Phys. A* **565** (2006), no. 1, 188 – 194, doi:10.1016/j.nima.2006.05.038, arXiv:physics/0511166.

[137] T. Rohe et al., "Radiation hardness of CMS pixel barrel modules", *Nucl. Instr. Meth. Phys. A* **624** (2010), no. 2, 414 – 418, doi:10.1016/j.nima.2010.03.157, arXiv:1001.0666.

[138] J. Hoss, "Radiation tolerance of the readout chip for the phase I upgrade of the CMS pixel detector", in *Proceedings of TWEPP*. Lisbon, Portugal, 2015. CMS-CR-2015-253.

[139] D. Hits and A. Starodumov, "The CMS Pixel Readout Chip for the Phase 1 Upgrade", *J. Instrum.* **10** (2015), no. 05, C05029, doi:10.1088/1748-0221/10/05/C05029.

[140] B. Meier, "CMS pixel detector with new digital readout architecture", *J. Instrum.* **6** (2011), no. 01, C01011, doi:10.1088/1748-0221/6/01/C01011.

[141] H. Kästli, "Frontend electronics development for the CMS pixel detector upgrade", *Nucl. Instr. Meth. Phys. A* **731** (2013) 88 – 91, doi:10.1016/j.nima.2013.05.056.

[142] B. Meier, "Drawings of the PSI46digV2.1 PUC". private communication, 2014.

[143] F. Gray, "Pulse Code Communication, United States Patent 2632058", March, 1953.

[144] R. Stringer, "A digital readout system for the CMS Phase I Pixel Upgrade", *J. Instrum.* **10** (2015), no. 04, C04037, doi:10.1088/1748-0221/10/04/C04037.

[145] E. Bartz, "Token Bit Manager 08C Chip Documentation", Technical Report CMS Document 12626-v1, Rutgers University, April, 2015.

[146] E. Bartz, "Token Bit Manager 09 Chip Documentation", Technical Report CMS Document 12625-v1, Rutgers University, April, 2015.

[147] B. Verlaat, M. Van Beuzekom, and A. Van Lysebetten, "CO_2 cooling for HEP experiments", in *TWEPP Conference*. Naxos, Greece, 2008. doi:10.5170/CERN-2008-008.328.

[148] L. Feld, W. Karpinski, J. Merz, and M. Wlochal, "CO_2 cooling for the CMS tracker at SLHC", *J. Instrum.* **6** (2011), no. 01, C01091, doi:10.1088/1748-0221/6/01/C01091.

[149] L. Feld et al., "DC–DC powering for the CMS pixel upgrade", *Nucl. Instr. Meth. Phys. A* **732** (2013) 493 – 496, doi:10.1016/j.nima.2013.06.053.

[150] C. Jacoboni and L. Reggiani, "The Monte Carlo method for the solution of charge transport in semiconductors with applications to covalent materials", *Rev. Mod. Phys.* **55** (Jul, 1983) 645–705, doi:10.1103/RevModPhys.55.645.

[151] M. Swartz, "CMS pixel simulations", *Nucl. Instr. Meth. Phys. A* **511** (2003), no. 1–2, 88 – 91, doi:10.1016/S0168-9002(03)01757-1.

[152] M. Swartz, "A Detailed Simulation of the CMS Pixel Sensor", Technical Report CMS-NOTE-2002-027, CERN, Geneva, Jul, 2002.

[153] M. Swartz et al., "Observation, modeling, and temperature dependence of doubly peaked electric fields in irradiated silicon pixel sensors", *Nucl. Instr. Meth. Phys. A* **565** (2006), no. 1, 212 – 220, doi:http://dx.doi.org/10.1016/j.nima.2006.05.002.

[154] M. Berger, J. Coursey, M. Zucker, and J. Chang, "ESTAR, PSTAR, and ASTAR: Computer Programs for Calculating Stopping-Power and Range Tables for Electrons, Protons, and Helium Ions (version 1.2.3)", 2005. Accessed: 08.08.2015.

[155] Synopsis, Inc., "Sentaurus Device". https://www.synopsys.com/Tools/TCAD/DeviceSimulation/Pages/SentaurusDevice.aspx. Accessed: 04.08.2015.

[156] S. Spannagel, B. Meier, and H. Perrey, "The pxarCore Library - Technical Documentation, Reference Manual, and Sample Applications", Technical Report CMS-NOTE-2016-001, CERN, Geneva, Oct, 2015.

[157] Altera Corp., "Nios II Classic Processor Reference Guide", 2015. https://www.altera.com/content/dam/altera-www/global/en_US/pdfs/literature/hb/nios2/n2cpu_nii5v1.pdf. Accessed: 18.11.2015.

[158] E. Corrin, "EUDAQ Software User Manual", *EUDET-Memo-2010-01* (2010).

[159] M. Minano Moya, "CMS Pixel Upgrade for the Phase I: Module Production and Qualification", in *Proceedings of the 10th International "Hiroshima" Symposium*. Xi'an, China, 2015. CMS-CR-2015-263.

[160] T. Behnke et al., "Test Beams at DESY", technical report, DESY, 2007.

[161] DESY Testbeam Coordinators, "DESY-II Test Beams web page". http://testbeam.desy.de/. Accessed: 29.07.2015.

[162] A. Schütz, "Simulation of Particle Fluxes at the DESY-II Test Beam Facility", Master's thesis, Karlsruher Institut für Technologie (KIT), 2015.

[163] P. Schütze, "Energy calibration of the DESY test beam in beamline 21", (2013). DESY Summer Student Report, unpublished.

[164] J. P. Boris, "Relativistic Plasma Simulation - Optimization of a Hybrid Code", in *Proceedings of the 4th Conference on Numerical Simulation of Plasmas*, Naval Res. Lab. Washington, D.C, 1970.

[165] L. Bauerdick et al., "Beam test of silicon strip sensors for the ZEUS micro vertex detector", *Nucl. Instr. Meth. Phys. A* **501** (2003), no. 2–3, 340 – 358, doi:10.1016/S0168-9002(03)00619-3.

[166] H. Jansen et al., "Performance of the EUDET-type beam telescopes", (2016). arXiv:1603.09669. submitted to *Eur. Phys. J. Tech. Instrum.*

[167] EUDET Consortium, "Infrastructure for Detector Research and Development towards the International Linear Collider", technical report, 2012. arXiv:1201.4657.

[168] S. El Yacoubi, "AIDA-2020 Kick-off meeting", technical report, Jun, 2015.

[169] C. Hu-Guo et al., "First reticule size MAPS with digital output and integrated zero suppression for the EUDET-JRA1 beam telescope", *Nucl. Instr. Meth. Phys. A* **623** (2010), no. 1, 480 – 482, doi:10.1016/j.nima.2010.03.043.

[170] J. Baudot et al., "First test results of MIMOSA-26, a fast CMOS sensor with integrated zero suppression and digitized output", in *Nuclear Science Symposium Conference Record (NSS/MIC), 2009 IEEE*, pp. 1169–1173. Oct, 2009. doi:10.1109/NSSMIC.2009.5402399.

[171] D. Cussans, "Description of the JRA1 Trigger Logic Unit (TLU), v0.2c", *EUDET-Memo-2009-04* (2009).

[172] D. Cussans, "Status of the TLU v0.2", *EUDET-Memo-2009-29* (2009).

[173] G. Claus et al., "IPHC & NI Flex RIO DAQ for EUDET Mimosa 26 Beam Telescope", *EUDET-Memo-2010-25* (2010).

[174] B. Bell, "Implementation of a Finite State Machine for the EUDAQ framework", (2015). DESY Summer Student Report, unpublished.

[175] R. Brun and F. Rademakers, "ROOT – An object oriented data analysis framework", *Nucl. Instr. Meth. Phys. A* **389** (1997), no. 1–2, 81 – 86, doi:10.1016/S0168-9002(97)00048-X. New Computing Techniques in Physics Research V.

[176] A. Bolz, "CMS Pixel Upgrade", (2014). DESY Summer Student Report, unpublished.

[177] I. Rubinskiy, "EUTelescope. Offline track reconstruction and DUT analysis software", *EUDET-Memo-2010-12* (2010).

[178] S. Aplin, J. Engels, and F. Gaede, "A production system for massive data processing in ILCSoft", *EUDET-Memo-2009-12* (2009).

[179] F. Gaede and J. Engels, "Marlin et al - A Software Framework for ILC detector R&D", *EUDET-Report-2007-11* (2007).

[180] S. Aplin et al., "LCIO: A persistency framework and event data model for HEP", in *Nuclear Science Symposium and Medical Imaging Conference (NSS/MIC), IEEE*, pp. 2075–2079. Anaheim, CA, Oct, 2012. doi:10.1109/NSSMIC.2012.6551478.

[181] Y. Allkofer et al., "Design and performance of the silicon sensors for the CMS barrel pixel detector", *Nucl. Instr. Meth. Phys. A* **584** (2008), no. 1, 25 – 41, doi:http://dx.doi.org/10.1016/j.nima.2007.08.151.

[182] A. Dorokhov et al., "Tests of silicon sensors for the CMS pixel detector", *Nucl. Instr. Meth. Phys. A* **530** (2004), no. 1–2, 71 – 76, doi:10.1016/j.nima.2004.05.050.

[183] T. Rohe et al., "Position dependence of charge collection in prototype sensors for the CMS pixel detector", *IEEE T. Nucl. Sci.* **51** (June, 2004) 1150–1157, doi:10.1109/TNS.2004.829487, arXiv:physics/0312009.

[184] S. Spannagel, "Test beam campaigns for the CMS Phase I Upgrade pixel readout chip", *J. Instrum.* **9** (2014), no. 12, C12001, doi:10.1088/1748-0221/9/12/C12001, arXiv:1410.1399.

[185] S. Spannagel, "Status of the CMS Phase I Pixel Detector Upgrade", *Nucl. Instr. Meth. Phys. A* (2016) doi:10.1016/j.nima.2016.03.028, arXiv:1511.06084.

[186] W. Weibull, "A statistical distribution function of wide applicability", *J. Appl. Mech.-Trans. ASME* **18** (1951), no. 3, 293–297.

[187] H.-C. Kästli. private communication, 2015.

[188] F. James, "Statistical Methods in Experimental Physics: 2nd Edition". World Scientific Publishing Company, 2006.

[189] D. N. Joanes and C. A. Gill, "Comparing measures of sample skewness and kurtosis", *J. R. Stat. Soc. D* **47** (1998), no. 1, 183–189, doi:10.1111/1467-9884.00122.

[190] S. W. Herb et al., "Observation of a Dimuon Resonance at 9.5 GeV in 400-GeV Proton-Nucleus Collisions", *Phys. Rev. Lett.* **39** (Aug, 1977) 252–255, doi:10.1103/PhysRevLett.39.252.

[191] W. Bernreuther, "Top-quark physics at the LHC", *J. Phys. G* **35** (2008), no. 8, 083001, doi:10.1088/0954-3899/35/8/083001, arXiv:0805.1333.

[192] J. R. Incandela, A. Quadt, W. Wagner, and D. Wicke, "Status and prospects of top-quark physics", *Prog. Part. Nucl. Phys.* **63** (2009), no. 2, 239–292, doi:10.1016/j.ppnp.2009.08.001, arXiv:0904.2499.

[193] ATLAS, CDF, CMS, and D0 Collaboration, "First combination of Tevatron and LHC measurements of the top-quark mass", Analysis Summary ATLAS-CONF-2014-008, CDF-NOTE-11071, CMS-PAS-TOP-13-014, D0-NOTE-6416, CERN, Geneva, 2014. arXiv:1403.4427.

[194] M. Baak et al., "The global electroweak fit at NNLO and prospects for the LHC and ILC", *Eur. Phys. J. C* **74** (2014), no. 9, doi:10.1140/epjc/s10052-014-3046-5, arXiv:1407.3792.

[195] S. Alekhin, A. Djouadi, and S. Moch, "The Top quark and Higgs boson masses and the stability of the electroweak vacuum", *Phys. Lett. B* **716** (2012), no. 1, 214–219, doi:10.1016/j.physletb.2012.08.024, arXiv:1207.0980.

[196] S. Moch et al., "High precision fundamental constants at the TeV scale", arXiv:1405.4781.

[197] U. Langenfeld, S. Moch, and P. Uwer, "Measuring the running top-quark mass", *Phys. Rev. D* **80** (Sep, 2009) 054009, doi:10.1103/PhysRevD.80.054009, arXiv:0906.5273.

[198] CMS Collaboration, "Measurement of the $t\bar{t}$ production cross section in the $e\mu$ channel in pp collisions at $\sqrt{s} = 7$ and 8 TeV", Technical Report CMS-PAS-TOP-13-004, CERN, Geneva, 2013.

[199] W. A. Bardeen, A. J. Buras, D. W. Duke, and T. Muta, "Deep-inelastic scattering beyond the leading order in asymptotically free gauge theories", *Phys. Rev. D* **18** (Dec, 1978) 3998–4017, doi:10.1103/PhysRevD.18.3998.

[200] P. Marquard, A. V. Smirnov, V. A. Smirnov, and M. Steinhauser, "Quark Mass Relations to Four-Loop Order in Perturbative QCD", *Phys. Rev. Lett.* **114** (Apr, 2015) 142002, doi:10.1103/PhysRevLett.114.142002, arXiv:1502.01030.

[201] ATLAS Collaboration, "Determination of the top-quark pole mass using $t\bar{t}$-jet events collected with the ATLAS experiment in 7 TeV *pp* collisions", *J. High Energy Phys.* **2015** (2015), no. 10, doi:10.1007/JHEP10(2015)121, arXiv:1507.01769.

[202] M. A. Dobbs et al., "Les Houches Guidebook to Monte Carlo Generators for Hadron Collider Physics", 2004.

[203] M. L. Mangano and T. J. Stelzer, "Tools for the Simulation of Hard Hadronic Collisions", *Annu. Rev. Nucl. Part. Sci.* **55** (2005), no. 1, 555–588, doi:10.1146/annurev.nucl.55.090704.151505.

[204] J. Alwall et al., "MadGraph 5: going beyond", *J. High Energy Phys.* **2011** (2011), no. 6, doi:10.1007/JHEP06(2011)128.

[205] T. Sjöstrand, S. Mrenna, and P. Skands, "PYTHIA 6.4 physics and manual", *J. High Energy Phys.* **2006** (2006), no. 05, 026, doi:10.1088/1126-6708/2006/05/026, arXiv:hep-ph/0603175.

[206] P. Skands, "Tuning Monte Carlo generators: The Perugia tunes", *Phys. Rev. D* **82** (Oct, 2010) 074018, doi:10.1103/PhysRevD.82.074018.

[207] G. Corcella et al., "HERWIG 6: an event generator for hadron emission reactions with interfering gluons (including supersymmetric processes)", *J. High Energy Phys.* **2001** (2001), no. 01, 010, doi:10.1088/1126-6708/2001/01/010, arXiv:hep-ph/0011363.

[208] S. Frixione and B. R. Webber, "Matching NLO QCD computations and parton shower simulations", *J. High Energy Phys.* **2002** (2002), no. 06, 029, doi:10.1088/1126-6708/2002/06/029, arXiv:hep-ph/0204244.

[209] P. Nason, "A new method for combining NLO QCD with shower Monte Carlo algorithms", *J. High Energy Phys.* **2004** (2004), no. 11, 040, doi:10.1088/1126-6708/2004/11/040.

[210] S. Frixione, P. Nason, and C. Oleari, "Matching NLO QCD computations with parton shower simulations: the POWHEG method", *J. High Energy Phys.* **2007** (2007), no. 11, 070, doi:10.1088/1126-6708/2007/11/070.

[211] S. Alioli, P. Nason, C. Oleari, and E. Re, "A general framework for implementing NLO calculations in shower Monte Carlo programs: the POWHEG BOX", *J. High Energy Phys.* **2010** (2010), no. 6, doi:10.1007/JHEP06(2010)043.

[212] E. Boos et al., "Generic User Process Interface for Event Generators", (2001). arXiv:hep-ph/0109068. Physics at TeV Colliders II Workshop, Les Houches, France.

[213] J. Alwall et al., "A standard format for Les Houches Event Files", *Comput. Phys. Commun.* **176** (2007), no. 4, 300 – 304, doi:10.1016/j.cpc.2006.11.010, arXiv:hep-ph/0609017.

[214] V. V. Sudakov, "Vertex parts at very high-energies in quantum electrodynamics", *Sov. Phys. JETP* **3** (1956) 65–71. Zh. Eksp. Teor. Fiz. (1956) **30** 87.

[215] B. Andersson, G. Gustafson, G. Ingelman, and T. Sjöstrand, "Parton fragmentation and string dynamics", *Phys.Rept.* **97** (1983), no. 2–3, 31–145, doi:10.1016/0370-1573(83)90080-7.

[216] B. Webber, "A QCD model for jet fragmentation including soft gluon interference", *Nucl. Phys. B* **238** (1984), no. 3, 492 – 528, doi:10.1016/0550-3213(84)90333-X.

[217] G. Marchesini and B. Webber, "Monte Carlo simulation of general hard processes with coherent QCD radiation", *Nucl. Phys. B* **310** (1988), no. 3–4, 461–526, doi:10.1016/0550-3213(88)90089-2.

[218] D. Amati and G. Veneziano, "Preconfinement as a property of perturbative QCD", *Phys. Lett. B* **83** (1979), no. 1, 87 – 92, doi:10.1016/0370-2693(79)90896-7.

[219] S. Argyropoulos and T. Sjöstrand, "Effects of color reconnection on $t\bar{t}$ final states at the LHC", *J. High Energy Phys.* **11** (2014) 43, doi:10.1007/JHEP11(2014)043, arXiv:1407.6653.

[220] T. Sjöstrand, "Colour reconnection and its effects on precise measurements at the LHC", in *Proceedings, 48th Rencontres de Moriond on QCD and High Energy Interactions*, pp. 247–251. 2013. arXiv:1310.8073.

[221] S. Agostinelli et al., "Geant4 – a simulation toolkit", *Nucl. Instr. Meth. Phys. A* **506** (2003), no. 3, 250 – 303, doi:10.1016/S0168-9002(03)01368-8.

[222] P. Artoisenet, R. Frederix, O. Mattelaer, and R. Rietkerk, "Automatic spin-entangled decays of heavy resonances in Monte Carlo simulations", *J. High Energy Phys.* **2013** (2013), no. 3, doi:10.1007/JHEP03(2013)015, arXiv:1212.3460.

[223] M. L. Mangano, M. Moretti, F. Piccinini, and M. Treccani, "Matching matrix elements and shower evolution for top-pair production in hadronic collisions", *J. High Energy Phys.* **0701** (2007), no. 01, 013, doi:10.1088/1126-6708/2007/01/013, arXiv:hep-ph/0611129.

[224] CMS Collaboration, "Measurement of the underlying event activity at the LHC with $\sqrt{s} = 7\,\text{TeV}$ and comparison with $\sqrt{s} = 0.9\,\text{TeV}$", *J. High Energy Phys.* **2011** (2011), no. 9, doi:10.1007/JHEP09(2011)109, arXiv:1107.0330.

[225] M. Czakon, P. Fiedler, and A. Mitov, "Total Top-Quark Pair-Production Cross Section at Hadron Colliders Through $\mathcal{O}(\alpha_S^4)$", *Phys. Rev. Lett.* **110** (Jun, 2013) 252004, doi:10.1103/PhysRevLett.110.252004, arXiv:1303.6254.

[226] S. Alioli, "Consultation concerning the POWHEG ttJ process". private communication, 2015.

[227] E. Re, "Single-top Wt-channel production matched with parton showers using the POWHEG method", *Eur. Phys. J. C* **71** (2011), no. 2, doi:10.1140/epjc/s10052-011-1547-z, arXiv:1009.2450.

[228] K. Melnikov and F. Petriello, "W Boson Production Cross Section at the Large Hadron Collider with $\mathcal{O}(\alpha_s^2)$ Corrections", *Phys. Rev. Lett.* **96** (Jun, 2006) 231803, doi:10.1103/PhysRevLett.96.231803, arXiv:hep-ph/0603182.

[229] K. Melnikov and F. Petriello, "Electroweak gauge boson production at hadron colliders through $\mathcal{O}(\alpha_s^2)$", *Phys. Rev. D* **74** (Dec, 2006) 114017, doi:10.1103/PhysRevD.74.114017, arXiv:hep-ph/0609070.

[230] N. Kidonakis, "Two-loop soft anomalous dimensions for single top quark associated production with a W^- or H^-", *Phys. Rev. D* **82** (Sep, 2010) 054018, doi:10.1103/PhysRevD.82.054018, arXiv:hep-ph/1005.4451.

[231] J. Campbell, R. Ellis, and C. Williams, "Vector boson pair production at the LHC", *J. High Energy Phys.* **1107** (2011), no. 7, 018, doi:10.1007/JHEP07(2011)018, arXiv:1105.0020.

[232] J. Campbell and R. Ellis, "$\mathrm{t\bar{t}W^{\pm}}$ production and decay at NLO", *J. High Energy Phys.* **52** (2012), no. 7, doi:10.1007/JHEP07(2012)052, arXiv:1204.5678.

[233] CMS Collaboration, "Particle-Flow Event Reconstruction in CMS and Performance for Jets, Taus, and MET", CMS Physics Analysis Summary CMS-PAS-PFT-09-001, CERN, Geneva, 2009.

[234] CMS Collaboration, "Particle-flow commissioning with muons and electrons from J/ψ and W events at 7 TeV", CMS Physics Analysis Summary CMS-PAS-PFT-10-003, CERN, Geneva, 2010.

[235] CMS Collaboration, "Commissioning of the Particle-Flow reconstruction in Minimum-Bias and Jet Events from pp Collisions at 7 TeV", Technical Report CMS-PAS-PFT-10-002, CERN, Geneva, 2010.

[236] W. Waltenberger, R. Frühwirth, and P. Vanlaer, "Adaptive vertex fitting", *J. Phys. G* **34** (2007), no. 12, N343, doi:10.1088/0954-3899/34/12/N01.

[237] CMS Collaboration, "Performance of CMS muon reconstruction in pp collision events at $\sqrt{s} = 7\,\mathrm{TeV}$", *J. Instrum.* **7** (2012), no. 10, P10002, doi:10.1088/1748-0221/7/10/P10002, arXiv:1206.4071.

[238] CMS Collaboration, "Electron reconstruction and identification at $\sqrt{s} = 7\,\mathrm{TeV}$", CMS Physics Analysis Summary CMS-PAS-EGM-10-004, CERN, Geneva, 2010.

[239] W. Adam, R. Frühwirth, A. Strandlie, and T. Todorov, "Reconstruction of electrons with the Gaussian-sum filter in the CMS tracker at the LHC", *J. Phys. G* **31** (2005), no. 9, N9, doi:10.1088/0954-3899/31/9/N01, arXiv:physics/0306087.

[240] Y. Dokshitzer, G. Leder, S. Moretti, and B. Webber, "Better jet clustering algorithms", *J. High Energy Phys.* **1997** (1997), no. 08, 001, doi:10.1088/1126-6708/1997/08/001, arXiv:hep-ph/9707323.

[241] S. D. Ellis and D. E. Soper, "Successive combination jet algorithm for hadron collisions", *Phys. Rev. D* **48** (Oct, 1993) 3160–3166, doi:10.1103/PhysRevD.48.3160.

[242] M. Cacciari, G. P. Salam, and G. Soyez, "The anti-k_T jet clustering algorithm", *J. High Energy Phys.* **2008** (2008), no. 04, 063, doi:10.1088/1126-6708/2008/04/063, arXiv:0802.1189.

[243] CMS Collaboration, "Determination of jet energy calibration and transverse momentum resolution in CMS", *J. Instrum.* **6** (2011), no. 11, P11002, doi:10.1088/1748-0221/6/11/P11002, arXiv:1107.4277.

[244] CMS Collaboration, "Performance of b tagging at $\sqrt{s} = 8\,\text{TeV}$ in multijet, $\mathrm{t\bar{t}}$ and boosted topology events", CMS Physics Analysis Summary CMS-PAS-BTV-13-001, CERN, Geneva, 2013.

[245] CMS Collaboration, "Performance of Missing Transverse Momentum Reconstruction Algorithms in Proton-Proton Collisions at $\sqrt{s} = 8\,\text{TeV}$ with the CMS Detector", CMS Physics Analysis Summary CMS-PAS-JME-12-002, CERN, Geneva, 2013.

[246] D0 Collaboration, "Measurement of the Top Quark Mass Using Dilepton Events", *Phys. Rev. Lett.* **80** (Mar, 1998) 2063–2068, doi:10.1103/PhysRevLett.80.2063, arXiv:hep-ex/9706014.

[247] CMS Collaboration, "Measurement of differential top-quark-pair production cross sections in pp collisions at $\sqrt{s} = 7\,\text{TeV}$", *Eur. Phys. J. C* **73** (2013), no. 3, doi:10.1140/epjc/s10052-013-2339-4, arXiv:1211.2220.

[248] CMS Collaboration, "Measurement of the $\mathrm{t\bar{t}}$ production cross section and the top quark mass in the dilepton channel in pp collisions at $\sqrt{s} = 7\,\text{TeV}$", *J. High Energy Phys.* **2011** (2011), no. 7, doi:10.1007/JHEP07(2011)049, arXiv:1105.5661.

[249] CMS Collaboration, "Measurement of the $\mathrm{t\bar{t}}$ production cross section in the dilepton channel in pp collisions at $\sqrt{s} = 7\,\text{TeV}$", *J. High Energy Phys.* **11** (2012) 67, doi:10.1007/JHEP11(2012)067, arXiv:1208.2671.

[250] C. Diez Pardos and J. Kieseler, "Dilepton trigger and lepton identification efficiencies for the top quark pair production cross section measurement at 8 TeV in the dilepton decay channel", CMS Analysis Note CMS-AN-2012-389, CERN, Geneva, 2013. Unpublished.

[251] CMS Collaboration, "Jet Energy Resolution in CMS at $\sqrt{s} = 7\,\text{TeV}$", CMS Physics Analysis Summary CMS-PAS-JME-10-014, CERN, Geneva, 2011.

[252] CMS Collaboration, "Identification of b-quark jets with the CMS experiment", *J. Instrum.* **8** (2013), no. 04, P04013, doi:10.1088/1748-0221/8/04/P04013.

[253] CMS Collaboration, "Measurement of the $\mathrm{t\bar{t}}$ production cross section in the dilepton channel in pp collisions at $\sqrt{s} = 8\,\text{TeV}$", *J. High Energy Phys.* **2014** (2014), no. 2, doi:10.1007/JHEP02(2014)024, arXiv:1312.7582.

[254] CMS Collaboration, "Measurement of the Jet Multiplicity in dileptonic Top Quark Pair Events at 8 TeV", Technical Report CMS-PAS-TOP-12-041, CERN, Geneva, 2013. arXiv:1510.03072.

[255] TOTEM Collaboration, "First measurement of the total proton-proton cross-section at the LHC energy of $\sqrt{s} = 7\,\text{TeV}$", *Europhys. Lett.* **96** (2011), no. 2, 21002, doi:10.1209/0295-5075/96/21002.

[256] CMS Collaboration, "Measurement of jet multiplicity distributions in $\mathrm{t\bar{t}}$ production in *pp* collisions at $\sqrt{s} = 7\,\mathrm{TeV}$", *Eur. Phys. J. C* **74** (2014), no. 8, doi:10.1140/epjc/s10052-014-3014-0, arXiv:1404.3171.

[257] CMS Collaboration, "Measurement of the differential cross section for top quark pair production in pp collisions at $\sqrt{s} = 8\,\mathrm{TeV}$", *Eur. Phys. J. C* **75** (2015), no. 11, doi:10.1140/epjc/s10052-015-3709-x, arXiv:1505.04480.

[258] CMS Collaboration, "Determination of the top-quark pole mass and strong coupling constant from the $\mathrm{t\bar{t}}$ production cross section in pp collisions at $\sqrt{s} = 7\,\mathrm{TeV}$", *Phys. Lett. B* **728** (2014) 496 – 517, doi:10.1016/j.physletb.2013.12.009, arXiv:1307.1907.

[259] V. Blobel, "Unfolding - Linear Inverse Problems", in *Alliance Workshop on Unfolding and Data Correction*, DESY. Hamburg, Germany, May, 2002. https://www.wiki.terascale.de/images/a/a8/Blobel_Unfold_Note_20100524.pdf. Accessed: 11.11.2015.

[260] A. Hocker and V. Kartvelishvili, "SVD approach to data unfolding", *Nucl. Instr. Meth. Phys. A* **A372** (1996) 469–481, doi:10.1016/0168-9002(95)01478-0, arXiv:hep-ph/9509307.

[261] V. Blobel, "An Unfolding method for high-energy physics experiments", in *Proceedings of Advanced statistical techniques in particle physics*, pp. 258–267. Durham, UK, March, 2002. arXiv:hep-ex/0208022.

[262] D.-J. Fischer, "Inclusive Neutral Current *ep* Cross Sections with HERA II and Two-dimensional Unfolding". PhD thesis, Hamburg U., 2011.

[263] A. Thikhonov, "On the solution of improperly posed problems and the method of regularization", *Sov. Math* **5** (1963) 1035.

[264] S. Schnake, "Material-mapping with multiple scattering of the CMS Pixel Detector", (2015). DESY Summer Student Report, unpublished.

[265] D. Pitzl, "Module Test Beam Measurements". private communication, 2015.

Acknowledgments

Finally, I would like to thank all those who supported me during my PhD and contributed to its success. First and foremost I would like to thank Doris Eckstein, Erika Garutti and Joachim Mnich for their supervision, help and support. Furthermore I am grateful to Martin Pohl, who volunteered his time to evaluate and review my thesis. I would also like to thank the committee of my disputation: María Aldaya Martín, Elisabetta Gallo and Jan Louis.

Thank you Doris Eckstein for always having an open door and open ears for my inquiries. I very much enjoyed working with you as you provided me with the freedom to chose my projects independently while always being there for constructive discussions.

Thank you Daniel Pitzl for sharing your in-depth knowledge of silicon detectors and your way of analytical thinking and problem solving – down at the test beam and in the final analysis.

Thank you Carmen Diez Pardos for being so patient with me. I learned a lot from you when we were working together on our analysis – this includes top physics, MC generators, but also collaboration politics. I am still very much impressed by your motivation, insistence and power.

I would like to thank everyone involved in the support, maintenance and upgrades of the beam telescopes at the DESY test beams and the related software projects – from both CMS and ATLAS. Somehow we managed to have a great time and being productive at the same time.

Thank you to all my colleagues in the CMS detector group and CMS top quark group as well as the CMS group of the University of Hamburg who made me enjoy my time at DESY. Thanks for the occasional barbecues, movie nights, theater visits, joint dinners, the Feierabend beers, picnics, Kicker, and the great time at all the DPGs we went to together!

I think it would be inappropriate to thank Ali Harb for being the best office mate possible – it seems more like a built-in feature than a forced attribute. But I do thank him for the great time we had together, the quick-and-restful holidays on Rügen and in the south, the countless cinema visits, Lebanese dinners, puns, brief Arabic lessons, you name it.

Special thanks go to Jan Hoß, Carmen Diez Pardos and Doris Eckstein for the diligent corrections, helpful advices and countless discussions which shaped this thesis. Also Adrian Perianu and Paul Schütze proofread and corrected some chapters, for which I am grateful.

And last but not least I would like to thank my parents Karin and Hans-Georg Spannagel and my sister Janika for supporting me all these years of my education. You have been a constant source of motivation, you were always interested in science in general and in my work in particular. You have always been reassuring and affirmative in difficult situations, be it professional or private nature, and have helped me enormously to finish this project successfully. Thank you!